



biosensors

Special Issue Reprint

Smart and Multifunctional Nanomaterials and Applications for Food Safety

Edited by
Long Wu, Xiaoqian Tang and Wenbo Yu

mdpi.com/journal/biosensors



Smart and Multifunctional Nanomaterials and Applications for Food Safety

Smart and Multifunctional Nanomaterials and Applications for Food Safety

Editors

Long Wu

Xiaoqian Tang

Wenbo Yu



Basel • Beijing • Wuhan • Barcelona • Belgrade • Novi Sad • Cluj • Manchester

Editors

Long Wu
College of Food Science
and Engineering
Hainan University
Haikou, China

Xiaoqian Tang
Oil Crops Research Institute
Chinese Academy of
Agricultural Sciences
Wuhan, China

Wenbo Yu
College of
Veterinary Medicine
China Agricultural University
Beijing, China

Editorial Office

MDPI
St. Alban-Anlage 66
4052 Basel, Switzerland

This is a reprint of articles from the Special Issue published online in the open access journal *Biosensors* (ISSN 2079-6374) (available at: https://www.mdpi.com/journal/biosensors/special_issues/nano_food).

For citation purposes, cite each article independently as indicated on the article page online and as indicated below:

Lastname, A.A.; Lastname, B.B. Article Title. <i>Journal Name</i> Year , <i>Volume Number</i> , Page Range.
--

ISBN 978-3-0365-9482-8 (Hbk)

ISBN 978-3-0365-9483-5 (PDF)

doi.org/10.3390/books978-3-0365-9483-5

© 2023 by the authors. Articles in this book are Open Access and distributed under the Creative Commons Attribution (CC BY) license. The book as a whole is distributed by MDPI under the terms and conditions of the Creative Commons Attribution-NonCommercial-NoDerivs (CC BY-NC-ND) license.

Contents

About the Editors	vii
Long Wu Smart and Multifunctional Nanomaterials and Applications for Food Safety Reprinted from: <i>Biosensors</i> 2023 , <i>13</i> , 928, doi:10.3390/bios13100928	1
Cheng Zhao, Shanshan Xu, Jing Wei, Siqi Xie, Jinlei Wei, Jingting Han, et al. Enhanced Response for Foodborne Pathogens Detection by Au Nanoparticles Decorated ZnO Nanosheets Gas Sensor Reprinted from: <i>Biosensors</i> 2022 , <i>12</i> , 803, doi:10.3390/bios12100803	5
Yuting Wang, Xingjun Xi, Liao Wang and Yisheng Chen HPTLC-Bioluminescent Bioautography Screening of Herbal Teas for Adulteration with Hypolipidemic Drugs Reprinted from: <i>Biosensors</i> 2023 , <i>13</i> , 392, doi:10.3390/bios13030392	19
Ming Zou, Yongkang Yin, Liuchuan Guo, Qidi Zhang, Jinyan Li, Hong Zhang, et al. A Europium Nanosphere-Based Time-Resolved Fluorescent Immunochromatographic Assay for the Rapid Screening of 4,4'-Dinitrocarbanilide: Aiming at Improving Strip Method Performance Reprinted from: <i>Biosensors</i> 2023 , <i>13</i> , 518, doi:10.3390/bios13050518	29
Ke Wang, Xiaogang Lin, Maoxiao Zhang, Yu Li, Chunfeng Luo and Jayne Wu Review of Electrochemical Biosensors for Food Safety Detection Reprinted from: <i>Biosensors</i> 2022 , <i>12</i> , 959, doi:10.3390/bios12110959	41
Muhammad Azhar Hayat Nawaz, Muhammad Waseem Fazal, Naeem Akhtar, Mian Hasnain Nawaz, Akhtar Hayat and Cong Yu Multifunctional Smart ZnSe-Nanostructure-Based Fluorescent Aptasensor for the Detection of Ochratoxin A Reprinted from: <i>Biosensors</i> 2022 , <i>12</i> , 844, doi:10.3390/bios12100844	67
Cheng Yang, Fathimath Abbas, Amina Rhouati, Yingying Sun, Xiaolin Chu, Shengnan Cui, et al. Design of a Quencher-Free Fluorescent Aptasensor for Ochratoxin A Detection in Red Wine Based on the Guanine-Quenching Ability Reprinted from: <i>Biosensors</i> 2022 , <i>12</i> , 297, doi:10.3390/bios12050297	83
Cheng Yang, Xiaolin Chu, Li Zeng, Amina Rhouati, Fathimath Abbas, Shengnan Cui and Daiqin Lin Development of Fluorescent Aptasensors Based on G-Quadruplex Quenching Ability for Ochratoxin A and Potassium Ions Detection Reprinted from: <i>Biosensors</i> 2022 , <i>12</i> , 423, doi:10.3390/bios12060423	95
Hui Xu, Xin You, Yue Lu, Peng Liang, Zhihui Luo, Yiwei Wang, et al. Analysis of Mn ²⁺ and Zn ²⁺ Ions in Macroalgae with Heteroelement-Doped Carbon-Based Fluorescent Probe Reprinted from: <i>Biosensors</i> 2022 , <i>12</i> , 359, doi:10.3390/bios12050359	107
Xiang Li, Junsong Wu, Huaguang Hu, Fangfang Liu and Jialian Wang A Smartphone Integrated Platform for Ratiometric Fluorescent Sensitive and Selective Determination of Dipicolinic Acid Reprinted from: <i>Biosensors</i> 2022 , <i>12</i> , 668, doi:10.3390/bios12080668	123

Chao Yuan, Yanan Zhao, Xingjun Xi and Yisheng Chen Non-Destructive Screening of Sodium Metabisulfite Residue on Shrimp by SERS with Copy Paper Loaded with AgNP Reprinted from: <i>Biosensors</i> 2023 , <i>13</i> , 575, doi:10.3390/bios13060575	131
Yihan Lang, Biao Zhang, Danfeng Cai, Wanjun Tu, Jingyi Zhang, Xuping Shentu, et al. Determination Methods of the Risk Factors in Food Based on Nanozymes: A Review Reprinted from: <i>Biosensors</i> 2023 , <i>13</i> , 69, doi:10.3390/bios13010069	141
Shuhong Zhou, Chen Liu, Jianguo Lin, Zhi Zhu, Bing Hu and Long Wu Towards Development of Molecularly Imprinted Electrochemical Sensors for Food and Drug Safety: Progress and Trends Reprinted from: <i>Biosensors</i> 2022 , <i>12</i> , 369, doi:10.3390/bios12060369	161
Si Wu, Shijing Wu, Xinyue Zhang, Tao Feng and Long Wu Chitosan-Based Hydrogels for Bioelectronic Sensing: Recent Advances and Applications in Biomedicine and Food Safety Reprinted from: <i>Biosensors</i> 2023 , <i>13</i> , 93, doi:10.3390/bios13010093	175

About the Editors

Long Wu

Long Wu graduated with a degree in Huazhong Agriculture University and a Ph.D. degree in Huazhong Agriculture University in 2017. Long is now an Associated Professor at the College of Food Science and Engineering of the Hainan University. His research interests include all kinds of biomaterials-based analytical techniques (electrochemistry, electrochemiluminescence, fluorometric analysis, SERS, etc.) and functional nanomaterials for food and environmental analyses, bioanalysis, and bioimaging. Long has participated in more than 10 scientific projects, being the coordinator of 6 projects. The knowledge developed in these projects has generated some development contracts and technology transfer to various companies. To date, Long has contributed 78 scientific publications, 70 of which are in SCI journals with referees. Long is a member of CCS and a reviewer for different international journals.

Xiaoqian Tang

Xiaoqian Tang received her Ph.D. degree from the Chinese Academy of Agricultural Sciences in 2020. She is now an associate professor at the Oil Crops Research Institute of the Chinese Academy of Agricultural Sciences. Her research mainly focuses on the development of bioreceptors (monoclonal antibody, nanobody, etc.) and immunoassays for hazard factors (such as mycotoxin, pesticide, and benzopyrene) in agri-food.

Wenbo Yu

Wenbo Yu received his Ph.D. degree from Ludwig-Maximilians-University in Munich in 2017. He is now an associate professor at the College of Veterinary Medicine of China Agricultural University. His research mainly focuses on: (I) The development of novel immunochemical methods and biosensors based on nanomaterials, such as nanoparticles, nanoclusters, and quantum dots. (II) Establishing microfluidic chip and compact device-based analytical platform for antibiotics, toxins, and pathogens detection. (III) Microfluidic single-cell analysis tools used for the discovery of bio-recognition materials (antibodies, receptors, aptamers, peptides, etc.)



Editorial

Smart and Multifunctional Nanomaterials and Applications for Food Safety

Long Wu ^{1,2}

¹ Hainan Engineering Research Center of Aquatic Resources Efficient Utilization in South China Sea, Key Laboratory of Seafood Processing of Haikou, School of Food Science and Technology, Hainan University, Haikou 570228, China; longquan.good@163.com; Tel.: +86-0898-66193581

² Key Laboratory of Tropical Fruits and Vegetables Quality and Safety for State Market Regulation, Hainan Institute for Food Control, Haikou 570314, China

Due to growing concerns about food safety and public health, the contaminants or residues of various harmful substances in food have received much attention in recent years [1–3]. With the increasing complexity of the food supply chain and the expansion of the scale of food production, more stringent regulations and standards are now required for food quality and safety [4–6]. Thus, it is indispensable to develop an efficient detection method to analyze all kinds of foodstuffs. Currently, the most commonly used detection methods, including high-performance liquid chromatography (HPLC), gas chromatography (GC), gas chromatography–mass spectrometry (GC-MS), and liquid chromatography–mass spectrometry (LC-MS), are demonstrated to have exceptional sensitivity and selectivity, but suffer from limitations such as being time-consuming procedures requiring expensive equipment and professional operations [7–10]. Fortunately, the advancement of smart and functional nanomaterials endows rapid detection methods with flexible construction strategies and facile applications, which include Raman technique-based [11,12], electrochemical [13], and electrochemiluminescence analyses [14], fluorescence measurement [15,16] and immunoassays, and so on [17,18]. By adopting nanomaterials, the sensitivity and accuracy of rapid detection methods can be greatly enhanced, making them highly applicable in the field of food safety analysis.

In this Special Issue, we focused on advances in nanomaterial-modified rapid detection methods for food safety detection and analysis. With the rapid development of nanotechnology, all kinds of new nanomaterials, including organic nanomaterials, fluorescent nanomaterials, nanozymes, and carbon-based nanomaterials, have been adopted in analytical methods [19,20]. Newly emerging nanomaterials have high specific surface areas, enabling higher catalytic and sensing responses as well as better optical, magnetic, and electrical performance [21]. Also, such nanomaterials can serve as smart and functional elements in many tools, such as in microfluidic assay devices (μ FADs) [22], micro-electromechanical systems [23], optical sensors [24,25], force or pressure sensors [26], magnetic relaxing sensors [27], etc. The application of such nanomaterials can greatly enhance the performance of biosensors, including their sensitivity, selectivity, and accuracy, thereby advancing the development of food safety detection technologies.

This Special Issue has collected a diversity of studies that focus on smart and functional nanomaterial-fabricated biosensors in food safety. It includes four review articles, three communications, and six research articles, which I briefly describe in the next paragraphs. This Editorial aspires to describe the advances of nanomaterials in food safety applications by covering all kinds of analytical methods for detecting food contaminants.

Ochratoxin A (OTA) is stabilized well in food and poses potential threats to human health, including nephrotoxicity, hepatotoxicity, teratogenicity, and carcinogenicity. In this Special Issue, Nawaz et al. conducted a comprehensive study on zinc selenide (ZnSe) nanostructures to construct an aptasensor for the detection of OTA in food. They synthesized six

Citation: Wu, L. Smart and Multifunctional Nanomaterials and Applications for Food Safety. *Biosensors* **2023**, *13*, 928. <https://doi.org/10.3390/bios13100928>

Received: 3 October 2023
Accepted: 13 October 2023
Published: 16 October 2023



Copyright: © 2023 by the author. Licensee MDPI, Basel, Switzerland. This article is an open access article distributed under the terms and conditions of the Creative Commons Attribution (CC BY) license (<https://creativecommons.org/licenses/by/4.0/>).

types of ZnSe nanostructures, including nanorods, μ -spheres, and nanoclusters, and further evaluated the fluorescence bursting efficiency of ZnSe nanostructures. Finally, multifunctional ZnSe-B6 nanostructures with high negative charges were synthesized and employed to develop a fluorescent aptasensor for the detection of OTA with a wide linear range of 0.1 to 200 ng/L and a limit of detection of 0.07 ng/L. In addition, Yang et al. constructed a guanine-quenched fluorescence sensing platform for the detection of OTA, which relies on monitoring fluorescence changes resulting from conformational alterations of the nucleic acid aptamer upon binding to OTA. Another research proposed by Yang et al. focused on exploring the fluorescence quenching ability of G-quadruplexes based on photo-induced electron transfer, wherein G-quadruplexes acted as quenchers and as a sensing platform for OTA and potassium ions (K^+). During the recognition process, the formation of the G-quadruplex structure occurs, causing the quenching of the labeled fluorescein fluorophore (FAM), thereby enabling the detection of OTA with a limit of detection (LOD) of 0.19 nM. All of the above research works are based on the principle of fluorescence quenching and show distinct fluorescence strategies, offering flexibility in the sensitive detection of OTA in food safety and environmental monitoring.

The rapid development of nanomaterials, metal–organic frameworks (MOFs), carbon dots (CDs), and metal nanoparticles in recent years has brought about new directions for fluorescence analysis. CDs have found broad applications in biomedical imaging and biosensors due to their unique optical properties, biocompatibility, affordability, sensitivity, and ease of functionalization. Xu's article constructed fluorescent probes based on red carbon dots for the detection of Mn^{2+} and Zn^{2+} in macroalgae. The results showed good linearity between fluorescence intensity and concentrations of Mn^{2+} and Zn^{2+} . In addition, Li et al. designed a lanthanide-based ratiometric fluorescent probe for the determination of bacterial endospore biomarkers. In the study, CDs were bound with europium ions (Eu^{3+}) to create Eu^{3+} /CDs fluorescent probes. The fluorescence intensity (PL) ratio of Eu^{3+} /CDs showed a good linear relationship ($R^2=0.9961$) and a low LOD (18.3 μ M) for the detection of dipicolinic acid. The ratiometric fluorescent sensor showed great potential for application in complex food matrices.

Silver nanoparticles (AgNPs) and gold nanoparticles (AuNPs) are widely employed to prepare surface-enhanced Raman scattering (SERS) substrates. The SERS signals can be enhanced on the surface of noble metal nanomaterials due to the abundant SERS "hotspots", thus achieving highly sensitive detection of targets. As an example, Yuan et al. prepared copy paper loaded with AgNPs (AgNP-CP) for the rapid and in situ detection of sodium metabisulfite on shrimp surfaces. Compared to textiles and other flexible materials, copy paper is the most commonly used substrate for loading AgNPs and AuNPs and is favorable for in situ SERS detection. In addition, the AgNP-CP substrates demonstrated improved performance for the sensitive and accurate detection of sodium metabisulfite, which can be further applied to the on-site and non-destructive testing of other contaminants in seafood in the future.

Due to the intrinsic enzyme-like properties of nanozymes, they are widely used in immunosensors to replace natural enzymes like horseradish peroxidase, which holds great potential for the real-time detection of pathogenic bacteria and evaluation of food risk factors. For instance, Lang et al. conducted a review of recent advancements in nanozyme-based methods for the determination of risk factors in food. The authors provide a detailed description of common methods employed for detecting risk factors in food, such as pathogenic microorganisms, toxins, heavy metals, and pesticide residues, and explain the principles and applications of nanozymes in immunosensors. The review provided new insights into developing different nanozyme-based sensors for food safety analysis, especially innovating the structure of immunosensors.

Electrochemical sensors are widespread in food safety detection because of their advantages of being low cost, simple to operate, and portable. In this Special Issue, Zhou et al. presented a review of recent advancements and trends in electrochemical sensors based on molecular imprinting technology (MIT). The authors conducted a comprehensive review

of molecularly imprinted electrochemical sensors (MIECs) in terms of design, operating principles, and functionality. In addition, the application of MIECs in food and pharmaceuticals safety was discussed, as well as the challenges and prospects for the development of new electrochemical methods. Furthermore, Wu et al. discussed recent advances in bioelectronic sensing based on chitosan-based hydrogels. With different types of chitosan-based hydrogels, including electrode-based hydrogels, conductive materials conjugated hydrogels, ionically conductive hydrogels, and redox-based hydrogels, the authors describe the properties of these materials and their wide range of applications in fields such as medicine and food safety. Wang et al. provided an overview of recent advancements on electrochemical biosensors for food safety detection, highlighting their advantages of miniaturization, low cost, rapid detection as well as high sensitivity and selectivity with the inclusion of nanomaterials. The three review articles on electrochemical sensing offered an in-depth exploration of the prospective contributions of electrochemical biosensors for detecting biological contaminants, chemical pollutants, and genetically modified crops. The reviews have highlighted the significant role of electrochemical sensors in food safety detection, and new breakthroughs have been made to address food safety issues with the aid of functional nanomaterials.

This Special Issue compiles a collection of research articles and reviews on the application of nanomaterials in food safety detection, including electrochemical detection, nanozymes-based immunosensors, fluorescent analysis, and SERS sensors. Using smart or functional nanomaterials, some limitations of those methods are overcome; for example, the conductivity and surface area of the electrode are increased, the loading capacities of antibodies and markers are improved, and the fluorescence intensity and SERS signal become stronger. Still, much more needs to be achieved to meet the needs of different application scenarios with more detection functions, such as on-site, nondestructive, multicomponent, and real-time monitoring. This Special Issue is the collective effort of several authors who have made important contributions to different detection methods on food safety and are paving an avenue towards the development of new analytical methods.

Conflicts of Interest: The author declares no conflict of interest.

References

- Zhang, J.; Huang, H.; Song, G.; Huang, K.; Luo, Y.; Liu, Q.; He, X.; Cheng, N. Intelligent biosensing strategies for rapid detection in food safety: A review. *Biosens. Bioelectron.* **2022**, *202*, 114003. [[CrossRef](#)] [[PubMed](#)]
- Sharma, A.; Pant, K.; Brar, D.S.; Thakur, A.; Nanda, V. A review on Api-products: Current scenario of potential contaminants and their food safety concerns. *Food Control* **2023**, *145*, 109499. [[CrossRef](#)]
- Hitabatuma, A.; Wang, P.; Su, X.; Ma, M. Metal-Organic Frameworks-Based Sensors for Food Safety. *Foods* **2022**, *11*, 382. [[CrossRef](#)]
- Jia, X.-X.; Li, S.; Han, D.-P.; Chen, R.-P.; Yao, Z.-Y.; Ning, B.-A.; Gao, Z.-X.; Fan, Z.-C. Development and perspectives of rapid detection technology in food and environment. *Crit. Rev. Food Sci. Nutr.* **2021**, *62*, 4706–4725. [[CrossRef](#)]
- Wu, L.; Zhang, C.; Long, Y.; Chen, Q.; Zhang, W.; Liu, G. Food additives: From functions to analytical methods. *Crit. Rev. Food Sci. Nutr.* **2022**, *62*, 8497–8517. [[CrossRef](#)] [[PubMed](#)]
- Kumar, A.; Mangla, S.K.; Kumar, P. An integrated literature review on sustainable food supply chains: Exploring research themes and future directions. *Sci. Total. Environ.* **2022**, *821*, 153411. [[CrossRef](#)]
- He, H.; Sun, D.W.; Wu, Z.; Pu, H.; Wei, Q. On-off-on fluorescent nanosensing: Materials, detection strategies and recent food applications. *Trends Food Sci. Technol.* **2022**, *119*, 243–256. [[CrossRef](#)]
- Sun, Y.; Lv, Y.; Qi, S.; Zhang, Y.; Wang, Z. Sensitive colorimetric aptasensor based on stimuli-responsive metal-organic framework nano-container and trivalent DNAzyme for zearalenone determination in food samples. *Food Chem.* **2021**, *371*, 131145. [[CrossRef](#)]
- Wang, M.; Cui, J.; Wang, Y.; Yang, L.; Jia, Z.; Gao, C.; Zhang, H. Microfluidic Paper-Based Analytical Devices for the Determination of Food Contaminants: Developments and Applications. *J. Agric. Food Chem.* **2022**, *70*, 8188–8206. [[CrossRef](#)]
- Suo, Z.; Niu, X.; Wei, M.; Jin, H.; He, B. Latest strategies for rapid and point of care detection of mycotoxins in food: A review. *Anal. Chim. Acta* **2023**, *1246*, 340888. [[CrossRef](#)] [[PubMed](#)]
- Sun, J.; Li, W.; Zhu, X.; Jiao, S.; Chang, Y.; Wang, S.; Dai, S.; Xu, R.; Dou, M.; Li, Q.; et al. A Novel Multiplex Mycotoxin Surface-Enhanced Raman Spectroscopy Immunoassay Using Functional Gold Nanotags on a Silica Photonic Crystal Microsphere Biochip. *J. Agric. Food Chem.* **2021**, *69*, 11494–11501. [[CrossRef](#)]
- Li, H.; Huang, X.; Hassan, M.; Zuo, M.; Wu, X.; Chen, Y.; Chen, Q. Dual-channel biosensor for Hg²⁺ sensing in food using Au@Ag/graphene-upconversion nanohybrids as metal-enhanced fluorescence and SERS indicators. *Microchem. J.* **2020**, *154*, 104563. [[CrossRef](#)]

13. Kong, L.; Hong, F.; Luan, P.; Chen, Y.; Feng, Y.; Zhu, M. A novel competitive electrochemical impedance biosensor for the ultrasensitive detection of umami substances based on Pd/Cu-TCPP(Fe). *Food Chem.* **2023**, 137631. [[CrossRef](#)]
14. Li, L.; Liu, X.; Su, B.; Zhang, H.; Li, R.; Liu, Z.; Chen, Q.; Huang, T.; Cao, H. An innovative electrochemical immunosensor based on nanobody heptamer and AuNPs@ZIF-8 nanocomposites as support for the detection of alpha fetoprotein in serum. *Microchem. J.* **2022**, 179, 107463. [[CrossRef](#)]
15. Su, B.; Zhang, Z.; Sun, Z.; Tang, Z.; Xie, X.; Chen, Q.; Cao, H.; Yu, X.; Xu, Y.; Liu, X.; et al. Fluonanobody-based nanosensor via fluorescence resonance energy transfer for ultrasensitive detection of ochratoxin A. *J. Hazard. Mater.* **2022**, 422, 126838. [[CrossRef](#)]
16. Shan, W.; Sun, J.; Liu, R.; Xu, W.; Shao, B. Duplexed aptamer-isothermal amplification-based nucleic acid-templated copper nanoparticles for fluorescent detection of okadaic acid. *Sens. Actuators B Chem.* **2022**, 352, 131035. [[CrossRef](#)]
17. Tang, X.; Su, S.; Luo, H.; Zhao, Y.; Feng, L.; Chen, J. Colorimetric detection of Aflatoxin B1 by using smartphone-assisted microfluidic paper-based analytical devices. *Food Control* **2022**, 132, 108497. [[CrossRef](#)]
18. Wu, L.; Zhou, M.; Wang, Y.; Liu, J. Nanozyme and aptamer-based immunosorbent assay for aflatoxin B. *J. Hazard. Mater.* **2020**, 399, 123154. [[CrossRef](#)]
19. Wu, L.; Zhou, S.; Wang, G.; Yun, Y.; Liu, G.; Zhang, W. Nanozyme Applications: A Glimpse of Insight in Food Safety. *Front. Bioeng. Biotechnol.* **2021**, 9, 727886. [[CrossRef](#)]
20. Wang, H.; Jiang, S.; Pan, J.; Lin, J.; Wang, J.; Li, M.; Xie, A.; Luo, S. Nanomaterials-based electrochemical sensors for the detection of natural antioxidants in food and biological samples: Research progress. *Microchim. Acta* **2022**, 189, 318. [[CrossRef](#)]
21. Chen, Y.; Xianyu, Y.; Jiang, X. Surface Modification of Gold Nanoparticles with Small Molecules for Biochemical Analysis. *Accounts Chem. Res.* **2017**, 50, 310–319. [[CrossRef](#)] [[PubMed](#)]
22. Liu, S.; Hou, Y.; Li, Z.; Yang, C.; Liu, G. μ PADs on Centrifugal Microfluidic Discs for Rapid Sample-to-Answer Salivary Diagnostics. *ACS Sens.* **2023**, 8, 3520–3529. [[CrossRef](#)]
23. Nazir, S.; Kwon, O.S. Micro-Electromechanical Systems-based Sensors and Their Applications. *Appl. Sci. Converg. Technol.* **2022**, 31, 40–45. [[CrossRef](#)]
24. Wu, L.; Yin, W.; Tan, X.; Wang, P.; Ding, F.; Zhang, H.; Wang, B.; Zhang, W.; Han, H. Direct reduction of H₂AuCl₄ for the visual detection of intracellular hydrogen peroxide based on Au-Pt/SiO₂ nanospheres. *Sens. Actuators B Chem.* **2017**, 248, 367–373. [[CrossRef](#)]
25. Nelis, J.; Tsagkaris, A.; Dillon, M.; Hajslova, J.; Elliott, C. Smartphone-based optical assays in the food safety field. *TrAC Trends Anal. Chem.* **2020**, 129, 115934. [[CrossRef](#)] [[PubMed](#)]
26. Yu, Z.; Cai, G.; Liu, X.; Tang, D. Pressure-Based Biosensor Integrated with a Flexible Pressure Sensor and an Electrochromic Device for Visual Detection. *Anal. Chem.* **2021**, 93, 2916–2925. [[CrossRef](#)]
27. Hu, X.; Zhao, J.; Cheng, X.; Wang, X.; Zhang, X.; Chen, Y. Polydopamine-mediated quantity-based magnetic relaxation sensing for the rapid and sensitive detection of chloramphenicol in fish samples. *Food Res. Int.* **2022**, 162, 111919. [[CrossRef](#)]

Disclaimer/Publisher's Note: The statements, opinions and data contained in all publications are solely those of the individual author(s) and contributor(s) and not of MDPI and/or the editor(s). MDPI and/or the editor(s) disclaim responsibility for any injury to people or property resulting from any ideas, methods, instructions or products referred to in the content.



Article

Enhanced Response for Foodborne Pathogens Detection by Au Nanoparticles Decorated ZnO Nanosheets Gas Sensor

Cheng Zhao ¹, Shanshan Xu ², Jing Wei ³, Siqi Xie ¹, Jinlei Wei ¹, Jingting Han ¹, Zhaohuan Zhang ¹, Haiquan Liu ¹, Jinsheng Cheng ⁴, Yong Zhao ^{1,*} and Yongheng Zhu ^{1,*}

¹ College of Food Science and Technology, Shanghai Ocean University, Shanghai 201306, China

² State Key Laboratory of Chemical Engineering, College of Chemical and Biological Engineering, Zhejiang University, Hangzhou 310027, China

³ The Key Laboratory of Biomedical Information Engineering of Ministry of Education, Institute of Analytical Chemistry and Instrument for Life Science, School of Life Science and Technology, Xi'an Jiaotong University, Xi'an 710049, China

⁴ Henry-Fork School of Food Sciences, Shaoguan University, Shaoguan 512005, China

* Correspondence: yzhao@shou.edu.cn (Y.Z.); yh-zhu@shou.edu.cn (Y.Z.);
Tel.: +86-15692165928 (Y.Z.); +86-15000137862 (Y.Z.)

Abstract: *Listeria monocytogenes* is a hazardous foodborne pathogen that is able to cause acute meningitis, encephalitis, and sepsis to humans. The efficient detection of 3-hydroxy-2-butanone, which has been verified as a biomarker for the exhalation of *Listeria monocytogenes*, can feasibly evaluate whether the bacteria are contained in food. Herein, we developed an outstanding 3-hydroxy-2-butanone gas sensor based on the microelectromechanical systems using Au/ZnO NS as a sensing material. In this work, ZnO nanosheets were synthesized by a hydrothermal reaction, and Au nanoparticles (~5.5 nm) were prepared via an oleylamine reduction method. Then, an ultrasonic treatment was carried out to modified Au nanoparticles onto ZnO nanosheets. The XRD, BET, TEM, and XPS were used to characterize their morphology, microstructure, catalytic structure, specific surface area, and chemical composition. The response of the 1.0% Au/ZnO NS sensors vs. 25 ppm 3-hydroxy-2-butanone was up to 174.04 at 230 °C. Moreover, these sensors presented fast response/recovery time (6 s/7 s), great selectivity, and an outstanding limit of detection (lower than 0.5 ppm). This work is full of promise for developing a nondestructive, rapid and practical sensor, which would improve *Listeria monocytogenes* evaluation in foods.

Citation: Zhao, C.; Xu, S.; Wei, J.; Xie, S.; Wei, J.; Han, J.; Zhang, Z.; Liu, H.; Cheng, J.; Zhao, Y.; et al. Enhanced Response for Foodborne Pathogens Detection by Au Nanoparticles Decorated ZnO Nanosheets Gas Sensor. *Biosensors* **2022**, *12*, 803. <https://doi.org/10.3390/bios12100803>

Received: 31 August 2022

Accepted: 23 September 2022

Published: 28 September 2022



Copyright: © 2022 by the authors. Licensee MDPI, Basel, Switzerland. This article is an open access article distributed under the terms and conditions of the Creative Commons Attribution (CC BY) license (<https://creativecommons.org/licenses/by/4.0/>).

Keywords: Au nanoparticles; ZnO nanosheets; MEMS gas sensor; 3-hydroxy-2-butanone; foodborne-pathogens detection; food safety

1. Introduction

Listeria monocytogenes (*LM*) is a foodborne pathogen that is able to cause acute meningitis, encephalitis, and sepsis. It has been found in food samples and raw materials, such as dairy products, meat products, vegetables, and seafood [1,2]. Since *LM* has a high mortality rate (20–30%), it is necessary to establish a rapid and accurate detection method for the bacteria in food samples and the environment [3]. At present, the detection methods applied to *LM* mainly include traditional physiological and biochemical measurements, molecular biological measurements targeting the virulence factors or specific genes of *LM*, and immunological measurements based on specific bindings of antigens and antibodies [4]. These methods generally require a long processing time, professional operators, or expensive instruments [5]. Thus, it is difficult to achieve rapid, nondestructive, and real-time in situ detection of the bacteria. According to previous studies, 3-hydroxy-2-butanone (3H-2B) is one of the characteristic microbial volatile organic compounds (MVOCs) of *LM*, whose abundance exceeds 32% [6]. Meanwhile, there is an excellent linear relationship between

the incubation time of *LM* and the concentration of 3H-2B [7]. Consequently, it is feasible to realize a nondestructive and rapid evaluation of *LM* by detecting 3H-2B.

The metal oxide semiconductor (MOS) gas sensors realize gas detection through the conductivity changes of the MOS materials caused by chemical reactions between materials and target gases. With their advantages of portability and being economically and environmentally friendly, they have quickly become the most practical and widely-used gas sensors [8]. Since Deng et al. firstly studied 3H-2B sensors using mesoporous WO_3 as sensing materials in 2017 [7], a variety of MOS materials with different morphologies has been developed and successfully applied to detect 3H-2B, such as WO_3 nanoflowers [9], SnO_2 - Al_2O_3 nanocables [10], ZnO - Al_2O_3 nanocables [11], and NiO nano cuboids [12]. However, these materials are not all satisfactory in terms of response/recovery time, sensitivity, limit of detection (LOD), and selectivity. As one of the common n-type semiconductors, ZnO has the properties of small particles, large exciton binding energy (60 meV), a wide band gap (3.4 eV), a large specific surface area, and a small size effect [13]. Moreover, changing the physical morphology of materials is an effective way to improve their performance. For example, ZnO nanosheets (NS) are considered significant gas-sensing materials due to their simple synthesis method and excellent properties compared with the original ZnO described above [14,15].

In addition to morphology control, noble metal modification is also one of the important means to improve the sensing performance of MOS materials [16–19]. Au is a typical noble metal and is often selected as a sensitizer to modify MOS because Au is able to decrease the chemical adsorption activation energy of the measured gases and accelerate the reaction speed of the material. Moreover, it can also form Schottky contact with the MOS, so carriers are transferred from the MOS to the noble metal, which increases the Schottky barrier. At the same time, Au promotes the adsorption of O_2 molecules, transfers them to the material surface to form oxygen negative ions, increases the thickness of the electron depletion layer (EDL), improves the conductivity, and finally improves the sensitivity [20,21]. For instance, Wang et al. showed that at 340 °C, Au/ ZnO nanowires had a fast recovery time, greater response, better selectivity, and lower LOD for benzene and toluene than pure ZnO nanowires [22]. Therefore, it is feasible to develop a new ZnO NS gas sensor modified by Au nanoparticles (NPs) to detect 3H-2B, which is important for realizing the nondestructive and rapid assessment of *LM* in situ.

In this research, we synthesized ZnO NS by hydrothermal reaction, and prepared Au NPs (~5.5 nm) via the oleylamine reduction method. Then, we developed an excellent 3-hydroxy-2-butanone gas sensor based on the microelectromechanical systems (MEMs) using Au/ ZnO NS as the sensing material. After working temperature tests, decoration material analysis, and load proportion optimization, the best performance of 1.0% Au/ ZnO sensors were further studied. The response of these sensors vs. 25 ppm 3H-2B was up to 174.04 at 230 °C. Moreover, the sensors presented fast response/recovery time (6 s/7 s), excellent LOD (lower than 0.5 ppm), a good linear relationship, and great selectivity. Moreover, we explored the sensing mechanism according to the surface depletion model and electric resistance analysis. Such an excellent sensor based on 1.0% Au/ ZnO NS signifies the amazing application potential in real-time, in addition to the nondestructive and efficient detection of 3H-2B. Considering the relationship between 3H-2B and *LM*, it opens up the opportunity to effectively and conveniently evaluate *LM* in foods, which will make a tremendous contribution to worldwide food safety.

2. Materials and Methods

2.1. Materials

We acquired chloroauric acid trihydrate ($\text{HAuCl}_4 \cdot 3\text{H}_2\text{O}$, $\geq 99.9\%$) and 3-hydroxy-2-butanone ($\text{CH}_3\text{COCH}(\text{OH})\text{CH}_3$, analytical standard) from Sigma-Aldrich, Saint Louis, United States. We purchased N-hexane from Shanghai Acme Biochemical Co. Ltd., Shanghai, China. We purchased zinc acetate ($\text{C}_4\text{H}_6\text{O}_4\text{Zn}$, $\geq 99.99\%$), urea ($\text{CO}(\text{NH}_2)_2$, $\geq 99.9\%$),

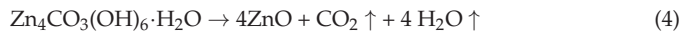
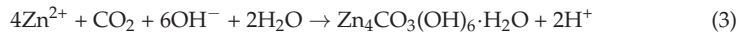
oleylamine (C₁₈H₃₇N, 80–90%), and other reagents for selective testing from Yasuda chemical (Jiangsu) Co. Ltd., Huaian, China. We did not refine reagents in this research.

2.2. Instruments

We determined the crystalline form by X-ray diffraction (XRD, X'Pert) with Ni-filtered Cu K α radiation (40 kV, 40 mA, 1.54056 Å) in the range of $2\theta = 20$ to 80° at 25°C . We applied transmission electron microscopy (TEM) and high-resolution TEM (HRTEM; JEOL JEM-2011) to determine the microstructure of materials at accelerating voltage of 200 kV. We analyzed the chemistry composition by X-ray photoelectron spectroscopy (XPS; PHI-5000C ESCA), operating with Al K α radiation ($h\nu = 1486.6$ eV). We charge-corrected binding energy values to C 1s = 284.6 eV. We tested the specific surface area by the Brunauer-Emmett-Teller method (BET; ASAP 2460), applying N₂ as adsorbate at 77 K.

2.3. Synthesis of ZnO NS

We prepared ZnO NS as in previous methods [23–25]. We added 7 g urea and 2 g zinc acetate to 80 mL deionized water, stirred for 45 min, transferred to 100 mL conical flask, and laid hermetically in an oven at 95°C for 6 h. After natural cooling, we centrifuged the white precipitate, washed, then dried at 80°C . We calcined precursors in a muffle oven at 300°C for 2 h to gain ZnO NS. These chemical reactions during the synthesis are shown in the following chemical equations:



2.4. Synthesis of Au NPs

We prepared Au NPs as in previous methods [26]. We transferred 20 mL oleylamine and 118 mg chloroauric acid trihydrate to a three-necked flask (50 mL) and heated to 120°C in constant-temperature oil bath, magnetically stirring and refluxing for 15 min. Then, we increased the temperature of the solution to 200°C for 15 min, and increased again to 240°C for 20 min. Next, we gathered Au NPs by centrifuging, cleaning, and drying. Finally, we dispersed Au NPs in N-hexane for further preserving. We carried out similar methods to prepare Pd and Pt NPs.

2.5. Synthesis of Au/ZnO NS

We prepared Au/ZnO NS as in previous methods [27]. We dispersed 100 mg ZnO NS in 30 mL deionized water. Then, we added various amounts of Au NPs to these solutions. Afterward, we ultrasonically stirred the solutions for 2 h. We set the mass percent of Au in the materials as 0.5, 1.0, 1.5, and 2.0 wt.%. Finally, we marked the nanocomposites as 0.5% Au/ZnO NS, 1% Au/ZnO NS, 1.5% Au/ZnO NS, and 2% Au/ZnO NS, and dried at 60°C . In order to compare with Au/ZnO NS, we decorated 1.0 wt.% Pd and Pt NPs on ZnO NS and marked as 1.0% Pd/ZnO NS and 1.0% Pt/ZnO NS.

2.6. Preparation of the Sensors

We prepared the MEMS sensors according to the previous research [27]. The sensors possessed an interdigital electrode and an integrated microheater (Figure S1). Specifically, the resistance changes can be observed by the interdigital electrode, and a stable working temperature can be provided by the microheater. First of all, we transferred the gas-sensitive material and deionized water into an agate mortar and polished for 5 min to obtain a paste. Then, we added a drop of the abovementioned sample to the Pt interdigital electrode. After drying in an oven, we aged the ZnO sensors at 160°C .

3. Results

3.1. Materials Characterization

As presented in Figure 1, ZnO NS were prepared by the one-step hydrothermal method combined with calcination, in which zinc acetate was the zinc source. Then, the oleylamine reduction method was used to synthesize Au NPs. Next, Au NPs were decorated on ZnO NS by ultrasonic treatment, in which the mass percentages of the Au element in Au/ZnO NS were set as 0.5, 1.0, 1.5, and 2.0 wt.%.

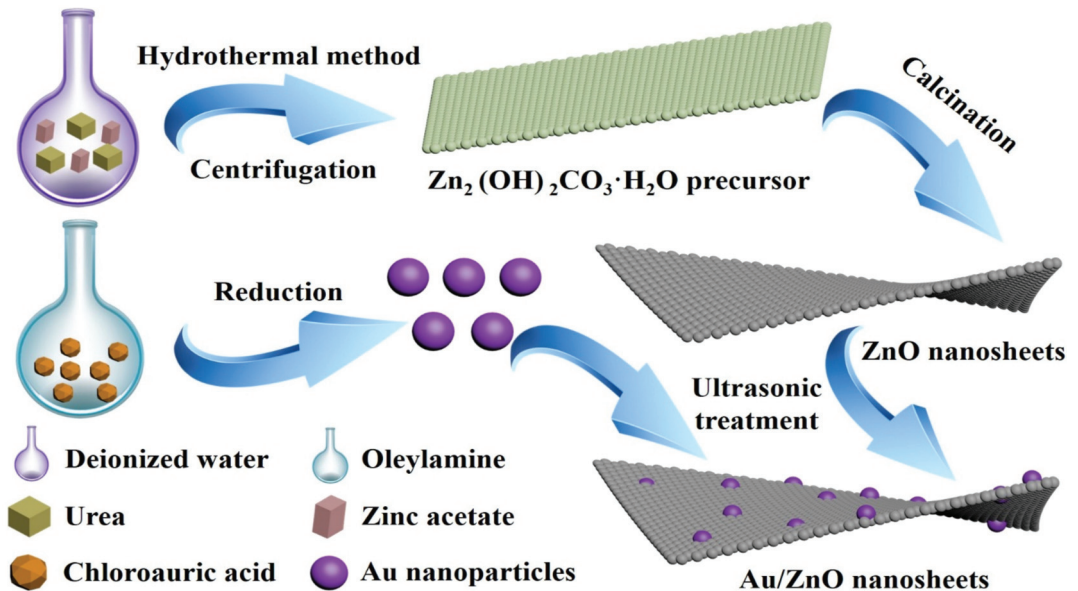


Figure 1. The synthesis schematic illustration of Au/ZnO NS.

The crystal structure and phase of pristine ZnO and 1.0% Au/ZnO NS were measured by XRD. According to Figure 2, the two peaks belonging to pristine ZnO NS and 1.0% Au/ZnO were indexed as hexagonal ZnO (JCPDS card no. 89-0510). The lattice constants of it were $a = 3.25 \times 10^{-10}$ m and $c = 5.20 \times 10^{-10}$ m. There were no other stray peaks except the peaks belonging to ZnO, which illustrated that ZnO NS as-prepared had excellent purity. Meanwhile, the characteristic patterns of Au were not presented in the peaks of 1.0% Au/ZnO NS because of the weak peak intensity and the low load rate of Au [28].

TEM was performed to determine the morphology of sensing materials. As shown in Figure 3a, ZnO NS with typical nanosheet characteristics had lengths of about 40–60 nm. Their edge was clear and their boundary with the background was obvious, indicating that they had very good crystallinity [29]. Figure 3b presents the lattice spacing of ZnO NS, which was 0.19 nm, corresponding to the hexagonal ZnO (0 0 2) plane [30]. Figure 3c,d show Au NPs with diameters around 5.5 nm are uniform in size with great dispersion and crystallinity. The interplanar spacing of Au NPs was 0.24 nm, corresponding to the Au (1 1 1) plane [31]. Figure 3e shows a number of Au NPs were loaded on ZnO NS. The lattice spacing of the ZnO (0 0 2) and Au (1 1 1) plane are clearly shown in the HRTEM image of 1.0% Au/ZnO NS (Figure 3f). This revealed that Au NPs had been favorably decorated on ZnO NS. Moreover, the STEM-EDS elemental mapping images in Figure 3g–i showed that Zn, O, and Au elements were uniformly distributed in ZnO NS, further proving the success of Au/ZnO NS synthesis.

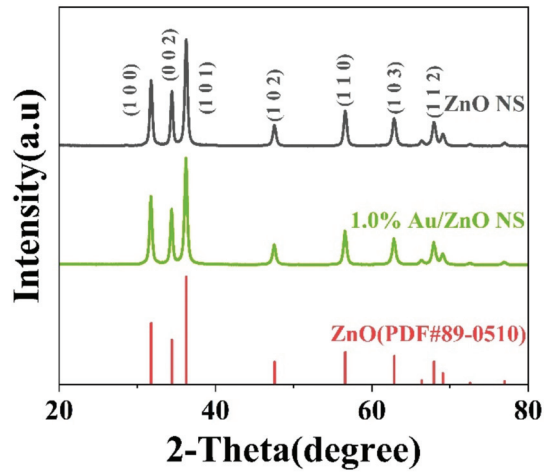


Figure 2. XRD patterns of ZnO NS and 1.0% Au/ZnO NS.

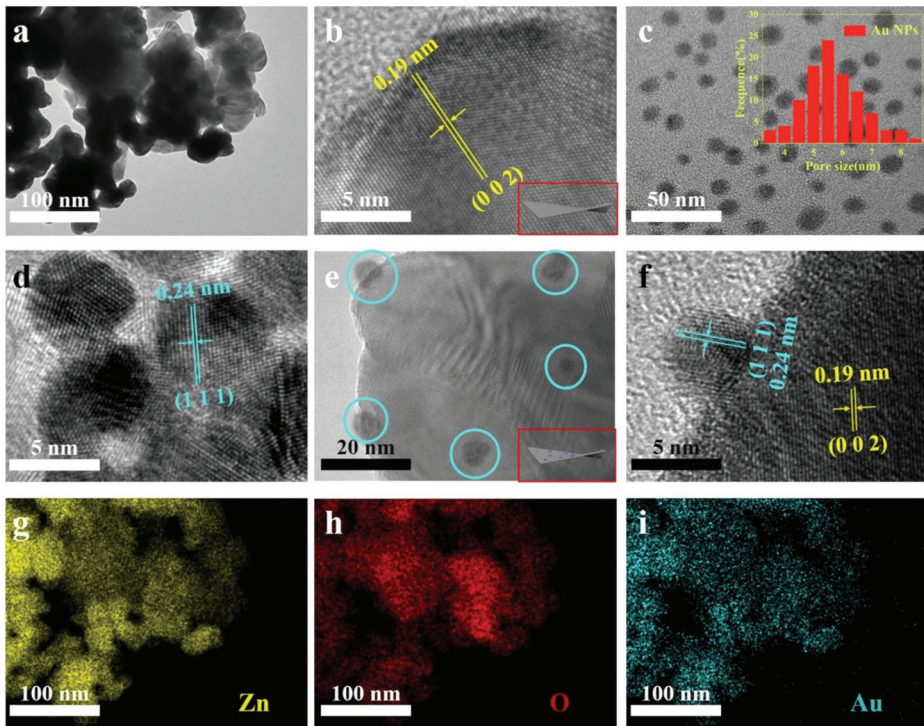


Figure 3. (a) TEM and (b) HRTEM images of pure ZnO NS. (c) TEM images and the particle size distribution of Au NPs. (d) HRTEM image of Au NPs. (e) TEM and (f) HRTEM images of 1.0% Au/ZnO NS. (g–i) STEM–EDS elemental mapping images of 1.0% Au/ZnO NS.

The chemical states of ZnO NS and the 1.0% Au/ZnO NS surface were applied by the XPS analysis. The full spectrum is displayed in Figure 4a, which shows the signal intensity of Zn 2p, O 1s, and C 1s. It further shows that as-prepared ZnO NS had very high purity. Moreover, in the spectra of 1.0% Au/ZnO NS (Figure 4b), two weak peaks

at 87.6 eV and 83.9 eV were distinguished to Au 4f_{7/2} and Au 4f_{5/2}, revealing the Au element was in the valence of Au⁰ [32,33]. The O 1s patterns exhibited in Figure 4c were resolved by a Gaussian function to three peaks at 529.6, 531.1, and 531.4 eV, which were characteristic peaks of adsorbed oxygen (O_{ads}), defect oxygen (O_{def}), and lattice oxygen (O_{lat}) [34,35]. The gas-sensing properties of sensitive materials were significantly affected by the valence of oxygen on their surfaces [28,36]. Figure 4c,d show the ratio of O_{ads} and O_{def} in pure ZnO NS increased from 10.2% and 21.0% to 14.8% and 27.2% after Au NPs sensitizing. In general, O_{lat} made little contribution to the electron transfer of n-type semiconductors because it was difficult to react with the measured gases. However, O_{def} and O_{ads} were in activity, so they could take part in a redox reaction and significantly increase the main charge-carriers' concentration [37]. Therefore, the modification of Au NPs significantly increased the proportion of oxygen that participated in the reaction on the surface of Au/ZnO NS. This change may improve the sensitivity of the materials [28].

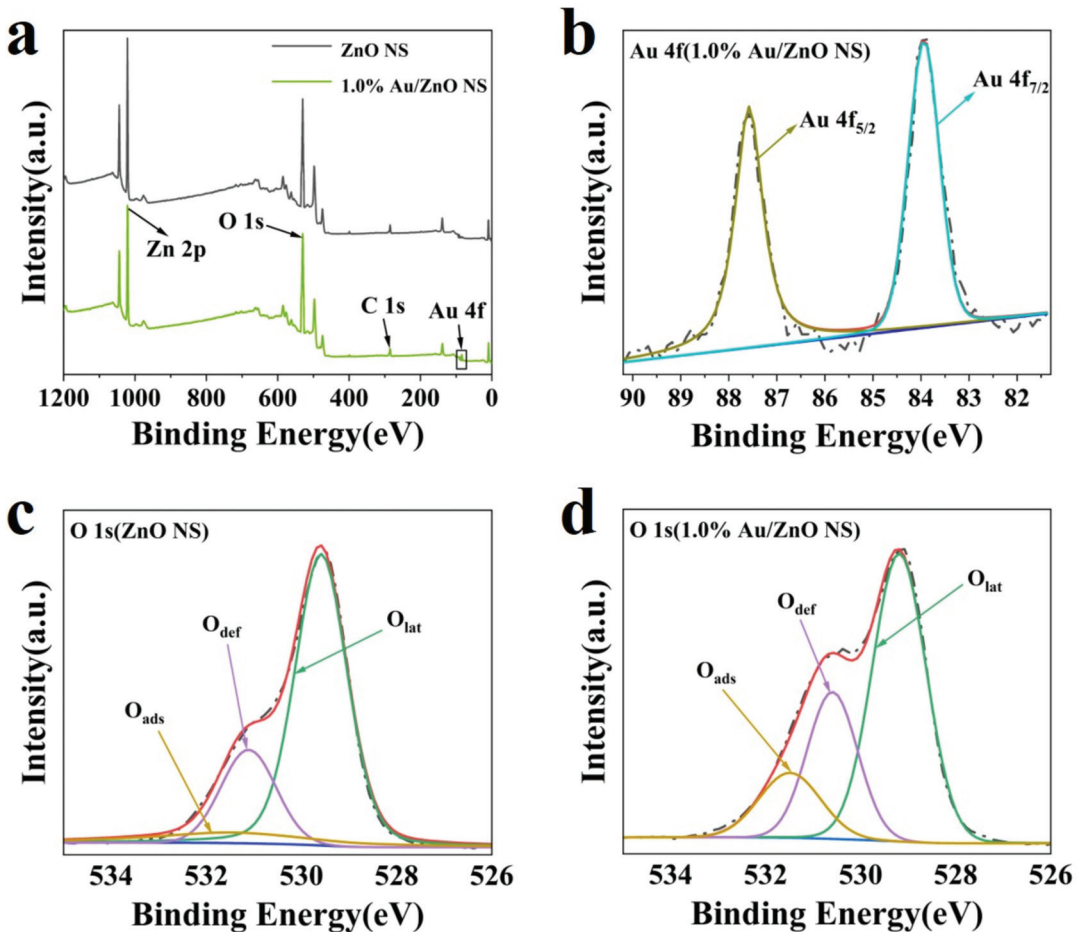


Figure 4. (a) Full XPS spectrum of ZnO NS and 1.0% Au/ZnO NS. (b) High-resolution Au 4f XPS spectra of 1.0% Au/ZnO NS. (c,d) High-resolution O 1s XPS spectra of ZnO NS and 1.0% Au/ZnO NS.

The N₂ adsorption–desorption isotherms and BJH pore size distribution of ZnO NS and 1.0% Au/ZnO NS are exhibited in Figure S2. Both the pristine ZnO NS and 1.0% Au/ZnO NS were consistent with the characteristic type IV adsorption isotherm due to the hysteresis loops shown in Figure S2a,b. It proved that as-prepared materials had

a mesoporous framework [38–40]. Compared with the specific surface area of ZnO NS ($24.74 \text{ m}^2/\text{g}$), the specific surface area of 1.0% Au/ZnO NS increased by 20.3% ($29.77 \text{ m}^2/\text{g}$). Thus, 1.0% Au/ZnO NS had more effective adsorption sites to further improve the sensitivity. Moreover, the results above also revealed that most Au NPs were uniformly distributed on ZnO NS [41,42].

3.2. Gas-Sensing Properties

As mentioned above, 3H-2B has a 32.2% abundance in the MVOCs of *LM*, and the concentration of it is linearly related with the number of *LM* [6,7]. Thus, it is a simple and efficient way to indirectly evaluate *LM* in foods by detecting 3H-2B, ensuring food safety. Based on this, the environmentally-friendly MEMS sensors with magnificent sensitivity, high throughput, and miniaturization were fabricated, the method of which was described in previous work [27] using as-synthesized materials for 3H-2B detection.

For all MOS gas sensors, the operating temperature is an important factor that significantly affects their sensitivity [43]. Therefore, the sensors were firstly analyzed at temperatures from $170 \text{ }^\circ\text{C}$ to $290 \text{ }^\circ\text{C}$ vs. 25 ppm 3H-2B. It must be noted that for the n-type MOS gas sensor and reducing target gases, the response is defined as the value of R_{air} divided by R_{gas} (see more details in Supplementary Material). The optimum operating temperature of the pure ZnO NS was $260 \text{ }^\circ\text{C}$ (Figure 5a), when the response reached about 25. Then, the sensitive properties of the sensors after being decorated by Au NPs were obviously improved. While 1.0% Au/ZnO NS had the highest response as 174.04, which was almost seven times that of ZnO NS, its optimum working temperature was reduced to $230 \text{ }^\circ\text{C}$. Moreover, most sensors presented the best performance at $230 \text{ }^\circ\text{C}$, so the optimum operating temperature was set to $230 \text{ }^\circ\text{C}$ for following tests. Figure 5b exhibits the dynamic responses of 1.0% Au/ZnO NS, 1.0% Pd/ZnO NS, 1.0% Pt/ZnO NS, and pure ZnO NS vs. 1–25 ppm 3H-2B. Similar to the above results, the 1.0% Au/ZnO NS sensors showed the greatest sensitivity. Moreover, the responses of all sensors increased with the injection quantity of 3H-2B from 1 to 25 ppm and decreased from 25 to 1 ppm. During the rise and fall of the response value, when the concentration of 3H-2B was the same, the responses were almost the same. This indicated that the sensors had outstanding reversibility and repeatability [44]. These characteristics were also observed in the dynamic responses of 0.5%, 1.0%, 1.5%, and 2% Au/ZnO NS to 1–25 ppm 3H-2B (Figure 5c). According to the results in Figure 5b,c, 1.0% Au/ZnO NS sensors are considered to be the most outstanding. Meanwhile, the Au/ZnO-based gas sensor also presented a good linear relationship with the 3H-2B concentration, in which the R^2 values were all greater than 0.99 (Figure 5d). To explore the LOD of the sensors, the response of 1.0% Au/ZnO NS vs. 3H-2B at 0.5 ppm was measured. As shown in Figure S3, the response of the 1.0% Au/ZnO NS sensor was vivid and evident (close to five) despite the 3H-2B concentration being only 0.5 ppm. Generally, the limit of the *LM* concentration in foods cannot exceed $100 \text{ CFU}/\text{g}^{-1}$. According to the previous study, when the concentration of *LM* was $100 \text{ CFU}/\text{g}^{-1}$, the corresponding concentration of 3H-2B was about 2.5 ppm [7]. However, the response of 1.0% Au/ZnO NS sensors was nearly 20 towards 2.5 ppm 3H-2B, which was significant enough to evaluate whether the foods were safe.

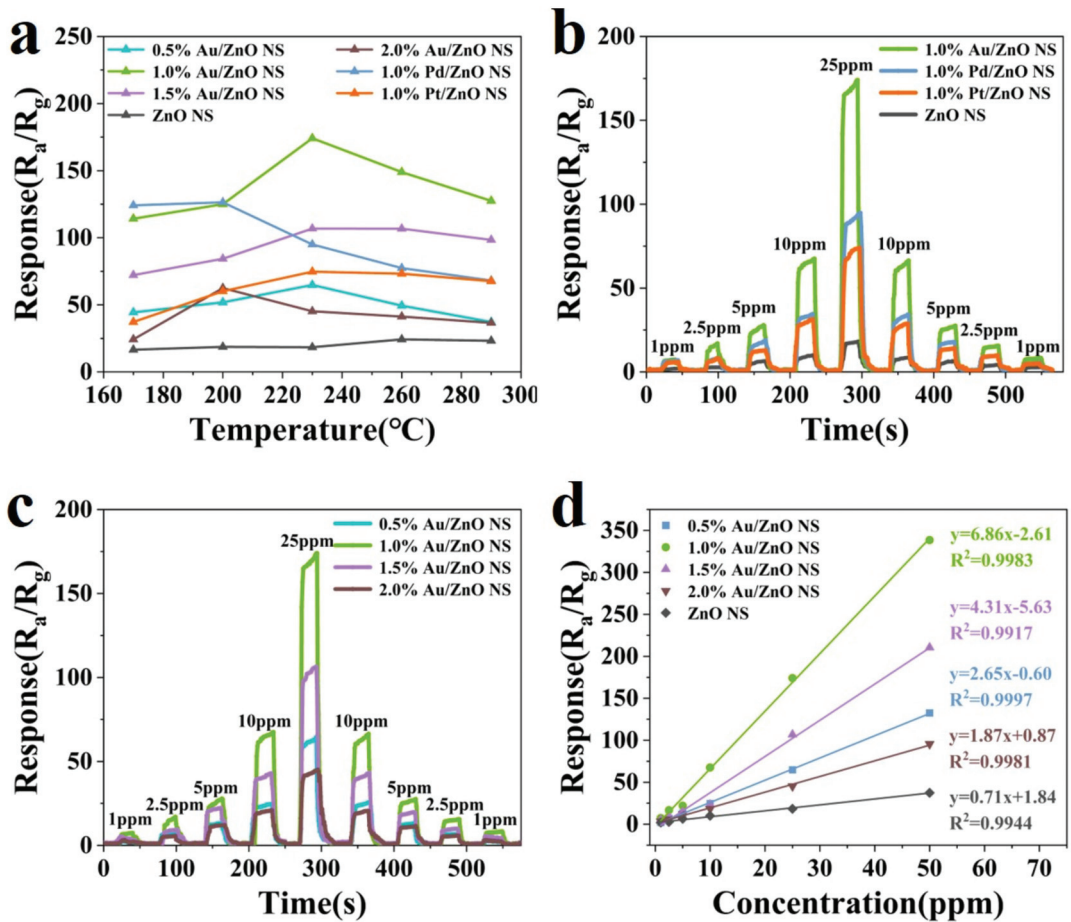


Figure 5. (a) Response of pure ZnO NS, 1.0% Pd/ZnO NS, 1.0% Pt/ZnO NS, and Au/ZnO NS to 25 ppm 3H-2B at working temperature from 170 °C to 290 °C. (b) Dynamic responses of 1.0% Au/ZnO NS, 1.0% Pd/ZnO NS, 1.0% Pt/ZnO NS, and pure ZnO NS to 1–25 ppm 3H-2B at 230 °C. (c) Dynamic responses of 0.5% Au/ZnO NS, 1.0% Au/ZnO NS, 1.5% Au/ZnO NS, and 2.0% Au/ZnO NS to 1–25 ppm 3H-2B at 230 °C. (d) Linear relationship between responses of 0.5% Au/ZnO NS, 1.0% Au/ZnO NS, 1.5% Au/ZnO NS, 2.0% Au/ZnO NS, and ZnO NS with 3H-2B concentrations (1–50 ppm) at 230 °C.

However, the rapid response/recovery time is one of the essential characteristics for gas sensors. So, that of Au/ZnO NS and ZnO NS towards 25 ppm 3H-2B was assessed and exhibited in Figure 6a. The response/recovery times of Au/ZnO NS were between 4 s and 15 s, and that of ZnO NS was 7 s and 20 s, respectively. This revealed that the modification of Au NPs significantly improved the response/recovery speed of the materials. Although the response/recovery time (6 s and 7 s) was not the fastest, it was still rapid enough to satisfy the urgent need for 3H-2B detection in real time. The responses of both 1.0% Au/ZnO NS and ZnO NS sensors were almost the same after five repeats of the test (Figure 6b), indicating that the reversibility and repeatability of these sensors were considerable, as mentioned above. Moreover, Figure S4 displayed the long-term stability of 0.5%, 1.0%, 1.5%, and 2.0% Au/ZnO NS sensors at 230 °C towards the concentration of 3H-2B at 10 ppm. The responses of these sensors fluctuated indistinctly when they were examined every 5 days in a month. This was enough to illustrate the good long-term stability of these sensors.

Then, the selectivity and discrimination analyses of these sensors were carried out due to the necessity of selectivity and discrimination characteristics for all sensors [45,46]. For studying the selectivity, the responses of Au/ZnO NS and ZnO NS sensors to formaldehyde, methanol, ethanol, ammonia, benzaldehyde, acetone, butanedione, and 3H-2B at 230 °C were investigated (Figure 6c). Their concentrations were all 25 ppm. Obviously, the responses of Au/ZnO NS and ZnO NS sensors toward 3H-2B were much higher than the responses towards other gases. Thus, the selectivity of these sensors, especially 1.0% Au/ZnO sensors, was quite outstanding. Meanwhile, the chemical sensitization effect was proven to be the most critical factor of enhanced sensitivity because the ratio of Au NPs decorated on ZnO NS barely influenced the selectivity [20,28]. The results of the discrimination evaluation are shown in Figure 6d. Compared with the response of the 1.0% Au/ZnO NS sensor to 25 ppm 3H-2B, the variation of the responses did not exceed 10%, no matter what interference gases were mixed with 3H-2B. Therefore, the selectivity and discrimination of the 1.0% Au/ZnO NS sensor were considerable.

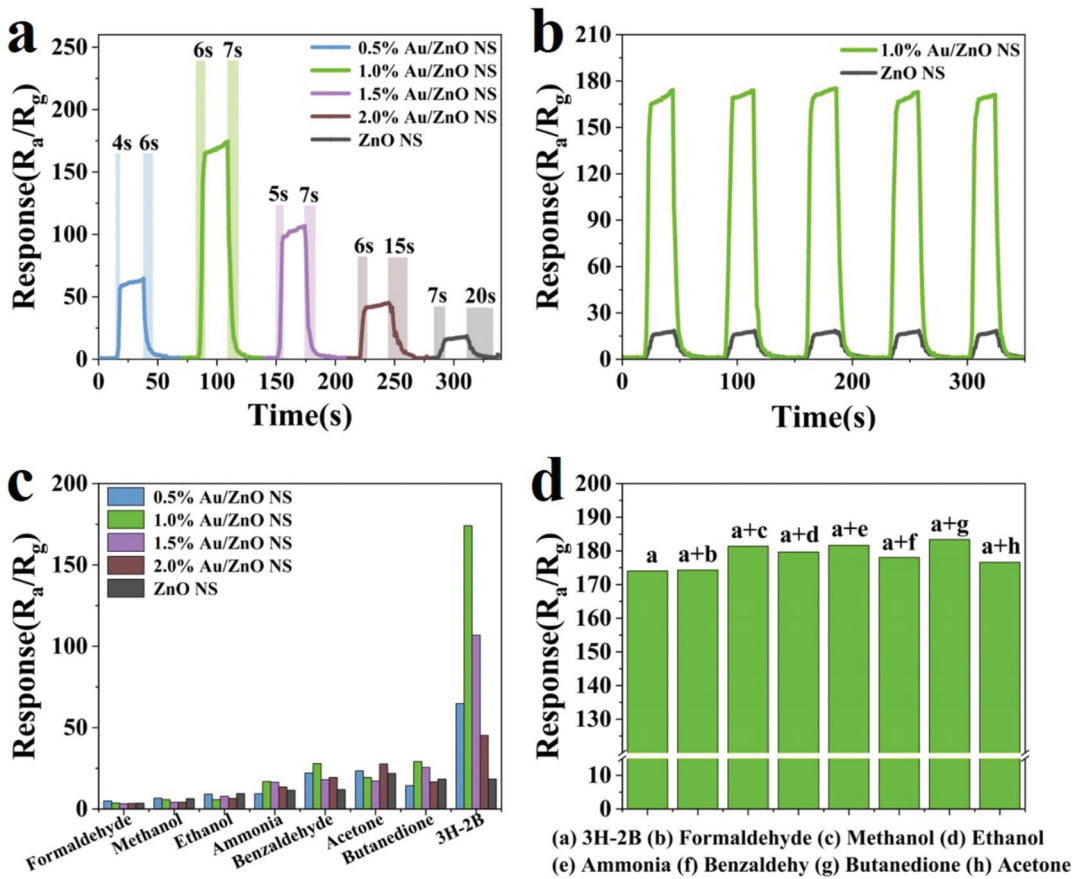


Figure 6. (a) The response/recovery time of 0.5% Au/ZnO NS, 1.0% Au/ZnO NS, 1.5% Au/ZnO NS, 2.0% Au/ZnO NS, and ZnO NS towards 25 ppm 3H-2B. (b) The repeatability of 1.0% Au/ZnO NS and ZnO NS to 3H-2B towards 25 ppm. (c) The selectivity of 0.5% Au/ZnO NS, 1.0% Au/ZnO NS, 1.5% Au/ZnO NS, 2.0% Au/ZnO NS, and ZnO NS towards 25 ppm interference gases and 3H-2B. (d) The discrimination test of 1.0% Au/ZnO NS sensors to the response of the mixed gas containing 25 ppm 3H-2B and other interference gases. All tests were operated at 230 °C.

Based on all the assessments and data above, the 1.0% Au/ZnO NS sensor has exhibited excellent gas-sensing performance. Furthermore, comparisons of its properties with other MOS-based 3H-2B sensors in the previous research are presented in Figure 7 and Table S1. The indicators for comparisons mainly included the optimum working temperature, response to 3H-2B, response/recovery time, and LOD. According to the comparison, the properties of the 1.0% Au/ZnO NS sensor were almost superior in every index compared with other recently reported sensors reported [5,7–11,36]. Thus, it verified that the 1.0% Au/ZnO NS sensor had amazing application potential for the rapid, high-sensitivity, and good-selectivity detection of 3H-2B. This was also the basis for the real-time, nondestructive, and efficient evaluation of LM.

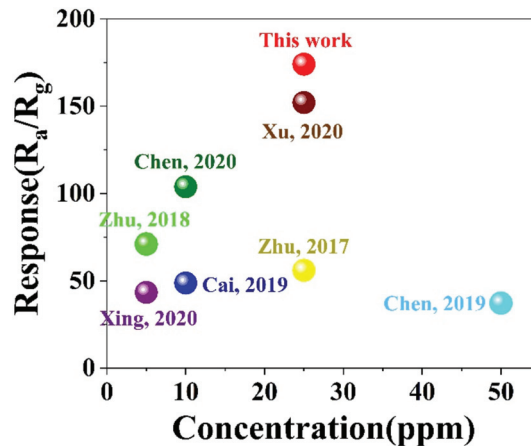
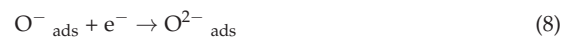


Figure 7. The comparison of the gas sensing performances of the 3H-2B sensors with other MOS-based 3H-2B sensors in previous research [5,7–11,36].

3.3. Gas-Sensing Mechanism

The sensing mechanism of ZnO NS adheres to a surface depletion model because ZnO NS is a kind of n-type MOS [47]. The reactions between the MOS surface and gas environment are the critical factors for the resistance change. Once ZnO NS is exposed to air, O₂ molecules are adsorbed to the surface of ZnO NS through capturing electrons from the conduction band. At the same time, oxygen molecules convert into various kinds of O_{ads}⁻ ions. The reactions during the procedure are shown in the following equations:



Meanwhile, the potential barriers and resistances of the materials are increasing due to the construction of thick EDL on the ZnO NS surface. However, when ZnO NS comes into contact with 3H-2B, active O_{ads}⁻ ions on the material's surface oxidize 3H-2B, which returns electrons to ZnO NS. The reaction is shown in the following equation [7]:



The electrons returned to ZnO NS are able to decrease the potential barriers and resistance of ZnO NS, which is displayed in Figure 8a,b [37]. In Au/ZnO NS, Au NPs can reduce the chemical adsorption activation energy of 3H-2B, which speeds up the reaction between 3H-2B and the O_{ads}⁻ ions. At the same time, the spillover effect occurs. Au NPs

improve the adsorption efficiency of oxygen molecules and transfer them to the Au/ZnO NS surface, leading to the increased concentration of O_{ads} . Moreover, the Schottky junction can be formed between Au NPs and the material interface. Moreover, compared with the work function of ZnO (4.65 eV), that of Au (5.1 eV) is higher; therefore, Au NPs attract more electrons from the conduction band of ZnO. All these processes greatly increase the thickness of EDL and the resistance of Au/ZnO NS, which improve the sensitivity significantly [20,21,48]. Figure 8c shows that the resistance of 1.0% Au/ZnO NS in the air was much higher compared with the resistance of pristine ZnO NS. Then, the resistance of 1.0% Au/ZnO NS decreased lower than that of ZnO NS after the 3H-2B injection. This phenomenon provided favorable support for the above mechanism analysis.

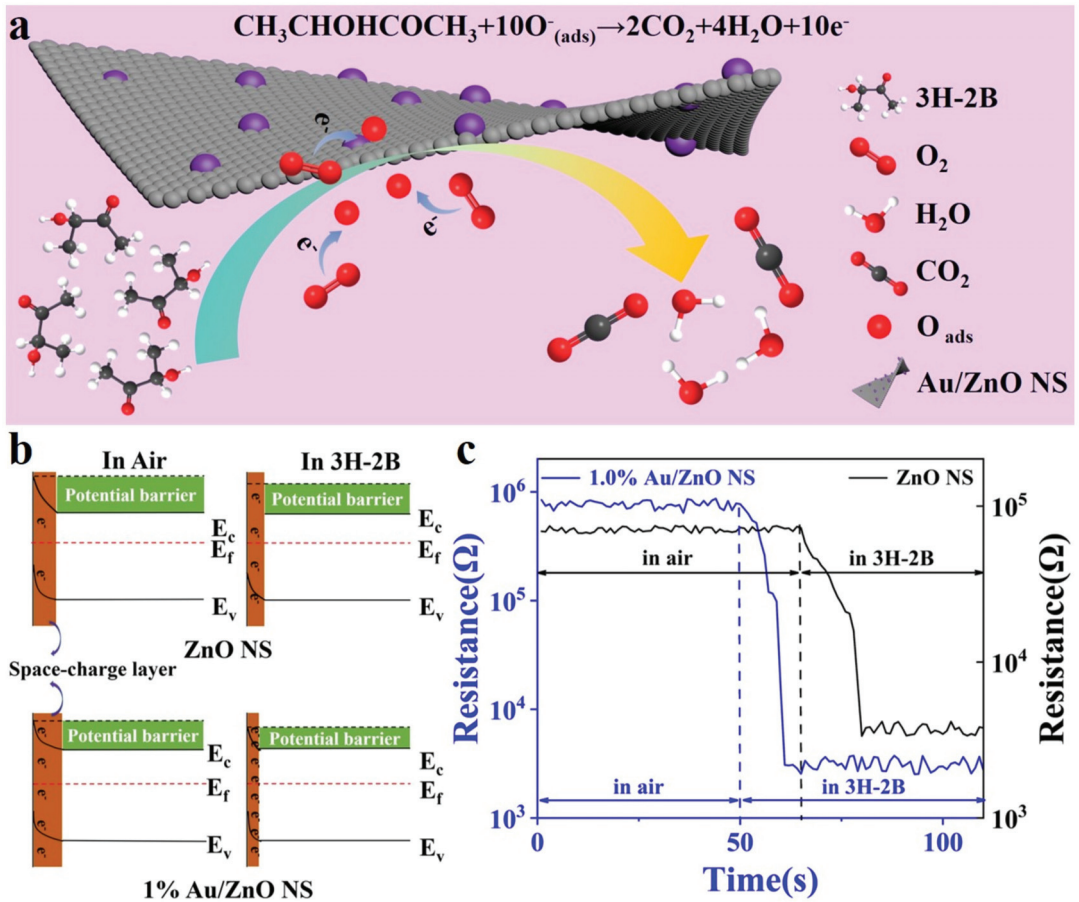


Figure 8. (a) The schematic illustration of 3H-2B sensing mechanism. (b) Electron structure change and (c) resistance change of ZnO NS and 1.0% Au/ZnO NS in air and 3H-2B.

4. Discussion and Conclusions

In this work, ZnO NS was synthesized by a hydrothermal reaction, and Au NPs (~5.5 nm) were prepared via the oleylamine reduction method. Then, an ultrasonic treatment was carried out to modified Au NPs and ZnO NS, which were represented as Au/ZnO NS. XRD, BET, TEM, and XPS were used to characterize their morphologies, microstructures, catalytic structures, specific surface areas, and chemical compositions. The efficient 3H-2B gas sensors based on the MEMS were constructed using Au/ZnO NS as the sensing material. The response of the sensors vs. 25 ppm 3H-2B was up to 174.04 at 230 °C.

Moreover, the Au/ZnO NS sensors presented fast response/recovery times (6 s/7 s), low LOD (0.5 ppm), a good linear relationship, and great selectivity. The gas sensors based on Pd/ZnO NS, Pt/ZnO NS, and pure ZnO NS were further studied to make comparisons with Au/ZnO NS. The enhanced responses of the sensors are primarily attributed to the morphology and structure improvements of Au/ZnO NS, the spillover effect, and the work function difference. Thus, such an excellent sensor signifies amazing application potential for the real-time, nondestructive, and efficient detection of LM, which will make a tremendous contribution toward worldwide food safety.

Supplementary Materials: The following supporting information can be downloaded at: <https://www.mdpi.com/article/10.3390/bios12100803/s1>, the “preparation of ZnO sensors” and “gas sensor measurement” sections; Figure S1: Schematic illustration for the description of MOSs sensors. (a) The panoramic view of the MEMS gas sensor test system. (b) The measuring circuit of MEMS gas sensor. (c) The test base schematic of the MEMS gas sensor. (d) The exploded views of the test base; Figure S2: The N₂ adsorption–desorption isotherms and BJH pore size distribution of (a) ZnO NS and (b) 0.5% Au/ZnO NS; Figure S3: The limit of detection of 1.0% Au/ZnO NS towards 0.5 ppm 3H-2B at 230 °C; Figure S4: The long-term stability of 0.5% Au/ZnO NS, 1.0% Au/ZnO NS, 1.5% Au/ZnO NS, and 2.0% Au/ZnO NS towards 10 ppm 3H-2B at 230 °C; Table S1: The comparison of the gas sensing properties of 1.0% Au/ZnO NS sensors with other MOS-based 3H-2B sensors in the previous research. References [5,7–11,27,36] are cited in Supplementary Materials.

Author Contributions: Conceptualization, C.Z., Y.Z. (Yong Zhao) and Y.Z. (Yongheng Zhu); methodology, C.Z.; validation, S.X. (Siqi Xie), J.W. (Jinlei Wei) and J.H.; formal analysis, C.Z.; resources, Y.Z. (Yong Zhao) and Y.Z. (Yongheng Zhu); writing—original draft preparation, C.Z. and S.X. (Shanshan Xu); writing—review and editing, C.Z. and S.X. (Shanshan Xu); supervision, J.W. (Jing Wei), Z.Z., H.L. and J.C.; project administration, J.W. (Jing Wei), Z.Z., H.L., Y.Z. (Yong Zhao) and Y.Z. (Yongheng Zhu); funding acquisition, Y.Z. (Yong Zhao) and Y.Z. (Yongheng Zhu). All authors have read and agreed to the published version of the manuscript.

Funding: This research was funded by the Agricultural Project of Shanghai Science and Technology Innovation Action Plan (19391901600), the Natural Science Foundation of Shanghai (21ZR1427500), the Shanghai Agriculture Applied Technology Development Program (2021-02-08-00-12-F00763), and the Key Basic Research Program of Science and Technology Commission of Shanghai Municipality (20JC1415300).

Institutional Review Board Statement: Not applicable.

Informed Consent Statement: Not applicable.

Data Availability Statement: Not applicable.

Conflicts of Interest: The authors declare no conflict of interest.

References

- De Noordhout, C.M.; Devleeschauwer, B.; Angulo, F.J.; Verbeke, G.; Haagsma, J.; Kirk, M.; Havelaar, A.; Speybroeck, N. The global burden of *Listeriosis*: A systematic review and meta-analysis. *Lancet Infect. Dis.* **2014**, *14*, 1073–1082. [CrossRef]
- Radoshevich, L.; Cossart, P. *Listeria monocytogenes*: Towards a complete picture of its physiology and pathogenesis. *Nat. Rev. Microbiol.* **2018**, *16*, 32–46. [CrossRef] [PubMed]
- Velusamy, V.; Arshak, K.; Korostynska, O.; Oliwa, K.; Adley, C. An overview of foodborne pathogen detection in the perspective of biosensors. *Biotechnol. Adv.* **2010**, *28*, 232–245. [CrossRef] [PubMed]
- Välilä, A.L.; Tilsala-Timisjärvi, A.; Virtanen, E. Rapid detection and identification methods for *Listeria monocytogenes* in the food chain—A review. *Food Control* **2015**, *55*, 103–114. [CrossRef]
- Zhu, Z.Y.; Zheng, L.J.; Zheng, S.Z.; Chen, J.; Liang, M.H.; Tian, Y.T.; Yang, D.C. Cr doped WO₃ nanofibers enriched with surface oxygen vacancies for highly sensitive detection of the 3-hydroxy-2-butanone biomarker. *J. Mater. Chem. A* **2018**, *6*, 21419–21427. [CrossRef]
- Yu, Y.X.; Sun, X.H.; Liu, Y.; Pan, Y.J.; Zhao, Y. Odor fingerprinting of *Listeria monocytogenes* recognized by SPME–GC–MS and E-nose. *Can. J. Microbiol.* **2015**, *61*, 367–372. [CrossRef]
- Zhu, Y.H.; Zhao, Y.; Ma, J.H.; Cheng, X.W.; Xie, J.; Xu, P.C.; Liu, H.Q.; Liu, H.P.; Zhang, H.J.; Wu, M.H.; et al. Mesoporous tungsten oxides with crystalline framework for highly sensitive and selective detection of foodborne pathogens. *J. Am. Chem. Soc.* **2017**, *139*, 10365–10373. [CrossRef]

8. Cai, H.J.; Liu, H.Q.; Ni, T.J.; Pan, Y.J.; Zhao, Y.; Zhu, Y.H. Controlled synthesis of Pt doped SnO₂ mesoporous hollow nanospheres for highly selective and rapidly detection of 3-hydroxy-2-butanone biomarker. *Front. Chem.* **2019**, *7*, 843. [\[CrossRef\]](#)
9. Xu, D.P.; Ge, K.J.; Qi, S.Y.; Chen, Y.; Qiu, J.X.; Liu, Q. Hydrangea-like mesoporous WO₃ nanoflowers with crystalline framework for 3-hydroxy-2-butanone sensing. *Anal. Bioanal. Chem.* **2020**, *412*, 8371–8378. [\[CrossRef\]](#)
10. Xing, X.X.; Zhu, Z.Y.; Du, L.L.; Feng, D.L.; Chen, J.; Li, S.; Yang, D.C. Burrs-shelled SnO₂@Al₂O₃ nanocables for detection of 3-hydroxy-2-butanone biomarkers. *Appl. Surf. Sci.* **2020**, *502*, 144106. [\[CrossRef\]](#)
11. Chen, J.; Zhu, Z.Y.; Zheng, S.Z.; Du, L.L.; Xing, X.X.; Feng, D.L.; Li, S.; Yang, D.C. Synthesis of zinc oxide-alumina nanocables for detection of 3-hydroxy-2-butanone biomarker. *Mater. Lett.* **2019**, *253*, 121–123. [\[CrossRef\]](#)
12. Zhu, Z.Y.; Zheng, L.J.; Zheng, S.Z.; Chen, J.; Xing, X.; Feng, D.L.; Yang, D.C. Multichannel pathway-enriched mesoporous NiO nanocuboids for the highly sensitive and selective detection of 3-hydroxy-2-butanone biomarkers. *J. Mater. Chem. A* **2019**, *7*, 10456–10463. [\[CrossRef\]](#)
13. Xu, J.Q.; Han, J.J.; Zhang, Y.; Sun, Y.A.; Xie, B. Studies on alcohol sensing mechanism of ZnO based gas sensors. *Sens. Actuators B Chem.* **2009**, *132*, 334–339. [\[CrossRef\]](#)
14. Meng, F.L.; Zheng, H.X.; Sun, Y.F.; Li, M.Q.; Liu, J.H. Trimethylamine sensors based on au-modified hierarchical porous single-crystalline ZnO nanosheets. *Sensors* **2017**, *17*, 1478. [\[CrossRef\]](#)
15. Choi, M.S.; Kim, M.Y.; Mirzaei, A.; Kim, H.S.; Kim, S.I.; Baek, S.H.; Chun, D.W.; Jin, C.H.; Lee, K.H. Selective, sensitive, and stable NO₂ gas sensor based on porous ZnO nanosheets. *Appl. Surf. Sci.* **2021**, *569*, 150910. [\[CrossRef\]](#)
16. Xu, D.S.; Xu, P.C.; Wang, X.Q.; Chen, Y.; Yu, H.T.; Zheng, D.; Li, X.X. Pentagon-shaped Ag@Pt core-shell nanostructures as high-performance catalysts for formaldehyde detection. *ACS Appl. Mater. Interfaces* **2020**, *12*, 8091–8097. [\[CrossRef\]](#)
17. Choi, S.J.; Lee, I.; Jang, B.H.; Youn, D.Y.; Ryu, W.H.; Park, C.O.; Kim, I.D. Selective diagnosis of diabetes using ptfunctionalized WO₃ hemitube networks as a sensing layer of acetone in exhaled breath. *Anal. Chem.* **2013**, *85*, 1792–1796. [\[CrossRef\]](#)
18. Jang, J.S.; Yu, S.; Choi, S.J.; Kim, S.J.; Koo, W.T.; Kim, I.D. Metal chelation assisted in situ migration and functionalization of catalysts on peapod-like hollow SnO₂ toward a superior chemical sensor. *Small* **2016**, *12*, 5989–5997. [\[CrossRef\]](#)
19. Wang, Y.L.; Cui, X.B.; Yang, Q.Y.; Liu, J.; Gao, Y.; Sun, P.; Lu, G.Y. Preparation of Ag-loaded mesoporous WO₃ and its enhanced NO₂ sensing performance. *Sens. Actuators B Chem.* **2016**, *225*, 544–552. [\[CrossRef\]](#)
20. Zhao, C.; Shen, J.B.; Xu, S.S.; Wei, J.; Liu, H.Q.; Xie, S.Q.; Pan, Y.J.; Zhao, Y.; Zhu, Y.H. Ultra-efficient trimethylamine gas sensor based on Au nanoparticles sensitized WO₃ nanosheets for rapid assessment of seafood freshness. *Food Chem.* **2022**, *392*, 133318. [\[CrossRef\]](#)
21. Majhi, S.M.; Rai, P.; Yu, Y.T. Facile approach to synthesize Au@ZnO core-shell NPs and their application for highly sensitive and selective gas sensors. *ACS Appl. Mater. Interfaces* **2015**, *7*, 9462–9468. [\[CrossRef\]](#)
22. Wang, L.W.; Wang, S.R.; Xu, M.J.; Hu, X.J.; Zhang, H.X.; Wang, Y.S.; Huang, W.P. A Au-functionalized ZnO nanowire gas sensor for detection of benzene and toluene. *Phys. Chem. Chem. Phys.* **2013**, *15*, 17179–17186. [\[CrossRef\]](#)
23. Meng, F.L.; Ge, S.; Jia, Y.; Sun, B.; Sun, Y.F.; Wang, C.; Wu, H.; Jin, Z.; Li, M.Q. Interlaced nanoflake-assembled flower-like hierarchical ZnO microspheres prepared by bisolvents and their sensing properties to ethanol. *J. Alloys Compd.* **2015**, *632*, 645–650. [\[CrossRef\]](#)
24. Meng, F.L.; Hou, N.N.; Ge, S.; Sun, B.; Jin, Z.; Shen, W.; Kong, L.T.; Guo, Z.; Sun, Y.F.; Wu, H.; et al. Flower-like hierarchical structures consisting of porous single-crystalline ZnO nanosheets and their gas sensing properties to volatile organic compounds (VOCs). *J. Alloys Compd.* **2015**, *626*, 124–130. [\[CrossRef\]](#)
25. Hou, N.N.; Jin, Z.; Sun, B.; Sun, Y.F.; Shen, W.; Guo, Z.; Kong, L.T.; Li, M.Q.; Meng, F.L. New strategy for rapid detection of the simulants of persistent organic pollutants using gas sensor based on 3-D porous single-crystalline ZnO nanosheets. *IEEE Sens. J.* **2015**, *15*, 3668–3674. [\[CrossRef\]](#)
26. Han, T.; Zhang, Y.; Xu, J.; Dong, J.; Liu, C.C. Monodisperse AuM (M = Pd, Rh, Pt) bimetallic nanocrystals for enhanced electrochemical detection of H₂O₂. *Sens. Actuators B Chem.* **2015**, *207*, 404–412. [\[CrossRef\]](#)
27. Shen, J.B.; Xu, S.S.; Zhao, C.; Qiao, X.P.; Liu, H.Q.; Zhao, Y.; Wei, J.; Zhu, Y.H. Bimetallic Au@Pt nanocrystal sensitization mesoporous alpha-Fe₂O₃ hollow nanocubes for highly sensitive and rapid detection of fish freshness at low temperature. *ACS Appl. Mater. Interfaces* **2021**, *13*, 57597–57608. [\[CrossRef\]](#)
28. Wang, D.; Deng, L.F.; Cai, H.J.; Yang, J.L.; Bao, L.P.; Zhu, Y.H.; Wang, X.Y. Bimetallic PtCu nanocrystal sensitization WO₃ hollow spheres for highly efficient 3-hydroxy-2-butanone biomarker detection. *ACS Appl. Mater. Interfaces* **2020**, *12*, 18904–18912. [\[CrossRef\]](#)
29. Zhang, B.; Wang, F.; Zhu, C.Q.; Li, Q.; Song, J.N.; Zheng, M.J.; Ma, L.; Shen, W.Z. A facile self-assembly synthesis of hexagonal ZnO nanosheet films and their photoelectrochemical properties. *Nano-Micro Lett.* **2016**, *8*, 137–142. [\[CrossRef\]](#)
30. Huang, M.H.; Wu, Y.Y.; Feick, H.; Tran, N.; Weber, E.; Yang, P.D. Catalytic growth of zinc oxide nanowires by vapor transport. *Adv. Mater.* **2001**, *13*, 113–116. [\[CrossRef\]](#)
31. Li, G.; Cheng, Z.; Xiang, Q.; Yan, L.; Wang, X.; Xu, J. Bimetal PdAu decorated SnO₂ nanosheets based gas sensor with temperature-dependent dual selectivity for detecting formaldehyde and acetone. *Sens. Actuators B Chem.* **2019**, *283*, 590–601. [\[CrossRef\]](#)
32. Song, X.; Xu, Q.; Zhang, T.; Song, B.; Li, C.; Cao, B. Room-temperature, high selectivity and low-ppm-level triethylamine sensor assembled with au decahedrons-decorated porous alpha-Fe₂O₃ nanorods directly grown on flat substrate. *Sens. Actuators B Chem.* **2018**, *268*, 170–181. [\[CrossRef\]](#)

33. Cao, P.J.; Huang, Q.G.; Navale, S.T.; Fang, M.; Liu, X.K.; Zeng, Y.X.; Liu, W.J.; Stadler, F.J.; Lu, Y.M. Integration of, esoporous ZnO and Au@ZnO nanospheres into sensing device for the ultrasensitive CH₃COCH₃ detection down to ppb levels. *Appl. Surf. Sci.* **2020**, *518*, 146223–146234. [[CrossRef](#)]
34. Pelicano, C.M.; Yanagi, H. Accelerated growth of nanostructured ZnO films via low temperature microwave-assisted H₂O oxidation for solar cell applications. *Appl. Surf. Sci.* **2020**, *506*, 144917. [[CrossRef](#)]
35. Ma, J.H.; Ren, Y.; Zhou, X.R.; Liu, L.L.; Zhu, Y.H.; Cheng, X.W.; Xu, P.C.; Li, X.X.; Deng, Y.H.; Zhao, D.Y. Pt nanoparticles sensitized ordered mesoporous WO₃ semiconductor: Gas sensing performance and mechanism study. *Adv. Funct. Mater.* **2018**, *28*, 1705268. [[CrossRef](#)]
36. Chen, J.; Feng, D.L.; Wang, C.; Xing, X.X.; Du, L.L.; Zhu, Z.Y.; Huang, X.H.; Yang, D.C. Gas sensor detecting 3-hydroxy-2-butanone biomarkers: Boosted response via decorating Pd nanoparticles onto the {010} facets of BiVO₄ decahedrons. *ACS Sens.* **2020**, *5*, 2620–2627. [[CrossRef](#)]
37. Lee, J.H.; Mirzaei, A.; Kim, J.Y.; Kim, J.H.; Kim, H.W.; Kim, S.S. Optimization of the surface coverage of metal nanoparticles on nanowires gas sensors to achieve the optimal sensing performance. *Sens. Actuators B Chem.* **2019**, *302*, 127196. [[CrossRef](#)]
38. Wan, L.; Song, H.Y.; Ma, J.H.; Ren, Y.; Cheng, X.W.; Su, J.C.; Yue, Q.; Deng, Y.H. Polymerization-induced colloid assembly route to iron oxide-based mesoporous microspheres for gas sensing and fenton catalysis. *ACS Appl. Mater. Interfaces* **2018**, *10*, 13028–13039. [[CrossRef](#)]
39. Xiao, X.Y.; Liu, L.L.; Ma, J.H.; Ren, Y.; Cheng, X.W.; Zhu, Y.H.; Zhao, D.Y.; Elzatahry, A.A.; Alghamdi, A.; Deng, Y.H. Ordered mesoporous tin oxide semiconductors with large pores and crystallized walls for high-performance gas sensing. *ACS Appl. Mater. Interfaces* **2018**, *10*, 1871–1880. [[CrossRef](#)]
40. Liu, C.; Wang, Y.; Zhao, P.; Li, W.; Wang, Q.; Sun, P.; Chuai, X.; Lu, G. Porous alpha-Fe₂O₃ microflowers: Synthesis, structure, and enhanced acetone sensing performances. *J. Colloid Interface Sci.* **2017**, *505*, 1039–1046. [[CrossRef](#)]
41. Zhang, F.D.; Dong, X.; Cheng, X.L.; Xu, Y.M.; Zhang, X.F.; Huo, L.H. Enhanced gas-sensing properties for trimethylamine at low temperature based on MoO₃/Bi₂Mo₃O₁₂ hollow microspheres. *ACS Appl. Mater. Interfaces* **2019**, *11*, 11755–11762. [[CrossRef](#)]
42. Liu, C.; Gao, H.; Wang, L.; Wang, T.; Yang, X.; Sun, P.; Gao, Y.; Liang, X.; Liu, F.; Song, H.; et al. Facile synthesis and the enhanced sensing properties of Pt-loaded α-Fe₂O₃ porous nanospheres. *Sens. Actuators B Chem.* **2017**, *252*, 1153–1162. [[CrossRef](#)]
43. Cai, H.J.; Qiao, X.P.; Chen, M.L.; Feng, D.S.; Alghamdi, A.A.; Alharthi, F.A.; Pan, Y.J.; Zhao, Y.; Zhu, Y.H.; Deng, Y.H. Hydrothermal synthesis of hierarchical SnO₂ nanomaterials for high-efficiency detection of pesticide residue. *Chin. Chem. Lett.* **2021**, *32*, 1502–1506. [[CrossRef](#)]
44. Chen, Y.P.; Li, Y.X.; Feng, B.X.; Wu, Y.; Zhu, Y.H.; Wei, J. Self-templated synthesis of mesoporous Au-ZnO nanospheres for seafood freshness detection. *Sens. Actuators B Chem.* **2022**, *360*, 131662. [[CrossRef](#)]
45. Wu, L.; Zhang, W.M.; Liu, C.; Foda, M.F.; Zhu, Y.H. Strawberry-like SiO₂/Ag nanocomposites immersed filter paper as SERS substrate for acrylamide detection. *Food Chem.* **2020**, *328*, 127106. [[CrossRef](#)]
46. Wu, L.; Xianyu, Y.L.; Wang, Z.L.; Dong, Y.Z.; Hu, X.B.; Chen, Y.P. Amplified magnetic resonance sensing via enzyme-mediated click chemistry and magnetic separation. *Anal. Chem.* **2020**, *91*, 15555–15562. [[CrossRef](#)]
47. Sakai, G.; Matsunaga, N.; Shimano, K.; Yamazoe, N. Theory of gas-diffusion controlled sensitivity for thin film semiconductor gas sensor. *Sens. Actuators B Chem.* **2001**, *80*, 125–131. [[CrossRef](#)]
48. Wang, L.L.; Dou, H.M.; Lou, Z.; Zhang, T. Encapsuled nanoreactors (Au@SnO₂): A new sensing material for chemical sensors. *Nanoscale* **2013**, *5*, 2686–2691. [[CrossRef](#)]



Communication

HPTLC-Bioluminescent Bioautography Screening of Herbal Teas for Adulteration with Hypolipidemic Drugs

Yuting Wang ¹, Xingjun Xi ^{2,*}, Liao Wang ³ and Yisheng Chen ^{4,*}¹ State Key Laboratory of Food Science and Technology, Nanchang University, Nanchang 330047, China² Sub-Institute of Agricultural Food Standardization, China National Institute of Standardization, Beijing 100191, China³ School of Food Science and Technology, Jiangnan University, Wuxi 214122, China⁴ College of Food Science and Engineering, Shanxi Agricultural University, Taigu 030801, China

* Correspondence: xixj@cnis.ac.cn (X.X.); chenisheng@sxau.edu.cn (Y.C.)

Abstract: Teas based on nutraceutical herbs are an effective tool against hyperlipidemia. However, the adulteration with chemical drugs is frequently detected. By coupling bioluminescent bioautography with high performance thin-layer chromatography (HPTLC), we developed a facile method suitable for screening hypolipidemic drugs (ciprofibrate and bezafibrate) adulteration in five different herbal teas (lotus leaf, Apocynum, Ginkgo biloba, Gynostemma and chrysanthemum). First, the sensitivity of a bioluminescent bacteria to the analyte was evaluated on different HPTLC layer materials, revealing that the best performance was achieved on the silica gel layer. On this basis, sample extracts were separated on silica gel plates via a standardized HPTLC procedure, forming a selective detection window for the targeted compound. Then, the separation results were rapidly visualized by the bioluminescence inhibition of bacteria cells within 6 min after dipping. The observed inhibition displayed an acceptable limit of detection (<20 ng/zone or 2 mg/kg) and linearity ($R^2 \geq 0.9279$) within a wide concentration range (50–1000 ng/zone). Furthermore, the optimized method was performed with artificially adulterated samples and the recovery rates were determined to be within the range of 71% to 91%, bracing its practical reliability. Showing superiorly high simplicity, throughput and specificity, this work demonstrated that the analytical method jointly based on HPTLC and bioautography was an ideal tool for screening bioactive compounds in complex biological matrix.

Keywords: HPTLC; bioluminescence; herbal tea; hypolipidemic activity; adulteration

Citation: Wang, Y.; Xi, X.; Wang, L.; Chen, Y. HPTLC-Bioluminescent Bioautography Screening of Herbal Teas for Adulteration with Hypolipidemic Drugs. *Biosensors* **2023**, *13*, 392. <https://doi.org/10.3390/bios13030392>

Received: 11 February 2023

Revised: 9 March 2023

Accepted: 10 March 2023

Published: 17 March 2023



Copyright: © 2023 by the authors. Licensee MDPI, Basel, Switzerland. This article is an open access article distributed under the terms and conditions of the Creative Commons Attribution (CC BY) license (<https://creativecommons.org/licenses/by/4.0/>).

1. Introduction

Hyperlipidemia is a metabolic disease characterized of abnormally increasing total cholesterol, low-density lipoprotein cholesterol and triglyceride levels or decreasing high-density lipoprotein cholesterol. Hyperlipidemia has been a highlighted risk factor for public health since it is closely related to cardiovascular diseases and is the major cause of morbidity and mortality world-widely. Remarkably, the prevalence of lipid metabolism disorder is rapidly increasing not only in the elderly people, but also in the adolescent, which may be attributed to the high-oil dietary and irregular lifestyle. The modern pharmacological medication is an effective way to maintain normal lipid profile but is associated with many side-effects.

In this regard, marked attention was paid to the health tea based on nutraceutical herbs. It has been experimentally demonstrated that phytochemicals from many nutraceutical herbs had hypolipidemic activities by modulating various molecular targets and related pathways [1–4]. For example, Weng reported that the dammarane-type glycosides from *Gynostemma* showed promising hypolipidemic activity by inhibiting proprotein convertase subtilisin/kexin type 9 in HepG2 cells [5]. The hypolipidemic effects of hot water leaf extract was also experimentally evidenced [6].

More importantly, these nutraceutical herbs have a long history as food stuff, guaranteeing their safety as important ingredients of health tea. As hypolipidemic active nutraceutical herbs have become increasingly popular in the health food markets around the world, the adulteration with synthetic potent drug poses a serious challenge to food safety agencies. Not surprisingly, this has been a common problem of herb products. For example, many “all natural” herb product claimed to improve sexual performance have artificially added a 5-phosphodiesterase inhibitor that is originally used as a relaxing cardiovascular smooth muscle drug [7].

Many methods had been proposed for authenticating herbal tea [8,9]. In contrast to the “gold method” based on column chromatography, high performance thin-layer chromatography (HPTLC) gained remarkable attention. Conventionally, HPTLC was underestimated for its relatively poor separation and low sensitivity. Nevertheless, the unique merit of its compatibility was highly acknowledged [10–14]. Apart from that, HPTLC also displayed many intrinsic advantages, such as simplicity, matrix-tolerance and high-throughput. This enabled the analyst to expand the capacity of HPTLC by easily integrating a large array of assays that conventionally performed interpendently, such as surface enhanced Raman spectroscopy [15–17] and IR [18,19]. Particularly, HPTLC separation in combination with elaborately chosen effect-directed assays, also termed bioautography, had been demonstrated a novel and promising tool for screening of compounds with specific bioactivity in bio-mixtures [20–23].

In this work, a selective and reliable HPTLC method for screening two hypolipidemic drugs, including ciprofibrate (CPF) and bezafibrate (BZF), was developed with a sensitive bioautography based on the response of microbial bioluminescence, which was completely different from conventional chemical derivatization. In addition, the established method was further validated with different herb extracts to evidence its applicability.

2. Materials and Methods

2.1. Chemicals and Instruments

The reference standard of ciprofibrate (purity $\geq 99\%$, HPLC) and bezafibrate (purity $\geq 96.0\%$, HPLC) were purchased from Aladdin (Shanghai, China). Na_2HPO_4 , KH_2PO_4 , glycerol and other reagents with analytical purity was purchased from Sigma-Aldrich (Shanghai, China). Peptone and yeast extract were from Sinopharm (Beijing, China). A Millipore Synergy system (Schwalbach, Saarland, Germany) was used to prepare Ultra-pure water. A HPTLC work station, including a semi-auto sampler Linomat 5, an automatic developing chamber ADC2 and biovisualizer was from CAMAG (MuttENZ, Basel, Switzerland). Ultrasonic water bath (CSSY-80) was from Yichen (Jintan, Jiangsu, China).

Six different glass backed plates was used: (1) silica gel F₂₅₄ plates (analytical grade, 10 cm × 20 cm, serial No. 1.05729.0001) were from Merck (Darmstadt, Germany); (2) NH_2 bonded silica gel F₂₅₄ plates (analytical grade, 10 cm × 20 cm, serial No. 811111) were from MN (Düren, Bayern, Germany); (3) the silica gel plates (10 cm × 20 cm), Neutralized aluminum oxide plates (10 cm × 10 cm), Acidified aluminum oxide plates (10 cm × 10 cm) and Diatomite plates (10 cm × 10 cm) were from Qingdao Haiyang (Qingdao, Shandong, China). Five authentic health teas based on lotus leaf (LL), Apocynum (AC), Ginkgo biloba (GB), Gynostemia (GS) and chrysanthemum (CT) were purchased from the local market.

2.2. Preparation of Bioluminescent Suspension

The bioluminescent bacteria strain *Photobacterium phosphoreum* was provided by Nanjing Institute of Soil Science, Chinese Academy of Sciences. The method of preparing bacterial suspension with bioluminescence was principally based on the steps previously described [23,24]. When strong greenish bioluminescence became observable to eye inspection, as shown in Figure 1, the bacterial suspension was diluted with another 100 mL liquid medium prior to usage.

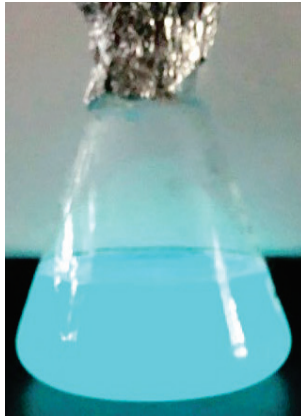


Figure 1. Bioluminescence of the bacteria suspension.

2.3. Preparation of Standard Solution

An amount of 10 ± 0.1 mg reference standards of CPF and BZF were added into a 10 mL volumetric flask, respectively. The flask was filled with 10 mL methanol, resulting in 1 mg/mL standard stock solution. The working solution was prepared by further diluting the stock solution to 0.02 mg/mL.

2.4. Preparation of Tea Samples

The dried tea samples were smashed to powder. An amount of 1 g sample powder was mixed with 10 mL methanol. The mixture was conditioned in ultrasound bath at 25 °C for 30 min, then centrifuged at 5000 rpm for 5 min. An amount of 5 mL of the obtained supernatant was evaporated and recovered with 0.5 mL methanol. Then, the extract was filtered through 0.45 μ m nylon membrane for further analysis.

2.5. HPTLC Steps

With a Linomat 5 semi-automatic sampler, solution of standards and samples extract (10 μ L) were sprayed as 6 mm bands, facilitated by a 0.5 MPa nitrogen stream. Dosage speed of spraying is 100 nL/s, with predosage volume at 0.2 nL. The band array was 10 mm from the plate bottom and at least 15 mm from both sides.

After evaporating the sample solvent in the application band, chromatography was performed in the ADC-2 automatic developing chamber using ethyl acetate+methanol (9 + 1 mL) as the mobile phase with constant settings: 3 min humidity control with saturated $MgCl_2$, 10 min chamber saturation, 10 min plate pre-conditions and 60 mm migration distance. Then, the mobile phase residue was completely evaporated at 80 °C for 5 min. Pictures of the separation results on the HPTLC plate was documented by a HPTLC image system DD70, illuminated by 254, 366 nm and with light, respectively.

2.6. Documentation and Analysis of the Bioluminescent Image

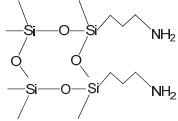
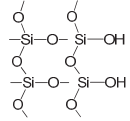
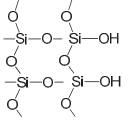
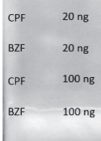
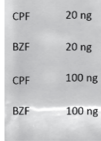
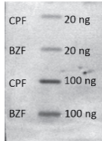
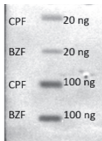
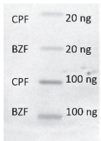
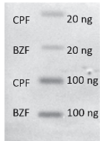
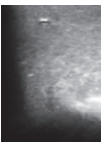
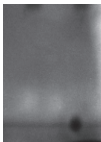
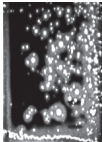
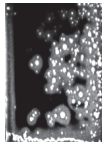


After chromatography, the dried plate was dipped into the prepared bacteria suspension with strong bioluminescence by a TLC immersion Device 3, with constant settings: dipping speed 1 mm/s and staying time 2 s. Then, the plate was immediately placed into the sample chamber of a biovisualizer. Then, documentation of bioluminescence images was saved in black/white and colorful format, respectively. The bioluminescent inhibition profile was quantitative evaluated by Videoscan, respectively, based on the grayscale value of pixels.

3. Result and Discussion

3.1. Optimization of HPTLC Layer Material

The spectroscopic character of the targeted analyte of this study was poor, neither with nature fluorescence nor fluorescence quenching. Therefore, they were hardly visible on the HPTLC plate, necessitating derivatization. Different from conventional chemical derivatization reactions, bioautography based on whole cell displayed strong dependence on layer materials, which had been experimentally evidenced in the HPTLC analysis of antibiotics [25] and alkaloid [26]. Such layer-induced sensitization can be employed to strength the detectability of analyte. In this regard, we evaluated the bioautography results of the analyte deposited on five most used HPTLC layer materials, including silica gel, NH₂-silica gel, acidified/neutralized aluminum oxide and diatomite. After dipping, the bioluminescence from the bacteria differed dramatically, as comparatively summarized in Table 1. Plate layers made of aluminum oxide and diatomite were demonstrated to be not suitable for the used bioautography because their exposure strongly inhibited the bioluminescence. Meanwhile, brilliant background can be observed both on silica gel and NH₂-silica gel. However, sensitive inhibition spots down to 20 ng/zone can be observed on the silica gel, while no inhibition spot was detected on NH₂-silica gel. Therefore, the F₂₅₄ silica gel plate was used for further study.

Table 1. Characterization of the effects of layer materials on the detectability. Note: Images were from plates without development after 8 min exposure to bacteria suspension.

Group 1												
Layer materials	NH ₂ -Silica gel F ₂₅₄		Silica gel F ₂₅₄		Silica gel							
												
Exposure time (min)	0	8	0	8	0	8						
Image												
	CPF 20 ng	CPF 20 ng	CPF 20 ng	CPF 20 ng	CPF 20 ng	CPF 20 ng						
	BZF 20 ng	BZF 20 ng	BZF 20 ng	BZF 20 ng	BZF 20 ng	BZF 20 ng						
	CPF 100 ng	CPF 100 ng	CPF 100 ng	CPF 100 ng	CPF 100 ng	CPF 100 ng						
	BZF 100 ng	BZF 100 ng	BZF 100 ng	BZF 100 ng	BZF 100 ng							
Usability	NO		YES		YES							
Group 2												
Layer materials	Neutral aluminum oxide Al ₂ O ₃		Acidified aluminum oxide Al ₂ O ₃		Diatomite SiO ₂							
Exposure time (min)	0	8	0	8	0	8						
Image												
Usability	NO		NO		NO							

3.2. Optimization of Bioluminescent Bioautography

Different from conventional derivative reactions, the targeted molecule must penetrate the membrane of bacterial before its cytotoxicity can be sensed. Therefore, the bioluminescence inhibition pattern showed strong time-dependence in the initial few minutes. Apart from that, it must be kept in mind that the area of inhibition zone also increased along with exposure time due to diffusion. To fix an optimal balance between detectability and resolution, we quantitatively evaluated the change of inhibition profiles in the initial 12 min of exposure. As shown in Figure 2a, weak inhibition spots can be observed immediately after exposure. Then, the inhibition strength increased rapidly along with incubation time. Figure 2b–c further analyzed the change quantitatively, from which it was clear that the intensity of inhibition caused by BZF reached a platform stage after 6 min exposure, while the time for CPF was 8 min. Thereafter, signal intensities changed insignificantly, while zone diffusion became apparent. Considering these results, pictures were documented at 8 min after dipping for further experiments.

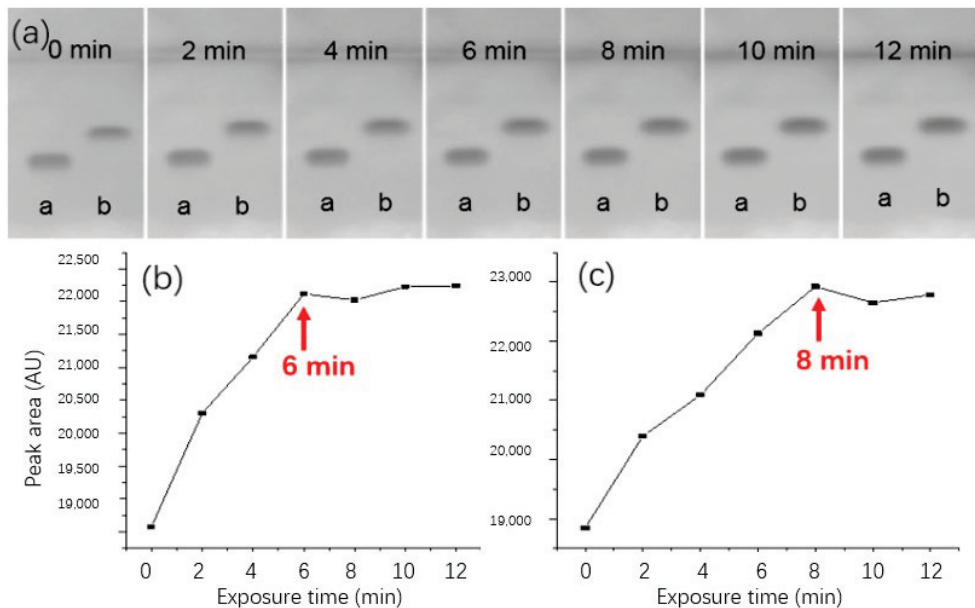


Figure 2. (a) The change of bioluminescent inhibition pattern within the initial 12 min after dipping. Track assignment: a—BZF, b—CPF; corresponding peak area variation profile for (b) BZF and (c) CPF.

3.3. Optimization of Chromatographic Conditions

The complexity of the targeted samples raised a serious challenge to the selectivity of detection. In order to prevent background interferences due to co-extractants, chromatographic conditions were optimized before bioautography. First, a trail of mixtures containing methanol, ethanol and ethyl acetate were tested for the separation. The selection of mobile phase was based on two principles: viscosity and toxicity being as low as possible. After comparison, it was found that the mixture of ethyl-acetate+methanol (9 + 1 mL) gave a preferable window of the targeted compound; in contrast, most endogenous substances that were not fully visible to 254 nm light were pushed upward, as shown in Figure 3a–c. This enabled straightforward identification of possible adulteration. Moreover, semi-quantitative data can be estimated simply by eye inspection, which was greatly suitable to screening tasks.

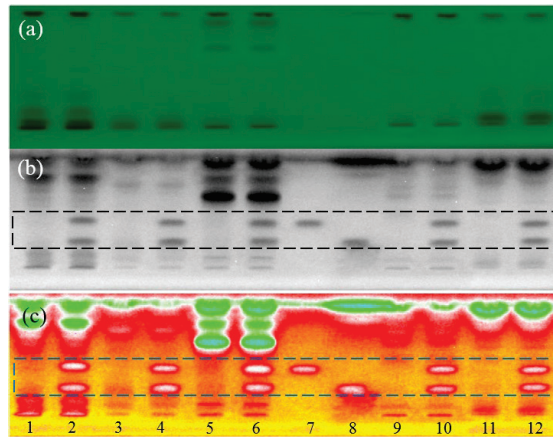


Figure 3. Images of a developed plate under different conditions: (a) underivatized-254 nm light, (b) dipped into bacterial suspension-bioluminescence inhibition (black/white mode) and (c) dipped into bacterial suspension-bioluminescence inhibition (color mode). Track assignment: 1 LL, 2 spiked LL, 3 AC, 4 spiked AC, 5 GB, 6 spiked GB, 7 CPF standard, 8 BZF standard, 9 GS, 10 spiked GS, 11 CT and 12 spiked CT; mobile phase ethyl acetate + methanol (9/1, *v/v*), standards concentration 150 ng/zone.

3.4. Precision and Sensitivity

As an alternative to straightforward eye inspection, evaluation of the digital image by software enabled a more precise analysis of the bioautographic results. This was principally based on virtually converting the grayscale pixel to chromatogram. Thus far, there had been a couple of software available to extract quantitative data from digitalized HPTLC images [27]. In this study, the software Videoscan tailored for analyzing HPTLC images were used for obtaining the integration result of chromatographic peak, which was exemplarily shown in Figure 4.

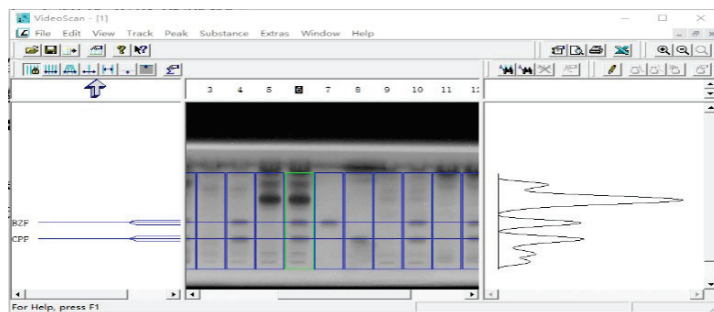


Figure 4. Quantitative analysis of the bioluminescence inhibition spots in HPTLC image by Videoscan software.

From the pixel analysis, it was revealed that the baseline drifting of the chromatogram was usually more serious than that of chemical derivatization. Therefore, the precision of detection was assessed first. From the obtained data, it was revealed that the overall RSD% of detection was <11.8% and therefore acceptable for screening analysis. In order to determine the limit of detection of the established method. Analyte zones at gradient concentrations from 25 to 5 ng/zone was assessed. Noticeably, the inhibition signal caused by the analyte did not display linear at concentrations <20 ng/zone. More specifically, spots of the analyte at 20 ng/zone were still visible. However, if the concentration was

reduced to the 15 ng/zone, the inhibition became invisible. In another word, the sensitivity of this method was >20 ng/zone. Taking the application volume into consideration, this detectability was equal to 2 mg/kg.

3.5. Linearity and Accuracy

Based on the optimized conditions, we further evaluated the signal–concentration relationship within the critical concentration range 50–1000 ng/zone. As shown in Figure 5, the chromatographic signals transformed from pixel grayscale values conformed dose-dependence with coefficient of determination $R^2 \geq 0.9279$, suggesting that the developed method was acceptable for quantitatively screening. In order to access the accuracy of analysis, blank samples with artificial adulteration were measured. As internal standard, three levels of the analyte at concentrations at 5 mg/kg, 10 mg/kg and 20 mg/kg, respectively, were spiked into the sample extraction mixture. As summarized in Table 2, the calculated recovery rates for all spiked extracts were within the range of 71% to 91%, showing little dependence on the sample matrices. These quantitative results conclusively evidenced that the established method could be a robust tool for screening the analyte in herbal tea samples.

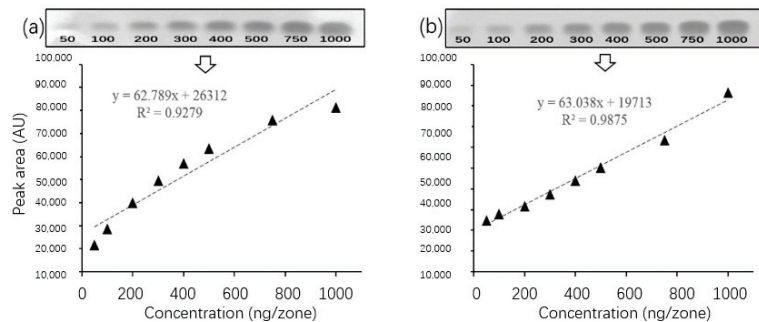


Figure 5. Dose-dependence profile of inhibition zones caused by the analyte from 50–1000 ng/zone: (a) BZF and (b) CPF.

Table 2. Accuracy evaluation of the established method.

Analyte	Spiked Levels (mg/kg)	Recovery Rate (%) *				
		LL	AC	GB	GS	CT
BZF	5	81 ± 7	79 ± 6	86 ± 8	80 ± 5	85 ± 5
	10	90 ± 8	89 ± 9	85 ± 7	78 ± 6	71 ± 4
	20	82 ± 8	84 ± 5	88 ± 8	72 ± 6	78 ± 7
CPF	5	74 ± 7	78 ± 7	83 ± 5	83 ± 7	85 ± 6
	10	89 ± 7	90 ± 9	83 ± 6	87 ± 6	81 ± 7
	20	78 ± 3	83 ± 8	91 ± 8	85 ± 7	90 ± 8

* The RSD% was calculated from three duplicates.

4. Conclusions

In this work, a fast and facile HPTLC method was developed for the screening of chemical adulteration in herbal tea with hypolipidemic activity. First, the bioluminescent assay was optimized with different HPTLC layer materials. Then, the strong background noises due to co-extracted sample matrices were prevented by separation on HPTLC plate. Under optimization of chromatography and bioautography conditions, the developed method gave an acceptable limit of detection and linearity ($R^2 \geq 0.9279$) within a wide concentration range (50–1000 ng/zone). Meanwhile, the validation with real samples suggested that this method had enough accuracy (spike-recover rate within 71% to 91%).

This work demonstrated that HPTLC was a promising platform for the effect-direct assay, which was able to greatly simplify the screening and identification of bioactive compounds in food.

Author Contributions: Conceptualization, Y.C. and X.X.; methodology, Y.W.; software, Y.W.; validation, L.W.; formal analysis, Y.W.; resources, Y.W.; data curation, L.W.; writing—original draft preparation, Y.W.; writing—review and editing, Y.W.; visualization, Y.W.; supervision, Y.C.; project administration, Y.W. and X.X.; funding acquisition, Y.C. and X.X. All authors have read and agreed to the published version of the manuscript.

Funding: This work was supported by the Open Project Program of State Key Laboratory of Food Science and Technology, Nanchang University (SKLF-KF-202001).

Institutional Review Board Statement: Not Applicable.

Informed Consent Statement: Informed consent was obtained from all subjects involved in the study.

Data Availability Statement: The data could be available on request.

Conflicts of Interest: The authors declare no conflict of interest.

References

- Lan, T.; Li, Q.; Chang, M.; Yin, C.; Zhu, D.; Wu, Z.; Li, X.; Zhang, W.; Yue, B.; Shi, J.; et al. Lei-gong-gen formula granule attenuates hyperlipidemia in rats via cGMP-PKG signaling pathway. *J. Ethnopharmacol.* **2020**, *260*, 112989. [[CrossRef](#)]
- Xie, W.; Zhao, Y.; Du, L. Emerging approaches of traditional Chinese medicine formulas for the treatment of hyperlipidemia. *J. Ethnopharmacol.* **2012**, *140*, 345–367. [[CrossRef](#)] [[PubMed](#)]
- Chu, S.-M.; Shih, W.-T.; Yang, Y.-H.; Chen, P.-C.; Chu, Y.-H. Use of traditional Chinese medicine in patients with hyperlipidemia: A population-based study in Taiwan. *J. Ethnopharmacol.* **2015**, *168*, 129–135. [[CrossRef](#)] [[PubMed](#)]
- Tsai, F.-J.; Li, T.-M.; Cheng, C.-F.; Wu, Y.-C.; Lai, C.-H.; Ho, T.-J.; Liu, X.; Tsang, H.; Lin, T.-H.; Liao, C.-C.; et al. Effects of Chinese herbal medicine on hyperlipidemia and the risk of cardiovascular disease in HIV-infected patients in Taiwan. *J. Ethnopharmacol.* **2018**, *219*, 71–80. [[CrossRef](#)] [[PubMed](#)]
- Weng, X.; Lou, Y.-Y.; Wang, Y.-S.; Huang, Y.-P.; Zhang, J.; Yin, Z.-Q.; Pan, K. New dammarane-type glycosides from *Gynostemma pentaphyllum* and their lipid-lowering activity. *Bioorg. Chem.* **2021**, *111*, 104843. [[CrossRef](#)] [[PubMed](#)]
- Du, H.; You, J.S.; Zhao, X.; Park, J.Y.; Kim, S.H.; Chang, K.J. Antiobesity and hypolipidemic effects of lotus leaf hot water extract with taurine supplementation in rats fed a high fat diet. *J. Biomed. Sci.* **2010**, *17* (Suppl. S1), S42. [[CrossRef](#)] [[PubMed](#)]
- Do, T.T.K.; Theocharis, G.; Reich, E. Simultaneous Detection of Three Phosphodiesterase Type 5 Inhibitors and Eight of Their Analogs in Lifestyle Products and Screening for Adulterants by High-Performance Thin-Layer Chromatography. *J. AOAC Inter.* **2015**, *98*, 1226–1233. [[CrossRef](#)]
- Wong, L.L.; Liang, Z.; Chen, H.; Zhao, Z. Ingredient authentication of commercial Xihuangcao herbal tea by a microscopic technique combined with UPLC-ESI-QTOF-MS/MS. *Anal. Method* **2015**, *7*, 4257–4268. [[CrossRef](#)]
- Ichim, M.C.; Booker, A. Chemical Authentication of Botanical Ingredients: A Review of Commercial Herbal Products. *Front. Pharmacol.* **2021**, *12*, 666850. [[CrossRef](#)]
- Xu, L.; Liu, S. Forecasting structure of natural products through color formation process by thin layer chromatography. *Food Chem.* **2021**, *334*, 127496. [[CrossRef](#)]
- Tang, C.; Guo, T.; Zhang, Z.; Yang, P.; Song, H. Rapid visualized characterization of phenolic taste compounds in tea extract by high-performance thin-layer chromatography coupled to desorption electrospray ionization mass spectrometry. *Food Chem.* **2021**, *355*, 129555. [[CrossRef](#)] [[PubMed](#)]
- Oellig, C.; Link, K.; Schwack, W. Characterization of E 472 food emulsifiers—determination of bound and free fruit acids, free glycerol and ash content. *J. Chromatogr. A* **2020**, *1619*, 460946. [[CrossRef](#)] [[PubMed](#)]
- Xu, L.; Shu, T.; Liu, S. Simplified Quantification of Representative Bioactives in Food Through TLC Image Analysis. *Food Anal. Method* **2019**, *12*, 2886–2894. [[CrossRef](#)]
- Hong, H.-J.; Yang, Q.; Liu, Q.; Leong, F.; Chen, X.-J. Chemical Comparison of Monk Fruit Products Processed by Different Drying Methods Using High-Performance Thin-Layer Chromatography Combined With Chemometric Analysis. *Front. Nutr.* **2022**, *9*, 887992. [[PubMed](#)]
- Chen, Y.; Chen, Q.; Wei, X. Separable surface enhanced Raman spectroscopy sensor platformed by HPTLC for facile screening of malachite green in fish. *Microchem. J.* **2021**, *170*, 106694. [[CrossRef](#)]
- Chen, Y.; Huang, C.; Hellmann, B.; Xu, X. HPTLC-Densitometry Determination of Riboflavin Fortified in Rice Noodle: Confirmed by SERS-Fingerprint. *Food Anal. Method* **2020**, *13*, 718–725. [[CrossRef](#)]
- Xie, Z.; Wang, Y.; Chen, Y.; Xu, X.; Jin, Z.; Ding, Y.; Yang, N.; Wu, F. Tuneable surface enhanced Raman spectroscopy hyphenated to chemically derivatized thin-layer chromatography plates for screening histamine in fish. *Food Chem.* **2017**, *230*, 547–552. [[CrossRef](#)]

18. Agatonovic-Kustrin, S.; Ramenskaya, G.; Kustrin, E.; Ortakand, D.B.; Morton, D.W. A new integrated HPTLC–ATR/FTIR approach in marine algae bioprofiling. *J. Pharm. Biomed. Anal.* **2020**, *189*, 113488. [[CrossRef](#)]
19. Agatonovic-Kustrin, S.; Morton, D.W. The Power of HPTLC–ATR–FTIR Hyphenation in Bioactivity Analysis of Plant Extracts. *Appl. Sci.* **2020**, *10*, 8232.
20. Sumudu Chandana, N.G.A.S.; Morlock, G.E. Eight different bioactivity profiles of 40 cinnamons by multi-imaging planar chromatography hyphenated with effect–directed assays and high-resolution mass spectrometry. *Food Chem.* **2021**, *357*, 129135. [[CrossRef](#)]
21. Klingelhöfer, I.; Hockamp, N.; Morlock, G.E. Non-targeted detection and differentiation of agonists versus antagonists, directly in bioprofiles of everyday products. *Anal. Chim. Acta* **2020**, *1125*, 288–298. [[CrossRef](#)] [[PubMed](#)]
22. Ristivojević, P.M.; Morlock, G.E. Effect-directed classification of biological, biochemical and chemical profiles of 50 German beers. *Food Chem.* **2018**, *260*, 344–353. [[CrossRef](#)] [[PubMed](#)]
23. Chen, Y.; Huang, C.; Hellmann, B.; Jin, Z.; Xu, X.; Xiao, G. A new HPTLC platformed luminescent biosensor system for facile screening of captan residue in fruits. *Food Chem.* **2020**, *309*, 125691. [[CrossRef](#)]
24. Chen, Y.; Huang, C.; Jin, Z.; Xu, X.; Cai, Y.; Bai, Y. HPTLC–bioautography/SERS screening nifedipine adulteration in food supplement based on Ginkgo biloba. *Microchem. J.* **2020**, *154*, 104647. [[CrossRef](#)]
25. Chen, Y.; Schwack, W. High-performance thin-layer chromatography screening of multi class antibiotics in animal food by bioluminescent bioautography and electrospray ionization mass spectrometry. *J. Chromatogr. A* **2014**, *1356*, 249–257. [[CrossRef](#)] [[PubMed](#)]
26. Chen, Y.; Morlock, G.E. Layer-Induced Sensitivity Enhancement in Planar Chromatography–Bioluminescence–Mass Spectrometry: Application to Alkaloids. *Chromatographia* **2016**, *79*, 89–96. [[CrossRef](#)]
27. Baumgartner, V.; Hohl, C.; Schwack, W. Rolling—A new application technique for luminescent bacteria on high-performance thin-layer chromatography plates. *J. Chromatogr. A* **2011**, *1218*, 2692–2699. [[CrossRef](#)]

Disclaimer/Publisher’s Note: The statements, opinions and data contained in all publications are solely those of the individual author(s) and contributor(s) and not of MDPI and/or the editor(s). MDPI and/or the editor(s) disclaim responsibility for any injury to people or property resulting from any ideas, methods, instructions or products referred to in the content.



Article

A Europium Nanosphere-Based Time-Resolved Fluorescent Immunochromatographic Assay for the Rapid Screening of 4,4'-Dinitrocarbanilide: Aiming at Improving Strip Method Performance

Ming Zou ^{1,†}, Yongkang Yin ^{1,†}, Liuchuan Guo ¹, Qidi Zhang ¹, Jinyan Li ¹, Hong Zhang ¹, Qian Song ¹, Zhaojie Li ¹, Li Wang ², Xiang Ao ³ and Xiao Liang ^{1,3,*}

¹ College of Veterinary Medicine, Qingdao Agricultural University, No. 700 Changcheng Road, Qingdao 266109, China

² College of Food Science and Engineering, Qingdao Agricultural University, No. 700 Changcheng Road, Qingdao 266109, China

³ Basic Medical College, Qingdao University, No. 308 Ningxia Road, Qingdao 266071, China

* Correspondence: liangxiao4000@163.com; Tel.: +86-139-6486-7357

† These authors contributed equally to this work.

Abstract: Considering that the strip method is simple and convenient for users, a Europium nanosphere-based time-resolved fluorescent immunochromatographic assay (TRFICA) for the rapid screening of 4,4'-dinitrocarbanilide (DNC) was developed to improve the performance of strip assays. After optimization, TRFICA showed IC₅₀, the limit of detection, and cut-off values of 0.4, 0.07, and 5.0 ng mL⁻¹, respectively. No significant cross-reactivity (CR < 0.1%) with 15 DNC analogs was observed in the developed method. TRFICA was validated for DNC detection in spiked chicken homogenates, and recoveries ranged from 77.3% to 92.7%, with coefficients of variation of <14.9%. Moreover, the time needed for the detection procedure, including the sample pre-treatment, was less than 30 min for TRFICA, which had never been achieved before in other immunoassays. The newly developed strip test is a rapid, sensitive, quantitative, and cost-effective on-site screening technique for DNC analysis in chicken muscle.

Keywords: NIC; DNC; residue; TRFICA; chicken muscle

Citation: Zou, M.; Yin, Y.; Guo, L.; Zhang, Q.; Li, J.; Zhang, H.; Song, Q.; Li, Z.; Wang, L.; Ao, X.; et al. A Europium Nanosphere-Based Time-Resolved Fluorescent Immunochromatographic Assay for the Rapid Screening of 4,4'-Dinitrocarbanilide: Aiming at Improving Strip Method Performance. *Biosensors* **2023**, *13*, 518. <https://doi.org/10.3390/bios13050518>

Received: 5 February 2023

Revised: 17 April 2023

Accepted: 24 April 2023

Published: 4 May 2023



Copyright: © 2023 by the authors. Licensee MDPI, Basel, Switzerland. This article is an open access article distributed under the terms and conditions of the Creative Commons Attribution (CC BY) license (<https://creativecommons.org/licenses/by/4.0/>).

1. Introduction

Coccidiosis is a widespread and economically significant livestock disease caused by protozoan parasites of the genus *Eimeria* [1]. Minor infections cause poor feed conversion and weight gain, whereas major infections can cause significant mortality [2]. Therefore, in addition to the diagnosis and treatment of animal diseases, strict biological prevention and control from the source are also necessary. Feed contaminated with mycotoxins may cause the release of toxic substances in edible tissues such as meat, fish, and dairy products [3], seriously endangering human health and safety. Aflatoxin B1 (AFB1), the most toxic secondary metabolite produced by *Aspergillus flavus*, has become a major food safety issue worldwide due to its contamination of poultry feed [4]. In terms of biological prevention and control, the assessment of residual toxicity of multiple veterinary drugs in animal-derived foods based on endocrine disruptors using a high-throughput exposure (HTE) model [5] and a risk assessment of low-dose dietary-related exposures concludes that a tolerable daily intake (TDI) is unlikely to have genotoxic effects leading to carcinogenicity [6], to achieve the goal of ensuring human food safety and life health safety. Nicarbazin (NIC), an equimolecular mixture of 4,4-dinitrocarbanilide (DNC) and 2-hydroxy-4,6-dimethylpyrimidine, is a synthetic coccidiostat used globally to cure coccidiosis in animals, especially poultry. The widespread use of NIC causes its residues to

be present in foods of animal origin, such as broiler tissues. Its residues can seriously affect the health of poultry and humans, such as by causing adverse heat stress and death in broilers and chronic toxicity in humans. Therefore, DNC is considered the residue of concern in edible chicken tissues [7]. The maximum residue limits (MRLs) for DNC in food matrices were established to assure food safety in poultry production. The Joint FAO/WHO Expert Committee on Food Additives in New Zealand and China has recommended an MRL of 200 μg of DNC/kg in all broiler tissues, and the EU recommended an MRL of 4000 μg of DNC/kg. Therefore, it is imperative to develop low-cost, sensitive, and effective methods for the detection of DNC in animal-derived foods. Multiple technologies have been applied to detect residues of DNC in food matrices. Instrumental methods, such as high-performance liquid chromatography (HPLC) [8–10], high-performance liquid chromatography-tandem mass spectrometry (HPLC-MS/MS) [2,11–13], and ultraperformance liquid chromatography-tandem mass spectrometry (UPLC-MS/MS) [14] are accurate and specific, but their experiments are complex and not suitable for on-site screening. Immunoassay, such as enzyme-linked immunosorbent assay (ELISA) [15–17], has the advantages of high throughput screening but has significant limitations and is not suitable for on-site screening. Compared with the other methods, the immunochromatographic assay (ICA) is a more portable and faster assay [18]. Different types of fluorescent nanobeads, such as quantum dots [19], fluorescent microspheres [20], and up-conversion phosphors [21], among them, time-resolved fluorescent nanoparticles have excellent fluorescence properties. Lanthanide labels possess long decay lifetimes, can be dissociated by altering the solution pH, resulting in a shift to a new highly fluorescent chelate, and have a large Stokes shift, high quantum yields, sharp emission profiles, and narrow emission peaks. Although the quantum yields are lower with the use of organic fluorescence dyes, packing them into nanosphere capsules can increase fluorescence thousands of times [22,23]. Therefore, these attributes enable time-resolved fluorescence immunochromatography (TRFICA) labeled with fluorescent microspheres to have higher sensitivity, lower matrix interference, and better reproducibility and stability.

As shown in previous studies, TRFICA has been successfully applied to the quantitative detection of contaminants in food. Shen et al. developed a TRFICA for detecting chlorpromazine residues in pork, with a limit of detection (LOD) of 0.32 $\mu\text{g kg}^{-1}$ and a wide dynamic range of 0.46–10.0 $\mu\text{g kg}^{-1}$ [24]. Du et al. used two fluorescent labels to establish a dual-labeled TRFICA for analyzing diethyl phthalate and dibutyl phthalate in aquatic environments. The LODs of the assay were 4.9 ng mL^{-1} and 3.9 ng mL^{-1} , respectively [25]. A TRFICA that uses lanthanides as labels, such as Eu nanospheres (EuNPs), is one of the most promising immunoassay methods. Xu et al. developed a TRFICA for the rapid quantification of FB1 in different grains, with a LOD of 8.26 $\mu\text{g kg}^{-1}$ and a wide detection range of 13.81–1000 $\mu\text{g kg}^{-1}$ [26]. Ma et al. established a TRFICA method for determining the contaminant in milk samples, with a LOD and limit of the quantity of 3.05 ng mL^{-1} and 6.63 ng mL^{-1} , respectively [27]. Therefore, this technology is widely used in the detection of specific pollutants with the advantages of high cost-effectiveness, high selectivity, high sensitivity, simple operation, and a wide dynamic range.

In the current study, a TRFICA with high sensitivity and low cost for screening DNC was innovatively developed. The reaction conditions for Eu-NP-mAb probe conjugation, coating antigen, recombinant buffer, coating buffer, incubation time, sample dilution buffer, and immunochromatographic bands were optimized to improve the reaction performance. Under optimal experimental conditions, the standard curve of the DNC was developed. TRFICA had high specificity for DNC and neglected cross-reactivity in drugs with 15 similar structures. TRFICA could be used in chicken detection without complicated sample preparation, and the time needed for the detection procedure, including sample pre-treatment, was less than 30 min.

2. Materials and Methods

2.1. Reagents and Materials

NIC, 4-nitroaniline, 2-nitroaniline, 3-nitroaniline, N-(4-nitrophenyl) propionamide, H-Val-pNA HCl, L-arginine-p-nitroanilide dihydrochloride, 4-nitrophenethylamine hydrochloride, N-methyl-4-nitrophenethylamine hydrochloride, H-Ala-pNA HCl, N, N-dimethyl-4-nitroaniline, H-Glu-pNA, halofuginone, toltrazuril, 1,3-diphenylguanidine, ronidazole, and dinitolmide were obtained from Sigma-Aldrich (St. Louis, MO, USA) (Figure 1). The coating antigen (DNC-4-BSA) and mAb 3B4 were acquired from China Agricultural University (Qianqian Tang May 2018). For other reagents materials were shown in the Supplementary Materials part.

2.2. Apparatus

Water was purified using a Milli-Q system from Millipore Inc. (Bedford, MA, USA). A NanoDrop 2000 ultraviolet spectrophotometer was purchased from Thermo Scientific (Waltham, MA, USA). An ultraviolet analyzer was obtained from Tianjin Huike Instrument Equipment Co., Ltd. (Tianjin, China). A time-resolved immunochromatography (TRF) reader was supplied by Beijing EDWK BIOTECH (Beijing, China).

2.3. Preparation of Eu-NP-mAb Probes and Eu-NP-Chicken IgY Probes

The EuNPs were developed using a modified method, as previously described [22,23]. Carboxylate-activated EuNP surfaces were conjugated with mAb 3B4 or IgY using a typical N-Hydroxysuccinimide (NHS)/ethyl dimethylamine carbonide (EDC) conjugation method, which maintained 4 °C to ensure the retention of mAb activity [22]. The preparation process of EuNPs and mAb 3B4 conjugates is described as follows: In brief, 20 µL of EuNPs (200 nM) was added to 200 µL 50 mM MES (pH 5.0) containing EDC and sulfo-NHS at 0.1 mM and 0.2 mM. The reaction was reacted at room temperature for 15 min, and centrifuged $15,000\times g$ at high speed for 10 min at 4 °C to separate the supernatant. After being washed twice, an ultrasound was performed in 200 µL sodium borate for 2 min. The mAb 3B4 or IgY (5 µL) was then added, and the mixtures were shaken before centrifugation. The residue was suspended in 100 µL of 10 mM phosphate buffer and reacted for 2 h at 25 °C. After centrifugation, the residue was suspended in 2 mL 0.2 mM Tris-HCl containing 0.5% PVP (pH 7.4).

2.4. TRFICA Procedure

Initially, 200 µL of DNC standard solution or sample extract, Eu-NP-mAb probes, and Eu-NP-chicken IgY probes were injected into the micropore and mixed for 1 min. Afterward, the mixture was added to the sample pad well, and the liquid migrated slowly toward the absorption pad through capillary action. After 8 min of incubation, the fluorescence intensities of the T and C lines were observed by a TRF reader. In the presence of DNC, the absence of fewer Eu-NP-mAb probes was captured by the T line, weakening the fluorescence intensity on the T line, and the Eu-NP-chicken IgY probes were captured by the C line. The quantitative analysis of the DNC was conducted by recording the fluorescence intensities of the T and C lines. The T/C ratio was used to offset the background and inherent heterogeneity of the strip. This was expected to be inversely proportional to the increasing concentration of DNC in the samples. The standard curve was prepared at nine levels of DNC concentration (0, 0.07, 0.19, 0.56, 1.67, 1.37, 5, and 15 ng mL⁻¹), and each concentration was tested in triplicate. A four-parameter logistic equation was performed and calculated using Origin 8.0 (Origin Lab, Northampton, MA, USA).

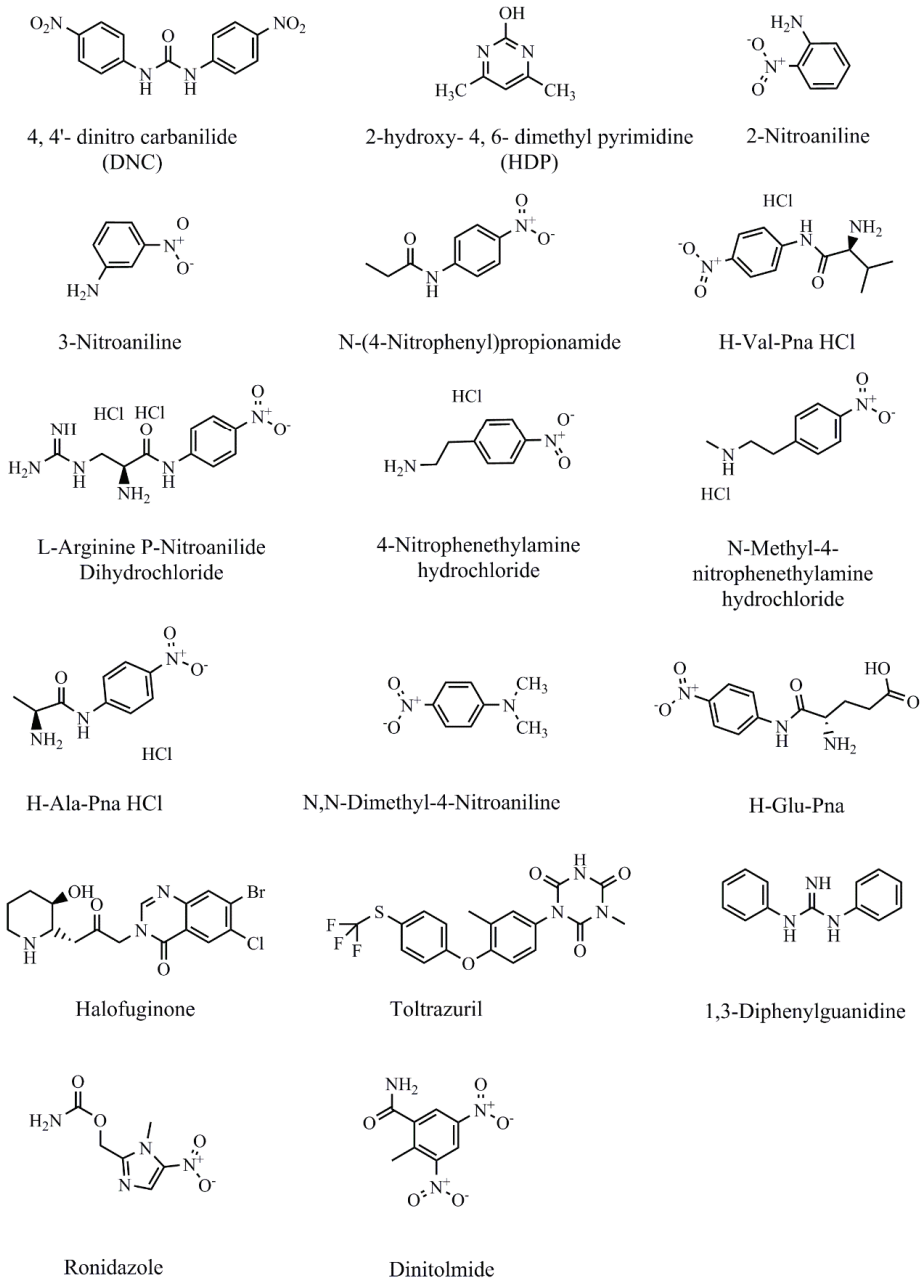


Figure 1. Chemical structures of NIC and other analytes.

2.5. TRFICA Development and Optimization

The immunochromatographic strips used for TRFICA testing were composed of a sample pad, a conjugate pad, an NC membrane coated with capture reagents, an absorbent pad, and a polyvinyl chloride sheet with adhesive tape (Figure 2). The controls included in the strip were DNC-4-BSA conjugate (test 'T' line) and goat-anti-chicken IgG (control 'C' line), and they were immobilized on the NC membrane and separated by a distance of 3 mm.

The coated membrane was dried at 37 °C overnight. The NC membrane, sample pad, and absorbent pad were successively laminated and pasted onto the PVC base plate. The entire assembly was cut into 3–4 mm-wide strips and stored desiccated at room temperature.

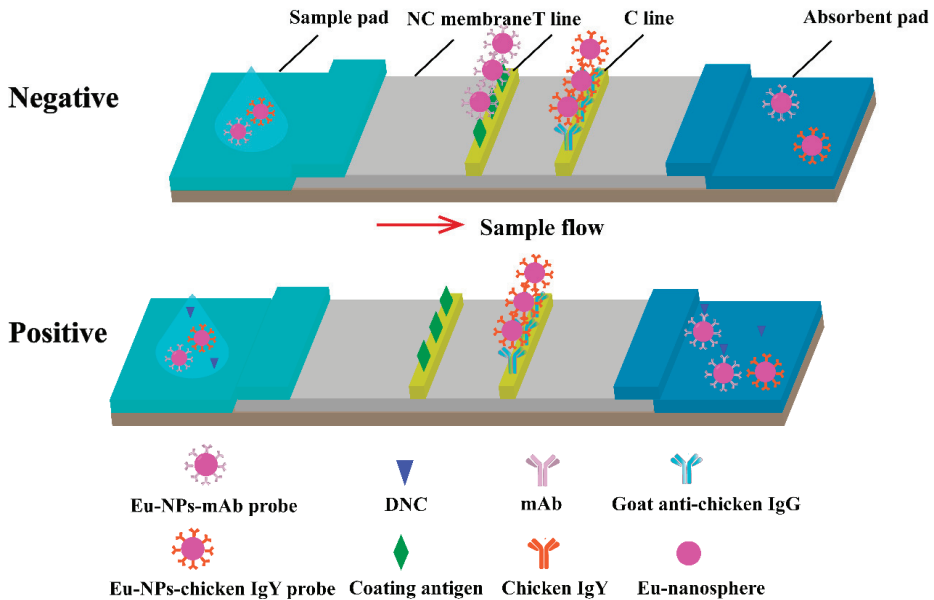


Figure 2. Schematic illustration of TRFICA. The schematic illustrates the working principles of TRFICA. T line is the test line, and the C line is the control line. After dripping the sample, the sample migrated along the NC membrane through capillary action. For a negative sample, the fluorescence intensity of the T line and the C line can be detected by the TRF reader. For a positive sample, only the T line had fluorescence intensity, and the C line had no fluorescence intensity. The surplus probe complexes migrated to the absorption pad.

The assay was optimized by optimizing single analytical parameters, while the others remained constant. The fluorescence intensity and inhibition rate $[(F_0 - F)/F_0] \times 100\%$ were used to assess the sensitivity of the immunoassays. F and F_0 were the fluorescence values of DNC at 5 ng mL^{-1} and without DNC, respectively. The tested parameters included the conjugation of Eu-NP-mAb probes, the concentrations of antibody and coating antigen, reconstitution buffers, probe amounts, coating buffers, incubation time, sample dilution buffer, and the immunochromatographic strip type. After optimizing and determining the optimum experimental parameters, a standard curve was obtained by plotting T/C against the DNC concentration. A four-parameter logistic equation was used to calculate the performance parameters.

2.6. Curve Fitting and Statistical Analysis

A logistic equation used to fit the TRFICA data are shown in the Supplement information part. The cross-reactivity (CR) with DNC analogs was determined after the optimized conditions, and the specificity of TRFICA was evaluated. The CR was calculated by the following equation [28]:

$$\text{CR (\%)} = (\text{IC}_{50} \text{ of DNC} / \text{IC}_{50} \text{ of DNC analog}) \times 100 \quad (1)$$

2.7. Chicken Sample Analysis for TRFICA

Samples of chicken muscle (2 g) were added to 2 mL acetonitrile in 10 mL polypropylene tubes and sonicated for 10 min. The mixture was centrifuged at $8000 \times g$ for 10 min, and

the supernatant was diluted 20-fold with an assay buffer for subsequent TRFICA analysis. Matrix interference was determined by comparing the DNC standard curve prepared in the assay buffer and the chicken extract after a 20-fold dilution with an assay buffer.

Additionally, the accuracy and precision of TRFICA were evaluated and conducted as indicated. DNC-negative chicken homogenate samples were spiked with DNC at 6, 16, and 30 $\mu\text{g kg}^{-1}$. Five replicates were determined at each concentration for both intra-assay and inter-assay determinations.

3. Results and Discussion

3.1. Development and Optimization of TRFICA

3.1.1. Optimization of the Conjugation of Eu-NP-mAb Probes

An appropriate ratio of the antibody and EuNPs was selected to improve the performance of TRFICA. Thus, the Eu-NP-mAb probes were initially prepared using different mass ratios of the antibody and EuNPs, and the use of the nanospheres at 2.5, 5, 10, and 20 μL was examined. As the EuNPs increased from 2.5 μL to 10 μL , the fluorescent intensity of the T line increased but decreased at 20 μL . Moreover, the chromatogram was incomplete, the fluorescent intensity of the background increased, and the T-line boundary was no longer obvious at 20 μL EuNPs. Although the strongest fluorescent intensity for the T line was obtained at 10 μL EuNPs, the inhibition rate was lower. The inhibition rate was better at 5 μL EuNPs, along with better fluorescent intensity on the T line (Figure 3A).

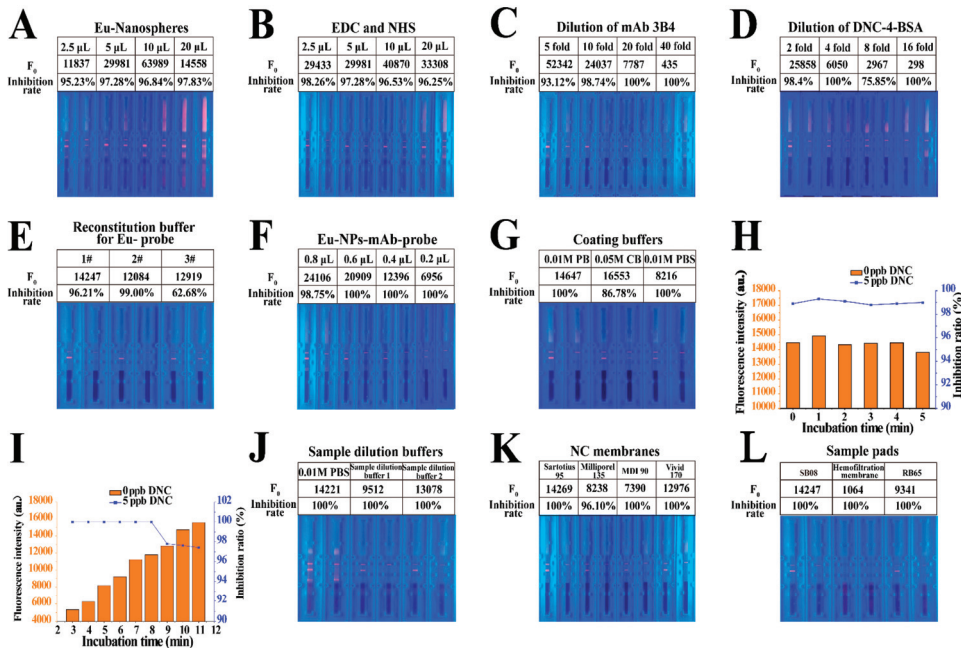


Figure 3. Optimization of TRFICA performance. (A) Use of EuNPs. (B) Use of EDC and NHS. (C) Dilution of mAb 3B4. (D) Dilution of DNC-4-BSA. (E) Reconstitution buffer for Eu-NP-mAb probes. (F) Use of Eu-NP-mAb probes. (G) Coating buffer. (H) Incubation time for the Eu probe and the DNC. (I) Incubation time for immunochromatography. (J) Sample dilution buffer. (K) NC membranes. (L) Sample pads.

Typical EDC conjugation methods were used for reagent development, as mild conditions maintained antibody activity. EDC and NHS can directly affect the coupling efficiency of antibodies and EuNPs by activating the carboxyl group on the microspheres, which then allows coupling with mAb amino groups.

We used EDC and NHS at 2.5, 5, 10, and 20 μL , and following optimization, 2.5 μL EDC and NHS were used to activate a 1-mL EuNP solution. This resulted in a better inhibition rate and acceptable fluorescent intensity on the T line (Figure 3B).

The Eu-NP-mAb probes were characterized by high-resolution transmission electron microscope studies. After coupling, the EuNP surface modified by the immobilized mAb was characterized by high-resolution transmission electron microscopy. The results validated the distribution of the elements on the surface of EuNPs attached to C, N, O, and other elements (Figure 4). The existence of the N element proved the successful coupling of EuNPs with mAb 3B4.

Mapping-HRTEM

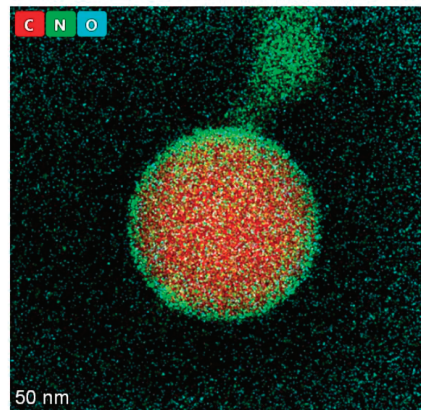


Figure 4. Elemental mapping images of the Eu-NP-mAb. The existence of the N element and the O element observed in the elemental mapping image confirms the successfully modified mAb on the EuNPs.

3.1.2. Optimization of the Concentrations of mAb and Coating Antigen

The specific binding of immunoreagents is the basis of TRFICA, as with other immunoassays. An appropriate antigen–antibody ratio can enhance the binding of specific sites and improve TRFICA performance [29]. Thus, the concentrations of mAb 3B4 and the coating antigen DNC-4-BSA were screened using checkerboard titration. According to the results, a 10-fold dilution of mAb 3B4 was selected due to the acceptable fluorescent intensity inhibition rate (Figure 3C). Moreover, a high dilution of DNC-4-BSA decreased the fluorescent intensity and increased the inhibition rate. Thus, a two-fold dilution of DNC-4-BSA was selected (Figure 3D).

3.1.3. Optimization of the Reconstitution Buffer for Eu-NP-mAb Probes

In this study, we also evaluated three reconstitution buffers for Eu-NP-mAb probes based on the inhibition ratios and F_0 values (Table S1). According to Figure 3E, the three F_0 values that were obtained differed little, and the highest inhibition ratio was observed with the reconstitution buffer 2[#]. Therefore, reconstitution buffer 2[#] was selected.

3.1.4. Optimization of Eu-NP-mAb Probe Usage

The effects of the quantity of Eu-NP-mAb probes present in the TRFICA system were also examined. As the number of Eu-NP-mAb probes decreased, the F_0 value of the T line also decreased, while the inhibition rate increased only gradually. The F_0 value was controlled at about 12,000; therefore, 0.4 μL of Eu probe was selected as the optimal amount to be used for the assay (Figure 3F).

3.1.5. Optimization of Coating Buffers

For the optimization of coating buffers, three typical coating buffers were tested in the system: 0.01 M phosphate buffer (PB) at pH 7.4, 0.05 M carbonate buffer (CB) at pH 9.6, and 0.01 M phosphate buffer solution (PBS) at pH 7.4. The F_0 values decreased dramatically in PBS, whereas both PB and CB resulted in significant increases in F_0 . In particular, the use of PB led to a higher inhibition ratio (Figure 3G). Thus, 0.01 M PB at pH 7.4 was selected as the best coating buffer.

3.1.6. Optimization of Incubation Times

Incubation time can significantly influence the performance of TRFICA. Initially, we examined the incubation times of 0, 1, 2, 3, 4, and 5 min for the DNC standard solution or sample extract, Eu-NP-mAb probes, and Eu-NP-chicken IgY probes. As these times had no significant effect on fluorescence intensity or inhibition ratio, 1 min was selected (Figure 3H). We then compared different incubation times (3, 4, 5, 6, 7, 8, 9, 10, and 11 min) for immunochromatography. We found that longer incubation times enhanced the binding efficiency of the assay (Figure 3I). However, when the incubation time exceeded 9 min, the sensitivity decreased dramatically. Therefore, 8 min was selected as the best incubation time for immunochromatography in this study.

3.1.7. Optimization of Sample Dilution Buffers

Using the appropriate sample dilution buffers for TRFICA resulted in better performance. In this section, three sample dilution buffers were examined: PBS and sample dilution buffers 1 and 2 (Table S2). The use of sample dilution buffer 1 resulted in a decrease in fluorescence intensity, while PBS generated a high background, most likely due to the release of the probes. Thus, sample dilution buffer 2 was selected as the optimal sample dilution buffer, with satisfactory fluorescence intensity and inhibition rate (Figure 3J).

3.1.8. Optimization of Immunochromatographic Strips

The use of the NC membrane affected the TRFICA sensitivity primarily through the membrane pore and the protein binding forces. Four NC membranes, Sartorius 95, Millipore 135, MDI 90, and Vivid 170, as well as their corresponding F_0 values and inhibition rates, were evaluated. After optimization, the Sartorius 95 membrane was selected as the optimum (Figure 3K). Immunochromatography was also affected by the speed and release effect of the sample pad. Three sample pads, namely SB08, hemofiltration membrane, and RB65 were assessed, and the strongest fluorescence intensity was obtained using sample pad SB08 (Figure 3L).

3.2. Sensitivity and Cross-Reactivity of TRFICA

The standard curve of TRFICA in the buffer was established under optimized conditions. To evaluate the sensitivity of the method, the sensitivity of TRFICA was evaluated using the IC_{50} , working range, and LOD. The LOD was examined and defined as the IC_{10} from the standard curve. According to curve fitting, the IC_{50} , linear working range, LOD, and cut-off value of the method were 0.43 ng mL^{-1} , $0.13\text{--}1.37 \text{ ng mL}^{-1}$, 0.07 ng mL^{-1} , and 5 ng mL^{-1} , respectively (Figure 5A,B). These values represent a significantly improved performance relative to previous reports in which the LOD of the colloidal gold-based immunochromatographic test method was 0.86 ng mL^{-1} . This indicates that TRFICA performed as an ultrasensitive detector of DNC.

The specificity of TRFICA was determined using cross-reactivity with 15 DNC analogs. As shown in Table 1, the CR was $<0.1\%$ and no inhibitions were observed even though the concentration of the standards was 1000 ng mL^{-1} . The results of the CRs were highly similar to those from the fluorescence polarization immunoassay (FPIA) using mAb 3B4 [30]. These results indicate that the developed TRFICA was specific to DNC detection.

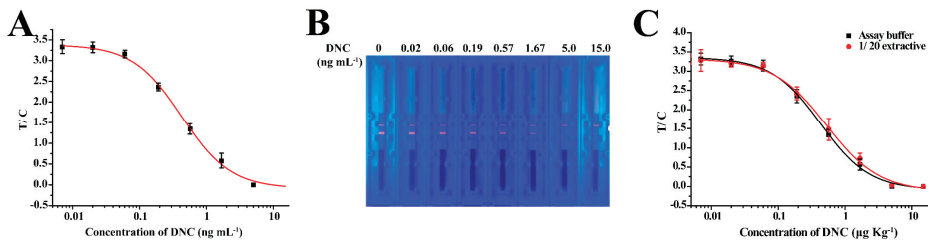


Figure 5. Standard curve of the TRFIA. (A) Standard curves of TRFICA for DNC in an assay buffer under optimized conditions. (B) Fluorescent image of the TRFICA strip acquired under ultraviolet light for 0, 0.02, 0.06, 0.19, 0.57, 1.67, 5.0, and 15 ng mL⁻¹ in an assay buffer (left to right). (C) Comparison of the TRFICA curves obtained from the standards prepared in the assay buffer and the 20-fold diluted chicken extracts.

Table 1. IC₅₀ values and cross-reactivity of DNC and 15 structurally related analogs for TRFICA.

Analogues	IC ₅₀ (ng mL ⁻¹)	CR (%)
DNC	0.43	100
2-Nitroaniline	>1000	<0.1
3-Nitroaniline	>1000	<0.1
N-(4-Nitrophenyl) propionamide	>1000	<0.1
H-Val-pNA HCl	>1000	<0.1
L-Arginine P-Nitroanilide Dihydrochloride	>1000	<0.1
4-Nitrophenethylamine hydrochloride	>1000	<0.01
N-Methyl-4-nitrophenethylamine hydrochloride	>1000	<0.1
H-Ala-pNA HCl	>1000	<0.1
N, N-Dimethyl-4-Nitroaniline	>1000	<0.1
H-Glu-pNA	>1000	<0.1
Halofuginone	>1000	<0.1
Toltrazuril	>1000	<0.1
1,3-Diphenylguanidine	>1000	<0.1
Ronidazole	>1000	<0.1
Dinitolmide	>1000	<0.1

3.3. Chicken Sample Analysis for TRFICA

The chicken muscle was examined for the applicability of the developed TRFICA. In TRFICA, the complexity of the chicken muscle was directly related to the sensitivity and accuracy of the immunoassay. In this study, organic solvents were chosen as the extraction solvent for DNC from muscle tissues. We initially examined seven extraction solvents (Table S3). However, with the exception of acetonitrile, all the extraction solvents resulted in significant decreases in F₀ values. Therefore, acetonitrile was selected as the extraction buffer for further investigation. The standard curves of DNC in chicken muscle extracts using acetonitrile after 20-fold dilutions and when included in the assay buffer sufficiently reduced the matrix effects (Figure 5C). Under optimized conditions, this allowed the detection of DNC with a LOD and working range of 1.4 and 2.96–37.06 µg kg⁻¹, respectively. The total analysis time, including the sample pre-treatment, was less than 30 min, which has not been achieved in other immunoassays, such as ELISA [15–17], FPIA [30], and the colloidal gold-based immunochromatographic test method [18]. Thus, due to its efficiency and easy operation, TRFICA was better suited for the analysis of DNC.

To further evaluate the utility of TRFICA, we determined the DNC recoveries from the chicken matrix. All samples were fortified with DNC at three levels (6, 16, and 30 µg kg⁻¹), and the average recoveries ranged from 77.3% to 92.7%, with a coefficient of variation (CV) < 7.0% (Table 2). This perfectly met the requirements for DNC residue detection.

Therefore, the developed method is suitable for the determination of DNC residues in chicken muscle.

Table 2. Recovery studies from chicken muscle matrices using TRFICA.

Sample	Spiked ($\mu\text{g kg}^{-1}$)	Intra-Assay ($n = 5$)		Inter-Assay ($n = 5$)	
		Recovery (%)	CV (%)	Recovery (%)	CV (%)
Chicken	6.0	77.3	2.5	80.3	4.0
	16.0	81.9	2.4	88.9	3.8
	30.0	87.6	7.0	92.7	5.4

4. Conclusions

In summary, a TRFICA was developed for the simple, sensitive, and quantitative detection of DNC in chicken samples. The optimization of the nanosphere–probe conjugation, concentrations of antibody and coating antigen, reconstitution buffers, probe amounts, coating buffers, incubation times, sample dilution buffers, and immunochromatographic strip types was clearly demonstrated in this study. The performance of TRFICA was significantly improved under optimum conditions. Notably, the reliability and robustness of the assay were successfully demonstrated for the analysis of DNC in chicken muscle matrices without complicated pre-treatment processes. Furthermore, the total analysis time, including sample pre-treatment, was less than 30 min, which had not yet been achieved in other immunoassays for DNC residues.

Supplementary Materials: The following supporting information can be downloaded at: <https://www.mdpi.com/article/10.3390/bios13050518/s1>, Table S1: Three reconstitution buffers for the Eu3+-labeled antibody; Table S2: Sample dilution buffers used in TRFICA; Table S3: Seven extraction solvents used in TRFICA.

Author Contributions: Conceptualization, X.L. and M.Z.; methodology, J.L.; software, Y.Y.; formal analysis, J.L.; investigation, L.W.; data curation, J.L. and X.L.; writing—original draft preparation, Q.S. and X.L.; writing—review and editing, L.G., H.Z., Z.L., X.A. and Q.Z.; supervision, X.A. and M.Z.; project administration, Q.Z. All authors have read and agreed to the published version of the manuscript.

Funding: This study is supported by the Natural Science Foundation of Shandong Province (ZR2020MC187), the Postdoctoral Innovation Project of Shandong Province (202002027), the Postdoctoral Fund of Qingdao, the High-Level Talent Fund of Qingdao Agricultural University (663/1115026), the Scientific and Technological Projects of Qingdao (21-1-4-ny-10-nsh), College Students' Innovative Entrepreneurial Training Plan Program (202210435028) and the Natural Science Foundation of Shandong Province (ZR2020MC188). We gratefully acknowledge their assistance.

Institutional Review Board Statement: Not applicable.

Informed Consent Statement: Not applicable.

Data Availability Statement: Not applicable.

Conflicts of Interest: The authors declare no conflict of interest.

References

- Chapman, H.D.; Barta, J.R.; Blake, D.; Gruber, A.; Jenkins, M.; Smith, N.C.; Suo, X.; Tomley, F.M. A selective review of advances in coccidiosis research. *Adv. Parasitol.* **2013**, *83*, 93–171. [[PubMed](#)]
- Delahaut, P.; Pierret, G.; Ralet, N.; Dubois, M.; Gillard, N. Multi-residue method for detecting coccidiostats at carry-over level in feed by HPLC-MS/MS. *Food Addit. Contam.* **2010**, *27*, 801–809. [[CrossRef](#)] [[PubMed](#)]
- Tolosa, J.; Rodríguez-Carrasco, Y.; Ruiz, M.J.; Vila-Donat, P. Multi-mycotoxin occurrence in feed, metabolism and carry-over to animal-derived food products: A review. *Food Chem. Toxicol.* **2021**, *158*, 112661. [[CrossRef](#)] [[PubMed](#)]

4. Qiao, B.; He, Y.; Gao, X.; Liu, H.; Rao, G.; Su, Q.; Ruan, Z.; Tang, Z.; Hu, L. Curcumin attenuates AFB1-induced duck liver injury by inhibiting oxidative stress and lysosomal damage. *Food Chem. Toxicol.* **2023**, *172*, 113593. [[CrossRef](#)]
5. Luo, Y.S.; Chiu, Z.Y.; Wu, K.Y.; Hsu, C.-C. Integrating high-throughput exposure assessment and in vitro screening data to prioritize endocrine-active potential and dietary risks of pesticides and veterinary drug residues in animal products. *Food Chem. Toxicol.* **2023**, *173*, 113639. [[CrossRef](#)]
6. Guth, S.; Baum, M.; Cartus, A.T.; Diel, P.; Engel, K.-H.; Engeli, B.; Epe, B.; Grune, T.; Haller, D.; Heinz, V.; et al. Evaluation of the genotoxic potential of acrylamide: Arguments for the derivation of a tolerable daily intake (TDI value). *Food Chem. Toxicol.* **2023**, *173*, 113632. [[CrossRef](#)]
7. Capurro, E.; Danaher, M.; Anastasio, A.; Cortesi, M.L.; O'Keeffe, M. Efficient HPLC method for the determination of nicarbazin, as dinitrocarbanilide in broiler liver. *J. Chromatogr. B* **2005**, *822*, 154–159. [[CrossRef](#)]
8. Marta, P.; Piotr, J.; Jan, Z. Comparison of different sample preparation procedures for multiclass determination of selected veterinary drug, coccidiostat and insecticide residues in eggs by liquid chromatography-tandem mass spectrometry. *Anal. Methods* **2014**, *6*, 3034–3044.
9. Edyta, P.; Malgorzata, O.; Teresa, S.J.; Jedziniak, P.; Zmudzki, J. Determination of Nicarbazin in Animal Feed by High-Performance Liquid Chromatography with Interlaboratory Evaluation. *Anal. Lett.* **2015**, *48*, 2183–2194.
10. Juan, M.S.; Federico, J.A.; Gaston, K.; Sosa, J.S.; Carrizo, D.B.; Boschetti, C.E. Multiple response optimization of a QuEChERS extraction and HPLC analysis of diclazuril, nicarbazin and lasalocid in chicken liver. *Food Chem.* **2020**, *311*, 126014.
11. Barreto, F.; Ribeiro, C.; Hoff, R.B.; Costa, T.D. A simple and high-throughput method for determination and confirmation of 14 coccidiostats in poultry muscle and eggs using liquid chromatography—Quadrupole linear ion trap—Tandem mass spectrometry (HPLC-QqLIT-MS/MS): Validation according to European Union 2002/657/EC. *Talanta* **2017**, *168*, 43–51. [[PubMed](#)]
12. Dmitrovic, J.; Durden, D.A. A new approach to the analysis of nicarbazin and ionophores in eggs by HPLC/MS/MS. *J. AOAC Int.* **2011**, *94*, 428–435. [[CrossRef](#)] [[PubMed](#)]
13. Matus, J.L.; Boison, J.O. A multi-residue method for 17 anticoccidial drugs and ractopamine in animal tissues by liquid chromatography-tandem mass spectrometry and time-of-flight mass spectrometry. *Drug Test Anal.* **2016**, *8*, 465–476. [[CrossRef](#)] [[PubMed](#)]
14. Muharem, M.; Yan, H.; Xu, S.; Feng, N.; Hao, J.; Zhu, C.; Guo, S.; Zhang, Z.; Han, N. Determination of six anticoccidials in chicken using QuEChERS combined with ultra high liquid chromatography-high resolution mass spectrometry. *Se Pu= Chin. J. Chromatogr.* **2015**, *33*, 1199–1204. [[CrossRef](#)]
15. Connolly, L.; Fodey, T.L.; Crooks, S.R.; Delahaut, P.; Elliott, C.T. The production and characterisation of dinitrocarbanilide antibodies raised using antigen mimics. *J. Immunol. Methods* **2002**, *264*, 45–51. [[CrossRef](#)]
16. Huet, A.C.; Bienenmann-Ploum, M.; Vincent, U.; Delahaut, P. Screening methods and recent developments in the detection of anticoccidials. *Anal. Bioanal. Chem.* **2013**, *405*, 7733–7751. [[CrossRef](#)]
17. Huet, A.C.; Mortier, L.; Daeseleire, E.; Fodey, T.; Elliott, C.; Delahaut, P. Screening for the coccidiostats halofuginone and nicarbazin in egg and chicken muscle: Development of an ELISA. *Food Addit. Contam.* **2005**, *22*, 128–134. [[CrossRef](#)]
18. Wu, A.; Wu, X.; Zheng, Q.; Xu, L.; Kuang, H. Preparation of an anti-4,4'-dinitrocarbanilide monoclonal antibody and its application in an immunochromatographic assay for anticoccidial drugs. *Food Agric. Immunol.* **2018**, *29*, 1162–1172. [[CrossRef](#)]
19. Yao, J.; Xing, G.; Han, J.; Sun, Y.; Wang, F.; Deng, R.; Hu, X.; Zhang, G. Novel fluoroimmunoassays for detecting ochratoxin A using CdTe quantum dots. *J. Biophotonics* **2017**, *10*, 657–663. [[CrossRef](#)]
20. Zhang, X.; Wen, K.; Wang, Z.; Jiang, H.; Beier, R.C.; Shen, J. An ultra-sensitive monoclonal antibody-based fluorescent microsphere immunochromatographic test strip assay for detecting aflatoxin M 1 in milk. *Food Control* **2016**, *60*, 588–595. [[CrossRef](#)]
21. Wang, P.; Wang, R.; Zhang, W.; Su, X.; Luo, H. Novel fabrication of immunochromatographic assay based on up conversion phosphors for sensitive detection of clenbuterol. *Biosens. Bioelectron.* **2016**, *77*, 866–870. [[CrossRef](#)] [[PubMed](#)]
22. Wang, D.; Zhang, Z.; Li, P.; Zhang, Q.; Ding, X.; Zhang, W. Europium Nanospheres-Based Time-Resolved Fluorescence for Rapid and Ultrasensitive Determination of Total Aflatoxin in Feed. *J. Agric. Food Chem.* **2015**, *63*, 10313–10318. [[CrossRef](#)] [[PubMed](#)]
23. Wang, D.; Zhang, Z.; Li, P.; Zhang, Q.; Zhang, W. Time-Resolved Fluorescent Immunochromatography of Aflatoxin B1 in Soybean Sauce: A Rapid and Sensitive Quantitative Analysis. *Sensors* **2016**, *16*, 1094. [[CrossRef](#)]
24. Wang, W.; Wang, J.; Wang, M.; Shen, J. Rapid Quantification of Chlorpromazine Residues in Pork Using Nanosphere-Based Time-Resolved Fluorescence Immunoassay Analyzer. *Int. J. Anal. Chem.* **2021**, *2021*, 6633016. [[CrossRef](#)] [[PubMed](#)]
25. Zhu, F.; Zhang, H.; Qiu, M.; Wu, N.; Zeng, K.; Du, D. Dual-label time-resolved fluoroimmunoassay as an advantageous approach for investigation of diethyl phthalate and dibutyl phthalate in surface water. *Sci. Total Environ.* **2019**, *695*, 133793. [[PubMed](#)]
26. Guo, L.; Wang, Z.; Xu, X.; Xu, L.; Kuang, H.; Xiao, J.; Xu, C. Europium nanosphere-based fluorescence strip sensor for ultrasensitive and quantitative determination of fumonisin B1. *Anal. Methods Adv. Methods Appl.* **2020**, *12*, 5229–5235. [[CrossRef](#)]
27. Ma, L.; Wang, Z.; Liu, H.; Wu, C.; Ding, Y. Monoclonal antibody production and the development of a quantitative time-resolved fluoroimmunoassay for rifaximin in milk. *Food Agric. Immunol.* **2019**, *30*, 1135–1141. [[CrossRef](#)]
28. Liang, X.; Ni, H.; Beier, R.C.; Dong, Y.; Li, J.; Luo, X.; Zhang, S.; Shen, J.; Wang, Z. Highly Broad-Specific and Sensitive Enzyme-Linked Immunosorbent Assay for Screening Sulfonamides: Assay Optimization and Application to Milk Samples. *Food Anal. Methods* **2014**, *7*, 1992–2002. [[CrossRef](#)]

29. Fang, S.; Zhang, Y.; Liu, X.; Qiu, J.; Liu, Z.; Kong, F. Development of a highly sensitive time-resolved fluoroimmunoassay for the determination of trace salbutamol in environmental samples. *Sci. Total Environ.* **2019**, *679*, 359–364. [[CrossRef](#)]
30. Zhang, Q.; Zou, M.; Wang, W.; Li, J.; Liang, X. Design, Synthesis, and Characterization of Tracers and Development of a Fluorescence Polarization Immunoassay for Rapid Screening of 4,4'-Dinitrocarbanilide in Chicken Muscle. *Foods* **2021**, *10*, 1822. [[CrossRef](#)]

Disclaimer/Publisher's Note: The statements, opinions and data contained in all publications are solely those of the individual author(s) and contributor(s) and not of MDPI and/or the editor(s). MDPI and/or the editor(s) disclaim responsibility for any injury to people or property resulting from any ideas, methods, instructions or products referred to in the content.



Review

Review of Electrochemical Biosensors for Food Safety Detection

Ke Wang ¹, Xiaogang Lin ^{1,*}, Maoxiao Zhang ¹, Yu Li ¹, Chunfeng Luo ¹ and Jayne Wu ^{2,*}

¹ Key Laboratory of Optoelectronic Technology and Systems of Ministry of Education of China, Chongqing University, Chongqing 400044, China

² Department of Electrical Engineering and Computer Science, The University of Tennessee, Knoxville, TN 37996, USA

* Correspondence: xglin@cqu.edu.cn (X.L.); jaynewu@utk.edu (J.W.)

Abstract: Food safety issues are directly related to people's quality of life, so there is a need to develop efficient and reliable food contaminants' detection devices to ensure the safety and quality of food. Electrochemical biosensors have the significant advantages of miniaturization, low cost, high sensitivity, high selectivity, rapid detection, and low detection limits using small amounts of samples, which are expected to enable on-site analysis of food products. In this paper, the latest electrochemical biosensors for the detection of biological contaminants, chemical contaminants, and genetically modified crops are reviewed based on the analytes of interest, electrode materials and modification methods, electrochemical methods, and detection limits. This review shows that electrochemical biosensors are poised to provide miniaturized, specific, selective, fast detection, and high-sensitivity sensor platforms for food safety.

Keywords: electrochemistry; biosensor; food safety; high sensitivity; high selectivity

1. Introduction

Safe food is a fundamental need for human health. Food safety can be affected by harmful substances such as allergens, pathogens (e.g., parasites, bacteria, viruses, prions, etc.), toxic agents or radioactive substances [1]. To safeguard human health, regulatory agencies such as the United States Food and Drug Administration (USFDA), the European Food Safety Authority (EFSA), and the Chinese Food and Drug Administration (CFDA) have imposed limits on the maximum levels of various contaminants in food. Nevertheless, in 2015, the World Health Organization (WHO) estimated that more than 600 million cases of foodborne diseases and 420,000 deaths are likely to occur each year, due to foodborne diseases caused by 31 foodborne pathogens at the global and subregional levels [2]. In agriculture, pesticides control pests and diseases in crops and ensure crop yield and quality. However, the overuse of pesticides can leave residues on crops that threaten human health through the food chain [3]. In addition, many food additive safety incidents had occurred around the world, such as aquatic products containing malachite green, red-hearted duck eggs dyed with Sudan red, melamine milk powder, industrial gelatin yogurt, etc., causing distrust and fear among people [4]. In order to screen and monitor the safety of food and prevent harm from food contaminants, a sensitive and reliable on-site analysis technology for food contaminants is highly desired.

At present, there are many mature technologies for food safety detection, such as gas chromatography (GC), high-performance liquid chromatography (HPLC), gas chromatography-mass spectrometry (GC-MS), liquid chromatography-mass spectrometry (LCMS), and enzyme-linked immunosorbent assay (ELISA) [5]. However, most of these methods have disadvantages, such as complicated operation, high detection costs, long detection time, and high requirements for the samples tested, which are prone to false positives. To improve this situation, simple, rapid, economical, and portable electrochemical biosensors have attracted much attention. They could not only achieve high specificity

Citation: Wang, K.; Lin, X.; Zhang, M.; Li, Y.; Luo, C.; Wu, J. Review of Electrochemical Biosensors for Food Safety Detection. *Biosensors* **2022**, *12*, 959. <https://doi.org/10.3390/bios12110959>

Received: 30 September 2022

Accepted: 31 October 2022

Published: 2 November 2022



Copyright: © 2022 by the authors. Licensee MDPI, Basel, Switzerland. This article is an open access article distributed under the terms and conditions of the Creative Commons Attribution (CC BY) license (<https://creativecommons.org/licenses/by/4.0/>).

and sensitivity, but also enable real-time monitoring in the field. The basic components and principles of an electrochemical biosensor for food contaminants detection are shown in Figure 1. It can convert the biological signal generated by the specific combination of the target analytes and the sensitive elements into an electrical signal, which is detected by the electrochemical methods. Finally, signal processing is performed by a computer to achieve quantitative or qualitative detection of food contaminants.

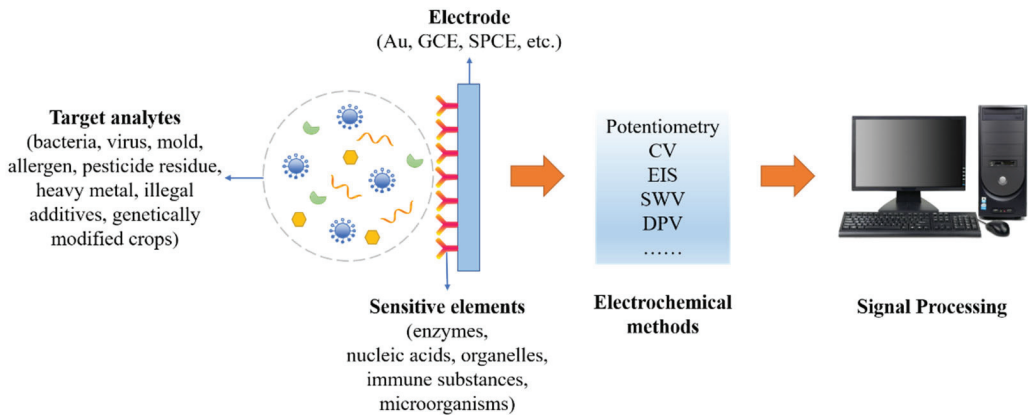


Figure 1. Schematic diagram of an electrochemical biosensor for food contaminants detection.

Common electrochemical methods include potentiometry, cyclic voltammetry (CV), electrochemical impedance spectroscopy (EIS), square wave voltammetry (SWV), and differential pulse voltammetry (DPV). Potentiometry is one of the simplest electrochemical techniques, characterized by a short response time, high selectivity, and extremely low detection limit [6]. Cyclic voltammetry is performed with the applied electrical potential oscillating over a range, while electrochemical impedance spectroscopy is usually performed at a fixed potential over a frequency range [7]. Square wave voltammetry is one of the most advanced and versatile members of the pulse voltammetry technology family, which has high analytical sensitivity and measurement speed [8]. Differential pulse voltammetry is more sensitive than conventional pulse, derivative conventional pulse, and cyclic voltammetry, and is suitable for studying the electrochemical process at the interface of metal-electrolyte solution [9]. Although electrochemical biosensors have not been widely used in food safety detection, their significant advantages deserve further investigation.

This review presents various electrochemical biosensors for the detection of biological food contaminants, chemical food contaminants, and genetically modified crops based on the types of analytes of interest. Figure 2 shows the factors that affect food safety. A search was conducted in the Web of Science database using the keywords “electrochemistry”, “food” and the influencing factors in Figure 2, and a total of 96 articles from 2018–2022 were retrieved, from which 31 articles were selected based on the relevance and creativity of the article content. The electrode materials, modification methods, electrochemical methods, linear range, detection limits and detection times of these electrochemical biosensors are discussed in detail. The advantages and disadvantages of these electrochemical biosensors are evaluated based on their selectivity, reproducibility, and sensitivity. The organization is as follows: Sections 2–4 analyze the research progress of electrochemical biosensors for the detection of biological food contaminants, chemical food contaminants, and genetically modified crops, respectively. Section 5 discusses the methods to improve the performance of electrochemical biosensors in food safety testing and summarizes the development prospects and future challenges of electrochemical biosensors in the field of food safety testing. This review features a discussion of electrochemical biosensors related to genetic

engineering, microfluidics, and molecular imprinting analysis, which can be instructive for the innovation of such sensors.

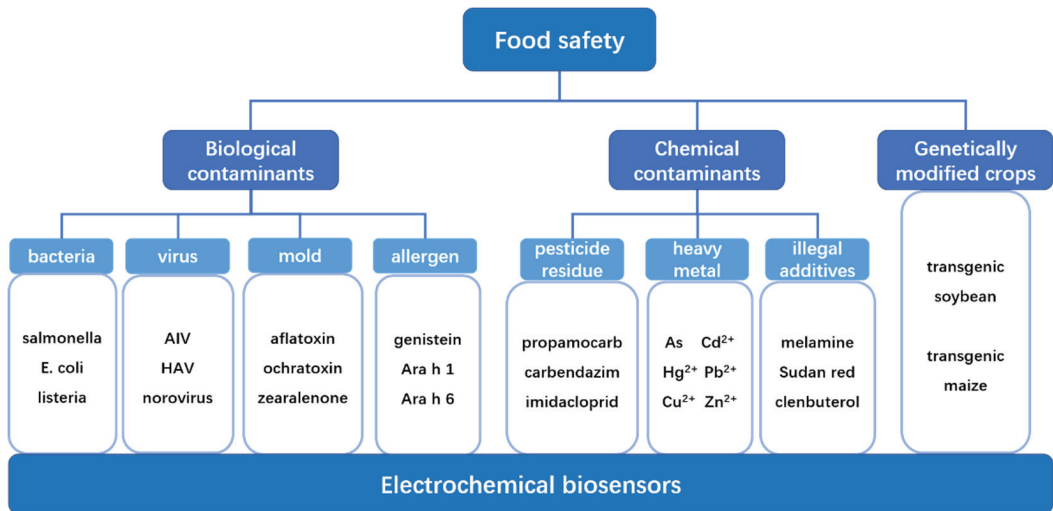


Figure 2. Diagram of the factors affecting food safety.

2. Biological Contamination

Biological contaminants include allergens, mycotoxins, pests, and microorganisms [10]. In the process from raw material production to final consumption, food may become contaminated with biological or chemical agents through contact with polluted water, air, soil, and food processing environment [11]. In the following, different electrochemical sensing strategies for the detection of bacteria, viruses and molds are discussed based on recent literature reports.

2.1. Bacteria

Bacteria are microorganisms that usually exist in the environment and food matrices, including meat, poultry, fish, eggs, unpasteurized milk, and dairy products [12]. Salmonella, Escherichia coli, and Listeria are among the most monitored bacteria for food safety, which cause foodborne illness in the gastrointestinal tract after consumption. Electrochemical biosensors for the detection of Salmonella, Escherichia coli and Listeria are discussed below (Table 1).

Salmonella is one of the leading causative pathogens responsible for foodborne disease outbreaks. Traditional methods for detecting Salmonella in food are based on culture, including pre-enrichment, selective enrichment, and selective differential plating, and require at least 24 h of pre-concentration to increase the number of target bacteria and reach the detection limit of the assay [13]. Biosensing methods with fast response, high sensitivity, and easy use are of great interest for field applications.

In 2021, Li et al. [14] developed for the first time a novel cloth-based super-sandwich electrochemical aptasensor (CSEA) for the direct detection of Salmonella typhimurium pathogens. Figure 3 is a schematic of CSEA for the direct detection of Salmonella typhimurium. Cloth electrodes and hydrophilic/hydrophobic areas were made using carbon ink and wax-based screen printing as sensing devices. Two specific single-stranded DNA sequences produced a cascading hybridization reaction to form a DNA super sandwich (DSS). Methylene blue (MB) was inserted in its groove to amplify the current signal and thus improve detection sensitivity. The aptamers became bound to Salmonella typhimurium to form a target adaptor complex that could be combined with both the capture probe and DSS to detect Salmonella typhimurium by DPV. In addition, the addition of the aptamer

tail sequence made the proposed CSEA universal. In the range of 10^2 to 10^8 CFU/mL, the electrochemical signal increased linearly with the logarithmic concentration of *Salmonella typhimurium* with a detection limit of 16 CFU/mL. In addition, to prove that the aptamer sensor is suitable for the detection of actual samples, milk samples were spiked with 100, 500, and 1000 CFU/mL of *Salmonella typhimurium*, and the resulting samples were 1:10 diluted with deionized water before testing. CSEA can effectively determine the level of *Salmonella typhimurium* in milk samples. The prepared CSEA had successfully achieved label-free, nucleic acid-free amplification and cost-effective detection of *Salmonella typhimurium*. The cloth base used for this sensor is malleable as a flexible substrate, is not easily damaged, and is less costly to mass produce.

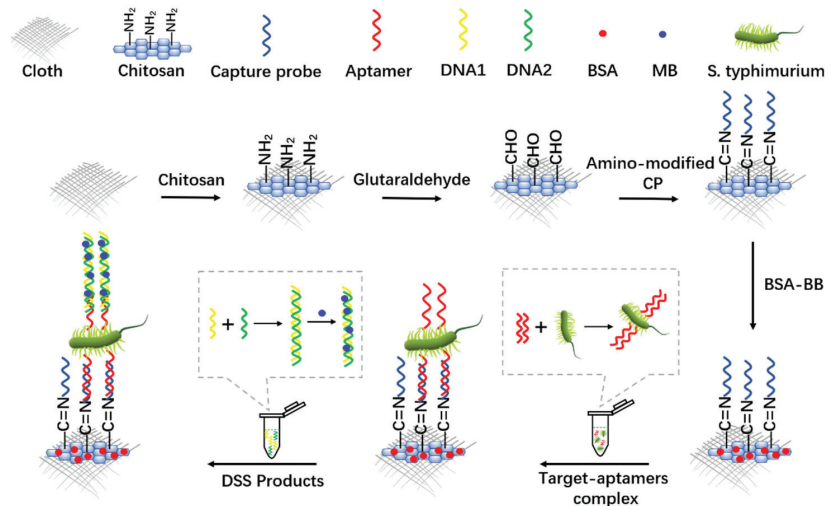


Figure 3. CSEA schematic for direct detection of *Salmonella typhimurium* (Adapted with permission from Ref. [14]. 2021, Li et al.).

In 2022, Yu et al. [15] constructed a proportional electrochemical biosensor based on saltatory rolling circle amplification (SRCA) and dual-signal electrochemical readings. The mercapto-modified β -cyclodextrin (SH- β -CD) was fixed to the surface of the glassy carbon electrode (GCE) by binding to gold nanoparticles (AuNPs) to form Au-S bonds, forming SH- β -CD/AuNPs/GCE. AuNPs not only have good electrical conductivity, but also increase the specific surface area. After the SRCA reaction with primers, a large number of amplification products containing ferrocene (Fc) were obtained within 1 h of double-stranded DNA (dsDNA), which can bind to SH- β -CD through the interaction between the subject and the object. In addition, MB was embedded in the phosphate backbone of dsDNA due to the electrostatic attraction between MB and DNA. SWV was used for electrochemical monitoring; the peak current of the blank group Fc was higher than MB, and the peak current of MB was significantly greater than Fc when *Salmonella typhi* is present. This ratio metric electrochemical biosensor had a linear detection range of 30 fg/ μ L to 30 ng/ μ L with a detection limit of 15.8 fg/ μ L. By testing food samples, the proportional electrochemical biosensor agrees with RT-qPCR results and the test time is shorter. Therefore, this sensor can be used as an alternative to RT-qPCR.

Foodborne diseases caused by *Escherichia coli* (*E. coli*) are causing morbidity and mortality worldwide, threatening human health [16]. Contamination by this pathogen plays an important role in the food industry, environment, and health sectors, making *E. coli* detection crucial. However, current analysis procedures require at least 18 h from sample collection to results [17]. Therefore, it is necessary to develop an accurate, sensitive, rapid, and cost-effective method for *E. coli* detection.

Raj et al. [18] used Au@MoS₂-polyaniline (PANI) nanocomposites to develop a simple, label-free, and highly sensitive immunosensor based on electrochemical detection for the detection of *E. coli*. PANI and AuNPs can increase the conductivity and surface area of MoS₂ and improve the conductivity of GCE. The sensing strategy of the immune sensor is shown in Figure 4. Self-assembled thiol propionate monolayers were introduced on the surface of the AuNP to covalently immobilize antibodies and prevent nonspecific adsorption of the target pathogen on the electrode surface. CV and DPV were used to confirm the successful preparation of the biosensor on the surface of GCE, and EIS was used to characterize the electrochemical performance of the modified electrodes. CV and DPV experiments were performed in 5 mM [Fe(CN)₆]^{3-/4-} containing 0.1M KCl solution. The peak value of DPV current in [Fe(CN)₆]^{3-/4-} decreased with increasing *E. coli* concentration on the electrode surface due to the formation of antibody-antigen complexes between *E. coli* and the antibodies of the biosensor, resulting in a spatial barrier to electrical current from the solution to the electrode surface. The biosensor achieved simple and sensitive detection of *E. coli* as low as 10 CFU/mL within 30 min, with a linear detection range of 10–10⁷ CFU/mL. The sensor is capable of detecting *E. coli* in urine samples and the electrodes may be regenerated. However, it has high sample requirements and cannot accurately detect *E. coli* in clinical samples with a complex composition such as serum, sputum, and whole blood.

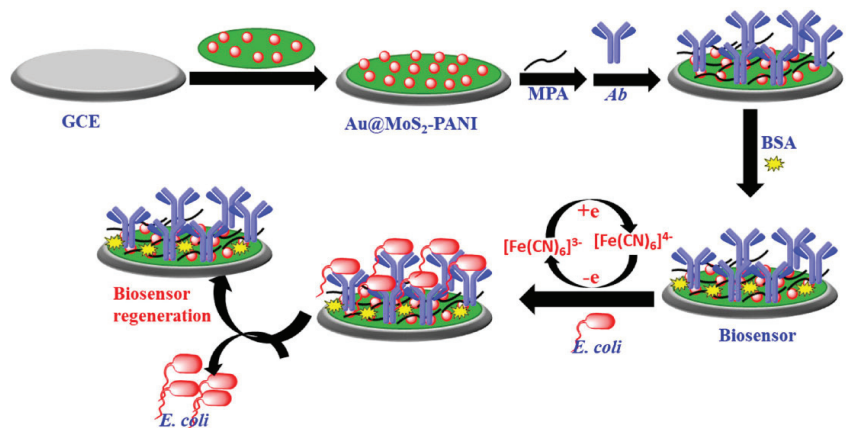


Figure 4. Schematic diagram of electrochemical biosensor for *E. coli* (Reprinted with permission from Ref. [18]. 2021, Raj et al.).

El-Moghazy et al. [19] developed a genetically engineered phage T7-based electrochemical biosensor for the rapid detection of *E. coli* in fresh produce. The sensing platform inserted the gene encoding alkaline phosphatase (ALP) into the T7 phage genome to form a genetically engineered phage, which was used as a biorecognition element, and targeted cleavage of the target bacteria by the phage can trigger overexpression of ALP. As shown in Figure 5, 1 g of spinach leaves purchased from a local supermarket were weighed, placed in a sterile Petri dish, and then inoculated with different concentrations of *E. coli*. The overexpression of ALP was tracked electrochemically using a single-walled carbon nanotube-modified screen-printed electrode (SWCNT-SPE), and electrochemical measurements were performed by DPV. The current signal increased with increasing *E. coli* concentration, and the peak current was linear in the range of 1–10⁴ CFU/mL versus the logarithm of the bacterial concentration. The detection limit was 1 CFU/mL. The electrochemical sensor was capable of rapid and accurate quantitative detection of pathogenic *E. coli* on spinach leaves within 1 h after pre-enrichment. In addition, this biosensor exhibited high specificity for *E. coli* in the presence of other common food bacterial contaminants and reduced analysis time through the coupling between specially designed phage and

electrochemical methods. Compared to the study by Raj et al. [18], the method reduces complexity, does not require expensive materials, and has a lower detection limit, which can be extended to highly sensitive and selective detection of different bacterial contaminants in food samples, but with a small linear range and longer detection time.

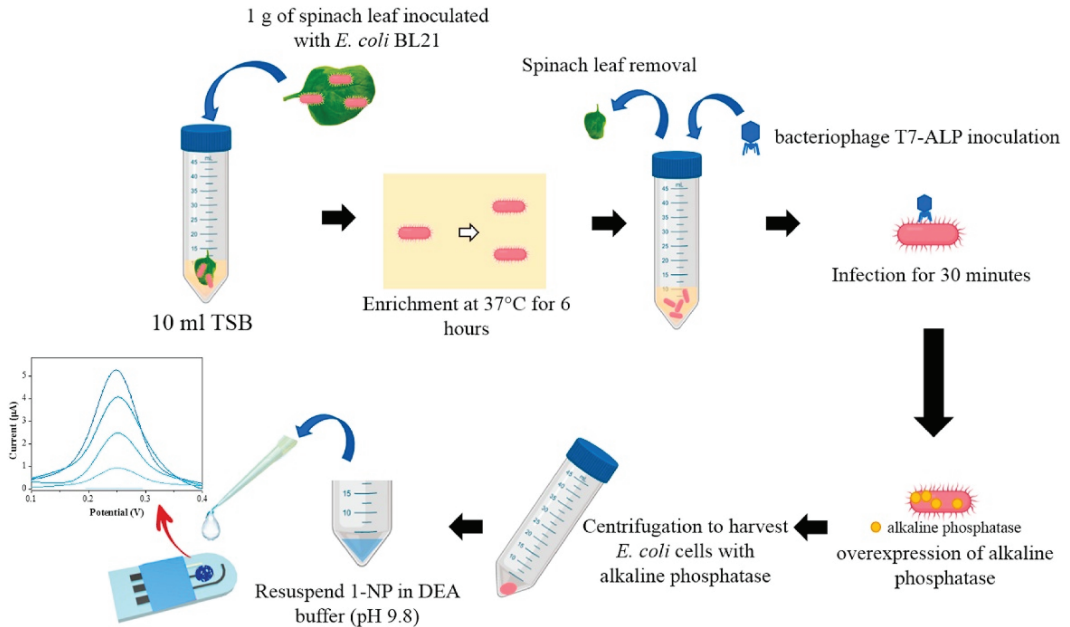


Figure 5. Schematic diagram of a phage electrochemical biosensor for the detection of *E. coli* on spinach leaves (Reprinted with permission from Ref. [19]. 2022, El-Moghazy et al.).

Listeria monocytogenes (LM) can cause Listeriosis, a serious food-borne infection that is mainly seen in immunocompromised patients. It also leads to maternal and neonatal infections, mainly manifesting as sepsis and neuropathy [20]. In recent years, electrochemiluminescence (ECL) [21], cell culture [22], ELISA, and oligonucleotide-based sensors [23] have been successfully established for the detection of *Listeria monocytogenes* in the food industry. Nonetheless, the detection sensitivity of the first three methods is not sufficient to determine trace levels of monocytobacter, thus limiting their utility.

To overcome these limitations, Jampasa et al. [24] designed an ultra-sensitive electrochemiluminescence sensor based on nitrogen-modified carbon dots (NCDs) for the determination of LM using screen-printed carbon electrodes (SPCE), combining the advantages of earlier developed ECL methods. The preparation and detection processes of the sensor are shown in Figure 6. Carbon dots (CDs) were synthesized using citric acid as the carbon source and ethylenediamine (a molecule containing nitrogen atoms) as the nitrogen source. Approximately 4 nm NCD with uniform size distribution can be prepared by a one-step green microwave-assisted method. Carboxyl graphene (GOOH) was used as an electrode modifier to directly introduce the assigned functional groups and to increase the conductivity of the proposed platform. The ECL sensor was constructed by modifying SPCE with GOOH, activating the surface of the GOOH-modified SPCE with EDC/NHS at room temperature, and then immobilizing the trapping antibody (Ab1) on the GOOH-modified SPCE. The addition of the immune complex Ab2-NCD resulted in a significant increase in the ECL signaling response in the presence of $K_2S_2O_8$. ECL signal gradually monotonically increased with the further increase in monocytosis concentration. This modified ECL sensor has a LOD of 1.0×10^{-1} CFU/mL, a linear range of 2 to 1.0×10^6 CFU/mL, and a sensitivity of 1.0×10^{-1} CFU mL $^{-1}$. The accuracy and precision of

the sensor were confirmed by measuring LM in milk, sausage and ham and comparing the results with the standard SO 11290-2:2017 method (horizontal method for *Listeria monocytogenes*). Nitrogen doping is a key step in improving the signal of this sensor, making it competitive with other related LM sensing platforms in terms of sensitivity, reproducibility and operational cost.

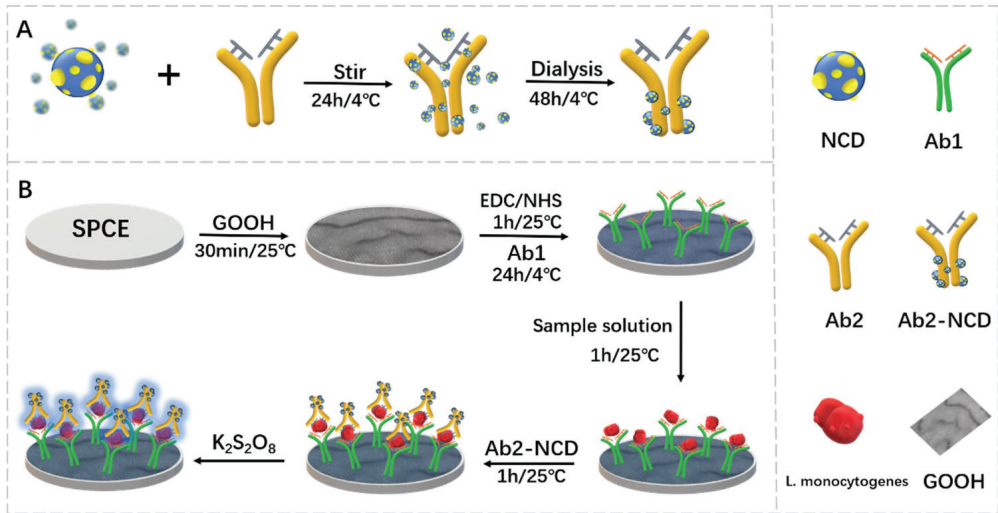


Figure 6. Schematic of (A) NCD conjugated with secondary antibody and (B) the developed ECL sensor for monocytic bacteria (Adapted with permission from Ref. [24]. 2021, Jampasa et al.).

Mishra et al. [25] reported a novel aptamer sensor based on an electrochemical paper-based analytical device (ePAD). As shown in Figure 7, the device used tungsten disulfide (WS_2) and aptamer modifications to detect *Listeria monocytogenes* on a screen-printed paper electrode. EIS was used to analyze ePADs obtained after modification by WS_2 nanostructures (WS_2N_5), aptamer ssDNA, and bacteria. EIS is not only for characterizing the step-by-step assembly of ePADs, but also to evaluate the sensing performance of *Listeria monocytogenes*. The experimental results show that the resistance value increased with the increase in aptamer concentration, which was attributed to the DNA aptamer depositing an insulating layer on the surface of ePAD. In the linear range of 10^1 – 10^8 CFU/mL, the detection limit and quantitative limit of the nucleic acid aptamer sensor are 10 and 4.5 CFU/mL. The sensor successfully detected LM in dairy samples. This aptamer sensor uses a paper-based platform as a substrate, reducing the manufacturing cost of the sensor and the volume of analyte required, facilitating mass production and application.

Table 1. Electrochemical biosensors for bacterial detection.

Analyte	Electrode	Electrochemical Method	Linearity Range	LOD	Assay Time	Ref.
Salmonella	SPCIE	DPV	10^2 – 10^8 CFU/mL	16 CFU/mL	—	[14]
	GCE	SWV	30 fg/ μ L–30 ng/ μ L	15.8 fg/ μ L	—	[15]
<i>E. coli</i>	GCE	DPV	10 – 10^7 CFU/mL	10 CFU/mL	30 min	[18]
	SPE	DPV	1 – 10^4 CFU/mL	1 CFU/mL	1 h	[19]
<i>Listeria</i>	SPCE	CV	2 – 1.0×10^6 CFU/mL	0.1 CFU/mL	—	[24]
	SPPE	EIS	10^1 – 10^8 CFU/mL	10 CFU/mL	—	[25]

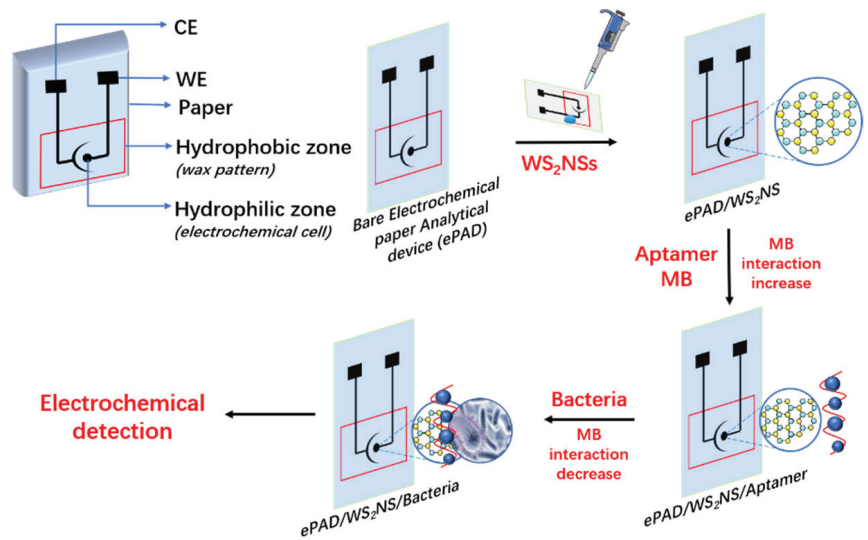


Figure 7. Schematic of a screen-printed paper-based aptamer sensor for the detection of *Listeria monocytogenes* (Adapted with permission from Ref. [25]. 2022, Mishra et al.).

2.2. Virus

Viruses are a common cause of foodborne disease outbreaks. Viral diseases have a low mortality rate but can be transmitted to humans through food due to improper food handling [26]. The rapid replication and high transmissibility of the virus can have serious consequences not only for individuals but also for the health of communities, and even cause serious economic impacts. Therefore, a quick, accurate, and low-cost test diagnostic tool for a large number of people is very important. In the following, electrochemical biosensors for common avian influenza virus, hepatitis A virus, and norovirus are discussed (Table 2).

Avian influenza virus (AIV) is one of the pathogens that endanger human health. Avian influenza viruses can also affect the safety of food supply and cause significant economic losses [27]. Therefore, an accurate, sensitive, and fast detection method is the key to decision-making. Lee et al. [28] used electrochemical technology to prepare a label-free AIV H5N1 biosensor composed of multifunctional DNA structure on electrodes made of porous gold nanoparticles (pAuNPs), and its structure and detection principle are shown in Figure 8. DNA 3 way-junction (3WJ) was introduced as a multifunctional bioprobe, and each fragment was assembled into DNA 3WJ for AIV detection, and the assembly structure was confirmed by native magnesium trisborate polyacrylamide gel electrophoresis (TBM-PAGE). In order to improve the sensitivity of electrochemical signals, pAuNPs were synthesized, and DNA 3WJ was modified on pAuNPs-modified gold electrodes by a layer-by-layer (LbL) assembly method. The surface morphology of pAuNPs-modified gold electrodes was studied by FE-SEM and AFM. The binding of HA protein to DNA 3WJ modified electrode was confirmed by CV. The manufactured biosensor was observed to have a linear range of 1 pM–100 nM in HEPES buffer, a LOD of 9.43 pM, and 1 μ M HA protein could be detected in diluted chicken serum. Each DNA fragment of the sensor has a specific function. These nucleic acid fragments are well assembled and there is no loss of function. Compared to other reports, the sensor does not require additional labeling and signal amplification processes and can be applied for multi-target detection.

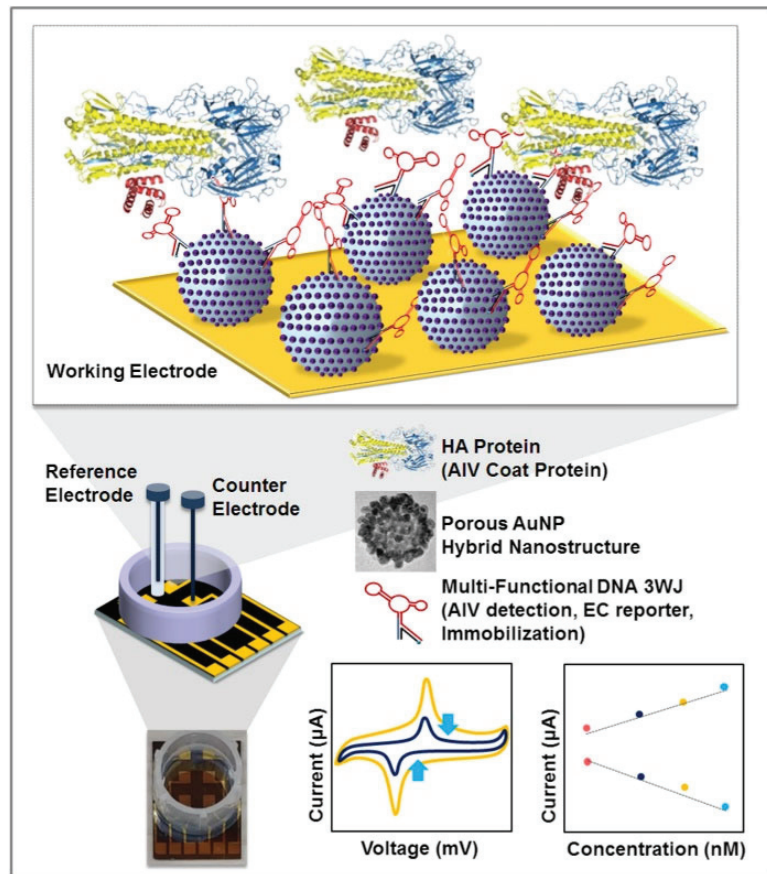


Figure 8. Schematic diagram of a biosensor for detection of avian influenza virus (Reprinted with permission from Ref. [28]. 2019, Lee et al.).

Hepatitis A virus (HAV) can be transmitted through the fecal-oral route, which is mainly related to the ingestion of food or water contaminated with infected feces and is a common cause of clinical hepatitis and acute liver failure [29]. Manzano et al. [30] developed an electrochemical method based on DNA pairing to detect the hepatitis A virus. Its sensing strategy is shown in Figure 9. A single-stranded DNA probe (capture probe) was designed for the hepatitis A virus and the DNA of samples containing the virus was detected by nested reverse transcriptase polymerase chain reaction (RNT-PCR). To develop electrochemical devices, disposable gold electrodes were functionalized using specific capture probes and tested on complementary single-stranded DNA and HAV cDNA. CV was used to monitor the oxidation peak potential of the indicator tripropylamine, and the DNA pairing on the electrode was measured. To prevent non-specific binding, the gold surface was treated with 3% BSA before assay. High-resolution atomic force microscopy (AFM) confirmed the efficiency of electrode functionalization and on-electrode pairing. The linear range of HAV detection was $10 \text{ fg}/\mu\text{L}$ – $10 \text{ pg}/\mu\text{L}$, and the detection limit was $1.08 \text{ fg}/\mu\text{L}$. This electrochemical analysis method is less time-consuming than conventional PCR analysis. The sensor has shown comparable sensitivity to nRT-PCR assays, in addition to its great potential to reduce costs and time in hepatitis A virus detection.

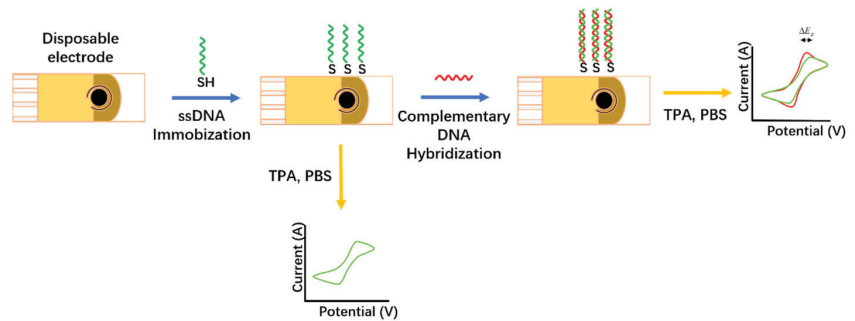


Figure 9. Disposable DNA biosensor constructed by thiol gold coupling of thiolated single-stranded DNA probes (Adapted with permission from Ref. [30]. 2018, Manzano et al.).

Norovirus is one of the causes of a high degree of gastrointestinal infection, mainly from contaminated water or contaminated food [31]. Focusing on promising alternatives for more sensitive and accurate detection of norovirus, Jiang et al. [32] constructed a 3D electrochemical aptamer sensor for norovirus-sensitive detection. As shown in Figure 10, it is characterized by the modification of movable spherical working electrodes (WE) with gold phosphate nanocomplexes (BP-AuNCs). The BP-AuNCs were prepared by restoring phosphorene nanosheets (BPNSs) in situ on chloroauric acid (HAuCl_4). The removable spherical WE was made by hand applying carbon ink to the ball head and then baking it in the oven at 50°C , a design that helps increase surface area, simplify sampling, and avoid cross-contamination. Mercaptan-modified aptamers can easily bind to the surface of BP-AuNCs by covalent bonding without altering the structural or functional properties of aptamers. This sensing strategy is based on a specific binding between norovirus and aptamers, and then the resulting complex can cause diffusion barriers on the WE, altering the electrochemical signal. DPV was used to characterize the electrochemistry of 3D aptamer sensors with a detection limit of 0.28 ng/mL and a linear range of 1 ng/mL to $10\text{ }\mu\text{g/mL}$. The proposed 3D electrochemical aptamer sensor had been successfully applied to the detection of norovirus in oyster samples with an average detection time of 35 min. The spherical working electrode design effectively reduces the size of the sensor and facilitates the miniaturization of the sensor. The sensor provides a simple, low-cost strategy for sensitive and selective detection of norovirus.

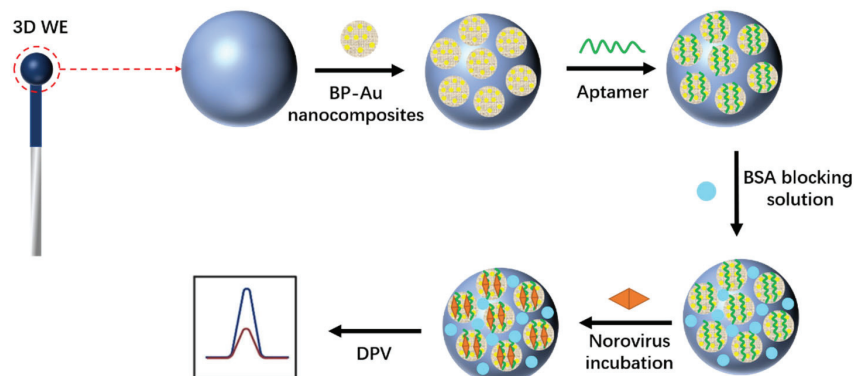


Figure 10. Schematic of a 3D electrochemical aptamer sensor for the detection of norovirus (Adapted with permission from Ref. [32]. 2022, Jiang et al.).

Table 2. Electrochemical biosensors for virus detection.

Analyte	Electrode	Electrochemical Method	Linearity Range	LOD	Assay Time	Ref.
AIV	Au	CV	1 pM–100 nM	9.43 pM	—	[28]
HAV	Au	CV	10 fg/μL–10 pg/μL	1.08 fg/μL	—	[30]
Norovirus	CIE	DPV	1 ng/mL–10 μg/mL	0.28 ng/mL	35 min	[32]

2.3. Mold

Mycotoxin contamination of food and feed is considered one of the most serious food safety problems in the world because these fungal metabolites may be teratogenic, mutagenic, carcinogenic, and immunosuppressive, and may seriously damage animal and human health. Early common mycotoxin detection methods mainly include high-performance liquid chromatography, thin layer chromatography, mass spectrometry, gas chromatography, and ELISA [33]. These methods provide accurate and reliable detection of mycotoxin, but these methods have some problems, such as complex sample preparation and long detection time. Electrochemical biosensors have attracted much attention in mycotoxin analysis because of their rapid, sensitive, specific, and portable advantages. The following is a description of several electrochemical biosensing strategies used to detect aflatoxin, ochratoxin, and zearalenone (Table 3).

Aflatoxin has a carcinogenic effect and is one of the most important factors affecting the safety of the food industry [34]. To meet the detection requirements, Wang et al. [35] developed a simple, efficient, and sensitive electrochemical immunosensor for the detection of aflatoxin B1 (AFB1) in peanut oil. Figure 11 is a schematic of an electrochemical immunosensor for the detection of aflatoxin B1. Bare GCEs were modified with graphene, bimetallic organic framework materials (Zn/Ni-ZIF-8-800), chitosan and AuNPs. Electrochemical immunosensors were characterized by CV and the changes in electrochemical signals after antibody and AFB1 binding were studied in detail. The results show that the electrochemical reaction of AFB1 on this electrochemical immunosensor is a diffusion control process. The signal response of AFB1 at different concentrations was measured with DPV, and the DPV response signal gradually decreased as the AFB1 concentration increased. Electrochemical immunosensors have a linear range of 0.18–100 ng/mL and a detection limit of 0.18 ng/mL. The prepared sensors provide the basis for simple, fast and sensitive detection of AFB1 in peanut oil. Although modification of the electrodes with graphene, Zn/Ni-ZIF-8-800, chitosan and AuNPs can improve the electrode surface conductivity, the material preparation process is complex and requires specific reagents, equipment, and methods, which is operationally difficult for non-specialists.

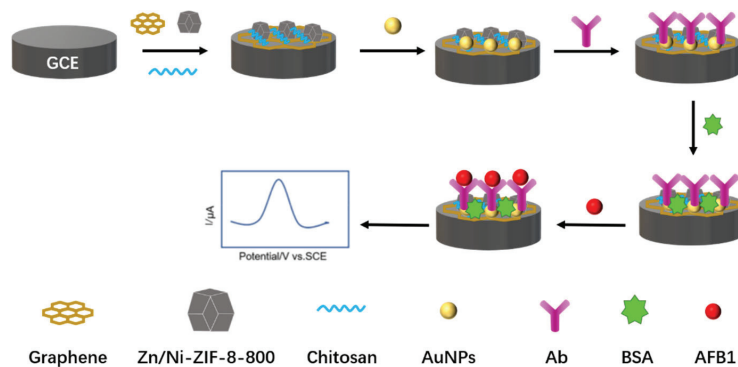


Figure 11. Schematic of an electrochemical immunosensor for the detection of aflatoxin B1 (Adapted with permission from Ref. [35]. 2022, Wang et al.).

Mazaafrianto et al. [36] developed an electrochemical sensor for the quantitative detection of ochratoxin A (OTA) by using an aptamer with two dithiol groups that exhibited higher stability on gold electrodes than a single thiol-based aptamer. The sensor is also based on a signal-on scheme that generates a signal current through structural switching of aptamers upon interaction with the OTA. To simplify the fabrication of the sensor, the non-covalent interaction of methylene blue with the aptamer was also used as an electrochemical indicator. In addition, the sensor performance was characterized, including the dissociation constants of the aptamer-OTA complex. The sensor is highly reproducible and sensitive enough to detect the minimum amount of OTA required for the analysis of actual food samples, with a detection limit of 113 pM. The aptamer modification scheme of the sensor has been successfully applied to microprocessed electrodes. By varying the appropriate aptamer according to the target analyte, the sensor is able to provide a simple, portable and versatile platform for in situ detection.

Zearalenone (ZEA) is a mycotoxin produced by *Fusarium* fungi, which is highly toxic to animal and human health [37]. Radi et al. [38] used CV, DPV, and EIS to study the electrochemical behavior of zearalenone on a single-wall carbon nanotube screen printing electrode (SWCNT-SPCE) and observed a single irreversible oxidation peak. Due to the adsorption of ZEA on the electrode surface, the peak DPV current on SWCNT-SPCE was significantly enhanced. Maize GA was determined by differential pulse adsorption vapor voltammetry (DPASV). Under optimized conditions, the peak anode current of ZEA varies linearly with ZEA concentration in the range of 2.5×10^{-8} – 1.0×10^{-6} M, and the detection limit is 5.0×10^{-9} M. The results showed that the method could be used for the quantitative analysis of zearalenone in cornflakes. It is worth mentioning that the electrode surface of the sensor is not contaminated by oxidation products and the electrodes can be reused, reducing the cost of the sensor.

Table 3. Electrochemical biosensors for mold detection.

Analyte	Electrode	Electrochemical Method	Linearity Range	LOD	Assay Time	Ref.
Aflatoxin	GCE	DPV	0.18–100 ng/mL	0.18 ng/mL	—	[35]
Ochratoxin	Au	DPV	0.25–750 nM	113 pM	—	[36]
Zearalenone	SWCNT-SPCE	DPASV	2.5×10^{-8} – 1.0×10^{-6} M	5.0×10^{-9} M	—	[38]

2.4. Allergen

Components of food that can cause abnormal reactions in the body's immune system are known as allergens. National and international agencies are enacting laws, regulations, and food labeling standards to avoid allergies in people by labeling allergen components on foods [39]. Rapid on-site detection of allergic components in food can safeguard the health and quality of life of food allergy patients [40]. Currently, electrochemical biosensors have become an important tool for the rapid detection of food allergens, and the electrochemical biosensors used for the detection of soybean and peanut allergens are discussed below (Table 4).

Table 4. Electrochemical biosensors for soy allergen detection.

Analyte	Electrode	Electrochemical Method	Linearity Range	LOD	Assay Time	Ref.
Genistein	Carbon	DPV	100 ppb–10 ppm	100 ppb	—	[41]
Ara h 1	SPCE	LSV	0–1000 ng/mL	5.2 ng/mL	2 h 20 min	[42]
Ara h 6			0–1.0 ng/mL	0.017 ng/mL		

Sundhoro et al. [41] applied MIPs for the first time to achieve the detection of the soybean allergenicity marker genistein in complex foods. The electrode coated with MIPs showed high sensitivity (lower limit of detection of 100 ppb) and successfully distinguished genistein from several structurally similar isoflavone and flavonoid molecules. The sensor's

results for soybean allergens were comparable to or better than the performance of other commercially available portable allergen detection devices, including lateral flow devices (LFDs) and ELISA. Although the sensor's performance has not yet exceeded the highest sensitivity for soybean allergens obtained using complex, expensive and labor-intensive methods such as mass spectrometry and PCR, its high selectivity, short detection time, and low-cost offer significant advantages over leading detection technologies.

Freitas et al. [42] developed an electrochemical dual immunosensor for the simultaneous analysis of two major peanut allergens, Ara h 1 and Ara h 6. As shown in Figure 12, Sandwich immunoassays were performed using monoclonal antibodies on a double-working screen-printed carbon electrode. The assay time was 2 h 20 min and the actual operating time was 30 min. The limit of detection for Ara h 1 was 5.2 ng/mL. The limit of detection for Ara h 6 was 0.017 ng/mL. The dual immunosensor has been successfully applied to the analysis of several food products and was able to quantify peanuts down to 0.05%. The accuracy of the results was confirmed by recovery studies and comparison with ELISA. The sensor is equally suitable for complex food matrices.

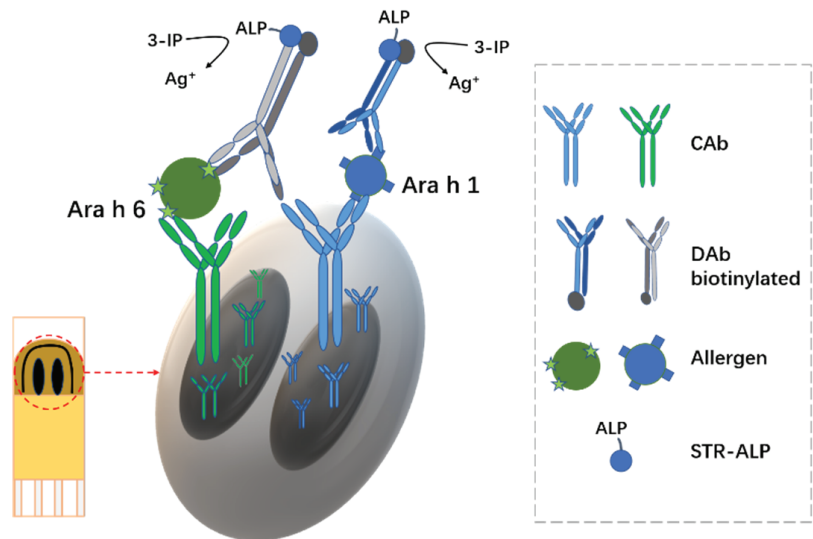


Figure 12. Schematic diagram of the immune sensor configuration and structure (Adapted with permission from Ref. [42]. 2021, Freitas et al.).

3. Chemical Contamination

Chemical contamination in food has a wide range of sources, variety and complex compositions. Most foods are inevitably contaminated by pesticides, heavy metals, food additives and other common chemicals [43]. Excessive intake of these substances can have negative effects on human health. In the following, different biosensing strategies for the detection of pesticide residues, heavy metals, and illegal additives are discussed based on existing electrochemical biosensors for food safety detection.

3.1. Pesticide Residue

Pesticides can prevent crop pests and diseases, but they accumulate in vegetables, fruits, and meat throughout the food chain [44]. Consumption of food with excessive pesticide residues will endanger human health. At present, the most commonly used pesticide detection methods include GC, GC-MS, liquid chromatography (LC), and LCMS. These methods have high sensitivity, selectivity, and accuracy with the potential for multi-component analysis. However, they are time-consuming and expensive, often requiring sample preparation [45]. In recent years, electrochemical-based biosensors have been

investigated to detect pesticide residues in order to overcome the limitations of traditional methods (Table 5).

Nevin et al. [46] used a green ultrasound-microwave assisted method to prepare reduced-GO (rGO) and studied rGO-based non-enzymatic electrochemical sensors for the detection of synthetic fungicides used as propamocarb (PM) pesticides. To test whether the rGO-based non-enzymatic electrochemical sensor detected PM residues in real vegetables, the sensor was tested on cucumber samples with 5 different concentrations of PM pesticides. The sensor was able to detect PM pesticide on actual cucumber samples with high sensitivity within a cycle time of 1 min, with a detection limit as low as 0.6 μM , a sensitivity of 101.1 $\mu\text{A } \mu\text{M}^{-1} \text{cm}^{-2}$, and a linear range of 1 to 5 μM . The results show that the modification of rGO on the sensor surface can accelerate the response of the sensor. The most outstanding advantage of the sensor is that it takes only 1 min to complete the detection, and can be used in portable detection kits for rapid on-site detection of PM-type pesticides in food.

Carbendazim (CBZ) is one of the most commonly used benzimidazole fungicides. It is widely used to promote food production and its residues pose a great threat to human health and the environment [47]. Liu et al. [48] prepared a novel electrochemical sensor for CBZ determination based on β -cyclodextrin (β -CD) functionalized carbon nanosheets @ carbon nanotubes (CNS@CNT). Its sensing strategy is shown in Figure 13. CNS@CNT combines the large surface area of CNS with the excellent conductivity of CNT to significantly improve the electrocatalytic performance of the sensor. In addition, β -CD is well capable of host GUEST supramolecular recognition, which can improve the selective recognition and enrichment ability of CBZ. The β -CD/CNS@CNT/GCE sensor has a lower detection limit of 9.4 nM in the linear CBZ concentration range from 0.03 to 30 μM . The fabricated sensor has good stability, high sensitivity (30.86 $\text{A } \mu\text{M}^{-1} \text{cm}^{-2}$), and reliable reproducibility (RSD = 3.6%). In particular, β -CD/CNS@CNT/GCE sensor can be used for the detection of CBZ in apple juice. Compared with the detection performance of other CBZ sensors, the β -CD/CNS@CNT/GCE sensor has a relatively low LOD, good long-term stability, anti-interference, and selectivity.

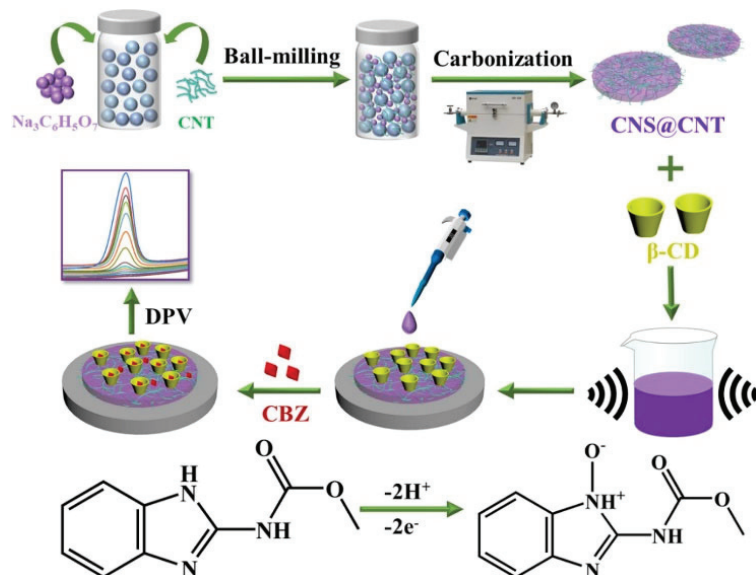


Figure 13. Fabrication schematic of β -CD/CNS@CNT/GCE sensor (Reprinted with permission from Ref. [48], 2022, Liu et al.).

Imidacloprid (IM) has been widely used in crop pest control and disease resistance, and the high sensitivity detection of imidacloprid concentration has put forward strong requirements in the field of food safety [49]. Tang et al. [50] reported a sensitive ECL sensor based on upconverting nanoparticle functional zeolite imidazolate framework (UCNPs@ZIF-8) nanocomposites combined with molecularly imprinted polymers (MIPs), which successfully realized the quantitative detection of IM. UCNPs@ZIF-8 composites were characterized by a multi-sided prismatic structure with a large surface area and good biocompatibility. In conjunction with Molecular imprinting technology (MIT), a recognition cavity was left to capture the target. In addition, MIPs/UCNPs@ZIF-8 modified glass carbon electrodes (MIPs/UCNPs@ZIF-8/GCE) offered excellent selectivity. The modified electrode was characterized using EIS, and ECL performance was tested by CV. The results show that the intensity of ECL gradually decreases as the IM concentration increases, which proves that the presence of IM has a quenching effect on the response signal. The sensor exhibited a good linear response to IM over a wide concentration range (0.1 ng/L–1 mg/L) with a detection limit as low as 0.01 ng/L. MIPs have specific recognition and selective adsorption capabilities that improve the selective recognition and enrichment of target analytes by the sensor, thereby reducing detection time. It has been successfully applied to the determination of IM concentrations in fish, shrimp, and lettuce, providing a new means for the rapid detection of trace pesticide residues in crops and aquatic products. In addition to MIPs, the ACEK effect can also be employed to accelerate the enrichment of target analytes on the electrode surface.

Pesticides and chemical nerve agents containing organophosphorus compounds are harmful to human health. Pham et al. [51] developed a chip-based electrochemical biosensor for the detection of OP in food. The principle of the detection platform is based on the inhibition of leucovorin (DMT), a typical OP that specifically inhibits acetylcholinesterase (AChE) activity. A gold electrode modified with poly diallyl dimethyl ammonium chloride (PDDA) and oxidized nanocellulose (NC) functionalized with carbon nanotubes was used to detect OP, and the composite electrode showed a 4.8-fold higher sensitivity than the bare gold electrode. The sensor was successfully used to detect food samples spiked with organophosphates with a DMT detection limit of 4.1 nM, a quantification limit of 12.6 nM, and a linear range of 10–1000 nM. The sensor creatively uses microfluidic chip technology to miniaturize the sensor by integrating the electrodes on the chip. It has the prospect of mass production and broad application.

Table 5. Electrochemical biosensors for pesticide residue detection.

Analyte	Electrode	Electrochemical Method	Linearity Range	LOD	Assay Time	Ref.
PM	Au	CV	1 μ M–5 μ M	0.6 μ M	1 min	[46]
CBZ	GCE	DPV	0.03–30 μ M	9.4 nM	—	[48]
IM	GCE	CV	0.1 ng/L–1 mg/L	0.01 ng/L	—	[50]
DMT	Au	CV	10–1000 nM	4.1 nM	—	[51]

3.2. Heavy Metal

Heavy metal pollution is becoming a serious environmental and social problem, because the long-term accumulation of non-biodegradable heavy metal ions in the human body leads to most diseases, such as kidney failure, chronic toxic symptoms, and liver injury [52]. Therefore, lead, cadmium, chromium, and other heavy metals in food sources must be controlled to ensure public safety [53]. A typical heavy metal analysis is performed using conventional spectroscopic techniques, such as atomic absorption spectrometry (AAS) and inductively coupled plasma optical mass spectrometry (ICP-MS). However, electrochemical methods offer significant advantages over optical analytical techniques, including low cost, simplicity, and the possibility of field applications [54]. Several electrochemical biosensors for the quantitative detection of As, Hg²⁺, Cd²⁺, Pb²⁺, Cu²⁺, and Zn²⁺ were discussed below (Table 6).

Table 6. Electrochemical biosensors for heavy metal detection.

Analyte	Electrode	Electrochemical Method	Linearity Range	LOD	Assay Time	Ref.
As	SPGE	SWASV	0.1–3.0 ppm	0.03 ppm	<3 min	[55]
Hg ²⁺	SPCE	SWASV	0.8–12.0 nM	0.23 nM	—	[56]
Cd ²⁺ Pb ²⁺	Au	SWV	0.1–1000 nmol/L	89.31 pmol/L 16.44 pmol/L	15 min	[57]
Hg ²⁺ Cd ²⁺ Pb ²⁺ Cu ²⁺ Zn ²⁺	GCE	SWASV	6–7000, 4–6000, 6–5000, 4–4000, 6–5000 µg/L	0.08, 0.09, 0.05, 0.19, 0.01 µg/L	—	[58]

Khamcharoen et al. [55] created a small electrochemical platform for detecting As (III) contamination in herbal medicines. To reduce the procedure for modification and determination, only one drop of mixed standard Au (III) and sample solution were used for electrochemical measurements using a screen-printed graphene electrode (SPGE). Square wave anode dissolution voltammetry (SWASV) was used to characterize modification and determination processes. When the reduction potential was maintained at -0.5 V, an Au–As intermetallic alloy was formed. For electrochemical determination of As (III), As was stripped away. This electrochemical sensing system can detect As (III) in the concentration range of 0.1 to 3.0 ppm with a LOD of 0.03 ppm, and a total analysis time within 3 min. The applicability and accuracy of the proposed sensor was verified by determining As (III) in the herbal sample. The advantages of simple operation, fast detection, portability, and low cost (<1 USD) make it a more powerful tool for routine monitoring and field analysis applications. It is worth noting that the proposed method is a simple and inexpensive analytical method, especially for the determination of the As (III) of herbal clocks in the context of limited resources. In situ one-step assays using standard gold solution modification SPGE is beneficial to save time, budget, and reduce the number of experimental samples.

Narouei et al. [56] reported a novel conductive nanofiber structure with a large number of nitrogen binding sites, which improved the sensitivity of SPCE for Hg²⁺ detection. The nanofibers were made of conductive copolymer polyaniline-co-o-aminophenol (PANO), which was modified with AuNPs by electrochemical deposition. Because of the high affinity of AuNPs for Hg²⁺, the nanofibers provided high detection sensitivity for SWASV. The linear dynamic range of the sensor for Hg²⁺ is 0.8–12.0 nM, and the detection limit is 0.23 nM. The sensor is selective for Hg²⁺ under the interference of As, Pb, Cu, Zn, and Cd ions. It is also used in the detection of Hg²⁺ in river water and fish samples. This method provides a widely applicable strategy for improving the sensitivity of electrochemical sensors to heavy metal ion contamination. Compared to PANO or AuNPs modified electrodes alone, Au-PANO modified electrodes increase the sensitivity of the sensor to detect Hg²⁺ and have good selectivity for Hg²⁺. This strategy is very suitable for the modification of low-cost disposable SPCE electrodes, which provides a feasible solution for miniaturization and low-cost on-site detection of metal ion contamination.

Yuan et al. [57] designed an aptamer-based electrochemical aptamer sensor for the first time, which can simultaneously detect Cd²⁺ and Pb²⁺ in fruits and vegetables. The detection principle of the electrochemical aptamer sensor is shown in Figure 14. Double-stranded DNA containing aptamers is immobilized to gold electrodes by Au-S bonds. In the absence of Cd²⁺ and Pb²⁺, the sensor has a high-intensity electrochemical signal. Otherwise, after the addition of Cd²⁺ and Pb²⁺, the metal ions bind specifically to the aptamer, breaking the rigid double-stranded structure and keeping the aptamer away from the gold electrode. Therefore, the electrochemical signal of the modified electrode is weakened. The changes in electrochemical signals were measured by square wave voltammetry, and Cd²⁺ and Pb²⁺ were detected simultaneously. The results showed that the electrochemical aptamer sensor showed a linear response to Cd²⁺ and Pb²⁺ in the

range of 0.1–1000 nmol/L, and the detection limits of Cd^{2+} and Pb^{2+} reached 89.31 pmol/L and 16.44 pmol/L, respectively. The electrochemical aptamer sensor showed significant response to Cd^{2+} and Pb^{2+} only. For the first time, ultra-sensitive detection of Cd^{2+} and Pb^{2+} at pmol/L levels simultaneously was achieved. Compared with other methods for simultaneous detection of Cd^{2+} and Pb^{2+} , this study has the advantages of high sensitivity, strong selectivity, and simple operation.

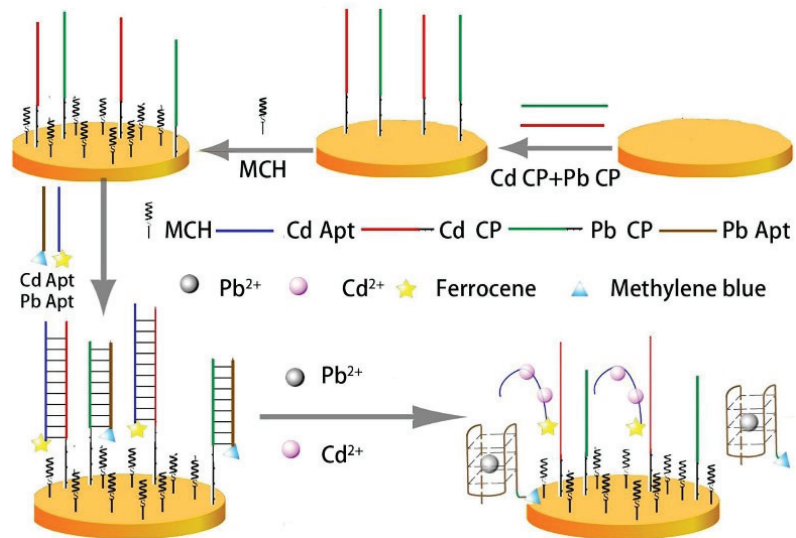


Figure 14. Schematic diagram of electrochemical aptamer sensor for Cd^{2+} and Pb^{2+} detection (Reprinted with permission from Ref. [57], 2022, Yuan et al.).

Tan et al. [58] developed fluorinated ink/gold nanocage (FGP/AuNC) nanocomposites for simultaneous determination of heavy metals using square-wave anodic stripping voltammetry. The synergistic effect of AuNC and FGP can enhance the electrochemical active center and cation affinity, and improve the catalytic activity of FGP/AuNC composites for simultaneous electrochemical determination of Hg^{2+} , Cd^{2+} , Pb^{2+} , Cu^{2+} , and Zn^{2+} . Under the conditions of buffer pH 5.0, deposition potential -1.25 V, and deposition time 140 s, this method can obtain the best results. The detection limits of FGP/AuNC electrodes were low (0.08, 0.09, 0.05, 0.19, 0.01 $\mu\text{g/L}$) and the linear ranges were wide (6–7000, 4–6000, 6–5000, 4–4000, 6–5000 $\mu\text{g/L}$). In addition, FGP/AuNC electrodes were also used for simultaneous determination of Zn^{2+} , Cd^{2+} , Pb^{2+} , Cu^{2+} , and Hg^{2+} in real samples (peanut, rapeseed and tea). The results of electrochemical method and atomic fluorescence spectrometry/inductively coupled plasma mass spectrometry are in good agreement. The method has been successfully applied to the determination of heavy metal ions in agricultural products. The sensor detects multiple heavy metal ions simultaneously, which saves the cost of the sensor and ensures the accuracy and sensitivity of the detection results. However, it has high requirements for detection samples and is susceptible to interference from impurities for the detection of complex samples, such as soil and feed.

3.3. Illegal Food Additives

Improper use of food additives may pose a threat to human health, so it is important to develop sensitive and selective detection methods. According to their functions, food additives can be divided into colorants, preservatives, sweeteners, thickeners, emulsifiers, promoters, and acidity regulators, etc. [59]. For the quantitative detection of food additives, many methods based on liquid chromatography, mass spectrometry and electrochemistry have been reported [60]. Compared with other methods, the electrochemical methods

have the characteristics of simple operation, low cost, and high accuracy. In the following, electrochemical biosensing strategies for the detection of melamine (MEL), Sudan Red I, and clenbuterol are discussed (Table 7).

Melamine is a nitrogen-rich organic compound commonly used to increase apparent protein levels in liquid milk and milk powder. Excessive consumption of melamine can cause damage to the urinary system and increase the risk of acute kidney failure, urolithiasis, and bladder cancer in infants and children [61]. Rahman et al. [62] In order to detect melamine in an aqueous solution, the cadmium-doped antimony oxide (Cd-doped Sb_2O_4) nanostructures (CAO-NSs) were synthesized by low-temperature alkaline hydrothermal method. GCE was modified with CAO-NSs and its sensing performance against melamine was studied by I-V in phosphate buffer solution (PBS). Melamine undergoes a reduction reaction in the presence of CAO-NSs/GCE in PBS, and the current response gradually decreases with the increase in melamine concentration at 25.0 °C. To verify the performance of the sensor, melamine in actual milk samples was determined using CAO-NSs/GCE, and the aggregated CAO-NSs exhibited extraordinary electrocatalytic activity. CAO-NSs/GCEs have high sensitivity ($3.153 \mu\text{A}\mu\text{M}^{-1}\text{cm}^{-2}$) with a linear monitoring range of 0.05 nM–0.5 mM and a detection limit of $14.0 \pm 0.05 \text{ pM}$. Compared with other electrochemical sensors for melamine detection, this sensor has a wider detection range and a lower detection limit at the pM level, providing better versatility. This is an effective way to develop melamine and its derivatives-sensitive sensors that can be used for safety detection in large-scale biomedical and healthcare fields.

An et al. [63] reported a simple sensor for MEL detection in milk. Due to the low electrochemical activity of MEL, ferrocene glutathione (Fc-ECG) was used as an electron transfer medium to assist SPCE in the detection of MEL. Figure 15 depicts the preparation and signal enhancement effect of the improved SPCE, which was prepared using a step-by-step drip method for the modified electrode (MEL/Fc-ECG/SPCE). The relationship between MEL concentration and sensor current response in milk samples was investigated using DPV. The results show that since three p- π conjugated double bonds promote electron transfer, MEL significantly enhances the signal of the Fc-ECG/SPCE sensor. The sensor exhibited two linear lines in the range of 0.20–2.00 μM and 8.00–800 μM , with a detection limit of 0.13 μM . It has good stability and reproducibility, while being resistant to interference from other compounds. It has been successfully used to detect MEL in milk. However, the linear range is not continuous, and the application may be limited.

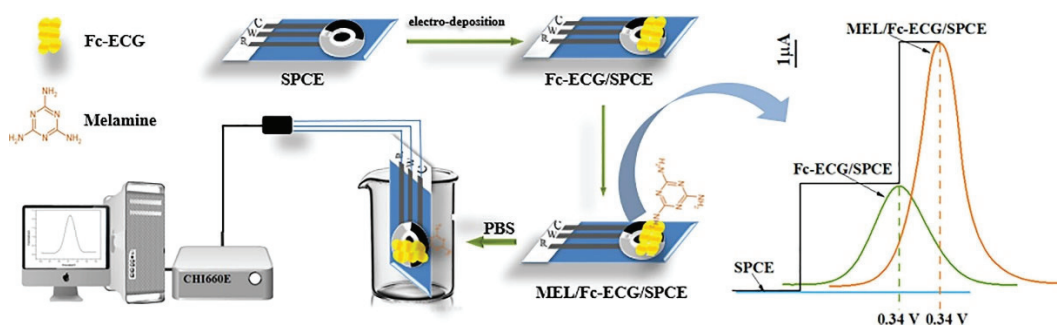


Figure 15. The process of making an Fc-ECG/SPCE sensor for MEL detection (Reprinted with permission from Ref. [63]. 2022, An et al.).

Sudan red is used in the chemical industry as a colorant in oils, fats, plastics, waxes, gasoline, shoes, printing inks, floor polish, and alcohol varnishes, and can also give red color to chili sauce, ketchup, and many other common foods [64]. However, Sudan red is a potential carcinogen, so the quantitative detection of Sudan red in food is imperative. Yang et al. [65] studied the electrochemical properties of MWCNTs/ AuNPs/ GCE for the quantitative detection of Sudan I. The surface of GCE was modified by electrodeposition of

AuNPs and synthesis of MWCNTs by spray pyrolysis. The morphology and structure of the synthesized AuNPs and MWCNTs were investigated by field emission scanning electron microscopy (FESEM) and X-ray diffractometry (XRD). The results show that the MWCNTs and Au nanoparticles have high density and porous structure. The electrochemical properties of MWCNTs/AuNPs/GCE were studied by cyclic voltammetry and amperometry. Electrochemical studies showed that MWCNTs/AuNPs/GCE had high stability and sensitivity, a linear response range of 10–260 μM , and detection limit of 4 nM, which could be used for the determination of Sudan I in chili paste samples. Compared with other Sudan I electrochemical sensors, this sensor exhibits a wide linear detection range, but the detection limit is not the lowest and the sensor performance can be further improved.

Heydari et al. [66] synthesized zinc oxide nanoparticles (ZnONPs) by precipitation and used it as a novel electrocatalyst for the detection of Sudan II dye. The nanoparticles were characterized by X-ray diffraction spectroscopy and scanning electron microscopy techniques with an average diameter of 25 nm. To study the electrocatalytic effect of ZnONPs, carbon paste electrodes (CPEs) were modified with nanoparticles. The central composite rotational design and response surface method were used to optimize the influence of chemical and instrumental parameters on the oxidation reaction of Sudan II. Then, the electrochemical response of Sudan II was studied on the surface of the nanostructured modified electrode by DPV. The anode peak current of Sudan II was linearly related to its concentration in the range of 0.01–20 mM, with a detection limit of 0.0017 mM. The application of ZnONPs increased the active area of the electrode and improved the electron transfer between Sudan Red II and the electrode surface, resulting in a 2.4 folds increase in the voltammetric peak current of this sensor over the bare electrode. In addition, the method was satisfactory for the detection of Sudan II in chili sauce. The detection limit of this nanostructured sensor was superior compared to other electrochemical sensors for the detection of Sudan II.

Clenbuterol (CLB) was originally used to treat human depression and lung disease [67]. In recent years, clenbuterol has been illegally used to feed live pigs because of its anabolic effects that promote muscle growth and reduce fat mass [68]. However, it can remain in the muscle tissue and internal organs of animals that are being raised, endangering the health of those who eat it. Sun et al. [68] prepared two kinds of rGO/Fe₃O₄ nanocomposites by solvothermal and hydrothermal methods and modified them onto the surface of glassy carbon electrodes to prepare a Clenbuterol electrochemical sensor for direct electrochemical detection of clenbuterol residues in animal metabolism. CV and DPV were used for electrochemical characterization and measurement, and the detection performance of the sensor for clenbuterol was investigated. The electrochemical sensor can detect clenbuterol linearly in the range of 1–128 μM , and the detection limit is 120 nM (S/N = 3). The electrochemical sensor has been successfully used to detect clenbuterol in pig urine. Compared to other clenbuterol sensors, this sensor does not have an outstanding detection limit, but has a wider linear range and is more versatile.

Jing et al. [69] proposed a new method for electrochemical detection of clenbuterol using boron carbon-oxynitrogen (BCNO) nanosheets as a sensing medium. BCNO nanosheets were prepared using a sodium chloride/potassium chloride eutectic mixture as a molten base, and the samples prepared were BCNO crystal with a nano-sheet structure. Modification of BCNO on GCE can significantly improve electron transport capacity and provide more electrochemically active sites. Clenbuterol was detected by using differential pulse dissolution voltammetry (DPSV), and the DPSV signal increases as the CLB increases. BCNO-modified GCE (BCNO/GCE) exhibited superior analytical performance when detecting Clenbuterol. The sensor had a lower detection limit of 17 nM and a linear concentration range of 0.03–16.0 μM . Finally, the method was applied to the determination of clenbuterol in porcine serum and tablets, and satisfactory recovery was obtained. The results suggest that BCNO nanostructures are expected to be candidates for electrochemical sensors. The sensor has good interference immunity, repeatability and stability for CLB de-

fection. It shows a wide linear range and low LOD compared to the analytical performance of other electrochemical sensors, which is superior to most previous reports.

Table 7. Electrochemical biosensors for the detection of illicit additives.

Analyte	Electrode	Electrochemical Method	Linearity Range	LOD	Assay Time	Ref.
Melamine	GCE	I-V	0.05 nM–0.5 mM	14.0 ± 0.05 pM	—	[62]
	SPCE	DPV	0.20–2.00 µM 8.00–800 µM	0.13 µM	—	[63]
Sudan red	GCE	CV	10–260 µM	4 nM	—	[65]
	CPE	Amperometry DPV	0.01–20 mM	0.0017 mM	—	[66]
Clenbuterol	GCE	CV DPV	1–128 µM	120 nM	—	[68]
	GCE	DPSV	0.03–16.0 µM	17 nM	—	[69]

4. Genetically Modified Crops

Genetically Modified Crops (GMC) are plants in which genes with target traits are modified by genetic engineering techniques and then introduced into the genome of the recipient plant [70]. These exogenous genes are not only stably inherited in the offspring, but can also lead to beneficial traits such as insect resistance, herbicide resistance, and disease resistance in the crop. However, the biosafety of GMC has been controversial. Currently, the detection of GMC components mainly includes gene nucleic acid detection, protein detection, and metabolite detection [70]. although traditional detection methods such as PCR, ELISA, and HPLC are mature and reliable, they cannot meet the practical needs of high speed and low cost. Therefore, a fast, accurate, and low-cost field detection platform for transgenic crops is needed. The following is a discussion of electrochemical biosensors for GM soybean and maize detection (Table 8).

Table 8. Electrochemical biosensors for the detection of GMC.

Analyte	Electrode	Electrochemical Method	Linearity Range	LOD	Assay Time	Ref.
CP4 EPSPS	Au	SWV	0.005–0.3 mg/mL	38 ng/mL	—	[71]
SHZD32-1	SPCE	EIS	1.0×10^{-7} – 1.0×10^{-13} M	3.1×10^{-14} M	—	[72]
Ruifeng12-5	SPCE	EIS	0.10–5.0%	0.10%	—	[73]

Marcos et al. [71] developed an electrochemical immunosensor for the detection of the transgenic soy protein CP4 EPSPS in soybean seeds, which does not require a labeling and signal amplification system. The sensor schematic is shown in Figure 16. The CP4 EPSPS antibodies were first modified on the gold electrodes, and the modified gold electrode was incubated in soy protein solutions of different concentrations at 37 °C for 30 min. After washing with ultrapure water, the electrodes were immersed in an electrochemical cell containing $K_4[Fe(CN)_6]$ (1 mM) and LiCl (0.1 M) solutions. Electrochemical measurements were performed using SWV, and the peak current was linearly related to the concentration of soy protein in the range of 0.005–0.3 mg/mL, with a detection limit of 38 ng/mL CP4 EPSPS (below 0.00038% CP4 EPSPS). Since many countries recommend labeling foods containing higher than 0.9% CP4 EPSPS, the detection limit of this sensor meets the detection needs.

Gao et al. [72] also established a label-free electrochemical sensing platform for the detection of transgenic soybean SHZD32-1. Soybean SHZD32-1 seeds were ground into powder and then genomic DNA samples were extracted by a CTAB-based method. GCDs modified on the SPCE surface can be attached to single-stranded DNA probes via Au-S bonds while improving the conductivity of the DNA sensor. After binding of the DNA probes to transgenic soybean DNA, the electron transfer resistance (R_{et}) on the sensor surface was quantified by the R_{et} response increased with logarithmic increase in target DNA concentration over a linear range of 1.0×10^{-7} – 1.0×10^{-13} M, with a detection limit

of 3.1×10^{-14} M. This label-free sensor is made by inserting the SPCE into a handheld EI analyzer is conveniently fabricated, demonstrating simplicity of construction and operation, requiring no additional indicators or cumbersome procedures, and can be used in a friendly manner by non-specialists.

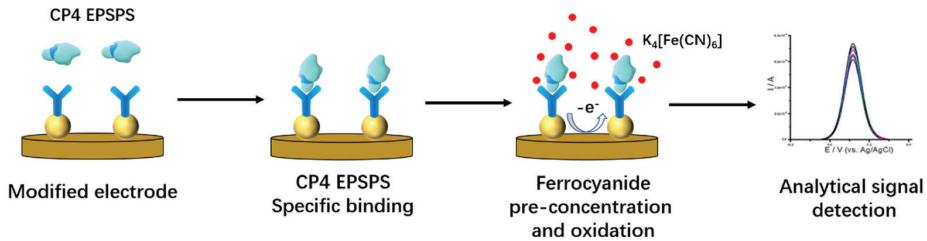


Figure 16. Schematic diagram of the electrochemical immunosensor for the detection of CP4 EPSPS (Adapted with permission from Ref. [71]. 2022, Marcos et al.).

Cui et al. [73] developed a label-free electrochemical impedance gene sensor using gold carbon dots (GCDs) and an easy-to-use portable device. It consists of a handheld electrochemical impedance (EI) analyzer equipped with a coin-sized SPCE. Figure 17 shows the preparation process of this sensor, GCDs were used to modify a screen-printed carbon electrode and capture probes were immobilized by Au-S bonding. Transgenic maize sample DNA was extracted using a one-step extraction method with direct plant lysis buffer and amplified by recombinase polymerase amplification (RPA). The capture probes immobilized on the sensor were identical to the forward RPA primer. After the amplification products bound to the capture probes, the EI signal increased due to the formation of a biocomplex that hindered the interfacial electron transfer. The proposed genetic sensor combined with RPA can detect maize Ruifeng12-5 in a linear range of 0.10–5.0% with a detection limit of 0.10%, roughly calculated as 36 copies/ μ L based on the size of the maize haploid genome. The sensor device is simple to prepare and does not require expensive instruments or specialized personnel and has wide application prospects.

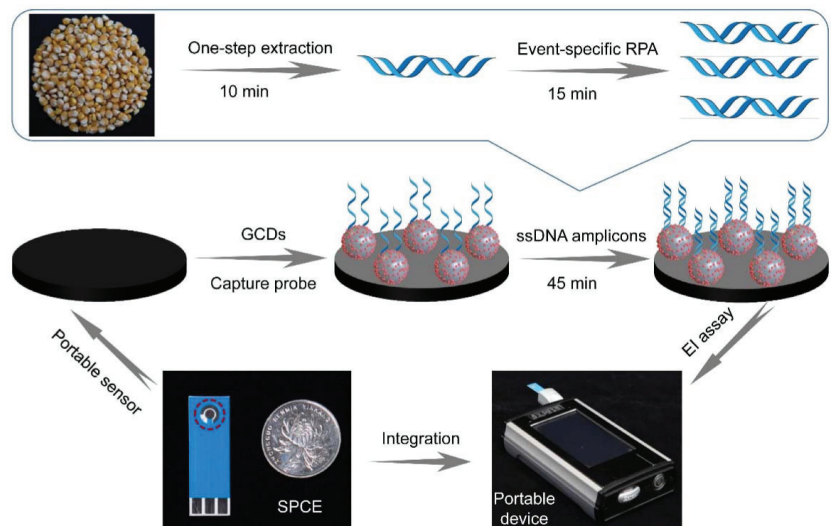


Figure 17. Fabrication process of EI gene sensor based on GCD (Reprinted with permission from Ref. [73]. 2022, Cui et al.).

5. Summary and Outlook

As food imports and consumption continue to grow in all regions of the world, there is an increasing need for rapid and accurate testing of potentially contaminated foods. Electrochemical biosensors offer a platform to address this challenge due to their rapid testing, portability, and low cost. This article provides a detailed review of electrochemical biosensors for the detection of biological food contaminants, chemical food contaminants, and genetically modified crops.

Although these sensors have shown excellent performance, further research is needed. Not only do researchers need to simplify sample preparation, but also need to enable sensors to detect target analytes in samples at very low concentrations. Research shows that the inclusion of nanomaterials on the electrode surface increases the conductivity and surface area of the electrode, loading more antibodies and markers and improving the electrocatalytic performance of the sensor. In another case, adding nitrogen binding sites or doping nitrogen on the electrode surface can improve the electrical signal and improve the sensitivity of the sensor. Furthermore, real-time monitoring needs to be done on-site. In the future, with the emergence of new nanomaterials, microfluidics, and molecular biology techniques, more new electrochemical biosensors will be designed with higher detection performance to ensure food safety.

Author Contributions: Methodology, formal analysis, investigation, data curation, writing—original draft, K.W., M.Z. and Y.L.; conceptualization, validation, writing—review and editing, supervision, project administration, funding acquisition, X.L. and J.W.; resources, writing—original draft, C.L. and J.W. All authors have read and agreed to the published version of the manuscript.

Funding: This research was funded by the National foreign expert project (grant number G2022165024L), Natural Science Foundation of Chongqing, China (grant number CSTB2022NSCQ-MSX0560), Graduate Research and Innovation Foundation of Chongqing, China (grant number CYS22108), Venture & Innovation Support Program for Chongqing Overseas Returnees and Fundamental Research Funds for the Central Universities (grant number 10611CDJXZ238826).

Institutional Review Board Statement: Not applicable.

Informed Consent Statement: Not applicable.

Data Availability Statement: Not applicable.

Conflicts of Interest: The authors declare no conflict of interest. The funders had no role in the design of the study; in the collection, analyses, or interpretation of data; in the writing of the manuscript; or in the decision to publish the results.

References

1. Fukuda, K. Food safety in a globalized world. *Bull. World Health Organ.* **2015**, *93*, 212. [[CrossRef](#)]
2. World Health Organization. *Food Safety*; WHO: Geneva, Switzerland, 2022.
3. Jia, M.; Zhongbo, E.; Zhai, F.; Bing, X. Rapid Multi-Residue Detection Methods for Pesticides and Veterinary Drugs. *Molecules* **2020**, *25*, 3590. [[CrossRef](#)]
4. Pang, G. Sequence “Food safety testing” album. *J. Mass Spectrom.* **2019**, *40*, 3–4.
5. Lv, M.; Liu, Y.; Geng, J.H.; Kou, X.H.; Xin, Z.H.; Yang, D.Y. Engineering nanomaterials-based biosensors for food safety detection. *Biosens. Bioelectron.* **2018**, *106*, 122–128. [[CrossRef](#)]
6. Düzgün, A.; Zelada-Guillén, G.A.; Crespo, G.A.; Macho, S.; Riu, J.; Rius, F.X. Nanostructured materials in potentiometry. *Anal. Bioanal. Chem.* **2011**, *399*, 171–181. [[CrossRef](#)]
7. Pajkossy, T. Voltammetry coupled with impedance spectroscopy. *J. Solid State Electrochem.* **2020**, *24*, 2157–2159. [[CrossRef](#)]
8. Mirceski, V.; Skrzypek, S.; Stojanov, L. Square-wave voltammetry. *ChemTexts* **2018**, *4*, 17. [[CrossRef](#)]
9. Ortuño, J.A.; Serna, C.; Molina, A.; Gil, A. Differential Pulse Voltammetry and Additive Differential Pulse Voltammetry with Solvent Polymeric Membrane Ion Sensors. *Anal. Chem.* **2006**, *78*, 8129–8133. [[CrossRef](#)] [[PubMed](#)]
10. Ortiz, D. Biological Contamination of Grains in Transportation—Farm to Fork. *Cereal Foods World.* **2020**, *65*, 1.
11. Ferrari, A.G.M.; Crapnell, R.D.; Banks, C.E. Electroanalytical Overview: Electrochemical Sensing Platforms for Food and Drink Safety. *Biosensors* **2021**, *11*, 291. [[CrossRef](#)] [[PubMed](#)]
12. Saravanan, A.; Kumar, P.S.; Hemavathy, R.V.; Jeevanantham; Kamalesh, R.; Sneha, S.; Yaashikaa, P.R. Methods of detection of food borne pathogens: A review. *Environ. Chem. Lett.* **2021**, *19*, 189–207. [[CrossRef](#)]

13. Melo, A.M.A.; Alexandre, D.L.; Furtado, R.F.; Borges, M.F.; Figueiredo, E.A.T.; Biswas, A.; Cheng, H.N.; Alves, C.R. Electrochemical immunosensors for Salmonella detection in food. *Appl. Microbiol. Biotechnol.* **2016**, *100*, 5301–5312. [[CrossRef](#)] [[PubMed](#)]
14. Li, J.; Jiang, J.; Su, Y.; Liang, Y.; Zhang, C. A novel cloth-based supersandwich electrochemical aptasensor for direct, sensitive detection of pathogens. *Anal. Chim. Acta* **2021**, *1188*, 339176. [[CrossRef](#)] [[PubMed](#)]
15. Yu, H.; Yuan, N.; Zhang, Y.; Guo, W.; Lu, X.; Yang, Q.; Zhang, W. Saltatory Rolling Circle Amplification-Based Ratiometric Electrochemical Biosensor for Rapid Detection of Salmonella enterica serovar Typhimurium in Food. *Food Anal. Methods* **2022**, *15*, 820–832. [[CrossRef](#)]
16. YHuang, i.; Su, Z.; Li, W.; Ren, J. Recent Progresses on Biosensors for Escherichia coli Detection. *Food Anal. Methods* **2022**, *15*, 338–366.
17. Couto, R.A.S.; Chen, L.; Kuss, S.; Compton, R.G. Detection of Escherichia coli bacteria by impact electrochemistry. *Analyst* **2018**, *143*, 4840. [[CrossRef](#)]
18. Raj, P.; Oh, M.H.; Han, K.; Lee, T.Y. Label-Free Electrochemical Biosensor Based on Au@MoS₂-PANI for Escherichia coli Detection. *Chemosensors* **2021**, *9*, 49. [[CrossRef](#)]
19. El-Moghazy, A.Y.; Wisuthiphaet, N.; Yang, X.; Sun, G.; Nitin, N. Electrochemical biosensor based on genetically engineered bacteriophage T7 for rapid detection of *Escherichia coli* on fresh produce. *Food Control* **2022**, *135*, 108811. [[CrossRef](#)]
20. Blot, M.; Disson, O.; Leclercq, A.; Moura, A.; Bracq-Dieye, H.; Thouvenot, P.; Valès, G.; Burrone, B.; Lupo, A.; Lecuit, M. Listeria-Associated Lymphadenitis: A Series of 11 Consecutive Cases and Review of the Literature. *Open Forum Infect. Dis.* **2022**, *9*, ofab598. [[CrossRef](#)]
21. Liu, R.; Zhang, Y.; Ali, S.; Haruna, S.A.; He, P.; Li, H.; Ouyang, Q.; Chen, Q. Development of a fluorescence aptasensor for rapid and sensitive detection of *Listeria monocytogenes* in food. *Food Control* **2021**, *122*, 107808. [[CrossRef](#)]
22. Qia, X.; Wang, Z.; Luc, R.; Liua, J.; Lia, Y.; Chen, Y. One-step and DNA amplification-free detection of *Listeria monocytogenes* in ham samples: Combining magnetic relaxation switching and DNA hybridization reaction. *Food Chem.* **2021**, *338*, 127837. [[CrossRef](#)] [[PubMed](#)]
23. Zhao, X.; Lin, C.; Wang, J.; Oh, D.H. Advances in Rapid Detection Methods for Foodborne Pathogens. *J. Microbiol. Biotechnol.* **2014**, *24*, 297–312. [[CrossRef](#)] [[PubMed](#)]
24. Jampasa, S.; Ngamrojanavanich, N.; Rengpipat, S.; Chailapakul, O.; Kalcher, K.; Chaiyo, S. Ultrasensitive electrochemiluminescence sensor based on nitrogen-decorated carbon dots for *Listeria monocytogenes* determination using a screen-printed carbon electrode. *Biosens. Bioelectron.* **2021**, *188*, 113323. [[CrossRef](#)]
25. Mishra, A.; Pilloton, R.; Jain, S.; Roy, S.; Khanuja, M.; Mathur, A.; Narang, J. Paper-Based Electrodes Conjugated with Tungsten Disulfide Nanostructure and Aptamer for Impedimetric Detection of *Listeria monocytogenes*. *Biosensors* **2022**, *12*, 88. [[CrossRef](#)] [[PubMed](#)]
26. Kahyaoglu, L.N.; Irudayaraj, J. New approaches in microbial pathogen detection. *Adv. Microb. Food Saf.* **2013**, *78*, 202–226.
27. Yee, M.Y.; Shamsuddin, S.; Nizam, Q.N.H.; Sidik, M.R.; Yusop, F.F.M.; Saeid, F.H.M.; Aziah, I. Detection methods of avian influenza—Current and novel approaches. *Malays. J. Microbiol.* **2019**, *15*, 492–504.
28. Lee, T.; Park, S.Y.; Jang, H.; Kim, G.; Lee, Y.; Park, C.; Mohammadniaei, M.; Lee, M.; Min, J. Fabrication of electrochemical biosensor consisted of multi-functional DNA structure/porous au nanoparticle for avian influenza virus (H5N1) in chicken serum. *Mater. Sci. Eng. C* **2019**, *99*, 511–519. [[CrossRef](#)]
29. Panigrahy, B.; Senne, D.A.; Pedersen, J.C.; Shafer, A.L.; Pearson, J.E. Susceptibility of pigeons to avian influenza. *Avian Dis.* **1996**, *40*, 600–604. [[CrossRef](#)]
30. MaManzano, r.; Viezzi, S.; Mazerat, S.; Marks, R.S.; Vidic, J. Rapid and label-free electrochemical DNA biosensor for detecting hepatitis A virus. *Biosens. Bioelectron.* **2018**, *100*, 89–95. [[CrossRef](#)]
31. Hwang, H.J.; Ryu, M.Y.; Park, C.Y.; Ahn, J.; Park, H.J.; Choi, C.; Ha, S.D.; Park, T.J.; Park, J.P. High sensitive and selective electrochemical biosensor: Label-free detection of human norovirus using affinity peptide as molecular binder. *Biosens. Bioelectron.* **2017**, *87*, 164–170. [[CrossRef](#)]
32. Jiang, H.; Sun, Z.; Zhang, C.; Weng, X. 3D-architected aptasensor for ultrasensitive electrochemical detection of norovirus based on phosphorene-gold nanocomposites. *Sens. Actuators B Chem.* **2022**, *354*, 131232. [[CrossRef](#)]
33. Dong, S.; Yan, J.; Zhou, S.; Zhou, Q. Mycotoxins Detection Based on Electrochemical Approaches. *Electroanalysis* **2022**, *34*, 132–147. [[CrossRef](#)]
34. Meng, D.; Gan, X.; Tian, T. An Electrochemical Sensing Method for Aflatoxin B1 Detection Based on Pt-coordinated Titanium-based Porphyrin. *MOF* **2022**, *17*, 220247. [[CrossRef](#)]
35. Wang, N.; Liu, Q.; Hu, X.; Wang, F.; Hu, M.; Yu, Q.; Zhang, G. Electrochemical immunosensor based on AuNPs/Zn/Ni-ZIF-8-800@graphene for rapid detection of aflatoxin B1 in peanut oil. *Anal. Biochem.* **2022**, *650*, 114710. [[CrossRef](#)]
36. Mazaafrianto, D.N.; Ishida, A.; Maeki, M.; Tani, H.; Tokeshi, M. An Electrochemical Sensor Based on Structure Switching of Dithiol-modified Aptamer for Simple Detection of Ochratoxin A. *Anal. Sci.* **2019**, *35*, 1221–1226. [[CrossRef](#)]
37. Ji, Y.M.; Zhang, K.H.; Pan, Z.N.; Ju, J.Q.; Zhang, H.L.; Liu, J.C.; Wang, Y.; Sun, S.C. High-dose zearalenone exposure disturbs G2/M transition during mouse oocyte maturation. *Reprod. Toxicol.* **2022**, *110*, 172–179. [[CrossRef](#)]
38. Radi, A.E.; Eissa, A.; Wahdan, T. Voltammetric behavior of mycotoxin zearalenone at a single walled carbon nanotube screen-printed electrode. *Anal. Methods* **2019**, *11*, 4494–4500. [[CrossRef](#)]

39. Curulli, A. Recent Advances in Electrochemical Sensing Strategies for Food. *Biosensors* **2022**, *12*, 503. [[CrossRef](#)]
40. Sundhoro, M.; Agnihotra, S.R.; Khan, N.D.; Barnes, A.; BelBruno, J.; Mendecki, L. Rapid and accurate electrochemical sensor for food allergen detection in complex foods. *Sci. Rep.* **2021**, *11*, 20831. [[CrossRef](#)]
41. Sundhoro, M.; Agnihotra, S.R.; Amberger, B.; Augustus, K.; Khan, N.D.; Barnes, A.; BelBruno, J.; Mendecki, L. An electrochemical molecularly imprinted polymer sensor for rapid and selective food allergen detection. *Food Chem.* **2021**, *344*, 128648. [[CrossRef](#)]
42. Freitas, M.; Neves, M.M.P.S.; Nouws, H.P.A.; Delerue-Matos, C. Electrochemical Immunosensor for the Simultaneous Determination of Two Main Peanut Allergenic Proteins (Ara h 1 and Ara h 6) in Food Matrices. *Foods* **2021**, *10*, 1718. [[CrossRef](#)] [[PubMed](#)]
43. Li, Y.; Su, R.; Li, H.; Guo, J.; Hildebrandt, N.; Sun, C. Fluorescent Aptasensors: Design Strategies and Applications in Analyzing Chemical Contamination of Food. *Anal. Chem.* **2022**, *94*, 193–224. [[CrossRef](#)] [[PubMed](#)]
44. Hu, H.; Yang, L. Development of enzymatic electrochemical biosensors for organophosphorus pesticide detection. *J. Environ. Sci. Health Part B* **2021**, *56*, 168–180. [[CrossRef](#)] [[PubMed](#)]
45. Maltzman, S.L.; Minter, S.D. Mitochondrial-based voltammetric sensor for pesticides. *Anal. Methods* **2012**, *4*, 1202. [[CrossRef](#)]
46. Nevin, T.; Selcan, K.; Cihat, T.; Gülsen, B. Highly sensitive and selective rGO based Non-Enzymatic electrochemical sensor for propamocarb fungicide pesticide detection. *Food Chem.* **2022**, *372*, 131267.
47. Ma, Y.; Jiang, H.; Shen, C.; Hou, C.; Huo, D.; Wu, H.; Yang, M. Detection of Carbendazim Residues with a Colorimetric Sensor Based on Gold Nanoparticles. *J. Appl. Spectrosc.* **2017**, *84*, 460–465. [[CrossRef](#)]
48. Liu, R.; Li, B.; Li, F.; Dubovyk, V.; Chang, Y.; Li, D.; Ding, K.; Ran, Q.; Wang, G.; Zhao, H. A novel electrochemical sensor based on β -cyclodextrin functionalized carbon nanosheets@carbon nanotubes for sensitive detection of bactericide carbendazim in apple juice. *Food Chem.* **2022**, *384*, 132573. [[CrossRef](#)]
49. Yang, J.; Qi, L.; Uqaili, J.A.; Shi, D.; Yin, L.; Liu, Z.; Tao, X.; Dai, L.; Lan, C. The terahertz metamaterial sensor for imidacloprid detection. *Int. J. RF Microw. Comput. Aided Eng.* **2021**, *31*, e22840. [[CrossRef](#)]
50. Tang, F.; Hua, Q.; Wang, X.; Luan, F.; Wang, L.; Li, Y.; Zhuang, X.; Tian, C. A novel electrochemiluminescence sensor based on a molecular imprinting technique and UCNPs@ZIF-8 nanocomposites for sensitive determination of imidacloprid. *Analyst* **2022**, *147*, 3917. [[CrossRef](#)]
51. Pham, D.S.; Nguyen, X.A.; Marsh, P.; Chu, S.S.; Lau, M.P.H.; Nguyen, A.H.; Cao, H. A Fluidics-Based Biosensor to Detect and Characterize Inhibition Patterns of Organophosphate to Acetylcholinesterase in Food Materials. *Micromachines* **2021**, *12*, 397. [[CrossRef](#)]
52. Surucu, O. Trace determination of heavy metals and electrochemical removal of lead from drinking water. *Chem. Pap.* **2021**, *75*, 4227–4238. [[CrossRef](#)]
53. Chailapakul, O.; Korsrisakul, S.; Siangproh, W.; Grudpan, K. Fast and simultaneous detection of heavy metals using a simple and reliable microchip-electrochemistry route: An alternative approach to food analysis. *Talanta* **2008**, *74*, 683–689. [[CrossRef](#)] [[PubMed](#)]
54. Lahrich, S.; el Mhammedi, M.A. Review—Application of Deficient Apatites Materials in Electrochemical Detection of Heavy Metals: Case of Mercury (II) in Seawater and Fish Samples. *J. Electrochem. Soc.* **2019**, *166*, B1567–B1576. [[CrossRef](#)]
55. Wisarut, K.; Pichanan, D.; Kriangsak, S.; Nuanlaorr, R.; Nunticha, L.; Piyada, J.; Thitirat, M.; Weena, S. An application of miniaturized electrochemical sensing for determination of arsenic in herbal medicines. *Methods* **2022**, *14*, 3087.
56. Narouei, F.H.; Livernois, L.; Andreescu, D.; Andreescu, S. Highly sensitive mercury detection using electroactive gold-decorated polymer nanofibers. *Sens. Actuators B Chem.* **2021**, *329*, 129267. [[CrossRef](#)]
57. Yuan, M.; Qian, S.; Cao, H.; Yu, J.; Ye, T.; Wu, X.; Chen, L.; Xu, F. An ultra-sensitive electrochemical aptasensor for simultaneous quantitative detection of Pb^{2+} and Cd^{2+} in fruit and vegetable. *Food Chem.* **2022**, *382*, 132173. [[CrossRef](#)]
58. Tan, Z.; Wu, W.; Feng, C.; Wu, H.; Zhang, Z. Simultaneous determination of heavy metals by an electrochemical method based on a nanocomposite consisting of fluorinated graphene and gold nanocage. *Microchim. Acta* **2020**, *187*, 414. [[CrossRef](#)]
59. Wu, L.; Zhang, C.; Long, Y.; Chen, Q.; Zhang, W.; Liu, G. Food additives: From functions to analytical Methods. *Crit. Rev. Food Sci. Nutr.* **2021**, *61*, 1–21. [[CrossRef](#)]
60. Zhang, J.; Hu, S.; Du, Y.; Cao, D.; Wang, G.R.; Yuan, Z.Q. Improved food additive analysis by ever-increasing nanotechnology. *J. Food Drug Anal.* **2020**, *28*, 622–640. [[CrossRef](#)]
61. Rao, H.; Chen, M.; Ge, H.; Lu, Z.; Liu, X.; Zou, P.; Wang, X.; He, H.; Zeng, X.; Wang, Y. A novel electrochemical sensor based on Au@PANI composites film modified glassy carbon electrode binding molecular imprinting technique for the determination of melamine. *Biosens. Bioelectron.* **2017**, *87*, 1029–1035. [[CrossRef](#)]
62. Rahmana, M.M.; Ahmed, J. Cd-doped Sb_2O_4 nanostructures modified glassy carbon electrode for efficient detection of melamine by electrochemical approach. *Biosens. Bioelectron.* **2018**, *102*, 631–636. [[CrossRef](#)] [[PubMed](#)]
63. An, Q.; Feng, X.; Zhou, Z.; Zhan, T.; Lian, S.; Zhu, J.; Han, G.; Chen, Z.; Kraatz, H. One step construction of an electrochemical sensor for melamine detection in milk towards an integrated portable system. *Food Chem.* **2022**, *383*, 132403. [[CrossRef](#)] [[PubMed](#)]
64. Ensafi, A.A.; Rezaei, B.; Amini, M.; Heydari-Bafrooei, E. A novel sensitive DNA-biosensor for detection of a carcinogen, Sudan II, using electrochemically treated pencil graphite electrode by voltammetric methods. *Talanta* **2012**, *88*, 244–251. [[CrossRef](#)] [[PubMed](#)]
65. Yang, L.; Wang, S.; Zhang, L. Electrochemical Sensor Based on MWCNTs/AuNPs/GCE for Sensitive Determination of Sudan I Content in Food Samples. *ESG* **2020**, *15*, 11168–11179. [[CrossRef](#)]

66. Heydari, M.; Ghoreishi, S.M.; Khoobi, A. Novel electrochemical procedure for sensitive determination of Sudan II based on nanostructured modified electrode and multivariate optimization. *Measurement* **2019**, *142*, 105–112. [[CrossRef](#)]
67. Shi, Z.; Tian, Y.; Wu, X.; Li, C.; Yu, L. A one-piece lateral flow impedimetric test strip for label-free clenbuterol detection. *Anal. Methods* **2015**, *7*, 4957. [[CrossRef](#)]
68. Sun, Y.; Wang, T.; Chen, S.; Wang, X.; Reynoso, L.C. Highly Sensitive Electrochemical Sensor Based on rGO/Fe₃O₄ Composite as Electrocatalyst for Clenbuterol Detection in Doping Analysis. *Int. J. Electrochem. Sci.* **2022**, *17*, 220128. [[CrossRef](#)]
69. Jing, H.; Ouyang, H.; Li, W.; Long, Y. Molten salt synthesis of BCNO nanosheets for the electrochemical detection of clenbuterol. *Microchem. J.* **2022**, *178*, 107359. [[CrossRef](#)]
70. Zheng, Y.; Karimi-Maleh, H.; Fu, L. Advances in Electrochemical Techniques for the Detection and Analysis of Genetically Modified Organisms: An Analysis Based on Bibliometrics. *Chemosensors* **2022**, *10*, 194. [[CrossRef](#)]
71. Farias, M.E.; Correa, N.M.; Sosa, L.; Niebylski, A.M.; Molina, P.G. A simple electrochemical immunosensor for sensitive detection of transgenic soybean protein CP4-EPSPS in seeds. *Talanta* **2022**, *237*, 122910. [[CrossRef](#)]
72. Gao, H.; Cui, D.; Zhai, S.; Yang, Y.; Wu, Y.; Yan, X.; Gang, W. A label-free electrochemical impedimetric DNA biosensor for genetically modified soybean detection based on gold carbon dots. *Microchim. Acta* **2022**, *189*, 216. [[CrossRef](#)] [[PubMed](#)]
73. Cui, D.; Zhai, S.; Yang, Y.; Wu, Y.; Li, J.; Yan, X.; Shen, P.; Gao, H.; Wu, G. A Label-Free Electrochemical Impedance Genosensor Coupled with Recombinase Polymerase Amplification for Genetically Modified Maize Detection. *Agriculture* **2022**, *12*, 454. [[CrossRef](#)]



Article

Multifunctional Smart ZnSe-Nanostructure-Based Fluorescent Aptasensor for the Detection of Ochratoxin A

Muhammad Azhar Hayat Nawaz^{1,2,3}, Muhammad Waseem Fazal³, Naeem Akhtar⁴, Mian Hasnain Nawaz³, Akhtar Hayat^{3,*} and Cong Yu^{1,2,*}

¹ State Key Laboratory of Electroanalytical Chemistry, Changchun Institute of Applied Chemistry, Chinese Academy of Sciences, Changchun 130022, China

² University of Science and Technology of China, Hefei 230026, China

³ Interdisciplinary Research Centre in Biomedical Materials (IRCBM), COMSATS University Islamabad, Lahore Campus, Lahore 54000, Pakistan

⁴ Institute of Chemical Sciences, Bahauddin Zakariya University (BZU), Multan 60800, Pakistan

* Correspondence: akhtarhayat@cuilahore.edu.pk (A.H.); congyu@ciac.ac.cn (C.Y.)

Abstract: Herein, we present a comprehensive investigation of rationally designed zinc selenide (ZnSe) nanostructures to achieve highly negatively charged ZnSe nanostructures. A Microwave-assisted hydrothermal synthesis method was used to synthesize three types of ZnSe nanostructures, i.e., nanorods, μ -spheres and nanoclusters, as characterized by a zeta potential analyzer, X-ray diffraction (XRD), scanning electron microscopy (SEM), Raman spectroscopy and BET, which were labeled as type A, B and C. Three different solvents were used for the synthesis of type A, B and C ZnSe nanostructures, keeping other synthesis conditions such as temperature, pressure and precursors ratio constant. Based on two heating time intervals, 6 and 9 h, types A, B and C were further divided into types A6, A9, B6, B9, C6 and C9. ZnSe nanostructures were further evaluated based on their fluorescent quenching efficiency. The maximum fluorescence quenching effect was exhibited by the ZnSe-B6 type, which can be attributed to its highly negative surface charge that favored its strong interaction with cationic dye Rhodamine B (Rh-B). Further, the optimized ZnSe-B6 was used to fabricate an aptasensor for the detection of a food-based toxin, ochratoxin-A (OTA). The developed aptasensor exhibited a limit of detection of 0.07 ng/L with a wide linear range of 0.1 to 200 ng/L.

Keywords: Förster resonance energy transfer; ZnSe nanostructures; ochratoxin A; aptamer; zeta potential; fluorescence detection

Citation: Nawaz, M.A.H.; Fazal, M.W.; Akhtar, N.; Nawaz, M.H.; Hayat, A.; Yu, C. Multifunctional Smart ZnSe-Nanostructure-Based Fluorescent Aptasensor for the Detection of Ochratoxin A. *Biosensors* **2022**, *12*, 844. <https://doi.org/10.3390/bios12100844>

Received: 6 September 2022
Accepted: 30 September 2022
Published: 8 October 2022



Copyright: © 2022 by the authors. Licensee MDPI, Basel, Switzerland. This article is an open access article distributed under the terms and conditions of the Creative Commons Attribution (CC BY) license (<https://creativecommons.org/licenses/by/4.0/>).

1. Introduction

The development of biosensing devices that can monitor environmental and dietary hazards has grabbed much attention in recent years [1,2]. In particular, fluorescent biosensors based on bio-conjugated nanomaterials and involving a Förster resonance energy transfer (FRET) mechanism have great advantages in term of sensitivity and simple operating procedures [3]. The choice of materials used to develop fluorescent biosensors is very crucial because surface charge, electron transport behavior and structural and optical properties decide the ability of materials to perform selective, sensitive and reliable detection [3]. Thus, there is a dire need of such materials in which controlling their synthesis parameters can induce different properties and functionalities such as surface charge and morphology. Recently, diverse types of nanomaterials such as carbon nanotubes, 2D nanomaterials, gold nanoparticles and quantum dots have been explored and investigated as potential fluorescent quenchers for the development of fluorescent biosensors [4].

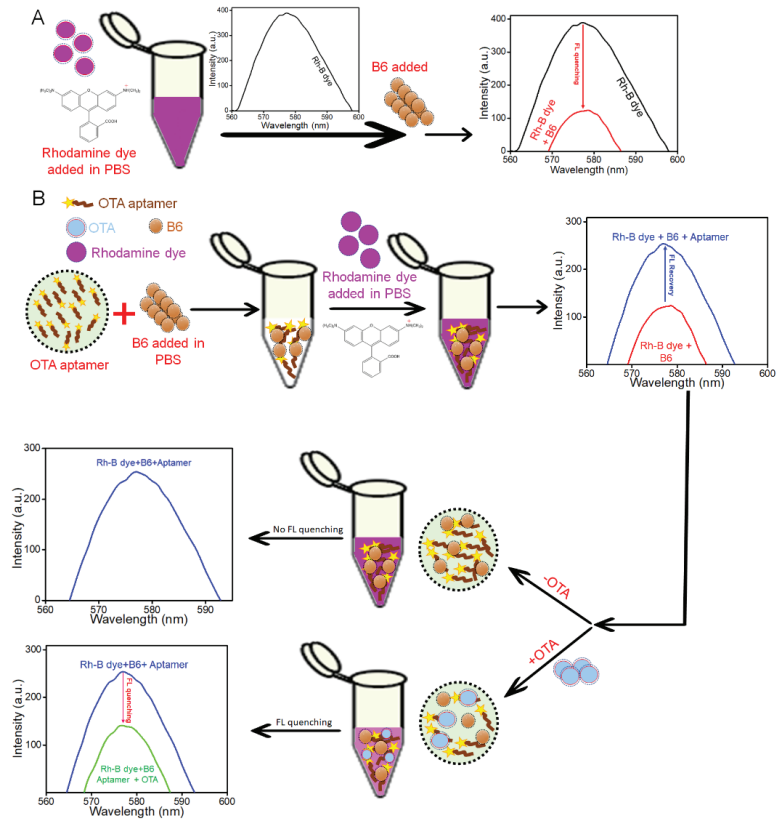
Zn-based II–VI nanostructures such as zinc selenide (ZnSe) exhibit wide direct bandgap (2.67 eV) along with high exciton binding energy (21 meV); thus, ZnSe has been considered as an excellent choice for optoelectronic devices [5–7]. In recent times, researchers working in the domain of nanostructured materials have reported a number of different

dimensional ZnSe nanostructures including nanorods, nanoplates, nanoneedles, nanobelts, nanoparticles and nanowires [8–14]. Diverse approaches have been applied for the synthesis of ZnSe nanostructures, such as microwave irradiation, hydrothermal, chemical vapor deposition and solvothermal [15–18]. Among these, the microwave-assisted synthesis technique has several advantages such as fast and uniform heating, higher product yield and short reaction time, low energy requirement, less expensive, high purity and small narrow particle size distribution as compared to other techniques [19]. As the fluorescent sensing performance is directly linked to surface charge, size, dispersity and morphology of nanostructures materials, thus the synthesis of ZnSe nanostructures with controlled surface charges, morphology, and physicochemical properties has great potential for biosensing applications [20–23].

Here, we show that by varying the synthesis reaction time and changing precursors, ZnSe nanostructures with different morphology, size, surface charge and physicochemical properties can be designed for fluorescent detection applications. The microwave-assisted synthesis route was used to synthesize three types of ZnSe nanostructures by changing their precursors and reaction time (6 and 9 h) at fixed temperatures. Based on synthesis conditions, three different shapes including spherical, rods and cluster-like morphologies were formed. XRD results of synthesized ZnSe nanostructures revealed through Williamson–Hall equations that nanostructures contain strains. It is well-established that due to the strain, defects are produced, which strongly influence the intrinsic properties [24] of synthesized ZnSe, resulting in improvements to their dispersion [25]. At the same time, defects induce negative charge; thus, the surface of the ZnSe nanostructures exhibited highly negative surface charges, which were confirmed by measuring their zeta potentials [26]. This highly negative surface charge made the synthesized ZnSe nanostructures highly stable and dispersive [27,28]. With the increase in size, the negative surface charge also increased, which may be ascribed to a larger steric hindrance [29]. The highly negative surface charges of ZnSe nanostructures were further exploited to interact with Rh-B a cationic dye and their behavior as nanoquencher was confirmed. Ochratoxin A (OTA) is a mycotoxin classified as a (Group-2B) carcinogen by the International Agency for Research on Cancer (IARC). OTA released in the form of *Aspergillus* and *Penicillium* results in the contamination of foods such cereals, fruit juices, beans, wine, corn, wheat and barley [30]. The European Commission has released guidelines about the permissible content of OTA, which is 5 µg/kg and 10 µg/kg in raw grains and soluble coffee and 2 µg/kg in grape juice or wine [31].

ZnSe nanostructures were exploited as nanoquencher to develop the fluorescent aptasensor for the detection of OTA. The quenching response of type ZnSe-B6 on the emission spectrum of Rh-B dye in the presence of an OTA aptamer was evaluated with and without an OTA target. Pure Rh-B exhibited a sharp fluorescence peak, which significantly reduced after the addition of ZnSe-B6 nanoquencher, which primarily can be attributed to an FRET mechanism based on the strong binding interaction between cationic Rh-B dye and the highly negatively charged surface of ZnSe-B6 [32,33]. Scheme 1B shows step by step details of the fabrication of a ZnSe-nanostructure-based fluorescent aptasensor for the detection of OTA. Firstly, exploiting very high negative surface charge of ZnSe-B6 and positive charge of amino modified OTA aptamer, the ZnSe-B6–aptamer complex was formed. Afterwards, when Rh-B dye was introduced to the ZnSe-B6–aptamer complex, fewer ZnSe-B6 particles were available to quench the fluorescence of the Rh-B dye, and thus a fluorescence recovery response was achieved. Finally, when target analyte (OTA) was introduced, it made specific interactions with the aptamer, which weakened aptamer and ZnSe-B6 interactions. The stronger conjugation between the amino-modified OTA aptamer and target analyte OTA resulted in ZnSe-B6 particles being released from the ZnSe-B6–aptamer complex, which quenched the fluorescence of the Rh-B dye, and thus fluorescence quenching recovered. There was a direct proportional relation between the fluorescence quenching percent and the concentration of OTA in the assay. In this work, based on synthesis reaction time and precursors, we have rationally designed ZnSe

nanostructures with highly negative surface charges and different morphologies and exploited these properties to develop an aptasensor for OTA detection.



Scheme 1. Schematic illustration of the fluorescence-quenching-based detection of OTA; quenching response of ZnSe-B6 on fluorescence emission spectra of Rh-B dye (A), quenching response of ZnSe-B6 on fluorescence emission spectra of Rh-B dye in the presence of OTA aptamer with and without OTA target (B).

2. Experimental

2.1. Synthesis of ZnSe Nanostructures

A microwave-assisted hydrothermal synthesis approach was used to synthesize three types of ZnSe nanostructures under control synthesis conditions by keeping temperature, pressure and precursors ratio constant by using three different solvents at two heating time intervals, including 6 and 9 h. Under controlled synthesis conditions, three different shapes, including spherical, rods and cluster-like morphologies, were obtained at two different time intervals. Brief detail about the synthesis of these morphologies is as follows.

2.1.1. Fabrication of ZnSe Nanorods

For the preparation of ZnSe nanorods, 1.6 mmol of zinc nitrate was mixed with 4 M KOH in 30 mL (water/ethanol) and kept heating at 80 °C in a microwave oven for 20 min. After that, 1.5 mmol of selenium tetrachloride in 20 mL hydrazine dihydrochloride was added drop wise into the previous solution and this reaction was kept for 6 and 9 h at 120 °C in a microwave-assisted oven to obtain two types of ZnSe, which were labeled as A6 and A9 respectively. The resultant precipitates of A6 and A9 were cooled down to room

temperature and then centrifuged and washed with water and ethanol, respectively. The obtained powder was next dried at vacuum in room temperature.

2.1.2. Fabrication of ZnSe μ -Spheres

Similarly, for the preparation of ZnSe μ -spheres, 1.6 mmol of zinc nitrate was mixed with 4 M KOH in 30 mL (water/ethanol) and kept heating at 80 °C in a microwave oven for 20 min. After that, 1.5 mmol of selenium tetrachloride in 20 mL ethylene glycol was added drop wise into the previous solution and this reaction was kept for 6 and 9 h at 120 °C in a microwave-assisted oven. The materials kept for 6 and 9 h were labeled as B6 and B9, respectively. The resultant precipitate was cooled down at room temperature and centrifuged and washed with water and ethanol and subjected to drying in a vacuum oven.

2.1.3. Fabrication of ZnSe Nanoclusters

Further, for the preparation of ZnSe nanoclusters, 1.6 mmol of zinc nitrate was mixed with 4 M KOH in 30 mL (water/ethanol) and kept under microwave in an oven for 20 min at 80 °C. In the next step, 1.5 mmol of selenium tetrachloride was prepared in 20 mL acetic acid and was added drop wise into the previous solution and this reaction was kept for 6 and 9 h at 120 °C in a microwave-assisted oven. After that, the solution was placed into a microwave oven for 6 and 9 h to obtain C6 and C9, respectively. The resultant precipitate was cooled down at room temperature and then centrifuged and washed with water and ethanol, respectively. The resultant precipitates were next dried in a vacuum oven.

2.2. ZnSe-Nanostructure-Based Fluorescence Quenching

Blank and fluorescence quenching measurements of organic fluorescence dye Rh-B were carried out without and with the addition of ZnSe nanoquenchers, respectively. First, a blank reagent fluorescence emission spectrum containing (160 ng/L) dye was measured. Afterwards, 1 μ L from each stock solution containing ZnSe nanostructures (A6, A9, B6, B9, C6, C9) were added into Rh-B (16 μ L) and a volume make up of 2000 μ L was achieved using PBS to get an end concentration of 450 μ g/L for ZnSe nanostructures. Subsequently, the mixture stayed for 10 min and then fluorescence quenching on the addition of all six ZnSe nanostructures was determined using 554 nm as the excitation wavelength while emission spectra were noted at 578 nm. The extent of fluorescence quenching was measured by calculating the difference between the mission spectra of the Rh-B and the maximum of emission induced by the ZnSe nanostructures. The maximum quenching was observed by the ZnSe nanostructure type B6, and thus used in the next experiments to develop the aptasensor for OTA detection. A 2000 μ L reaction volume with an optimum concentration of 450 μ g/L ZnSe was used for the experiments to detect OTA.

2.3. ZnSe-Nanostructure-Based Fluorescent Aptasensor for OTA Detection

The optimized amino-modified OTA aptamer (50 nM) was incubated with 1 μ L ZnSe type B6 (450 μ g/L) for 15 min. Afterwards, a total volume of 2000 μ L of the solution containing aptamer, ZnSe-B6 and dye Rh-B (160 ng/L) was made using PBS and further incubated for 10 min. Subsequently, the solution was subjected to fluorescence response and then ultimately varying concentrations of OTA (0.1–200 ng/L) were added. An optimized incubation time, i.e., 30 min, was used to incubate the OTA containing solution and then fluorescence measurements were taken at 554 nm for excitation and 578 nm for emission. The control experiment was also run, without the addition of OTA.

2.4. Interference and Real Sample Studies

The specificity of the developed OTA aptasensor was evaluated in the presence of the possible interfering analytes, i.e., ochratoxin-B, aflatoxin M1 and aflatoxin B1. The same concentration (100 ng/L) of each interfering species was employed to form an aptamer-interfering species complex using the same parameters as those applied for OTA detection. Further, a rice sample purchased from the local market of Lahore, Punjab and grinded in a

kitchen grinder machine was used to confirm the practical acceptability of the fabricated aptasensor. The rice extract was received following the already reported procedure [34]. Acetonitrile was used as an extracting solvent and one gram of grinded rice powder was introduced into a 10 mL solvent, and stirred for 15 min. Afterwards, a 15 min centrifugation of the mixture was carried out at 35,000 rpm, and then the received solid rice sample was dried under an inert atmosphere. For real sample validation, the rice extract and PBS (1:9 *v/v*), having a total volume of 1 mL, was firstly sonicated to get a well-mixed solution. Subsequently, 1 μ L of ZnSe-B6 (450 μ g/L), and for 50 nM end concentration, 20 μ L of amino-modified OTA aptamer, were used for the fabrication of an aptasensor. Percentages of quenching recoveries with OTA-spiked (5, 50 and 100) ng/L rice samples were determined, which presented excellent linear behavior with the increase of OTA concentration.

3. Results and Discussion

3.1. Morphological and Structural Characterization of ZnSe Nanostructures

The surface morphologies of the synthesized ZnSe nanostructures were characterized by scanning electron microscopy (SEM). SEM results showed the formation of ZnSe with different shapes and sizes. Briefly, Figure 1A and B shows the clear formation of nanorod shaped ZnSe with an average width of 200–260 and 150–210 nm, respectively. Similarly, Figure 1C and D clearly shows the successful formation of ZnSe μ -spheres with an average size of 2200–2400 and 1100–1500 nm, respectively. Further, Figure 1E and F shows the formation of ZnSe nanoclusters with an average size of 210–260 and 75–130 nm, respectively.

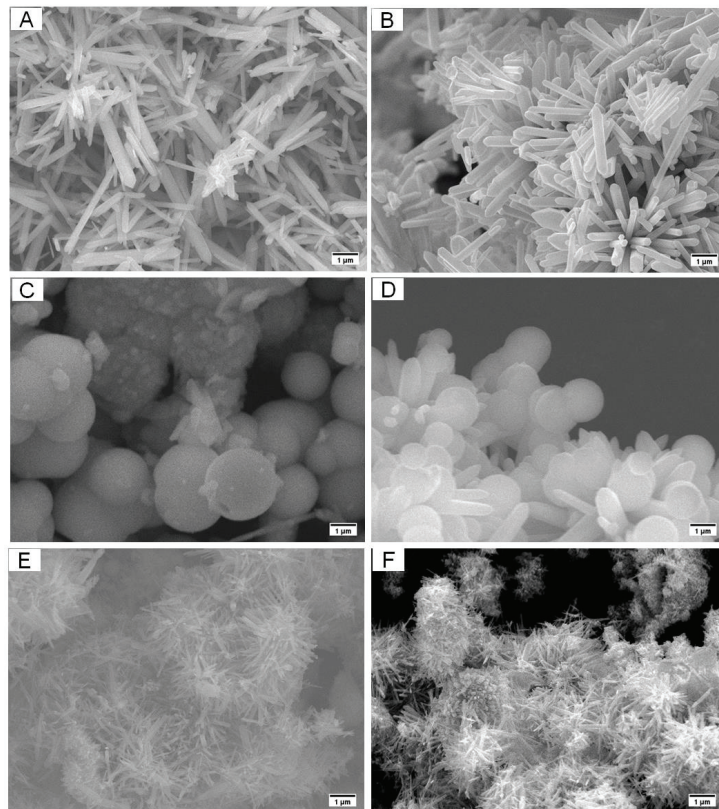


Figure 1. SEM images of ZnSe nanostructures: ZnSe nanorods (A,B), nanospheres (C,D) and nanoclusters (E,F).

The phase purity, crystallographic structure and crystal formation of zinc selenide was investigated via wide-angle XRD analysis within the range of 5–80° (Figure 2A).

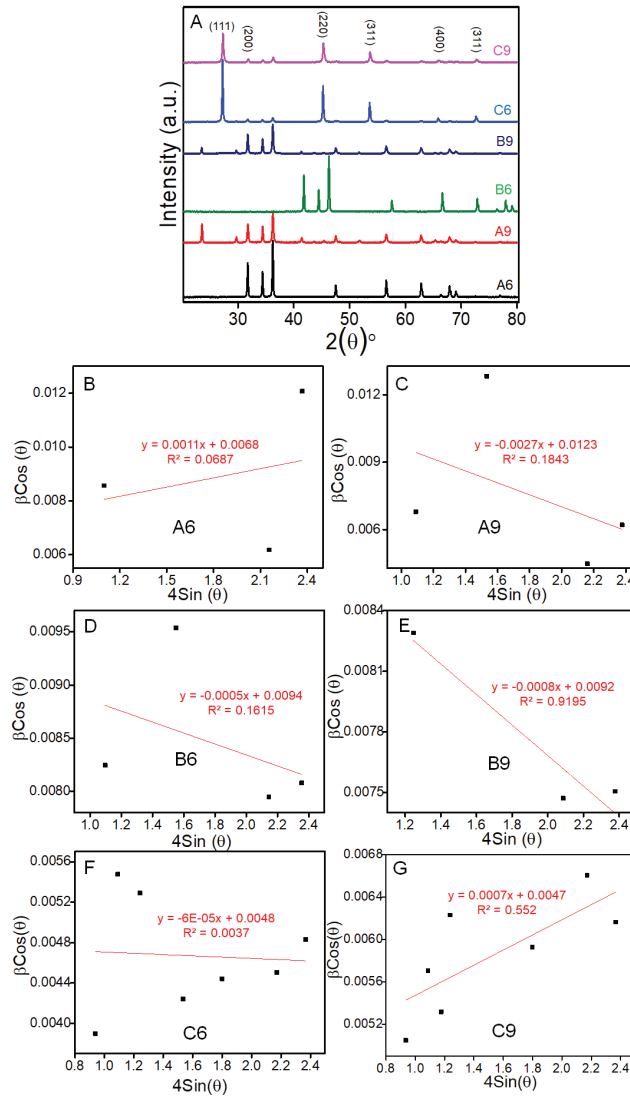


Figure 2. XRD Spectra representing formation of ZnSe nanostructures (A), and the crystallite size and strain of synthesized ZnSe calculated by using the W–H plot (B–G).

The XRD spectrum reflects a series of diffraction characteristic peaks centered at 2θ value of 26.99°, 31.55°, 44.55°, 53.45°, 65.78° and 72.48° corresponding to 111, 200, 220, 311, 400 and 331 crystal planes of face-centered cubic, respectively. These results clearly match with the Joint Committee on Powder Diffraction Standard (JCPDS No. 88-2345), thus confirming the formation of ZnSe.

Further, the average crystallite size and strain of synthesized ZnSe nanostructures were also calculated by using Scherrer (Supplementary Equation (S1)) and Williamson–Hall equations, respectively. The calculated average crystallite sizes of A6, A9, B6, B9, C6 and C9 were observed to be 16.69, 21.14, 16.48, 17.91, 30.05 and 23.91 nm, respectively

(Figure 2B–G and Supplementary Table S1). The micro strain was also calculated by using the Williamson–Hall equation. From the results, two types of micro strains were observed in which positive slopes of 1.1 and 0.7 for A6 and C9 showed a tensile strain, whereas negative slopes of -2.7 , -0.5 , -0.8 and -0.06 for A9, B6, B9 and C6 showed a compressive strain, respectively [34].

The bending, stretching, rotational and vibrational modes in the synthesized ZnSe nanoparticle were studied via Fourier transform infrared spectroscopy (FTIR). FTIR spectra of synthesized ZnSe showed the characteristic peaks at 482 , 561 , 651 , 671 and 970 cm^{-1} belonged to Zn–Se vibrations (Figure 3A). In addition, the characteristics peak at 3429 cm^{-1} and weak characteristics peak at 1595 cm^{-1} corresponded to O–H characteristic vibrations. In the case of C2 and C3, there was another sharp peak at 3199 cm^{-1} , which corresponded to the N–H stretching vibration band. Additionally, a slight shift of the N–H stretching vibration band toward the lower frequency could be attributed to the interaction of N_2H_4 with zinc ion and the regular periodic structure of the molecular precursor.

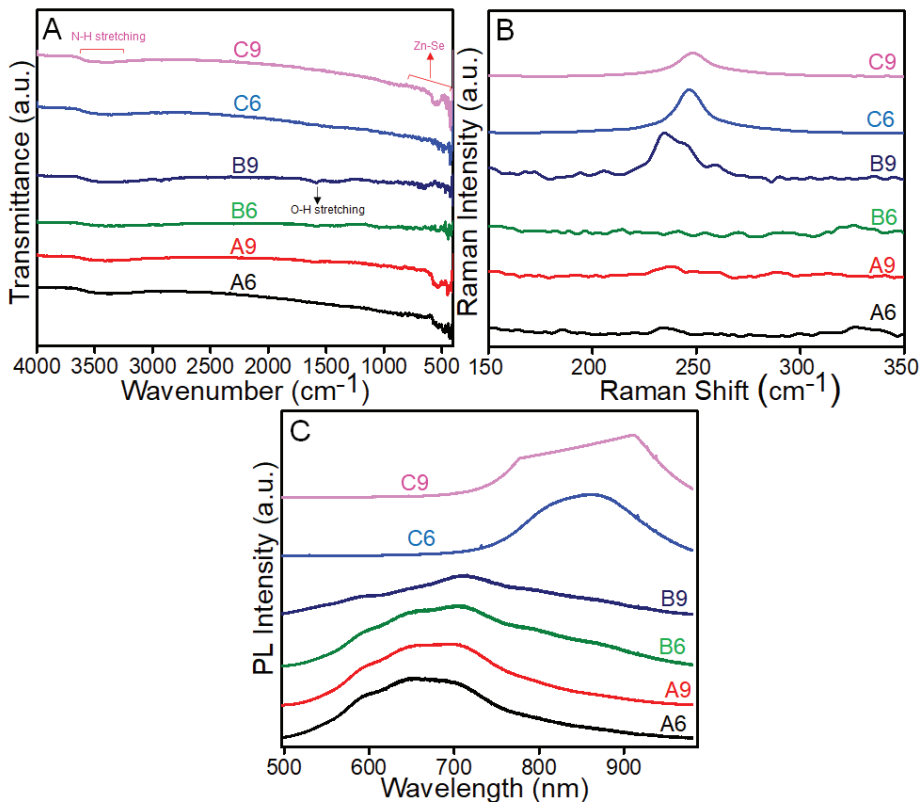


Figure 3. FTIR spectra of ZnSe nanostructures (A), Raman spectra (B) and PL spectra (C) of synthesized ZnSe nanostructures.

Furthermore, Raman (Figure 3B) and PL (Figure 3C) spectroscopy were also used to analyze the synthesized ZnSe nanostructures. Raman results showed the presence of TO (210 cm^{-1}) and LO (255 cm^{-1}) phonon frequencies for bulk ZnSe [35]. The transverse optic (TO) and longitudinal optic (LO) phonon modes of the crystalline ZnSe were responsible for the two Raman peaks with centers at 205 and 248 cm^{-1} , respectively. Results further showed that the synthesized ZnSe structures were of excellent crystalline quality and pure phase, as seen by the crisp and symmetrical Raman peaks. However, the TO and LO phonon

frequencies for ZnSe nanostructures were centered at 199 and 242 cm^{-1} , respectively, and both yielded a wide Raman peak as a result of the structures' high surface-to-volume ratio.

PL spectra of ZnSe nanostructures revealed a strong and wide emission band spanning 500–800 nm. The near-band-edge (NBE) emission of ZnSe is often responsible for the faint blue emission peak. Surface emissions and potential metal vacancies have been linked to the emission band between 520 and 780 nm in the case of A6, A9, B2 and B9. According to Geng et al. [36], certain donor–acceptor pairings connected to Zn vacancy and interstitial states, or linked to dislocation stacking faults and nonstoichiometric defects, are the reason behind the high emission at about 520 nm. Whereas, according to Zhang et al. [37], recombination of a donor–acceptor pair involving Zn vacancies and Zn interstitial was the cause of the emission. Thus, we believe that the high emission must be related to the interstitial Zn defect and nonstoichiometric defects since the products increased under Zn-rich conditions in the case of C6 and C9. Brunauer–Emmett–Teller (BET) has been used to characterize the surface area and porous texture of ZnSe. BET results showed specific surface areas of ZnSe of 0.004, 0.048, 0.016, 0.020, 0.016 and 0.014 m^2/g , corresponding to A6, A9, B6, B9, C6 and C9, respectively. The zeta potential of ZnSe nanostructures were also calculated to estimate the surface charge. All the ZnSe nanostructures exhibited higher values of negative zeta potential (Table 1). The negative zeta potential value for the synthesized ZnSe may be attributed to the dense electron of O around ZnSe. It can be seen in Table 1 that ZnSe-B6 (μ -sphere) had the highest negative zeta potential value, which makes ZnSe-B6 highly dispersive and stable.

Table 1. Zeta potential values of ZnSe nanostructures before and after the addition of Rh-B.

Sr. No.	Zeta (mV) ZnSe NP	Zeta (mV) ZnSe NP+ Rh-B
B6	−437	−229
B9	−95.2	−319
C6	−320	−284
C9	−409	−333
A6	−332	−366
A9	−379	−297

3.2. Morphological-Based Fluorescence Quenching of the ZnSe Nanostructures

Figure 4A shows the summary of fluorescence quenching behavior of ZnSe nanostructures (A6–C9) based on negative surface charge, size and morphology. The highest negative value of zeta potential exhibited by ZnSe-B6 (μ -sphere) showed a maximum %FL quenching signal because of extensive surface interaction with cationic dye Rh-B. Figure 4B shows comparative % fluorescence quenching behavior of all six ZnSe (A6–C9) nanostructures. Rh-B concentrations in the range of 10–250 ng/L were also optimized (Supplementary Materials, Figure S1) for the development of a ZnSe-nanostructure-based aptasensor. We further evaluated the effect of ZnSe-B6 concentration (Figure 5A) and found small difference of concentrations values greater than 450 $\mu\text{g}/\text{L}$, and thus opted for the development of an aptasensor. Next, sonication conditions and the incubation time were also employed to adjust the fluorescence measurements (Figure 5B,C). A 10 min sonication time and a 10 min incubation time were selected as optimized values for the next experiments.

3.3. Fabrication of the ZnSe-Based Aptasensor

To fabricate the ZnSe-nanostructure-based aptasensor, exploiting their quenching properties, the quenching response of selected ZnSe-B6 on fluorescence emission spectra of Rh-B dye in the presence of an OTA aptamer was evaluated with and without OTA target, as shown in Scheme 1.

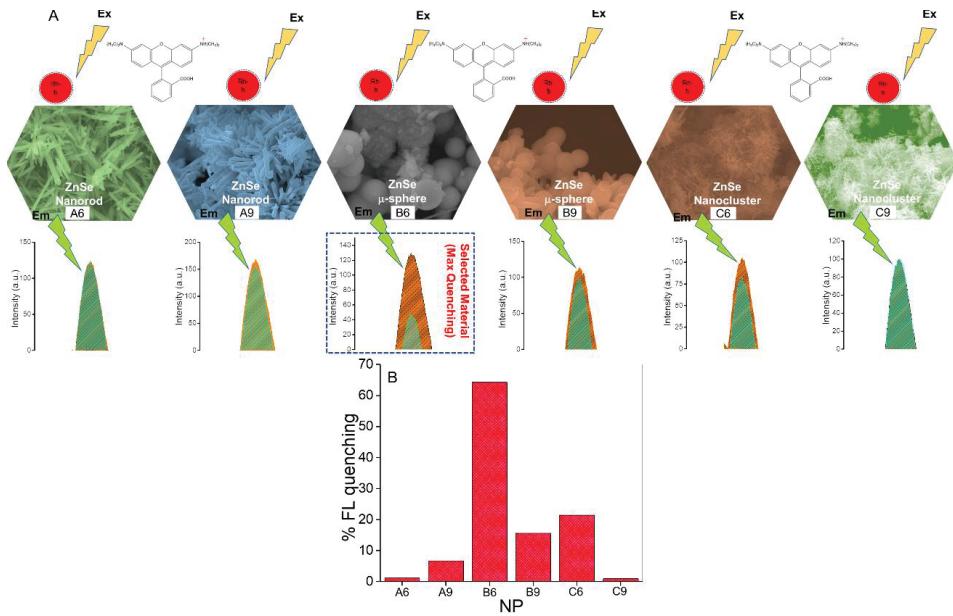


Figure 4. Summary of fluorescence quenching behavior of ZnSe nanostructures (A6–C9) (450 $\mu\text{g/L}$) based on structural morphology and negative surface charge (Rh-B: 160 ng/L) (A). % fluorescence quenching effect of ZnSe (A6, A9, B6, B9, C6, C9) (B).

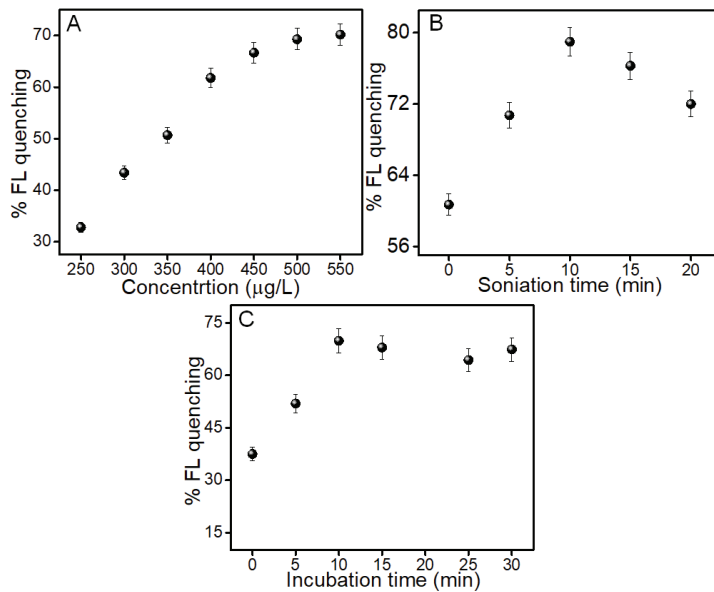


Figure 5. Effects of ZnSe-B6 concentrations (250–550 $\mu\text{g/L}$) (A), sonication time (B) and incubation (C) on the quenching (% FL) in the presence of Rh-B (160 ng/L).

As shown in Figure 6a, the pure dye solution (160 ng/L) presented a strong fluorescence maximum at 578 nm. On adding a ZnSe-B6 nanoquencher, an appreciable decrease in fluorescence response was found (Figure 6b), which is primarily can be attributed to Förster

resonance energy transfer (FRET), based on the strong binding interaction between cationic Rh-B dye and the highly negatively charged surface of ZnSe-B6 [32,33]. To develop the ZnSe-B6-based aptasensor, already optimized concentration, sonication time and incubation time values for the ZnSe-B6 were used. ZnSe-B6 (450 µg/L) and 50 nM amino-modified aptamer was chosen for the ZnSe-B6–aptamer complex formation. ZnSe-B6 exhibited very high negative surface charge while the amino-modified OTA aptamer contained a positive charge due to the attached amino group, which favored their surface interactions. The solution mixture was subjected to incubation for 15 min to enhance the surface interaction between ZnSe–aptamer conjugations.

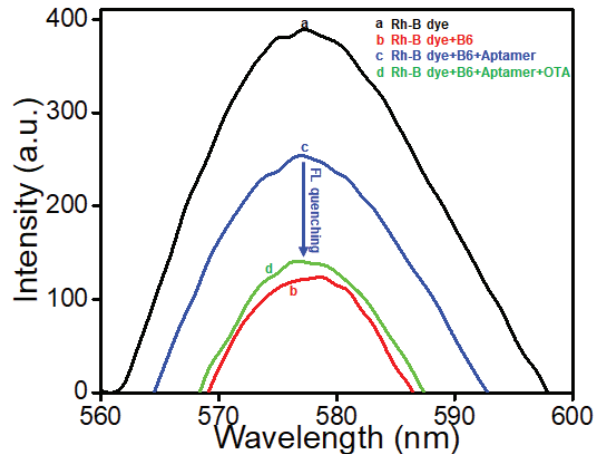


Figure 6. Fluorescence emission spectra of Rh-B (160 ng/L) (a); quenched fluorescence emission with ZnSe-B6 nanoquencher of 450 µg/L (b); fluorescence recovery with OTA aptamer (50 nM) stabilized with (450 µg/L) ZnSe-B6 (c); fluorescence quenching recovery with OTA (d).

Subsequently, when Rh-B dye was introduced to the ZnSe-B6–aptamer conjugation, a fluorescence recovery response was achieved (Figure 6c). Upon introduction of the OTA, conjugation between the aptamer and OTA formed, which weakened the link between the aptamer and ZnSe-B6. The OTA and aptamer’s stronger binding interaction resulted in the release of ZnSe-B6 particles from the ZnSe-B6–aptamer complex, which quenched the fluorescence of the Rh-B dye, and thus fluorescence quenching recovered (Figure 6c). There was a direct proportional relation between the fluorescence quenching percent and the concentration of OTA in the assay.

3.4. Optimization

After demonstration of the quenching properties of the ZnSe-B6 to develop the OTA aptasensor, the next experiments were carried out to fix the experimental conditions, including aptamer concentration, aptamer incubation time, pH and incubation time of OTA, to evaluate their influence on the aptasensor efficiency. Figure 7A demonstrates the influence of different concentrations of OTA aptamer (5–60 nM), which demonstrated an incremental fluorescence intensity with increases in the amount of aptamer. Based on this observation, a 50 nM concentration was selected to fabricate the aptasensor, as this concentration was appropriate to devise the aptasensor based on quenching and recovery signals. Figure 7B showed that with increases in incubation time (0–30 min), an increase in the fluorescence emission also took place. An aptamer incubation time of 15 min was selected for the development of the aptasensor. The effect of incubation time of OTA (0–30 min) on fluorescence quenching recovery and performance of the aptasensor was further assessed. Figure 8A shows that maximum fluorescence quenching (% FL quenched)

after OTA target conjugation with the aptamer complex took place after 30 min incubation. The fluorescence quenching on introduction of OTA at varying pH levels (pH 3–9) was also evaluated and the quenching response has been given in Figure 8B. An impressive %FL quenching response of ~70% was observed at 7 pH.

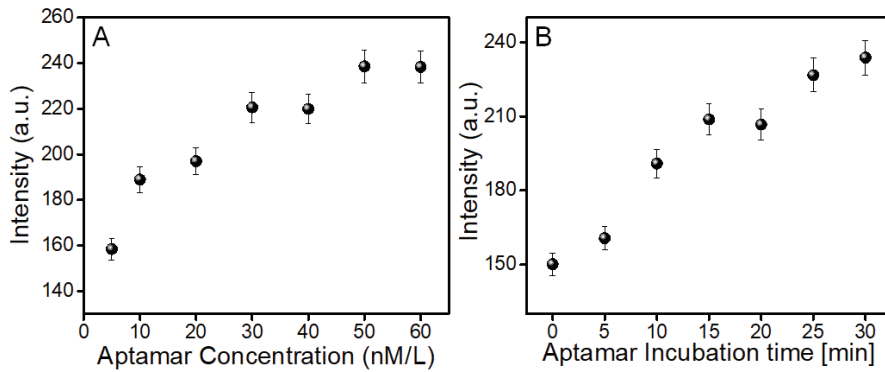


Figure 7. Effect of aptamer concentrations (5 to 60 nM) (A) and aptamer incubation time (0–30 min) (B) on fluorescence recovery of Rh-B (160 ng/L) in the presence of ZnSe-B6 (450 µg/L).

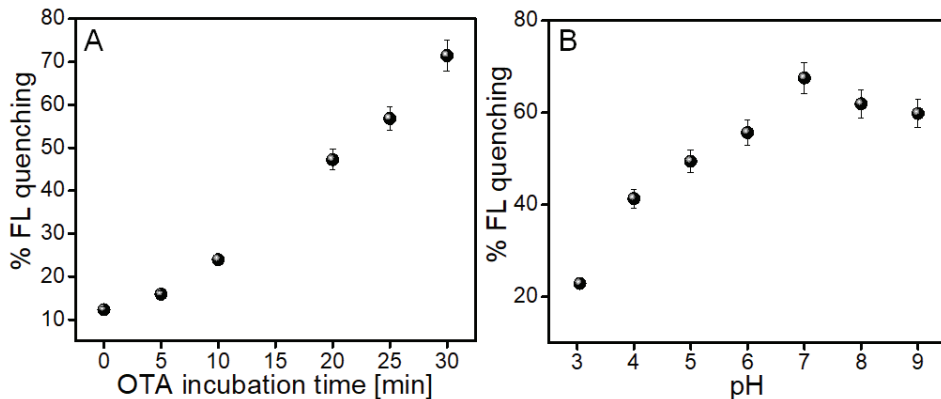


Figure 8. Effect of incubation time (0–30 min) of OTA (200 ng/L) (A) and pH (3–9) on % FL quenching (B).

3.5. Analytical Performance of the Developed Aptasensor

To confirm the practical applicability of the fabricated ZnSe-nanostructure-based aptasensor, the calibration curve based on % of recovered FL quenching with OTA concentrations ranging from 0.1–200 ng/L was evaluated. It can be seen in Figure 9. The %FL quenching signal increased in a directly proportional manner with higher concentration values of OTA due to the strong binding coordination of the amino-modified OTA aptamer with OTA to form an OTA aptamer–OTA reaction complex. Figure 9B shows that there is a good linear relationship, which can be confirmed with a linear equation ($y = 2.4x + 9.99$, $R^2 = 0.983$) between recovered %FL quenching and OTA concentration. A very low limit of detection (LOD) of 0.07 ng/L was achieved. The low LOD is an indication of the high specificity and selectivity of the ZnSe nanostructure-based aptasensing system.

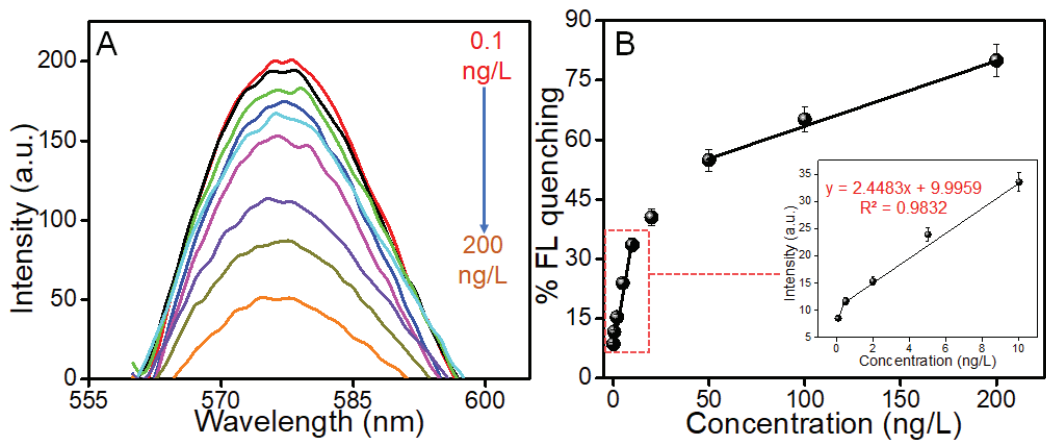


Figure 9. Fluorescence quenching spectra at different OTA concentrations (A); calibration plot (%FL quenching vs. OTA concentrations) (0.1, 0.5, 2.0, 5.0, 10, 20, 50, 100 and 200 ng/L) measured at 554 nm for excitation and 578 nm for emission (B).

The complex composition of samples is a big challenge for the development of aptasensors; thus, selectivity is the most important factor towards the practical application of aptasensors [34]. Selectivity of the ZnSe-nanostructure-based fluorescent aptasensor towards OTA was assessed using OTA interfering species such as ochratoxin-B (OTB), aflatoxin-M1 and aflatoxin-B1 (AFB1). Firstly, %FL quenching recovery was evaluated in the presence of 200 ng/L OTA. Afterwards, the relative %FL quenching recovery was evaluated in the presence of some common OTA interfering species, each at a concentration of 200 ng/L, under the same experimental parameters as those followed for OTA. Figure 10 shows a comparative % recovered FL quenching response of interfering compounds, which suggests that all interfering mycotoxins exhibited very little %FL quenching recovery as compared to OTA, which is a clear indication that there is negligible interaction between the OTA aptamer and the interfering analytes. The relative percentages of recovered FL quenching were ~83% for OTA, ~6.51% for OTB, ~7.38 for AFM1 and ~6.59% for AFB1. The results demonstrate high selectivity of the developed aptasensor, which is due to the high specificity interaction and binding of the OTA with the aptamer [38,39].

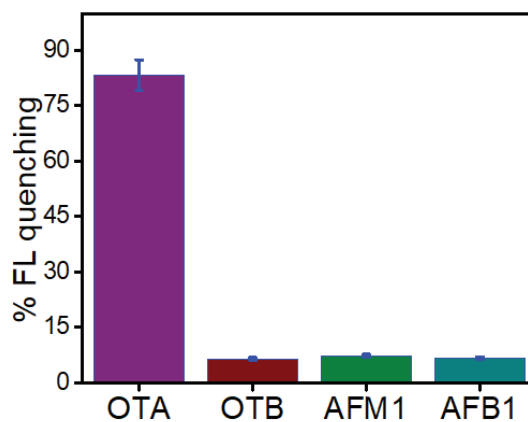


Figure 10. Response of developed aptasensor for OTA and other interfering species at a concentration of 200 ng/L in PBS (pH 7) under optimized conditions.

The analytical accuracy, practical applicability, reliability and reproducibility of the ZnSe-nanostructure-based fluorescent aptasensor was validated by detecting OTA in rice extracts. Three varying concentrations of OTA, i.e., 5, 50 and 100 ng/L were spiked to rice samples purchased from a local market. The recovery of spiked OTA was determined using the developed aptasensor. As shown in Table 2, the recovery and reproducibility were acceptable in all cases. The FL quenching recovery % response of OTA in buffer was in strong agreement with OTA spiked samples. The relative standard deviation (R.S.D %) of these recovery experiments were 0.56%, 0.22% and 0.218% for n = 3, which demonstrates good stability, reproducibility and practical applicability of the developed aptasensor. Comparison of some recent nanostructure-based fluorescent sensors for OTA detection is presented in Supplementary Table S2.

Table 2. Determination of OTA spiked in rice extract (n = 3).

Sr. No.	OTA Added (ng/L)	OTA Found (ng/L)	R.S.D %	R.E %	R %
1.	5	5.04	0.5634	0.8	100.8
2.	50	50.16	0.2259	0.32	100.32
3.	100	100.31	0.2188	0.31	100.31

R.S.D % = relative standard deviation percentage; R.E % = relative error percentage; R% = recovery percentage.

4. Conclusions

In the present work, precursor and synthesis reaction time dependent multifunctional ZnSe nanostructures, with a highly negative surface charge and different sizes and morphologies were successfully synthesized. We further exploited ZnSe μ -sphere nanoquenchers for the development of a fluorescent aptasensor for the detection of ochratoxin A. Fluorescence results confirmed that ZnSe μ -spheres had maximum quenching efficiency as compared to other types of synthesized ZnSe nanostructures, because of their highly negative surface charge and large size. Highly dispersive, stable and negatively charged ZnSe μ -spheres exhibited strong interaction with cationic Rh-B dye. Similarly, amino-modified OTA aptamer also strongly interacted with ZnSe μ -spheres. Exploiting these interactions, a ZnSe- μ -sphere-based fluorescent aptasensor was successfully fabricated for the detection of ochratoxin A. The proposed OTA aptasensor demonstrated a low detection limit of 0.07 ng/L with an excellent wide linear range of 0.1 to 200 ng/L. Moreover, we also evaluated the practical applicability of the developed aptasensor by checking its response towards common interfering mycotoxins and found negligible response. Similarly, real sample analysis was also performed using spiked rice samples, which showed satisfactory recovery percentages. Overall, the current study has paved a way for ZnSe-nanostructure-based fluorescent sensors for the detection of different biomolecular targets.

Supplementary Materials: The following supporting information can be downloaded at: <https://www.mdpi.com/article/10.3390/bios12100844/s1>, “Instruments and reagents” section, Figure S1: Optimization of Rh-B dye concentration (10–250 ng/L) for the development of ZnSe nanostructures based aptasensor, Table S1: The crystalline size of nanoparticles calculated using Scherrer and strain by applying Williamson-Hall plot, Table S2: Comparison of some recent nanostructured based fluorescent sensors for OTA detection. References [35,39–46] are cited in Supplementary Materials.

Author Contributions: Conceptualization, A.H. and M.A.H.N.; methodology, A.H., M.A.H.N. and M.W.F.; formal analysis, M.A.H.N.; investigation, A.H., N.A. and C.Y.; data curation, A.H., N.A. and M.H.N.; writing—original draft preparation, M.A.H.N., M.W.F.; writing—review and editing, A.H., N.A., M.H.N. and C.Y.; supervision, A.H. and C.Y. All authors have read and agreed to the published version of the manuscript.

Funding: This research received no external funding.

Institutional Review Board Statement: Not applicable.

Informed Consent Statement: Not applicable.

Data Availability Statement: Not applicable.

Conflicts of Interest: The authors declare no conflict of interest.

References

- Bankole, O.E.; Verma, D.K.; González, M.L.C.; Ceferino, J.G.; Sandoval-Cortés, J.; Aguilar, C.N. Recent trends and technical advancements in biosensors and their emerging applications in food and bioscience. *Food Biosci.* **2022**, *47*, 101695. [[CrossRef](#)]
- Luong, J.H.; Male, K.B.; Glennon, J.D. Biosensor technology: Technology push versus market pull. *Biotechnol. Adv.* **2008**, *26*, 492–500. [[CrossRef](#)]
- Bai, X.; Wang, K.; Chen, L.; Zhou, J.; Wang, J. Semiconducting polymer dots as fluorescent probes for in vitro biosensing. *J. Mater. Chem. B* **2022**, *10*, 6248–6262. [[CrossRef](#)] [[PubMed](#)]
- Wang, W. Bright, Compact and Biocompatible Quantum Dot/Rod-Bioconjugates for Förster Resonance Energy Transfer Based Ratiometric Biosensing and Cellular Imaging. University of Leeds: Leeds, UK, 2017.
- Fang, X.; Zheng, Y.; Duan, Y.; Liu, Y.; Zhong, W. Recent advances in design of fluorescence-based assays for high-throughput screening. *Anal. Chem.* **2018**, *91*, 482–504. [[CrossRef](#)] [[PubMed](#)]
- Feng, B.; Cao, J.; Yang, J.; Yang, S.; Han, D. Characterization and photocatalytic activity of ZnSe nanoparticles synthesized by a facile solvothermal method, and the effects of different solvents on these properties. *Mater. Res. Bull.* **2014**, *60*, 794–801. [[CrossRef](#)]
- Gudiksen, M.S.; Wang, J.; Lieber, C.M. Synthetic Control of the Diameter and Length of Single Crystal Semiconductor Nanowires. *J. Phys. Chem. B* **2001**, *105*, 4062–4064. [[CrossRef](#)]
- Wang, L.; Xu, X.; Yuan, X. Preparation and photoluminescent properties of doped nanoparticles of ZnS by solid-state reaction. *J. Lumin.* **2010**, *130*, 137–140. [[CrossRef](#)]
- Hong, H.S.; Kim, M.-S.; Byun, E.K.; Lee, Y.L. Facile synthesis and characterization of zinc selenide nanoparticles in aqueous solution at room temperature. *J. Cryst. Growth* **2020**, *535*, 125523. [[CrossRef](#)]
- Song, Y.; Yin, W.; Fernandes, C.; Ruda, H.E. Fabrication of one-dimension ZnSe and ZnO nanostructures via anodic alumina template assisted vapor–liquid–solid growth process. *Thin Solid Films* **2013**, *548*, 130–137. [[CrossRef](#)]
- Wang, C.; Wang, J.; Li, Q.; Yi, G.C. ZnSe–Si Bi-coaxial Nanowire Heterostructures. *Adv. Funct. Mater.* **2005**, *15*, 1471–1477. [[CrossRef](#)]
- Fang, X.; Xiong, S.; Zhai, T.; Bando, Y.; Liao, M.; Gautam, U.K.; Koide, Y.; Zhang, X.; Qian, Y.; Golberg, D. High-performance blue/ultraviolet-light-sensitive ZnSe-nanobelt photodetectors. *Adv. Mater.* **2009**, *21*, 5016–5021. [[CrossRef](#)] [[PubMed](#)]
- Chen, L.; Lai, J.; Fu, X.; Sun, J.; Ying, Z.; Wu, J.; Lu, H.; Xu, N. Growth of ZnSe nano-needles by pulsed laser deposition and their application in polymer/inorganic hybrid solar cells. *Thin Solid Films* **2013**, *529*, 76–79. [[CrossRef](#)]
- Zhang, H.; Fang, Y. Temperature dependent photoluminescence of surfactant assisted electrochemically synthesized ZnSe nanostructures. *J. Alloys Compd.* **2019**, *781*, 201–208. [[CrossRef](#)]
- Yang, J.; Wang, G.; Liu, H.; Park, J.; Gou, X.; Cheng, X. Solvothermal synthesis and characterization of ZnSe nanoplates. *J. Cryst. Growth* **2008**, *310*, 3645–3648. [[CrossRef](#)]
- Huang, L.; Han, H. One-step synthesis of water-soluble ZnSe quantum dots via microwave irradiation. *Mater. Lett.* **2010**, *64*, 1099–1101. [[CrossRef](#)]
- Jiang, C.; Zhang, W.; Zou, G.; Yu, W.; Qian, Y. Synthesis and characterization of ZnSe hollow nanospheres via a hydrothermal route. *Nanotechnology* **2005**, *16*, 551. [[CrossRef](#)]
- Fu, H.; Li, H.; Jie, W.; Yang, L. The growth and characterization of ZnSe nanoneedles by a simple chemical vapor deposition method. *J. Cryst. Growth* **2006**, *289*, 440–444. [[CrossRef](#)]
- Chiang, M.-H.; Fu, Y.-S.; Shih, C.-H.; Kuo, C.-C.; Guo, T.-F.; Lin, W.-T. Effects of hydrazine on the solvothermal synthesis of Cu₂ZnSnSe₄ and Cu₂CdSnSe₄ nanocrystals for particle-based deposition of films. *Thin Solid Films* **2013**, *544*, 291–295. [[CrossRef](#)]
- Gupta, D.; Jamwal, D.; Rana, D.; Katoch, A. Microwave synthesized nanocomposites for enhancing oral bioavailability of drugs. In *Applications of Nanocomposite Materials in Drug Delivery*; Elsevier: Amsterdam, The Netherlands, 2018; pp. 619–632.
- Singh, P.; Kachhap, S.; Singh, P.; Singh, S. Lanthanide-based hybrid nanostructures: Classification, synthesis, optical properties, and multifunctional applications. *Coord. Chem. Rev.* **2022**, *472*, 214795. [[CrossRef](#)]
- Nguyen, V.K.; Pham, D.K.; Tran, N.Q.; Dang, L.H.; Nguyen, N.H.; Nguyen, T.V.; Nguyen, T.H.; Luong, T.B. Comparative Studies of Blue-Emitting Zinc Selenide Nanocrystals Doped with Ag, Cu, and Mg towards Medical Applications. *Crystals* **2022**, *12*, 625. [[CrossRef](#)]
- Ramanavicius, A.; Ryskevicius, N.; Oztekin, Y.; Kausaite-Minkstimiene, A.; Jursenas, S.; Baniukevicius, J.; Kirlyte, J.; Bubniene, U.; Ramanaviciene, A. Immunosensor based on fluorescence quenching matrix of the conducting polymer polypyrrole. *Anal. Bioanal. Chem.* **2010**, *398*, 3105–3113. [[CrossRef](#)]
- Ramanavicius, A.; Kurilcik, N.; Jursenas, S.; Finkelsteinas, A.; Ramanaviciene, A. Conducting polymer based fluorescence quenching as a new approach to increase the selectivity of immunosensors. *Biosens. Bioelectron.* **2007**, *23*, 499–505. [[CrossRef](#)]
- Singh, D.K.; Iyer, P.K.; Giri, P.K. Role of molecular interactions and structural defects in the efficient fluorescence quenching by carbon nanotubes. *Carbon* **2012**, *50*, 4495–4505. [[CrossRef](#)]

26. Kim, J.H.; Kataoka, M.; Shimamoto, D.; Muramatsu, H.; Jung, Y.C.; Tojo, T.; Hayashi, T.; Kim, Y.A.; Endo, M.; Terrones, M. Defect-Enhanced Dispersion of Carbon Nanotubes in DNA Solutions. *ChemPhysChem* **2009**, *10*, 2414–2417. [[CrossRef](#)] [[PubMed](#)]
27. Wang, Y.; Yang, C.; Hu, R.; Toh, H.T.; Liu, X.; Lin, G.; Yin, F.; Yoon, H.S.; Yong, K.-T. Assembling Mn: ZnSe quantum dots-siRNA nanoplexes for gene silencing in tumor cells. *Biomater. Sci.* **2015**, *3*, 192–202. [[CrossRef](#)]
28. Zhang, S.; Khan, A.; Ali, N.; Malik, S.; Khan, H.; Ali, N.; Iqbal, H.M.; Bilal, M. Designing, characterization, and evaluation of chitosan-zinc selenide nanoparticles for visible-light-induced degradation of tartrazine and sunset yellow dyes. *Environ. Res.* **2022**, *213*, 113722. [[CrossRef](#)] [[PubMed](#)]
29. Hanaor, D.; Michelazzi, M.; Leonelli, C.; Sorrell, C.C. The effects of carboxylic acids on the aqueous dispersion and electrophoretic deposition of ZrO₂. *J. Eur. Ceram. Soc.* **2012**, *32*, 235–244. [[CrossRef](#)]
30. Mirzaei, S.Z.; Somaghian, S.A.; Lashgarian, H.E.; Karkhane, M.; Cheraghipour, K.; Marzban, A. Phyco-fabrication of bimetallic nanoparticles (zinc-selenium) using aqueous extract of *Gracilaria corticata* and its biological activity potentials. *Ceram. Int.* **2021**, *47*, 5580–5586. [[CrossRef](#)]
31. Zhang, F. Fluorescent Sensors for Biosensing Applications: Immunosensors for Mycotoxins and Aptasensors for Interferon-Gamma. 2019. Available online: <https://www.researchonline.mq.edu.au/vital/access/manager/Repository/mq:71337> (accessed on 5 September 2022).
32. Yang, C.; Abbas, F.; Rhouati, A.; Sun, Y.; Chu, X.; Cui, S.; Sun, B.; Xue, C. Design of a Quencher-Free Fluorescent Aptasensor for Ochratoxin A Detection in Red Wine Based on the Guanine-Quenching Ability. *Biosensors* **2022**, *12*, 297. [[CrossRef](#)]
33. Li, L.; Liu, S.; Zhu, T. Application of activated carbon derived from scrap tires for adsorption of Rhodamine B. *J. Environ. Sci.* **2010**, *22*, 1273–1280. [[CrossRef](#)]
34. Wang, M.; Fu, J.; Zhang, Y.; Chen, Z.; Wang, M.; Zhu, J.; Cui, W.; Zhang, J.; Xu, Q. Removal of Rhodamine B, a cationic dye from aqueous solution using poly (cyclotriphosphazene-co-4, 4'-sulfonyldiphenol) nanotubes. *J. Macromol. Sci. Part A* **2015**, *52*, 105–113. [[CrossRef](#)]
35. Khan, A.; Nawaz, M.A.H.; Akhtar, N.; Raza, R.; Yu, C.; Andreescu, S.; Hayat, A. Morphology controlled NiO nanostructures as fluorescent quenchers for highly sensitive aptamer-based FRET detection of ochratoxin A. *Appl. Surf. Sci.* **2021**, *566*, 150647. [[CrossRef](#)]
36. Mosquera, E.; Carvajal, N.; Morel, M.; Marin, C. Fabrication of ZnSe nanoparticles: Structural, optical and Raman Studies. *J. Lumin.* **2017**, *192*, 814–817. [[CrossRef](#)]
37. Geng, B.; You, J.; Zhan, F.; Kong, M.; Fang, C. Controllable morphology evolution and photoluminescence of ZnSe hollow microspheres. *J. Phys. Chem. C* **2008**, *112*, 11301–11306. [[CrossRef](#)]
38. Zhang, L.; Yang, H.; Xie, X.; Zhang, F.; Li, L. Preparation and photocatalytic activity of hollow ZnSe microspheres via Ostwald ripening. *J. Alloys Compd.* **2009**, *473*, 65–70. [[CrossRef](#)]
39. Tian, J.; Wei, W.; Wang, J.; Ji, S.; Chen, G.; Lu, J. Fluorescence resonance energy transfer aptasensor between nanoceria and graphene quantum dots for the determination of ochratoxin A. *Anal. Chim. Acta* **2018**, *1000*, 265–272. [[CrossRef](#)]
40. Lv, L.; Jin, Y.; Kang, X.; Zhao, Y.; Cui, C.; Guo, Z. PVP-coated gold nanoparticles for the selective determination of ochratoxin A via quenching fluorescence of the free aptamer. *Food Chem.* **2018**, *249*, 45–50. [[CrossRef](#)] [[PubMed](#)]
41. Sharma, A.; Hayat, A.; Mishra, R.K.; Catanante, G.; Bhand, S.; Marty, J.L. Titanium dioxide nanoparticles (TiO₂) quenching based aptasensing platform: Application to ochratoxin A detection. *Toxins* **2015**, *7*, 3771–3784. [[CrossRef](#)] [[PubMed](#)]
42. Lu, Z.; Chen, X.; Hu, W. A fluorescence aptasensor based on semiconductor quantum dots and MoS₂ nanosheets for ochratoxin A detection. *Sens. Actuators B Chem.* **2017**, *246*, 61–67. [[CrossRef](#)]
43. Taghdisi, S.M.; Danesh, N.M.; Beheshti, H.R.; Ramezani, M.; Abnous, K. A novel fluorescent aptasensor based on gold and silica nanoparticles for the ultrasensitive detection of ochratoxin A. *Nanoscale* **2016**, *8*, 3439–3446. [[CrossRef](#)]
44. Jiang, H.; Li, X.; Xiong, Y.; Pei, K.; Nie, L.; Xiong, Y. Silver nanoparticle-based fluorescence-quenching lateral flow immunoassay for sensitive detection of ochratoxin A in grape juice and wine. *Toxins* **2017**, *9*, 83. [[CrossRef](#)] [[PubMed](#)]
45. Lv, X.; Zhang, Y.; Liu, G.; Du, L.; Wang, S. Aptamer-based fluorescent detection of ochratoxin A by quenching of gold nanoparticles. *Rsc. Adv.* **2017**, *7*, 16290–16294. [[CrossRef](#)]
46. Wei, M.; Wang, C.; Xu, E.; Chen, J.; Xu, X.; Wei, W.; Liu, S. A simple and sensitive electrochemiluminescence aptasensor for determination of ochratoxin A based on a nicking endonuclease-powered DNA walking machine. *Food Chem.* **2019**, *282*, 141–146. [[CrossRef](#)]



Article

Design of a Quencher-Free Fluorescent Aptasensor for Ochratoxin A Detection in Red Wine Based on the Guanine-Quenching Ability

Cheng Yang¹, Fathimath Abbas¹, Amina Rhouati², Yingying Sun¹, Xiaolin Chu¹, Shengnan Cui¹, Bingbing Sun¹ and Changying Xue^{3,*}

- ¹ State Key Laboratory of Fine Chemicals, Department of Chemistry, School of Chemical Engineering, Dalian University of Technology, Dalian 116024, China; yangcheng@dlut.edu.cn (C.Y.); ferthunabbas@mail.dlut.edu.cn (F.A.); sunyydlut@hotmail.com (Y.S.); 21907036@mail.dlut.edu.cn (X.C.); cuishengnan@mail.dlut.edu.cn (S.C.); bingbingsun@dlut.edu.cn (B.S.)
- ² Bioengineering Laboratory, Higher National School of Biotechnology, Constantine 25100, Algeria; amina.rhouati@gmail.com
- ³ State Key Laboratory of Fine Chemicals, School of Bioengineering, Dalian University of Technology, Dalian 116024, China
- * Correspondence: changyingxue@dlut.edu.cn

Abstract: This study describes a quencher-free fluorescent aptasensor for ochratoxin A (OTA) detection using the specific quenching ability of guanine for fluorescein (FAM) molecules based on photo-induced electron transfer (PIET). In this strategy, OTA is detected by monitoring the fluorescence change induced by the conformational change of the aptamer after target binding. A new shorter OTA aptamer comprising three guanine bases at the 5' end was used in this study. This new aptamer, named G3-OTAapt1-FAM (F1), was labeled with FAM on the 3' end as a fluorophore. In order to increase the binding affinity of the aptamer and OTA, G3-OTAapt2-FAM (F2) was designed; this added a pair of complementary bases at the end compared with F1. To prevent the strong self-quenching of F2, a complementary chain, A13, was added. Although the F1 aptasensor was simpler to implement, the sensitivity of the F2 aptasensor with A13 was better than that of F1. The proposed F1 and F2 sensors can detect OTA with a concentration as low as 0.69 nmol/L and 0.36 nmol/L, respectively.

Citation: Yang, C.; Abbas, F.; Rhouati, A.; Sun, Y.; Chu, X.; Cui, S.; Sun, B.; Xue, C. Design of a Quencher-Free Fluorescent Aptasensor for Ochratoxin A Detection in Red Wine Based on the Guanine-Quenching Ability. *Biosensors* **2022**, *12*, 297. <https://doi.org/10.3390/bios12050297>

Received: 8 April 2022
Accepted: 29 April 2022
Published: 5 May 2022



Copyright: © 2022 by the authors. Licensee MDPI, Basel, Switzerland. This article is an open access article distributed under the terms and conditions of the Creative Commons Attribution (CC BY) license (<https://creativecommons.org/licenses/by/4.0/>).

Keywords: aptasensor; quencher-free; photo-induced electron transfer; guanine-quenching fluorescence; ochratoxin A

1. Introduction

Aptamers are folded nucleic acid sequences with a single-stranded DNA or RNA structure, designed from 25 to 60 base pairs. They are selected via an in vitro process called the systematic evolution of ligands by exponential enrichment (SELEX) from an extensive random library with desirable properties. The sequence variation allows for the display of many structural arrangements; therefore, aptamers can form secondary structures that specifically bind to some targets, such as small molecules, proteins, amino acids, cells, and tissues, with a high affinity [1]. Aptamers are characterized by a target-induced conformational change that folds into stable three-dimensional structures, such as a hairpin, pseudo-knot, and G-quadruplex [2]. Aptamers have been identified as a promising alternative to replace antibodies because of their similar recognition function [3]. In addition, aptamers are superior because they offer several advantages over antibodies, which include easy modification, high affinity, and stable thermal and chemical stability. In addition, aptamers are selected by in vitro techniques, independent of animals or cells, which contribute to their low-cost production [4,5]. These make them a promising molecular receptor in bioanalytical applications [3]. Based on the outstanding merits of

aptamers, many aptasensors have been developed for different applications, such as electrochemistry [6,7], fluorescence [7,8], chemiluminescence [6,9], and colorimetry [6,7,10] assay approaches. Fluorescence-based aptasensors have attracted plenty of attention because they possess various advantages, including a convenient operation, quick response, and good reproducibility [11,12]. Nevertheless, the challenge for fluorescence methods is the high cost of labeling aptamers with the fluorophore and quencher.

Guanine is an excellent quenching group for quencher-free aptasensors. Oligonucleotides rich in guanines have been employed as sensing elements in various biosensors over the past few years [13]. Guanine is the most oxidizable base; this base-dye interaction is believed to be caused by the photo-induced electron transfer (PIET) mechanism [14,15]. Thus, the fluorescence of the fluorophore can be quenched by the neighboring guanine [13,16]. Recently, DNA, RNA, and metal ions analyses have emerged, based on PIET, between fluorophore and guanine bases [13,16,17]. For these methods, guanine is used as a quencher for FAM, which avoids employing quencher unit binding to the oligonucleotide, such as hemin or porphyrin. Conjugating an organic fluorescence quenching group such as BHQ1 (black hole quencher 1) or TAMRA for fluorescence detection increases the complexity of the detection method, and significantly increases the cost of testing [18]. Guanine is a low-cost and effective quencher for FAM. Moreover, guanines can be easily added to the aptamer sequence without the complex conjugations required for organic quenchers. Therefore, we tried to use this strategy to detect highly toxic small molecules, which are challenging to detect with a high sensitivity.

Ochratoxin A (OTA) is a mycotoxin that is considered a human carcinogen by the International Agency for Research on Cancer (IARC) [4]. OTA is found in various food-stuffs, including grains, coffee, wine, and beer. Certain fungal species produce ochratoxins as a secondary metabolite, such as *Aspergillus ochraceus*, *Aspergillus carbonarius*, and *Penicillium verrucosum*. Because of the extensive existence and chemically stable properties of OTA (even surviving at high temperatures and boiling), it is tough to eradicate from the food chain. Hence, the accumulation of OTA in the human body causes a potential threat to human health. Therefore, specific regulatory bodies have set strict food and feed regulations regarding the OTA content. The European Commission has stipulated that the maximum content of OTA is 2 µg/kg in grape juice or wine and 5 µg/kg and 10 µg/kg in raw grains and soluble coffee, respectively [19,20]. Therefore, it is essential to develop a new approach to detect OTA in a highly efficiency and low-cost manner. The application of aptamers has brought hope to this expectation. In 2008, Cruz-Aguado selected the first OTA aptamer for OTA detection [21]; since then, this aptamer has been widely used to construct many biosensors [11,22–24]. Among these, fluorescence aptasensors are the simplest, easiest to operate, and are extremely sensitive. Therefore, we have taken advantage of the excellent properties of aptamers, together with the quenching ability of guanine, to develop a fluorescence aptasensor for OTA detection using guanine as a quencher. For this purpose, a new aptamer with a blunt end was used on the platform. FAM as a fluorophore was labeled on the 3' end of the new aptamer, and three guanine bases as a quencher were extended at the 5' end (named G3-OTAapt1-FAM (F1)). In order to increase the binding affinity of the aptamer and OTA, a new aptamer called G3-OTAapt2-FAM (F2) was designed, which added a pair of complementary bases at the end of F1. When the target molecule OTA is present, the aptamer forms a recognition structure. It places FAM closer to the protruding guanines, leading it to be quenched by the guanines. As a result, OTA can be detected quantitatively through fluorescence quenching.

In this study, based on the quenching ability of guanine, we developed a fluorescence analysis method for OTA detection that is highly sensitive, and has a high throughput and low cost.

2. Experimental

2.1. Reagents and Chemicals

Sodium chloride (NaCl), calcium chloride (CaCl₂), and hydrochloric acid (HCl) were purchased from Sinopharm Chemical Reagent Co., Ltd. (Beijing, China). Tris (hydroxymethyl) carbamate (Tris, C₄H₁₁NO₃) was purchased from BBI Life Sciences (Shanghai, China). OTA, OchratoxinB (OTB), Aflatoxin B1 (AFB1), Fumonisin B1 (FB1), Deoxynivalenol (DON), and Zearalenone (ZEA) were purchased from Sigma-Aldrich (St. Louis, MO, USA). All of the oligonucleotides (listed in Table 1) were synthesized by Shanghai Sangon Biotechnology Co., Ltd. (Shanghai, China), and were annealed by heating at 95 °C for 5 min, and then quickly cooled down to 4 °C and maintaining this for 2.5 min before use. The ultra-pure water used in the experiment was purified by a Milli-Q system (18.2 MΩ; Millipore, Bedford, MA, USA). The 96-well micro-plates were purchased from Shanghai Wohong Biotechnology Co., Ltd. (Shanghai, China).

Table 1. DNA sequences used in this experiment.

Name	Complementary Chain Sequence	Number of Bases
Apt36F	5'-GGGGATCGGGTGTGGGTGGCGTAAAGGGAGCATC-GGACA-FAM-3'	39
F1	5'-GGGGATCGGGTGTGGGTGGCGTAAAGGGAGCATC-FAM-3'	34
F2	5'-GGGGATCGGGTGTGGGTGGCGTAAAGGGAGCATCC-FAM-3'	36
F2-A11	3'-TTCCCTCGTA-5'	11
F2-A12	3'-ATTCCCTCGTA-5'	12
F2-A13	3'-CATTCCCTCGTA-5'	13
F2-A14	3'-GCATTCCCTCGTA-5'	14
F2-A16	3'-CCGCATTCCCTCGTA-5'	16
F2-A18	3'-CACCGCATTCCCTCGTA-5'	18

2.2. Instrumentation

All of the fluorescence measurements were performed at room temperature on a Safire II multi-detection micro-plate reader (Tecan, Switzerland), with an excitation wavelength of 483 nm and an emission wavelength of 525 nm. The concentration of the aptamer was determined using UV absorption spectroscopy by a ReadMax 1900 Absorbance Microplate Reader (Shanghai Flash Spectrum Biotechnology Co., Ltd., Shanghai, China).

2.3. Experimental Method

2.3.1. Optimization of Reaction Conditions

In order to achieve the best experimental performances, the concentration of Ca²⁺, the complementary sequence, and the concentration of the complementary chain were optimized. The optimal concentration of Ca²⁺ was determined by mixing different concentrations of Ca²⁺ (0–100 nmol/L) with 20 nmol/L F1, 10 mmol/L Tris-HCl (pH = 8.4), and 120 mmol/L NaCl in the presence and absence of 50 nmol/L OTA at room temperature. To obtain the best complementary sequence, the calibration curves were obtained using different complementary sequences (A11–A18) of 60 nmol/L and 20 nmol/L F2 in 10 mmol/L Tris-HCl (pH = 8.4), 120 mmol/L NaCl, and 3 mmol/L CaCl₂ at room temperature. To determine the optimal concentration of the complementary sequence, different concentrations of A13 (0–1000 nmol/L) and 20 nmol/L F2 with 10 mmol/L Tris-HCl (pH = 8.4), 120 mmol/L NaCl, and 3 mmol/L CaCl₂ were mixed in the presence and absence of 50 nmol/L of OTA at room temperature. The fluorescence intensity was obtained using a Safire II multi-detection microplate reader, and all of the experiments were repeated three times independently.

2.3.2. OTA Aptasensing by Fluorescence Aptasensor

The testing solution for the F1 aptasensor was prepared by mixing 100 nmol/L F1 in a binding buffer (50 mmol/L Tris-HCl buffer solution containing 600 mmol/L NaCl and 15.0 mmol/L CaCl₂, pH = 8.4), and the F2 aptasensor was prepared by mixing 100 nmol/L F2 and 300 nmol/L A13 complementary chains in the binding buffer. Then, 80 µL of OTA with different concentrations was added into 96-well micro-plates. Then, 20 µL of the testing solution was added to the micro-plates and mixed well to a final volume of 100 µL. Finally, the fluorescence intensity was measured using a Safire II multi-detection microplate reader after 20 min of incubation. All of the experiments were repeated three times independently.

2.3.3. Specificity Assay

To verify the specificity of the developed aptasensor, OTB, AFB1, DON, FB1, and ZEA were used as the control samples. Then, 80 µL of the 62.5 nmol/L OTA solution or 250 nmol/L of the OTB, AFB1, DON, FB1, and ZEA solution was mixed with a 20 µL testing solution (described in Section 2.3.2) and incubated for 20 min at room temperature. The fluorescence intensity was determined using a Safire II multi-detection microplate reader, and all of the experiments were repeated three times independently.

2.3.4. Detection of OTA in Wine Samples

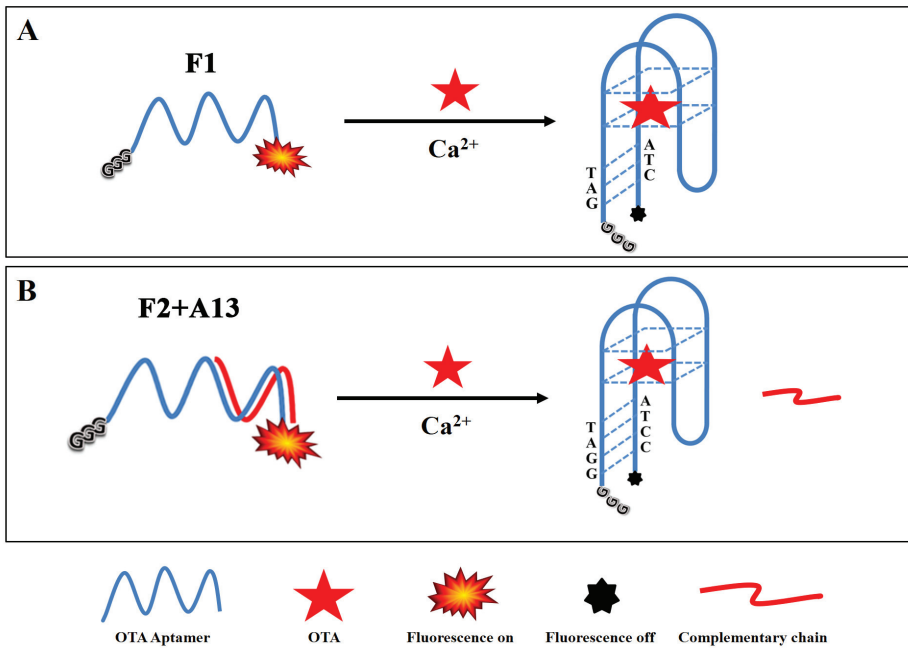
In a standard addition experiment, 1.0 µL, 2.0 µL, and 4.0 µL of 10 µmol/L OTA standard solutions were added to 10 mL of red wine samples, separately. The spike wine samples were obtained with 1.0 nmol/L, 2.0 nmol/L, and 4.0 nmol/L of OTA. The samples were pre-treated using the following process. According to the physical and chemical properties of OTA, sample pre-treatment was performed using a double liquid–liquid extraction scheme [25]. The operation process was as follows: 5.0 mL of red wine samples were mixed with an equal volume of toluene. After complete phase separation, 4.0 mL of the top organic layer was mixed with equal volumes of the alkaline buffer solution (10 mmol/L Tris-HCl, pH = 8.4). Then, complete phase separation was allowed. Then, 3.0 mL of the bottom aqueous layer was taken out and mixed with an equal volume of dichloromethane. Before mixing, the pH of the bottom aqueous layer was adjusted to 3.0 by adding hydrochloric acid. The two phases were allowed complete phase separation, and the bottom organic layer was collected and mixed with an equal volume of 10 mmol/L Tris-HCl buffer (pH = 8.4). Finally, after complete phase separation, the top aqueous phase was taken and used for subsequent analysis by the aptasensor.

Finally, 80 µL of the pre-treated samples were mixed and incubated with 20 µL of the testing solution (described in Section 2.3.2). The fluorescence intensity was detected by a Safire II multi-detection microplate reader, and all of the experiments were repeated three times independently.

3. Results and Discussion

3.1. Principle of OTA Detection

The principle of the proposed fluorescence assay for the detection of OTA is depicted in Scheme 1. First, the aptasensor was formed using the aptamer selected by Cruz-Aguado, the FAM was attached at the 3' end, and three guanines were extended at the 5' end as a quencher. Unfortunately, no fluorescence quenching was observed, even after increasing the OTA concentration. The reason for this is likely that the aptamer selected by Cruz-Aguado has five bases at the 3' end that are not required for OTA binding, which increases the distance between the FAM and the quencher. This is consistent with the previous research results of our group [12]. Therefore, these bases were truncated from the 3' end of the original aptamer (OTAapt36) to create a new blunt end aptamer. The new aptamer was labelled with FAM on the 3' end and extended using three guanine bases at the 5' end, which was named G3-OTAapt1-FAM (F1).



Scheme 1. Schematic illustration of the guanine-quenched fluorescence sensing platform F1 biosensor (A) and F2 + A13 biosensor (B) for the detection of OTA.

For the new aptamer, F1, the presence of OTA caused the aptamer to form a compact three-dimensional structure (an antiparallel G-quadruplex), making the bases of the two tails of the aptamer close to each other, forming a hybridization structure [12]. As a result, FAM fluorescence could be quenched by three unpaired guanines protruding at the 5' end. The distance between the FAM molecule and guanine bases decreased during this process, leading to fluorescence quenching by photo-induced electron transfer (PIET).

In order to further increase the binding affinity of the aptamer with OTA and lower the detection limit, a second aptamer was designed based on the fact that extending the number of complementary bases could stabilize a double-strand sequence. This aptamer was designed by adding a pair of G-C complementary bases at the end of the shorter OTA aptamer (31 bases), which was named G3-OTAapt2-FAM (F2). The F2 sequence has one more complementary base than F1, making the structure more stable and providing a higher affinity and quenching efficiency.

To demonstrate the feasibility of our aptasensor, the fluorescence property of the sensing system was investigated. As shown in Figure 1, no significant fluorescence quenching change was noted after adding OTA when using the original aptamer. This further validated our previous research results [12], that five bases at the 3' end widened the distance between FAM and the quencher, which is not helpful for OTA detection. Thus, five bases had to be truncated from the 3' end of the original aptamer (OTAapt36) to create a blunt end aptamer. As expected, after using the blunt tail aptamer (F1), better results were obtained. Although F2 was designed for further improvement, no significant fluorescence intensity change was noted when OTA was present. This was because of the tail chains of the newly designed aptamer already being hybridized with each other, even in the absence of OTA. Therefore, complementary chains were introduced into this detection system to prevent this occurrence. In general, the competition of complementary chains reduces the performance of the aptasensor, but here, the complementary chain amplifies the response without reducing the performance of the F2 aptasensor.

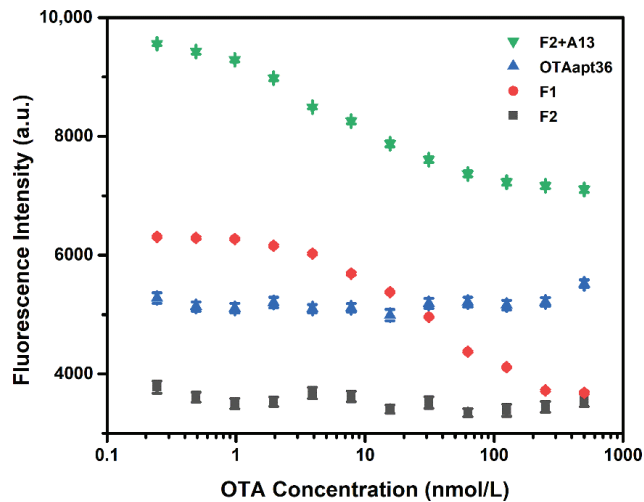


Figure 1. Comparison of the fluorescence intensity of the F1-based aptasensor and F2-based aptasensor with different OTA concentrations ($n = 3$). The concentration of the F1, F2, and OTAapt36 aptamers was 20 nmol/L, and the concentration of A13 was 60 nmol/L. The error bars denote the standard deviation of the triplicate measurements.

3.2. Optimization of OTA Detection Conditions

3.2.1. Optimization of the Ca^{2+} Concentration

The important parameters were first optimized to obtain the optimal performances of the two proposed sensors. It is worth noting that the composition and pH of the buffer directly affect the aptamer structure in the solution. The Tris-HCl buffer is commonly used in biological experiments because nucleic acids are more stable in this solution, and the reaction is mild. Hence, Tris-HCl pH 8.4 was chosen to perform the following experiments. In addition, studies have shown that bivalent ions can shield the negative charge on the phosphate skeleton of nucleic acids, contributing to the formation of the three-dimensional recognition structure of the aptamer [19]. The effect of the Ca^{2+} ion concentration on the change in fluorescence intensity in the presence and absence of OTA was studied. By increasing the Ca^{2+} concentration, a rapid increase in the fluorescence quenching percentage $((F_0 - F_{\text{OTA}})/F_0 \times 100)$ was observed. The fluorescence quenching reached a maximum at a concentration of 3.0 mmol/L. Therefore, the 3.0 mmol/L Ca^{2+} ion concentrations were chosen for the subsequent experiments, and the results are shown in Figure 2.

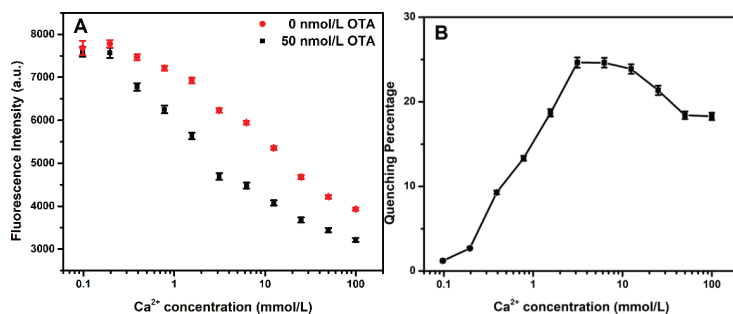


Figure 2. (A) Fluorescence intensity of the F1 aptasensor with different concentrations of Ca^{2+} (0–100 mmol/L) in the presence and absence of 50 nmol/L OTA ($n = 3$). (B) Quenching percentage with different concentrations of Ca^{2+} (0–100 mmol/L). The error bars denote the standard deviations of the triplicate measurements.

3.2.2. Optimization of the Complementary Sequence and Its Concentration for F2 Aptasensor

The newly designed F2-based aptasensor shows no significant fluorescence intensity change when adding different concentrations of OTA. In order to solve this problem, complementary chains were introduced into the system to enhance the fluorescence intensity of F2. In a competition reaction, there is no doubt that the binding of a competitor to the aptamer will reduce the affinity of the aptamer for the target, thus increasing the detection limit of the sensor. Therefore, seven complementary chains were designed to obtain the best performance of the sensor. The number of bases in the complementary chain influenced the detection performance of the sensor. The calibration curves of seven complementary chains are shown in Figure 3A. The maximum values of the fluorescence quenching (FQmax) and EC50 of the aptasensors were obtained by fitting the calibration curves with a four-parameter equation according to origin, as follows

$$FQ = \frac{FQ_{\min} - FQ_{\max}}{1 + (C_{OTA} / EC50)^P} + FQ_{\max} \quad (1)$$

As shown in Figure 3B, compared with the FQmax for different complementary chains, the increase in the number of the bases enhanced the fluorescence quenching. The EC50 value represented the strength of the interaction between the aptamer and the target molecule inhibited by different complementary strands. Hence, the number of bases in the chain promoted competitiveness, inhibited OTA binding to aptamers, and decreased the binding constant. Thus, to select the best complementary strand, (FQmax/EC50) was used to evaluate the sensitivity of the aptasensor, as shown in Figure 3C. The evaluation value of A13 was significant. Therefore, the sensor constructed with A13 provided a good aptasensing performance.

The complementary chain with an F2-based aptasensor in the system was in a competitive relationship with OTA, and its concentration directly affected the competitive ability and detection effect. Therefore, the optimal concentration of the complementary strand (A13) was determined by measuring the difference in fluorescence intensity in the presence and absence of OTA. The experiment investigated the fluorescence intensities of F2 with different concentrations of A13 in 50 nmol/L and 0 nmol/L of OTA. It was observed that the fluorescence intensity increased with the increase in concentration of A13, as shown in Figure 3D. As for A13, within a specific concentration range, the difference in fluorescence intensity between 50 nmol/L and 0 nmol/L of OTA increased with the increase in the concentration ratio. Accordingly, the fluorescence quenching (F₀-F) also increased with the rise in the molar concentration ratio of A13/F2. When the molar concentration ratio was about 3, the fluorescence quenching decreased with the molar concentration ratio. It is worth noting that the higher concentration of the complementary strand enhanced hybridization with the aptamer and reduced the fluorescence difference. Therefore, a complementary chain with a molar concentration ratio of about 3 (60 nmol/L) was selected. The results are shown in Figure 3E.

3.3. Quantitative Analysis of OTA

Under the optimized conditions, the sensitivity of the proposed aptasensors was investigated. The sensing performance of the sensor for signal amplification was assessed by adding different concentrations of OTA. Figure 4A shows the calibration curve for the quantitative measurement of OTA using an F1-based aptasensor. As shown in the figure, a linear relationship between the fluorescence quenching (F₀-F) and OTA concentration was obtained in the range of 0.69 to 8.0 nmol/L. The linear regression equation corresponded to fluorescence quenching (F₀-F) = 80.9 C_{OTA} (nmol/L) - 14.4, with a correlation coefficient of 0.982. The limit of detection (LOD) was calculated as 0.69 nmol/L, as per the 3σ rule. Figure 4B shows the calibration curve for the quantitative detection of OTA using F2 with an A13 aptasensor. A linear relationship between the fluorescence and OTA concentration was observed, ranging from 0.36 to 4.0 nmol/L. The linear regression equation corresponds to

the fluorescence quenching ($F_0 - F$) = 274.8 C_{OTA} (nmol/L) + 6.5, with a correlation coefficient of 0.998. The limit of detection (LOD) was calculated to be 0.36 nmol/L, as per the 3σ rule. Compared with the performance of the developed detection platforms, the sensitivity of F2 with the A13 aptasensor was 3.4 times that of F1. However, the F1 aptasensor was simpler to operate.

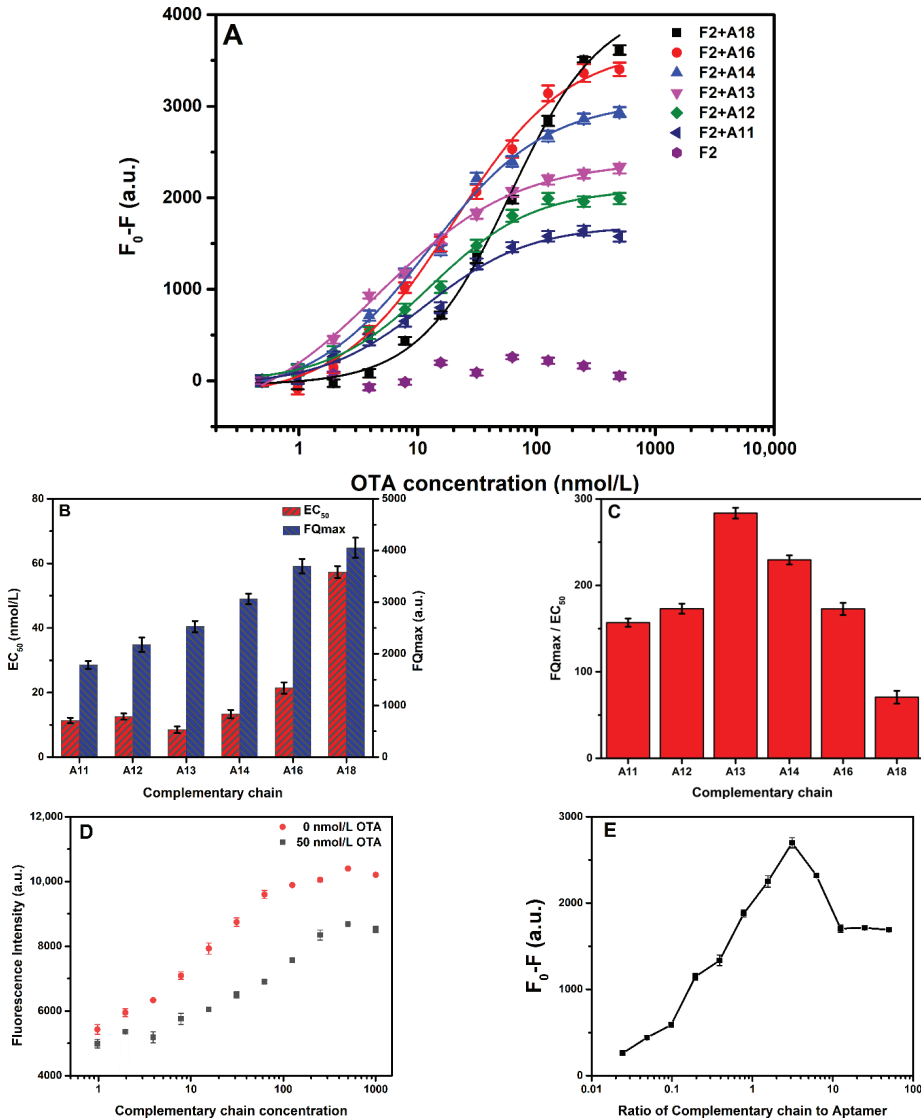


Figure 3. (A) Fluorescence quenching ($F_0 - F$) with different concentrations of OTA. (B) EC₅₀ of the sensor and the maximum values of fluorescence quenching (FQ_{max}) using different complementary sequences. (C) Sensitivity evaluation of the sensor using different complementary sequences. (D) Fluorescence intensity with different concentrations of the complementary chain (A13) (0–1000 nmol/L) in the absence and presence of 50 nmol/L OTA. (E) Fluorescence quenching ($F_0 - F$) with the ratio of the complementary chain (A13) to aptamer. The error bars denote the standard deviation of the triplicate measurements.

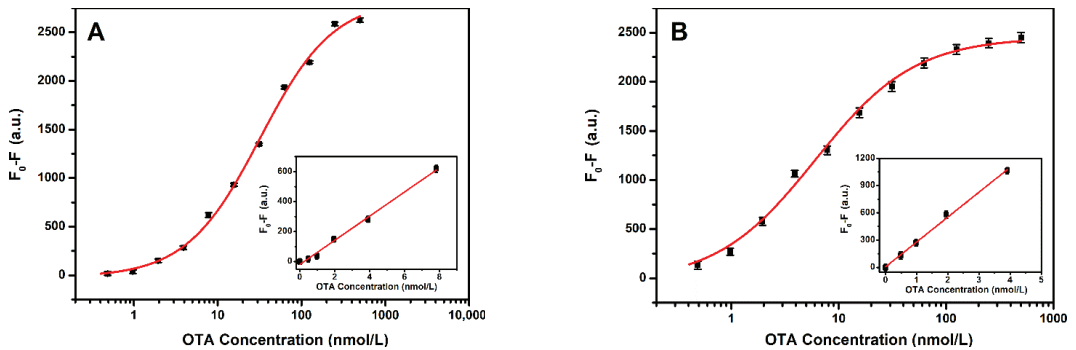


Figure 4. (A) F1 calibration curve for OTA ($n = 3$). (B) F2 with complementary chain (A13) calibration curve for OTA ($n = 3$). The inset shows the linearity of the fluorescence quenching (F_0-F) with respect to the OTA concentrations. The F1 and F2 aptamer, and complementary chain concentrations were 20 nmol/L and 60 nmol/L, respectively. The error bars represent the standard deviation of the triplicate measurements.

The sensing platform developed here was compared to other previously reported detection approaches for ochratoxin A (Table 2). As indicated in Table 2, the method developed here exhibited a lower LOD of 0.36 nmol/L than the techniques using high-affinity competitive substances such as gold nanoparticles (11.6 nmol/L) [26] and SWNTs (24.1 nmol/L) [22]. Indeed, the sensitivity of our biosensor was higher than that of the methods requiring enzyme amplification (10 nmol/L) [4,27] and that of the quencher-free fluorescence sensors (1.3 nmol/L) [13].

Table 2. Comparison of the analytical performance of the analytical methods for the detection of OTA.

Method/Material	Detection Limit (nmol/L)	Linear Range (nmol/L)	Reference
Fluorescence SYBR gold probe and exonuclease III	11.6	19.8–2476	[4]
Fluorescence PIET system	1.3	3–300	[13]
Fluorescence single-walled carbon-nanotubes (SWCNTs)	24.1	25–200	[22]
Fluorescence gold nanoparticles	22.7	25–300	[26]
Colorimetry G-quadruplex DNazymes	10	10–200	[27]
Electrochemistry polythiophene-3-carboxylic acid	0.31	0.31–12.4	[28]
Quencher-free fluorescence (F1)	0.69	0.69 to 8.0	This work
Quencher-free fluorescence (F2 with A13)	0.36	0.36 to 4.0	This work

3.4. Specificity Analysis and Application to Real Samples

The specificity of the constructed aptasensor for OTA was tested in a real sample. In addition, the system was applied to detect other common analogs, including OTB, AFB1, DON, FB1, and ZEA. The relevant detection process has been described in various reports [25]. The detection results are shown in Figure 5. The fluorescence quenching of 250 nmol/L of interference was much lower than for 62.5 nmol/L of OTA. These results demonstrate the excellent specificity and selectivity of the proposed platform for OTA determination.

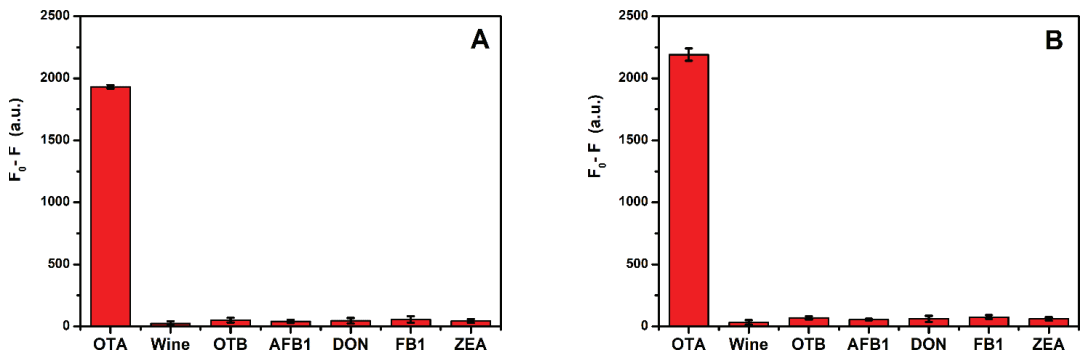


Figure 5. (A) Selectivity of the F1 aptasensor ($n = 3$). (B) Selectivity of the F2 with A13 aptasensor ($n = 3$). Fluorescence quenching ($F_0 - F$) of 62.5 nmol/L OTA and 250 nmol/L OTB, AFB1, DON, FB1, and ZEA. The error bars denote the standard deviation of the triplicate measurements.

The applicability of this sensing system for real sample analysis for OTA determination was conducted by standard addition and recovery analysis in actual red wine samples. The relevant detection process has been described in various reports [25]. The pre-treatment of the sample was performed using the scheme of double-liquid–liquid extraction, which was explicitly designed according to the chemical properties of OTA. OTA is only soluble in the aqueous phase under alkaline conditions, while it is soluble in the organic phase under acidic conditions. Therefore, cross-reactivity with interferents and other matrix components could be overcome in pre-treated red wine samples, even for some molecules with similar chemical properties to OTA. Therefore, the effective and specific detection of OTA in wine can be achieved by combining sample pre-treatment and fluorescent aptasensing.

To show the potential applicability and accuracy of the sensing strategy, the recovery rates were calculated based on three-level concentrations of OTA spiked in red wine samples. Excellent recoveries were obtained, varying between 88.7% and 107.7% by using the F1 aptasensor and between 95.7% and 104.3% using the F2 with A13 aptasensor in the samples spiked with OTA. These results demonstrate that the proposed method could be applied to OTA detection in real complex samples. The corresponding results are displayed in Table 3.

Table 3. Detection of OTA in red wine ($n = 3$).

Method	Sample	Found (nmol/L)	Added (nmol/L)	Total Found (nmol/L)	Recovery (%)
F1	1	Not detected	4.0	3.89 ± 0.28	97.3
F1	2	Not detected	2.0	2.15 ± 0.26	107.7
F1	3	Not detected	1.0	0.89 ± 0.13	88.7
F2 + A13	4	Not detected	4.0	3.85 ± 0.12	96.2
F2 + A13	5	Not detected	2.0	2.09 ± 0.15	104.3
F2 + A13	6	Not detected	1.0	0.96 ± 0.12	95.7

This kit can meet the maximum permissible concentration at 2 $\mu\text{g}/\text{kg}$ (corresponding to 5 nmol/L), as specified in European Commission No. 123/2005 [20]. It also provides promising potential for portable detection and in-field monitoring of small molecules such as OTA.

4. Conclusions

To summarize, a rapid and straightforward sensing platform is developed for the sensitive and selective detection of OTA based on a quencher-free fluorescence approach by a FAM-labelled aptamer probe. The detection principle relies on the high sensitivity, specificity, and high affinity between OTA and its aptamer, as well as the quenching ability

of guanine induced by PIET. By comparing the performances of the two aptasensors, the sensitivity of F2 with the A13 aptasensor (LOD is 0.36 nmol/L) was better than that of the F1 aptasensor (LOD is 0.69 nmol/L), while the F1 aptasensor was simpler to perform. The kits developed here based on the two designed aptasensors can meet the maximum permissible concentration at 2 µg/kg (corresponding to 5 nmol/L), as specified in European Commission No. 123/2005 [20]. The proposed strategy provides fast response, low cost, and high sensitivity and selectivity for OTA detection. It is simple and straightforward. It also shows good potential to be integrated into portable systems, which will facilitate on-site mycotoxin screening. In addition, the strategy of using a single-labeled fluorophore and guanine as a quencher without the necessity for a labeled quencher may be applied to detect various other targets in different fields, such as in environmental monitoring and food safety fields.

Author Contributions: C.Y., conceptualization, methodology, writing, project administration, and funding acquisition. F.A., methodology, validation, investigation, and writing. A.R., methodology, investigation, and reviewed the manuscript. Y.S., methodology, validation, and investigation. X.C., methodology, validation, and investigation. S.C., methodology, validation, and investigation. B.S., methodology, validation, and investigation. C.X., methodology, writing, supervision, project administration, and funding acquisition. All authors have read and agreed to the published version of the manuscript.

Funding: This work was supported by the National Natural Science Foundation of China (21876017), the Fundamental Research Funds for the Central Universities (DUT17LAB18), the Open Funds of the State Key Laboratory of Electroanalytical Chemistry (SKLEAC202105).

Institutional Review Board Statement: Not applicable.

Data Availability Statement: Not applicable.

Acknowledgments: Not applicable.

Conflicts of Interest: The authors declare no conflict of interest.

References

- Zhang, Y.; Lai, B.S.; Juhas, M. Recent Advances in Aptamer Discovery and Applications. *Molecules* **2019**, *24*, 941. [[CrossRef](#)] [[PubMed](#)]
- Amero, P.; Khatua, S.; Rodriguez-Aguayo, C.; Lopez-Berestein, G. Aptamers: Novel Therapeutics and Potential Role in Neuro-Oncology. *Cancers* **2020**, *12*, 2889. [[CrossRef](#)] [[PubMed](#)]
- Lv, L.; Li, D.; Liu, R.; Cui, C.; Guo, Z. Label-Free Aptasensor for Ochratoxin A Detection Using SYBR Gold as a Probe. *Sens. Actuators B Chem.* **2017**, *246*, 647–652. [[CrossRef](#)]
- Liu, R.; Wu, H.; Lv, L.; Kang, X.; Cui, C.; Feng, J.; Guo, Z. Fluorometric Aptamer Based Assay for Ochratoxin A Based on the Use of Exonuclease III. *Microchim. Acta* **2018**, *185*, 254. [[CrossRef](#)] [[PubMed](#)]
- Taghdisi, S.M.; Danesh, N.M.; Nameghi, M.A.; Ramezani, M.; Abnous, K. A Label-Free Fluorescent Aptasensor for Selective and Sensitive Detection of Streptomycin in Milk and Blood Serum. *Food Chem.* **2016**, *203*, 145–149. [[CrossRef](#)] [[PubMed](#)]
- Guo, X.; Wen, F.; Zheng, N.; Saive, M.; Fauconnier, M.L.; Wang, J. Aptamer-Based Biosensor for Detection of Mycotoxins. *Front. Chem.* **2020**, *8*, 195. [[CrossRef](#)] [[PubMed](#)]
- Rhouati, A.; Yang, C.; Hayat, A.; Marty, J.L. Aptamers: A Promising Tool for Ochratoxin A Detection in Food Analysis. *Toxins* **2013**, *5*, 1988–2008. [[CrossRef](#)]
- Peltomaa, R.; Benito-Peña, E.; Moreno-Bondi, M.C. Bioinspired Recognition Elements for Mycotoxin Sensors. *Anal. Bioanal. Chem.* **2018**, *410*, 747–771. [[CrossRef](#)]
- Shen, P.; Li, W.; Ding, Z.; Deng, Y.; Liu, Y.; Zhu, X.; Cai, T.; Li, J.; Zheng, T. A Competitive Aptamer Chemiluminescence Assay for Ochratoxin A Using a Single Silica Photonic Crystal Microsphere. *Anal. Biochem.* **2018**, *554*, 28–33. [[CrossRef](#)]
- Li, R.; Wen, Y.; Wang, F.; He, P. Recent Advances in Immunoassays and Biosensors for Mycotoxins Detection in Feedstuffs and Foods. *J. Anim. Sci. Biotechnol.* **2021**, *12*, 108. [[CrossRef](#)]
- Liu, M.; Li, X.; Li, B.; Du, J.; Yang, Z. A Fluorometric Aptamer-Based Assay for Ochratoxin A by Using Exonuclease III-Assisted Recycling Amplification. *Microchim. Acta* **2019**, *187*, 46. [[CrossRef](#)] [[PubMed](#)]
- Yang, C.; Dong, S.; Abbsd, F.; Chu, X.; Fan, A.; Rhouati, A.; Mao, J.; Liu, Y. Label-Free Fluorescence Aptasensor for Ochratoxin A Using Crystal Violet as Displacement-Type Probe. *Chin. J. Anal. Chem.* **2021**, *49*, 55–62. [[CrossRef](#)]
- Zhao, H.; Xiang, X.; Chen, M.; Ma, C. Aptamer-Based Fluorometric Ochratoxin A Assay Based on Photoinduced Electron Transfer. *Toxins* **2019**, *11*, 65. [[CrossRef](#)] [[PubMed](#)]

14. Torimura, M.; Kurata, S.; Yamada, K.; Yokomaku, T.; Kamagata, Y.; Kanagawa, T.; Kurane, R. Fluorescence-Quenching Phenomenon by Photoinduced Electron Transfer between a Fluorescent Dye and a Nucleotide Base. *Anal. Sci.* **2001**, *17*, 155–160. [[CrossRef](#)]
15. Heinlein, T.; Knemeyer, J.; Piestert, O. Photoinduced Electron Transfer between Fluorescent Dyes and Guanosine Residues in DNA-Hairpins. *J. Phys. Chem.* **2003**, *107*, 7957–7964. [[CrossRef](#)]
16. Liu, H.; Ma, L.; Ma, C.; Du, J.; Wang, M.; Wang, K. Quencher-Free Fluorescence Method for the Detection of Mercury (II) Based on Polymerase-Aided Photoinduced Electron Transfer Strategy. *Sensors* **2016**, *16*, 1945. [[CrossRef](#)]
17. Wang, W.; Jin, Y.; Zhao, Y.; Yue, X.; Zhang, C. Single-Labeled Hairpin Probe for Highly Specific and Sensitive Detection of Lead(II) Based on the Fluorescence Quenching of Deoxyguanosine and G-Quartet. *Biosens. Bioelectron.* **2013**, *41*, 137–142. [[CrossRef](#)]
18. Hwang, G.T. Single-Labeled Oligonucleotides Showing Fluorescence Changes upon Hybridization with Target Nucleic Acids. *Molecules* **2018**, *23*, 124. [[CrossRef](#)]
19. Yang, C.; Wang, Y.; Marty, J.L.; Yang, X. Aptamer-Based Colorimetric Biosensing of Ochratoxin A Using Unmodified Gold Nanoparticles Indicator. *Biosens. Bioelectron.* **2011**, *26*, 2724–2727. [[CrossRef](#)]
20. Mateo, R.; Medina, Á.; Mateo, E.M.; Mateo, F.; Jiménez, M. An Overview of Ochratoxin A in Beer and Wine. *Int. J. Food Microbiol.* **2007**, *119*, 79–83. [[CrossRef](#)]
21. Cruz-Aguado, J.A.; Penner, G. Determination of Ochratoxin A with a DNA Aptamer. *J. Agric. Food Chem.* **2008**, *56*, 10456–10461. [[CrossRef](#)] [[PubMed](#)]
22. Guo, Z.; Ren, J.; Wang, J.; Wang, E. Single-Walled Carbon Nanotubes Based Quenching of Free FAM-Aptamer for Selective Determination of Ochratoxin A. *Talanta* **2011**, *85*, 2517–2521. [[CrossRef](#)] [[PubMed](#)]
23. Yang, C.; Lates, V.; Prieto-Simón, B.; Marty, J.L.; Yang, X. Aptamer-DNAzyme Hairpins for Biosensing of Ochratoxin A. *Biosens. Bioelectron.* **2012**, *32*, 208–212. [[CrossRef](#)] [[PubMed](#)]
24. Li, Y.; Peng, Z.; Li, Y.; Xiao, M.; Tan, G.; Wang, W.; Wang, Y.; Fang, M.; Zhang, S.; Tang, C.; et al. An Aptamer-Array-Based Sample-to-Answer Biosensor for Ochratoxin a Detection via Fluorescence Resonance Energy Transfer. *Chemosensors* **2021**, *9*, 309. [[CrossRef](#)]
25. Yang, C.; Zhang, Y.; Li, D.; Liu, Y.; Sun, B. Chemiluminescence Sensor Based on Composite Functional Nucleic Acid for Detection of Ochratoxin A in Wine. *Chin. J. Anal.* **2021**, *49*, 496–503. [[CrossRef](#)]
26. Lv, L.; Cui, C.; Liang, C.; Quan, W.; Wang, S.; Guo, Z. Aptamer-Based Single-Walled Carbon Nanohorn Sensors for Ochratoxin A Detection. *Food Control.* **2016**, *60*, 296–301. [[CrossRef](#)]
27. Yu, X.; Lin, Y.; Wang, X.; Xu, L.; Wang, Z.; Fu, F. Exonuclease-Assisted Multicolor Aptasensor for Visual Detection of Ochratoxin A Based on G-Quadruplex-Hemin DNAzyme-Mediated Etching of Gold Nanorod. *Microchim. Acta* **2018**, *185*, 259. [[CrossRef](#)]
28. Zejli, H.; Goud, K.Y.; Louis, J. Talanta Label Free Aptasensor for Ochratoxin A Detection Using Polythiophene-3-Carboxylic Acid. *Talanta* **2018**, *185*, 513–519. [[CrossRef](#)]

Article

Development of Fluorescent Aptasensors Based on G-Quadruplex Quenching Ability for Ochratoxin A and Potassium Ions Detection

Cheng Yang ^{1,*}, Xiaolin Chu ¹, Li Zeng ², Amina Rhouati ³, Fathimath Abbas ¹, Shengnan Cui ¹ and Daiqin Lin ^{2,*}

¹ State Key Laboratory of Fine Chemicals, Department of Chemistry, School of Chemical Engineering, Dalian University of Technology, Dalian 116024, China; 21907036@mail.dlut.edu.cn (X.C.); ferthunabbas@mail.dlut.edu.cn (F.A.); cuishengnan@mail.dlut.edu.cn (S.C.)

² Institute of Inspection and Testing for Industrial Products of Jiangxi General Institute of Testing, Nanchang 330052, China; zengli19890610@163.com

³ Bioengineering Laboratory, Higher National School of Biotechnology, Constantine 25100, Algeria; amina.rhouati@gmail.com

* Correspondence: yangcheng@dlut.edu.cn (C.Y.); zzl0711@126.com (D.L.)

Abstract: G-quadruplexes have received significant attention in aptasensing due to their structural polymorphisms and unique binding properties. In this work, we exploited the fluorescence-quenching properties of G-quadruplex to develop a simple, fast, and sensitive platform for fluorescence detection of ochratoxin A (OTA) and potassium ions (K⁺) with a label-free fluorophore and quencher strategy. The quenching ability of G-quadruplex was confirmed during the recognition process after the formation of the G-quadruplex structure and the quenching of the labeled fluorescein fluorophore (FAM). The fluorescence-quenching mechanism was studied by introducing specific ligands of G-quadruplex to enhance the quenching effect, to show that this phenomenon is due to photo-induced electron transfer. The proposed fluorescence sensor based on G-quadruplex quenching showed excellent selectivity with a low detection limit of 0.19 nM and 0.24 μM for OTA and K⁺, respectively. Moreover, we demonstrated that our detection method enables accurate concentration determination of real samples with the prospect of practical application. Therefore, G-quadruplexes can be excellent candidates as quenchers, and the strategy implemented in the study can be extended to an aptasensor with G-quadruplex.

Keywords: G-quadruplex; label-free; fluorescence aptasensor; photo-induced electron transfer

Citation: Yang, C.; Chu, X.; Zeng, L.; Rhouati, A.; Abbas, F.; Cui, S.; Lin, D.

Development of Fluorescent Aptasensors Based on G-Quadruplex Quenching Ability for Ochratoxin A and Potassium Ions Detection.

Biosensors **2022**, *12*, 423. <https://doi.org/10.3390/bios12060423>

Received: 4 May 2022

Accepted: 10 June 2022

Published: 16 June 2022



Copyright: © 2022 by the authors. Licensee MDPI, Basel, Switzerland. This article is an open access article distributed under the terms and conditions of the Creative Commons Attribution (CC BY) license (<https://creativecommons.org/licenses/by/4.0/>).

1. Introduction

DNA is an important molecule responsible for storing and completing genetic information. It is well known that DNA can form different conformations under specific conditions, including single-stranded hairpins, double- or triple-stranded helices, and quadruplex structures [1–3]. The G-quadruplex is a unique secondary structure of DNA folding from a single-strand or several strands of DNA sequences rich in guanine with a highly ordered and diverse structure [4,5]. According to the direction of its DNA strands, it can be divided into parallel, antiparallel, and mixed structures [6]. The G-quadruplex structure mainly depends on the length of the DNA sequence, the orientation of the chain and loop, and the cation nature [7]. G-quadruplex has attracted the attention of relevant researchers, pushing them to develop various platforms based on G-quadruplex for the analysis and detection of a variety of substances, including metal ions [8,9], toxins [10–12], nucleic acids [13,14], and other small molecules.

According to previous reports, the fluorophore can be quenched at an appropriate distance using nucleotide bases by photo-induced electron transfer (PIET), especially between guanine bases [15–17]. Since G-quadruplex is a structure with a high accumulation of guanine and low oxidation potential [18], it can be ideally used as an electron donor.

Therefore, resonance energy transfer or photo electron transfer may occur between G-quadruplex and the fluorophore, resulting in significant fluorescence-quenching induced by G-quadruplex. Previous studies have established the detection of lead and silver ions using fluorescence-quenching between G-quadruplex and HEX [19]. It has been demonstrated that the quenching between the G4/hemin complex and fluorescent dyes can be employed as a logic circuit platform [20]. Unfortunately, the exact mechanism of fluorescence-quenching caused by the G-quadruplex has not been widely accepted by the academic community.

Ochratoxin A (OTA) and potassium ions (K^+) were used as model analytes to demonstrate that antiparallel and parallel G-quadruplex structures can act as quenchers for the label-free fluorescence probe, SYBR Green I (SGI). By replacing SGI with a fluorescent label FAM (fluorescein), we demonstrated that fluorescence-quenching was not caused by structural disassembly. However, this phenomenon was caused by the formed G-quadruplexes during the recognition process. In order to further investigate the quenching mechanism between G-quadruplex and fluorophore, we studied the fluorescence change in the system after the interaction between G-quadruplex and specific ligands of G-quadruplex, crystal violet (CV) for antiparallel G-quadruplex and hemin for parallel G-quadruplex, respectively. We found that adding the G-quadruplex specific ligand to the system leads to the accumulation and attachment of the ligand to the G-quadruplex, thus decreasing the fluorescence signal intensity. We believe that the fluorescence-quenching ability of the G-quadruplex is mainly due to PIET. Therefore, based on the excellent quenching ability of the G-quadruplex, we designed a simple label-free fluorophore and quencher fluorescence detection platform for OTA and K^+ with good sensitivity and selectivity.

2. Experimental Section

2.1. Reagents and Chemicals

The sequence forming the antiparallel G-quadruplex is a new aptamer, which truncated five useless bases from the 3' end of the original OTA aptamer (OTAapt36) to create a new blunt end aptamer (OTAapt31) [21]. OTA-A9 to OTA-A12 are the sequences to form a hybrid with an OTA aptamer. The parallel G-quadruplex sequence is 5'-GG GTG GGT GGG TGG G-3', called G4. By adding complementary bases to the 3' and 5' ends of G4, we obtained a series of sequences with different bases, named G4, 1AG4, 3AG4, 5AG4, 7AG4, 9AG4, 11AG4, 13AG4, and 15AG4 (the parts that can form complementary sequences are underlined in the list shown in Table S1). The sequence that forms a hybrid with the parallel aptamer is 5'-CCC ACC CAC CCA CCC-3', designated G4-C15. By shortening the bases at the 3' end of C15, we designed a series of sequences with different bases, named G4-C11 to G4-C15. OTAapt31-FAM and 5AG4-FAM were the antiparallel and parallel G-quadruplex labeled with fluorescein (FAM) at the 3' end. The nucleotide sequence is shown in Table S1.

All synthesized oligonucleotides were purchased from Shanghai Sangon Biotechnology Co. Ltd. (Shanghai, China). A stock solution of 100 μ M for each oligonucleotide was prepared by dissolving them in ultra-pure water and then diluting the samples to the required concentrations before use. The concentrations were determined by measuring solution absorbance at 260 nm by the ReadMax 1900 Absorbance Microplate Reader. DNA stock solutions were stored at 4 °C before use. Sodium chloride (NaCl), potassium chloride (KCl), calcium chloride ($CaCl_2$), magnesium chloride ($MgCl_2$), ammonium chloride (NH_4Cl), zinc chloride ($ZnCl_2$), hydrochloric acid (HCl), methanol, Dimethyl sulfoxide (DMSO), Toluene ($C_6H_5CH_3$), and dichloromethane (CH_2Cl_2) were purchased from Sinopharm Chemical Reagent Co., Ltd. (Beijing, China). Tris (hydroxymethyl) carbamate (Tris, $C_4H_{11}NO_3$), SYBR Green I (SGI), and Tween 20 were purchased from BBI Life Sciences (Shanghai, China). Ochratoxin A (OTA), Ochratoxin B (OTB), Aflatoxin B1 (AFB1), Aflatoxin G1 (AFG1), Patulin, Fumonisin B1 (FB1), Zearalenone (ZEN), Deoxynivalenol (DON), crystal violet (CV), and hemin were purchased from Sigma-Aldrich (St. Louis, MO, USA). All the chemicals were at least analytical grade.

2.2. Apparatus

All solutions were prepared with ultra-pure water from the Millipore Direct-Q Pure Water Treatment System (Millipore Corporation, Burlington, MA, USA). All fluorescence measurements were performed at room temperature on a Safire II multi-detection microplate reader (Tecan, Switzerland). The fluorescent groups SGI and FAM provide fluorescence in the system. The excitation wavelength was 483 nm, and the emission wavelength was 525 nm. The UV Absorbance spectra were performed at room temperature on the ReadMax 1900 Absorbance Microplate Reader (Shanghai Flash Spectrum Biotechnology Co., Ltd., Shanghai, China).

2.3. Demonstration of the Mechanism of Fluorescence-Quenching

For the antiparallel G-quadruplexes system, different concentrations of OTA were mixed with 20 nM OTA aptamer (antiparallel G-quadruplex) in 10 mM Tris-HCl buffer (pH = 8.4) containing $0.3\times$ SGI, 0.2% Tween 20 and 6.25 mM Ca^{2+} . For parallel G-quadruplexes, different concentrations of K^+ were mixed with 20 nM G-quadruplex (parallel) in 10 mM Tris-HCl buffer (pH = 8.4) with $0.3\times$ SGI, 0.2% Tween 20. All solutions were incubated at room temperature for 20 minutes, and the fluorescence intensity was measured using a Safire II microplate reader. CV (antiparallel structure-specific ligand) and hemin (parallel structure-specific ligand) were added to the parallel and antiparallel G-quadruplex systems, and the fluorescence was measured after three minutes of incubation. All experiments were repeated three times independently.

2.4. Fluorescent Detection of OTA and K^+

For OTA, 80 μL of different concentrations of OTA were mixed with 20 μL of 100 nM aptamer (antiparallel G-quadruplex) in a solution of 10 mM Tris-HCl buffer (pH = 8.4), with 1.5X SGI, 1.0% Tween 20 and 31.25 mM Ca^{2+} . For K^+ , 80 μL of different concentrations of K^+ were mixed with 20 μL of 100 nM parallel G-quadruplex in 10 mM Tris-HCl buffer (pH = 8.4), with 1.5 \times SGI, 1.0% Tween 20. All the test solutions were incubated at room temperature for 20 minutes, followed by the fluorescence measurement with a Safire II microplate reader. All experiments were repeated three times independently.

2.5. Specificity of the Aptasensor

To investigate the selectivity of the sensing method, we compared the fluorescence intensity changes induced by the two sensing systems with potential interfering toxins and ions, respectively. Under optimized conditions, OTB, AFB1, AFG1, FB1, patulin, ZEA, and DON were used as interfering substances for OTA detection. In parallel, NH_4^+ , Na^+ , Ca^{2+} , Mg^{2+} , Zn^{2+} , and Cd^{2+} were used as interfering substances for K^+ detection. The fluorescence intensity change was detected according to the method described in Section 2.4. All experiments were repeated three times independently.

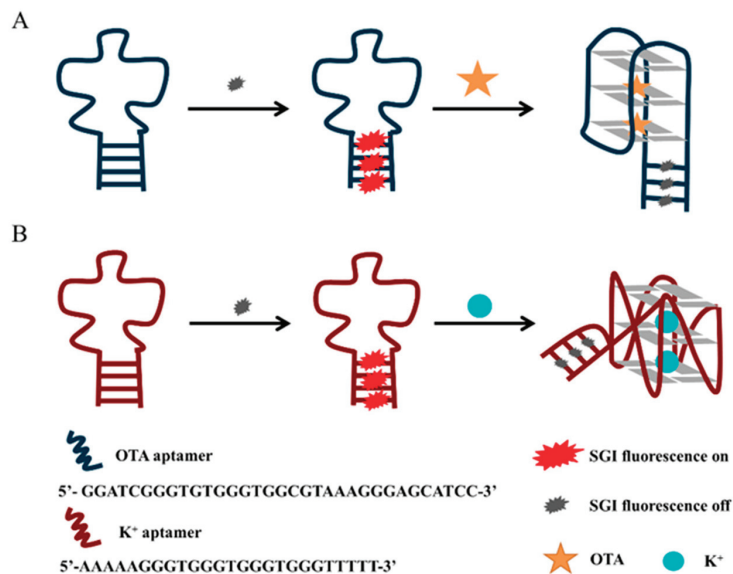
2.6. Detection of OTA and K^+ in Real Samples

To verify the feasibility of OTA and K^+ detection methods in real samples, red wine (purchased from local supermarkets) and goat serum were used as real samples. In the spike recovery experiment, 2.0 μL , 4.0 μL , and 8.0 μL of 10 μM OTA standard solution were added to 10 mL of red wine samples to obtain a series of spiked sample solutions. The spiked samples were pretreated using the extraction protocol described in our previous study [21]. The samples after pretreatment were detected according to the method described in Section 2.4, and the fluorescence intensity was recorded. Goat serum samples were diluted 1000-fold with Tris-HCl buffer (10 mM, pH 8.4). The corresponding concentrations of goat serum samples were calculated from the calibration curve and compared with the atomic absorption spectrometry (AAS) measurements. All experiments were repeated five times independently.

3. Results and Discussion

3.1. The Principle of Fluorescence Detection of OTA and Potassium Ions Based on G-Quadruplex Quenching

Scheme 1 illustrates the principle of the proposed platform for the detection of OTA and K^+ . In solution, the fluorescent dye SGI in the free state can only emit weak fluorescence, but the fluorescence is significantly enhanced when SGI binds to double-stranded DNA. The complementary sequences at the 5' and 3' ends of the designed DNA sequence will hybridize, hence the intercalation of SGI into the duplex helix, resulting in fluorescence. The PIET process can occur between the G-quadruplex and the fluorescent dye embedded in the duplex helix under the induction of the target, resulting in a clear fluorescence-quenching phenomenon. Therefore, based on this principle, OTA and K^+ can be quantitatively monitored in the solution. For an antiparallel G-quadruplex, we designed a new aptamer that truncated five useless bases from the 3' end of the original OTA aptamer (OTAapt36) to create a new blunt end aptamer (OTAapt31) [21], which can effectively shorten the distance between fluorophore and quencher, enabling a detection that could not be achieved before. As shown in Figure 1A, it was observed that the system exhibited a significant fluorescence intensity at 525 nm in the absence of OTA, which was attributed to the binding of SGI to the duplex helix under the induction of the target, resulting in a clear fluorescence-quenching phenomenon. The oligonucleotides originally in the random coil state were induced to form an antiparallel G-quadruplex structure by adding OTA. The increased number of the formed G-quadruplex structures leads to a more profound PIET phenomenon between the G-quadruplex and the intercalated SGI, where the fluorescence-quenching phenomenon is also more significant. For parallel G-quadruplexes, we designed oligonucleotides that can be induced to form parallel structures by K^+ . It can be easily seen that the parallel structure G-quadruplex formed under the induction of K^+ has a specific quenching effect on the fluorescent dye embedded in the double-strand (Figure 1B).



Scheme 1. Schematic illustration of fluorescent aptasensors based on G-quadruplex quenching ability (A) for the detection of OTA (B) for the detection of K^+ .

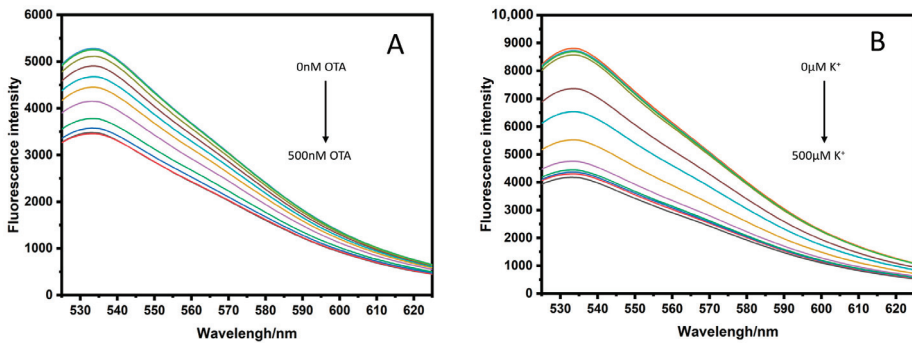


Figure 1. (A) Fluorescence emission spectra of unlabeled fluorescence antiparallel G-quadruplex with different concentrations of OTA (0, 0.48, 0.96, 1.95, 3.9, 7.8, 15.6, 31.2, 72.5, 125, 250, 500 nM), (B) Fluorescence emission spectra of unlabeled fluorescence parallel G-quadruplex with different concentrations of K^+ (0, 0.48, 0.96, 1.95, 3.9, 7.8, 15.6, 31.2, 72.5, 125, 250, 500 μM).

3.2. Discussion on the Fluorescence-Quenching Mechanism

Considering that the SGI escape due to double-strand helix dissociation can also lead to fluorescence decrease, we investigated using FAM-labeled G-quadruplexes (OTAapt31-FAM and 5AG4-FAM). We replaced the label-free fluorophore with a labeled fluorophore (FAM) at the end of the aptamer. FAM has similar fluorescence characteristics to SGI. The FAM is directly labeled on the nucleic acid chain at a ratio of 1:1, and it does not detach from the labeled nucleic acid. So, the fluorescence intensity can visually reflect changes in the environment surrounding the FAM. The target (OTA or K^+) induces the aptamer conformational change to a G-quadruplex structure (antiparallel or parallel). While the fluorescence intensity was still showing a downward trend with the increase of target (OTA or K^+) concentration (Figure S3). It can be noted that the quenching effect of G-quadruplex was effective for labeled fluorophore, indicating that the quenching is because of the PIET mechanism instead of the dissociation of duplex strands.

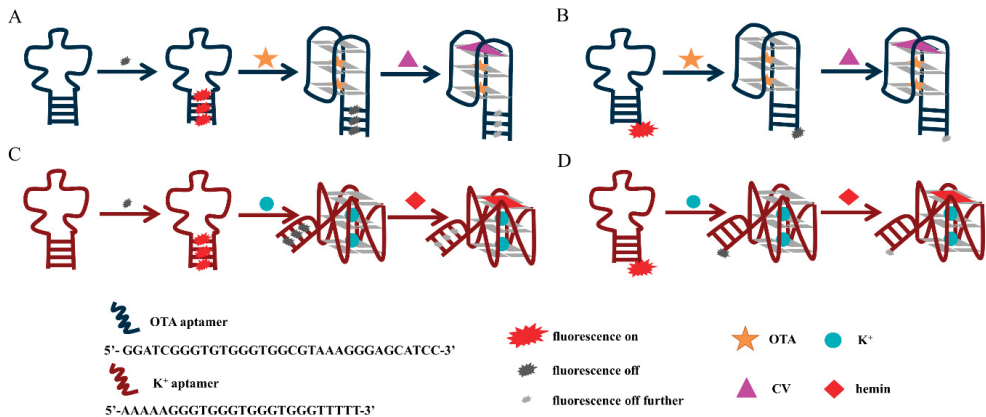
The fluorescence intensity increased after adding the complementary sequences to the FAM-labeled antiparallel G-quadruplex system. The results showed that the hybridization of the complementary strands destroyed the structure of the G-quadruplex (Figure S4), resulting in the inhibition of fluorescence-quenching. A previous study depicted an aptasensor utilizing guanines as a quencher based on PIET [22]. However, the quencher is different from the current study. The FAM-labeled aptamers used in this research display strong fluorescence, although they were rich in guanine (G). With the addition of the target, the G-rich sequence formed a G-quadruplex to quench FAM. Taken together, this further confirms and verifies that the presence of the G-quadruplex is responsible for the quenching phenomenon.

The fluorescence-quenching mechanism can be divided into dynamic quenching and static quenching. The static quenching depends on forming a non-fluorescent ground state complex between the fluorescent molecule and the quencher [23], which is reflected in the absorption spectrum change of the fluorophore. However, the position and intensity of the absorption peak of the fluorescent molecules do not change in the presence of the G-quadruplex. The dynamic quenching comprises energy transfer [24] or electron transfer [25], which changes only the excitation spectrum of the fluorophore but not its absorption spectrum. The prerequisite for the occurrence of fluorescence resonance energy transfer is that both the fluorescent donor and acceptor molecules can fluoresce [26]. However, the G-quadruplex absorbs approximately 260 nm and shows very low fluorescence quantum yields [27].

In order to confirm the basic principle of the fluorescence-quenching of G-quadruplexes, we introduced the ligands of G-quadruplex, crystal violet (CV) for antiparallel G-quadruplex,

and hemin for parallel G-quadruplex. Both complexes have a larger π -plane structure, and the binding sites of the complex and the G-quadruplex are on the outer G-tetrad.

CV is a triphenylmethane dye, and the fluorescence of CV bound to G-quadruplex with an antiparallel structure was significantly higher than that of G-quadruplex with a parallel structure in solution because the end loops of the antiparallel structure protect the bound CV from the solvent. It has been shown that the binding of the antiparallel G-quadruplexes to CV usually occurs in the outer G-quadrant [28]. Therefore, the principle of the verification process is shown in Scheme 2A,B, and the results are shown in Figure 2A,B. After the combination of CV with the antiparallel-G quadruplex, the fluorescence in the system was more significantly quenched. These results indicate that introducing CV increases the electron cloud density of the formed G-quadruplex/CV complex, and electrons are more easily transitioned from the G-quadruplex to the ground state positions released by the fluorophore. As a result, it is difficult for the electrons in the excited state of the fluorophore to return to the ground state, which manifests as a substantial decrease in the overall fluorescence intensity.



Scheme 2. Schematic illustration of verifying the G-quadruplex quenching mechanism with the ligands of G-quadruplex (A) Antiparallel G-quadruplex unlabeled (B) Antiparallel G-quadruplex FAM-labeled (C) Parallel G-quadruplex unlabeled (D) Parallel G-quadruplex FAM-labeled.

For the parallel G-quadruplex system, we explored the mechanism of fluorophore quenching by introducing hemin, one of the common G-quadruplex ligands which bind to the parallel G-quadruplex with strong affinity. The parallel G-quadruplex and hemin binding usually occurs at the 3' end of G-tetrad [29]. The principle of the verification process is shown in Scheme 2C,D, and the results are shown in Figure 2C,D. After adding hemin, the quenching phenomenon of fluorescence is more significant. This phenomenon can be attributed to the G-quadruplex/hemin complex, which provides more electrons. These electrons occupy the ground state position of the fluorophore, and more electrons in the fluorophore are excited, which is manifested in a substantial decrease in the overall fluorescence intensity.

The results demonstrate that the ligands add to an antiparallel or parallel G-quadruplex structure induce an increase in the electron cloud density of the structure, thus exhibiting a dramatic quenching of fluorescence. Moreover, we can confirm that the quenching of the fluorophore by the G-quadruplex was mainly caused by electron transfer. When the electrons of the fluorophore jump from the ground state to the excited state, the electrons of the G-quadruplex occupy the ground state of the fluorophore, and it will be difficult for the electrons of the fluorophore to return to the ground state, resulting in fluorescence quenching.

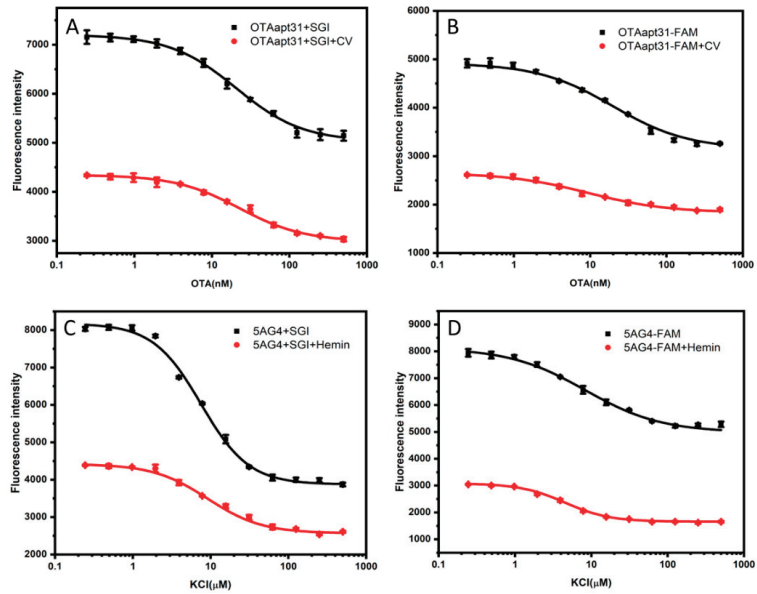


Figure 2. (A) Changes of SGI fluorescence response curves of antiparallel G-quadruplexes before and after adding CV at different OTA concentrations (B) Changes of FAM fluorescence response curves of antiparallel G-quadruplexes before and after adding CV at different OTA concentrations. (C) Changes of SGI fluorescence response curves of parallel G-quadruplexes before and after adding Hemin at different K^+ concentrations (D) Changes of FAM fluorescence response curves of parallel G-quadruplexes before and after adding Hemin at different K^+ concentrations. The error bar represents the standard deviations of the three parallel experiments.

3.3. G-Quadruplex-Based Label-Free and Quencher-Free Fluorescence Detection Platform for OTA and K^+

Based on the quenching effect of G-quadruplex on the fluorophore, we constructed an ultrasensitive detection platform with a label-free fluorophore and quencher, with no complementary strands. The sensitive detection platform allows the highly sensitive determination of OTA and K^+ . Considering the simplicity and practicality of the detection process, we achieved the detection of OTA and K^+ using an antiparallel G-quadruplex (OTAapt31) and parallel G-quadruplex (5AG4). The results are shown in Figure 3.

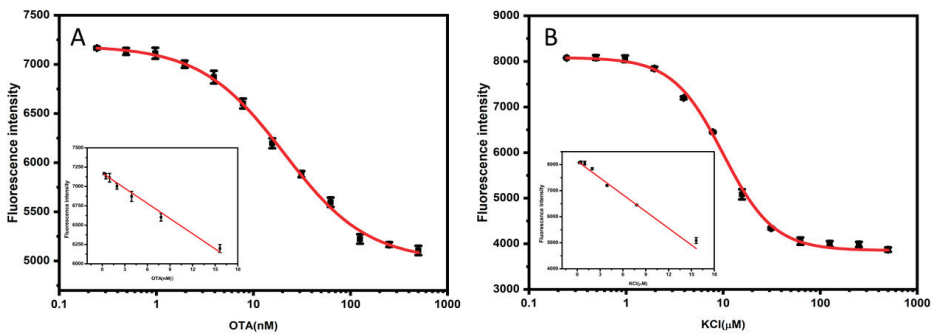


Figure 3. (A) Calibration curve for OTA. The inset shows the linear relationship between the fluorescence intensity and the concentration of the OTA (B) Calibration curve for K^+ . The inset shows the linear relationship between the fluorescence intensity and the concentration of K^+ . The error bar represents the standard deviations of the three parallel experiments.

The linear range of the OTA sensor was from 0.19 to 15.63 nM, and the limit of detection (LOD) was 0.19 nM; the linear equation was $F = 7174.24 - 65.42 C_{OTA}$ (nM), with a linear correlation coefficient of 0.987. The linear range of the K^+ sensor was from 0.24 to 15.63 μ M, and the LOD was 0.24 μ M; the linear equation was $F = 8130.76 - 214.47 C_{K^+}$ (μ M), with a linear correlation coefficient of 0.996. The performance of our bioassay was compared with previously reported sensors. As shown in Table S2, the detection performance of our method was comparable to that reported in most of the other studies. Our method adopts a non-competitive strategy, so the detection limit is one order of magnitude lower than that of the competitive strategy [22] and comparable to methods of enzymatic amplification strategies [30,31]. Therefore, it can be concluded that our assay technique may provide a simple, fast, and cost-effective method for sensitive quantification.

3.4. Specificity of the Aptasensor

The selectivity of the sensing method was evaluated by monitoring the fluorescence response of the sensing system in the presence of common analogs, metal ions, or toxins. For the antiparallel G-quadruplex system, we replace OTA with OTB, AFB1, AFG1, FB1, Patulin, ZEA, and DON; for the parallel G-quadruplex system, we replace K^+ with NH_4^+ , Na^+ , Ca^{2+} , Mg^{2+} , Zn^{2+} , Cd^{2+} .

As shown in Figure 4A, the sensor has no apparent response to OTB, AFB1, AFG1, FB1, patulin, ZEA, and DON, demonstrating the specificity of the bioassay. The results in Figure 4B also show that compared with K^+ , other metal ions cannot produce strong fluorescence response signal changes, proving that this fluorescence detection platform has high selectivity for K^+ sensing. The parallel G-quadruplex has a channel in its center with a diameter close to the ionic radius of K^+ (1.3 Å) [32]. By binding to the eight carbonyl oxygen atoms of the G-quadruplex, K^+ can be located in the cavity between two adjacent G-tetrads of the G-quadruplex. Of all the alkali metal cations, this coordination contributes to the highest efficiency of K^+ in stabilizing the G-quadruplex, which confers selectivity of the G-quadruplex DNA for K^+ [33].

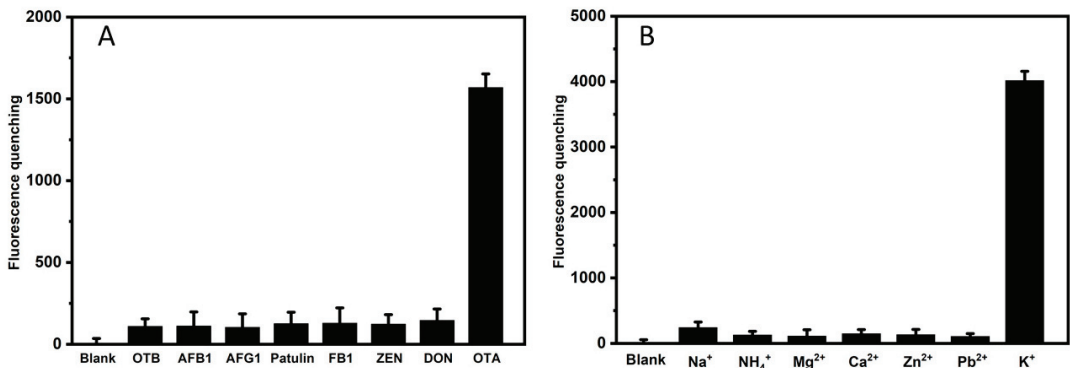


Figure 4. (A) Selectivity performance of sensing system for OTA detection with the addition of OTB, AFB1, AFG1, Patulin, FB1, ZEN, and DON to the solution. The concentration of ions is 62.5 nM. (B) Selectivity performance of sensing system for K^+ detection with the addition of NH_4^+ , Na^+ , Ca^{2+} , Mg^{2+} , Zn^{2+} , and Cd^{2+} ions to the solution. The concentration of toxins is 62.5 μ M. The fluorescence-quenching is the difference between response and blank. The error bar represents the standard deviations of the three parallel experiments.

3.5. Practical Application

To evaluate the practical application of the proposed fluorescence system, the method was applied in the detection of OTA in red wine and K^+ in sheep serum, respectively. The standard addition recovery experiment determined the OTA in the red wine sample. The spiked samples were pretreated using the extraction protocol described in our previous

study [21]. The samples after pretreatment were detected according to the method described in Section 2.4, and the fluorescence intensity was recorded. As shown in Table 1, the standard addition recovery rate of different concentrations of OTA was between 97.75% and 103.25%, showing that the method was reliable for detecting OTA in the red wine samples.

Table 1. Recovery experiments of OTA determination in red wine samples.

Sample Number	Added (nM)	Detected (nM)	Recovery (%)
1	2.00	1.98 ± 0.53	99.00
2	4.00	4.13 ± 0.35	103.25
3	8.00	7.82 ± 0.62	97.75

Goat serum samples were diluted 1000-fold with Tris-HCl buffer, and then the K⁺ concentration was calculated according to the linear correction equation. The results showed that the K⁺ concentration measured by this method was 6.54 ± 0.41 mmol/L (RSD = 2.1%, *n* = 5). The goat serum sample was determined by atomic absorption spectrometry and the K⁺ concentration obtained was 6.41 ± 0.54 mmol/L (RSD = 2.8%, *n* = 5). Comparing the two sets of data, we can conclude that the measured values are in good agreement with the standard values, showing that this method can be used to detect K⁺ concentration in serum.

4. Conclusions

In this study, we demonstrate that the fluorescence-quenching effect of G-quadruplex is based on the PIET principle. We introduced specific ligands for G-quadruplex leading to a further quenching and confirmed the mechanism of fluorescence-quenching of G-quadruplex based on PIET. A simple label-free fluorophore and quencher fluorescence platform was established and applied to detect OTA and K⁺ based on the high fluorescence-quenching ability of G-quadruplexes. In the presence of OTA or K⁺, the nucleic acid probe folds to form a G-quadruplex structure, leading to the fluorescence-quenching of the fluorophore. Besides the high sensitivity, the sensing system exhibits good selectivity and practical detection capability. Our method adopts a non-competitive strategy, so the detection limits were lower than that of the competitive strategy and even comparable to some methods of enzymatic amplification strategies. Consequently, G-quadruplexes can be excellent candidates as quenchers, and the strategy implemented in the study can be extended to an aptasensor with G-quadruplex.

Supplementary Materials: The following supporting information can be downloaded at: <https://www.mdpi.com/article/10.3390/bios12060423/s1>, Figure S1: Optimization of the SGI and Ca²⁺ concentration; Figure S2: Optimization of Ca²⁺ and the complementary sequence (A14) concentration; Figure S3: (A) Fluorescence emission spectra of FAM labeled fluorescence antiparallel G-quadruplex with different concentrations of OTA, (B) Fluorescence emission spectra of FAM labeled fluorescence parallel G-quadruplex with different concentrations of K⁺; Figure S4: Fluorescence response curve of OTAapt31-FAM with different complementary sequence and different concentrations of OTA; Figure S5: Fluorescence response curve of different sequences of parallel G-quadruplexes (unlabeled) under different concentrations of K⁺; Table S1: Sequences of the different constructs used in this study and their IC₅₀; Table S2: Comparison of different methods for OTA and K⁺ Determination.

Author Contributions: C.Y., Conceptualization, Methodology, Supervision, Project administration, Funding acquisition, Writing—Review & Editing. X.C., Methodology, Validation, Investigation, Writing—Original Draft. L.Z., Methodology, Investigation, Writing—Review & Editing. A.R., Methodology, Investigation, Writing—Review & Editing. F.A., Validation, Investigation, Writing—Original Draft. S.C., Methodology, Validation, Investigation. D.L., Writing—Review & Editing, Project administration, Funding acquisition. All authors have read and agreed to the published version of the manuscript.

Funding: This work was supported by the Fundamental Research Funds for the Central Universities (DUT17LAB18), the Open Funds of the State Key Laboratory of Electroanalytical Chemistry (SKLEAC202105), the Key Laboratory of Detection for Mycotoxins, Ministry of Agriculture (KLDM201702), Detection method and risk assessment of 5-Ethylidene-2-norbornene in Food Contact Materials and Articles (GSJK202013).

Institutional Review Board Statement: Not applicable.

Data Availability Statement: Not applicable.

Conflicts of Interest: The authors declare no conflict of interest.

References

- Zhang, Y.W.; Pan, V.; Li, X.; Yang, X.Q.; Li, H.F.; Wang, P.F.; Ke, Y.G. Dynamic DNA structures. *Small* **2019**, *15*, 1900228. [[CrossRef](#)] [[PubMed](#)]
- Kypr, J.; Kejnovska, I.; Renciuik, D.; Vorlickova, M. Circular dichroism and conformational polymorphism of DNA. *Nucleic Acids Res.* **2009**, *37*, 1713–1725. [[CrossRef](#)] [[PubMed](#)]
- Hu, Z.H.; Suo, Z.G.; Liu, W.X.; Zhao, B.Y.; Xing, F.F.; Zhang, Y.; Feng, L.Y. DNA conformational polymorphism for biosensing applications. *Biosens. Bioelectron.* **2019**, *131*, 237–249. [[CrossRef](#)] [[PubMed](#)]
- Burge, S.; Parkinson, G.N.; Hazel, P.; Todd, A.K.; Neidle, S. Quadruplex DNA: Sequence, topology and structure. *Nucleic Acids Res.* **2006**, *34*, 5402–5415. [[CrossRef](#)]
- Spiegel, J.; Adhikari, S.; Balasubramanian, S. The Structure and Function of DNA G-Quadruplexes. *Trends Chem.* **2020**, *2*, 123–136. [[CrossRef](#)]
- Luu, K.N.; Phan, A.T.; Kuryavyi, V.; Lacroix, L.; Patel, D.J. Structure of the human telomere in K⁺ solution: An intramolecular (3 + 1) G-quadruplex scaffold. *J. Am. Chem. Soc.* **2006**, *128*, 9963–9970. [[CrossRef](#)]
- Largy, E.; Marchand, A.; Amrane, S.; Gabelica, V.; Mergny, J. Quadruplex turncoats: Cation-dependent folding and stability of Quadruplex-DNA double switches. *J. Am. Chem. Soc.* **2016**, *138*, 2780–2792. [[CrossRef](#)]
- Li, T.T.; Zhang, Y.; Sun, X.H.; Zhang, Y.J.; Wang, Y.G.; Nie, Z.Y. Dual dye-labeled G-quadruplex aptasensor for detection of thallium(I) using ratiometric fluorescence resonance energy transfer. *Talanta* **2021**, *233*, 122508. [[CrossRef](#)]
- Zhu, Q.; Liu, L.H.; Xing, Y.P.; Zhou, X.H. Duplex functional G-quadruplex/NMM fluorescent probe for label-free detection of lead(II) and mercury(II) ions. *J. Hazard. Mater.* **2018**, *355*, 50–55. [[CrossRef](#)]
- Ma, D.L.; Wu, C.; Dong, Z.Z.; Tam, W.S.; Wong, S.W.; Yang, C.; Li, G.D.; Leung, C.H. The development of G-quadruplex-based assays for the detection of small molecules and toxic substances. *Chem. Asian J.* **2017**, *12*, 1851–1860. [[CrossRef](#)]
- Zhang, J.T.; Kang, T.S.; Wong, S.Y.; Pei, R.J.; Ma, D.L.; Leung, C.H. An iridium(III) complex/G-quadruplex ensemble for detection of ochratoxin A based on long-lifetime luminescent. *Anal. Biochem.* **2019**, *580*, 49–55. [[CrossRef](#)] [[PubMed](#)]
- Rhouati, A.; Yang, C.; Hayat, A.; Marty, J. Aptamers: A Promising Tool for Ochratoxin A Detection in Food Analysis. *Toxins* **2013**, *5*, 1988–2008. [[CrossRef](#)] [[PubMed](#)]
- Liu, Y.; Liao, R.; Wang, H.; Gong, H.; Chen, C.Y.; Chen, X.M.; Cai, C.Q. Accurate and sensitive fluorescence detection of DNA based on G-quadruplex hairpin DNA. *Talanta* **2018**, *176*, 422–427. [[CrossRef](#)]
- Xi, H.; Juhas, M.; Zhang, Y. G-quadruplex based biosensor: A potential tool for SARS-CoV-2 detection. *Biosens. Bioelectron.* **2020**, *167*, 112494. [[CrossRef](#)] [[PubMed](#)]
- Xiang, D.S.; Li, F.Q.; Wu, C.Y.; Shi, B.; Zhai, K. The G-BHQ synergistic effect: Improved double quenching molecular beacons based on guanine and Black Hole Quencher for sensitive simultaneous detection of two DNAs. *Talanta* **2017**, *174*, 289–294. [[CrossRef](#)]
- Heinlein, T.; Knemeyer, J.; Piestert, O.; Sauer, M. Photoinduced electron transfer between fluorescent dyes and guanosine residues in DNA-Hairpins. *J. Phys. Chem. B* **2003**, *107*, 7957–7964. [[CrossRef](#)]
- Mao, H.H.; Luo, G.H.; Zhan, Y.X.; Zhang, J.; Yao, S.; Yu, Y. The mechanism and regularity of quenching the effect of bases on fluorophores: The base-quenched probe method. *Analyst* **2018**, *143*, 3292–3301. [[CrossRef](#)]
- Chiorcea-Paquim, A.; Santos, P.V.; Eritija, R.; Oliveira-Brett, A.M. Self-assembled G-quadruplex nanostructures: AFM and voltammetric characterization. *Phys. Chem. Chem. Phys.* **2013**, *15*, 9117–9124. [[CrossRef](#)]
- Zhang, Y.L.; Chen, W.H.; Dong, X.T.; Fan, H.; Wang, X.H.; Bian, L.J. Simultaneous detection of trace toxic metal ions, Pb²⁺ and Ag⁺, in water and food using a novel single-labeled fluorescent oligonucleotide probe. *Sens. Actuators B Chem.* **2018**, *261*, 58–65. [[CrossRef](#)]
- Wang, S.; Sun, J.; Zhao, J.H.; Lu, S.S.; Yang, X.R. Photo-Induced electron transfer-based versatile platform with G-quadruplex/Hemin complex as quencher for construction of DNA logic circuits. *Anal. Chem.* **2018**, *90*, 3437–3442. [[CrossRef](#)]
- Yang, C.; Dong, S.N.; ABBAS, F.; Chu, X.L.; Fan, A.Q.; RHOUATI, A.; Mao, J.; Liu, Y. Label-free fluorescence aptasensor for ochratoxin A using crystal violet as displacement-type probe. *Chin. J. Anal. Chem.* **2021**, *49*, 55–62. [[CrossRef](#)]
- Zhao, H.; Xiang, X.Y.; Chen, M.J.; Ma, C.B. Aptamer-Based Fluorometric Ochratoxin A Assay Based on Photoinduced Electron Transfer. *Toxins* **2019**, *11*, 65. [[CrossRef](#)] [[PubMed](#)]

23. Kardar, Z.S.; Shemirani, F.; Zadmand, R. Determination of iron(II) and iron(III) via static quenching of the fluorescence of tryptophan-protected copper nanoclusters. *Microchim. Acta* **2020**, *187*, 81. [[CrossRef](#)] [[PubMed](#)]
24. Sergelen, K.; Fossati, S.; Turupcu, A.; Oostenbrink, C.; Liedberg, B.; Knoll, W.; Dostalek, J. Plasmon field-enhanced fluorescence energy transfer for hairpin aptamer assay readout. *ACS Sens.* **2017**, *2*, 916–923. [[CrossRef](#)] [[PubMed](#)]
25. Tian, J.Q.; Cheng, N.Y.; Liu, Q.; Xing, W.; Sun, X.P. Cobalt phosphide nanowires: Efficient nanostructures for fluorescence sensing of biomolecules and photocatalytic evolution of dihydrogen from water under visible light. *Angew. Chem. Int. Ed.* **2015**, *54*, 5493–5497. [[CrossRef](#)] [[PubMed](#)]
26. Miller, J.N. Fluorescence energy transfer methods in bioanalysis. *Analyst* **2005**, *130*, 265. [[CrossRef](#)] [[PubMed](#)]
27. Nguyen, Q.L.; Spata, V.A.; Matsika, S. Photophysical properties of pyrrolocytosine, a cytosine fluorescent base analogue. *Phys. Chem. Chem. Phys.* **2016**, *18*, 20189–20198. [[CrossRef](#)]
28. Kong, D.M.; Ma, Y.E.; Guo, J.H.; Yang, W.; Shen, H.X. Fluorescent sensor for monitoring structural changes of G-quadruplexes and detection of potassium ion. *Anal. Chem.* **2009**, *81*, 2678–2684. [[CrossRef](#)]
29. Cao, Y.W.; Li, W.J.; Gao, T.; Ding, P.; Pei, R.J. One terminal guanosine flip of intramolecular parallel G-quadruplex: Catalytic enhancement of G-quadruplex/Hemin DNAszymes. *Chem. A Eur. J.* **2020**, *26*, 8631–8638. [[CrossRef](#)]
30. He, Y.; Tian, F.Y.; Zhou, J.; Jiao, B.N. A fluorescent aptasensor for ochratoxin A detection based on enzymatically generated copper nanoparticles with a polythymine scaffold. *Microchim. Acta* **2019**, *186*, 199. [[CrossRef](#)]
31. Liu, M.; Li, X.Y.; Li, B.X.; Du, J.X.; Yang, Z.Q. A fluorometric aptamer-based assay for ochratoxin A by using exonuclease III-assisted recycling amplification. *Microchim. Acta* **2020**, *187*, 46. [[CrossRef](#)] [[PubMed](#)]
32. Sundquist, W.I.; Klug, A. Telomeric DNA dimerizes by formation of guanine tetrads between hairpin loops. *Nature* **1989**, *342*, 825–829. [[CrossRef](#)] [[PubMed](#)]
33. Liu, Y.Y.; Li, B.X.; Cheng, D.M.; Duan, X.Y. Simple and sensitive fluorescence sensor for detection of potassium ion in the presence of high concentration of sodium ion using berberine–G-quadruplex complex as sensing element. *Microchem. J.* **2011**, *99*, 503–507. [[CrossRef](#)]



Article

Analysis of Mn^{2+} and Zn^{2+} Ions in Macroalgae with Heteroelement-Doped Carbon-Based Fluorescent Probe

Hui Xu ^{1,2,3,*}, Xin You ³, Yue Lu ³, Peng Liang ³, Zhihui Luo ⁴, Yiwei Wang ³, Shaoxiao Zeng ^{1,2,3} and Hongliang Zeng ^{1,2,3}

¹ Engineering Research Centre of Fujian-Taiwan Special Marine Food Processing and Nutrition, Ministry of Education, Fuzhou 350002, China; zsxstf@fafu.edu.cn (S.Z.); zhlfst@fafu.edu.cn (H.Z.)

² Fujian Provincial Key Laboratory of Quality Science and Processing Technology in Special Starch, Fujian Agriculture and Forestry University, Fuzhou 350002, China

³ College of Food Science, Fujian Agriculture and Forestry University, Fuzhou 350002, China; 3210910056@fafu.edu.cn (X.Y.); luyueeee@fafu.edu.cn (Y.L.); liangpeng0412@fafu.edu.cn (P.L.); wangyw@fafu.edu.cn (Y.W.)

⁴ Guangxi Key Laboratory of Agricultural Resources Chemistry and Biotechnology, College of Chemistry and Food Science, Yulin Normal University, Yulin 537000, China; zhluo@ylyu.edu.cn

* Correspondence: xhuifst@fafu.edu.cn

Abstract: Kelp and laver are large economic macroalgae in China, which are rich in nutrients, especially Mn and Zn. Excessive intake of Mn and Zn can be harmful to the human body. Therefore, it is necessary to develop a convenient and efficient method to detect the contents of Mn and Zn in macroalgae. In this experiment, red carbon dots (R-CDs) doped with N and S elements were prepared by the thermal solvent method. The obtained R-CDs displayed excitation wavelength-independent fluorescent emission in the red spectral region. The R-CDs were used to construct a fluorescent probe for specific recognition of Mn^{2+} and Zn^{2+} , achieving high-sensitivity detection of Mn^{2+} and Zn^{2+} . The detection results showed a good linear relationship between fluorescence intensity and Mn^{2+} concentration, and the calculated detection limit was 0.23 nmol/L. For the detection of Zn^{2+} , the detection limit was estimated as 19.1 nmol/L. At the same time, the content distribution of Mn and Zn elements in macroalgae produced in Fujian was investigated by the constructed fluorescence probe. It was found that kelp, laver, and their products are rich in Mn and Zn elements, and the content of Mn and Zn elements in laver is higher than that in kelp, which can be used as the optimal food supplement for Mn and Zn elements.

Keywords: red carbon dots; manganese ion; zinc ion; fluorescence; macroalgae

Citation: Xu, H.; You, X.; Lu, Y.; Liang, P.; Luo, Z.; Wang, Y.; Zeng, S.; Zeng, H. Analysis of Mn^{2+} and Zn^{2+} Ions in Macroalgae with Heteroelement-Doped Carbon-Based Fluorescent Probe. *Biosensors* **2022**, *12*, 359. <https://doi.org/10.3390/bios12050359>

Received: 24 April 2022

Accepted: 19 May 2022

Published: 22 May 2022



Copyright: © 2022 by the authors. Licensee MDPI, Basel, Switzerland. This article is an open access article distributed under the terms and conditions of the Creative Commons Attribution (CC BY) license (<https://creativecommons.org/licenses/by/4.0/>).

1. Introduction

China is rich in seaweed resources, among which macroalgae are abundant in various nutrients necessary for the human body and have important economic value. Macroalgae have a strong adsorption capacity for heavy metals. The heavy metal content in all kinds of macroalgae is higher than that of water, and the enrichment coefficient of heavy metal elements varies from several times to hundreds of thousands of times [1]. Thus, macroalgae can be used not only as large nutrient reservoirs, but also as research samples for heavy metal pollution investigations. Through previous investigations, it has been found that the contents of Mn and Zn in macroalgae are very high. Mn and Zn, as essential elements, are of great significance to various physiological activities of the human body. However, excessive intake of Mn [2] and Zn [3] will also cause harm to the human body. Therefore, it is necessary and meaningful to establish a convenient analysis method for the detection of Mn^{2+} and Zn^{2+} in macroalgae.

So far, many analytical methods such as atomic absorption spectrometry (AAS), inductively coupled plasma mass spectrometry (ICP-MS), and electrochemistry have been

applied to the detection of Mn^{2+} and Zn^{2+} . However, these traditional detection methods all have the defects of complex operation and slow response time, and it is urgent to develop a method that is convenient to operate and quickly detect target elements. The fluorescent probe has attracted much attention because of its advantages of good selectivity, convenience, easy pretreatment, live-cell imaging use [4,5], and rapid detection of a variety of metal ions. At present, fluorescence probes commonly used in the detection of metal ions include organic small molecules, metal-organic frameworks (MOFs), aptamers, and nano-materials. Organic fluorescent molecules, such as rhodamine, coumarin, naphthalimide, benzothiazole, pyridine, and other typical fluorescent groups, have been widely used in the detection of metal ions in food. Yu et al. [6] designed a new coumarin-based ratiometric fluorescent probe using dithiothreitol as the recognition receptor for Hg^{2+} detection based on the change in the color of the fluorescent probe from light yellow to orange. Zhou et al. [7] designed and synthesized a novel fluorescence sensor based on fluoropyrrole and carboxyl mercaptan metal-bonded receptors for the detection of Hg^{2+} . The sensor was highly selective for Hg^{2+} , the detection limit of Hg^{2+} was 5.7 nM, and the sensor responded quickly to Hg^{2+} in aqueous solution in 30 s. However, poor solubility, serious photobleaching, poor bioavailability, and narrow excitation of these organic fluorescent dyes greatly limit detection and sensing. MOFs are hybrid crystalline porous materials, usually composed of inorganic nodes (metal ions or metal clusters) [8] and functional organic linkers [9,10]. However, due to the instability of many MOF materials in water [11], most current MOF-based fluorescence sensing research on metal ions is carried out in organic solvents, which are not suitable for the practical application of detection probes.

Carbon dots (CDs) have many advantages compared with traditional fluorescent materials, such as unique optical properties, excellent biocompatibility, excellent water dispersibility, low cost, high sensitivity, and easy surface functionalization [12,13]. These advantages make it possible to have great potential application in biomedical imaging and sensing [14], tumor therapy [15], light-emitting devices [16,17], and other fields. Much research has been conducted to synthesize CDs using chemicals [18] or natural products [19] as carbon sources. Xu et al. [20] reported a facile method to prepare copper-doped carbon dots (Cu-CDs) using citric acid and cuprous chloride as precursors under hydrothermal conditions, which showed strong luminescence performance at 440 nm and with 9.81% photoluminescence quantum yield. Cu-CDs with a detection limit of 1 nM can be used for the rapid detection of Fe^{3+} , and can be further applied to the detection of Fe^{3+} in human serum. Liu et al. [21] reported that Bombyx mori silk was used as a raw material in the coupling of citric acid to prepare nitrogen-doped CDs using a facile one-step hydrothermal route. The as-prepared nitrogen-doped CDs emitted blue fluorescence with a quantum yield of 61.1%, which can easily bind with Fe^{3+} as a consequence of fluorescence quenching, making a method for Fe^{3+} detection developed with high selectivity and sensitivity. He et al. [22] developed a hydrothermal method to synthesize Zn^{2+} -doped carbon quantum dots (Zn-CQDs) using zinc citrate chelate, with a fluorescence quantum yield of 48%. Zn-CQDs have stronger fluorescence sensing ability for Fe^{3+} and Hg^{2+} . They can be used in the fields of fluorescence sensors, biological imaging, photoelectronics, and catalysis. However, most of the CDs that have been synthesized have strong emission in the blue-green electromagnetic radiation region and weak emission in the red region with a low quantum yield. Due to the interference of the inherent blue self-fluorescence in the biological matrix, it is necessary to avoid blue emission during practical sample detection. Because of the low extinction coefficient of the biological matrix in the red and near-infrared range in biosensing, red carbon dots (R-CDs) will inevitably show a large signal-to-noise ratio, which is beneficial to improve the sensitivity and accuracy of practical sample detection. Therefore, fluorescent biological probes prepared by using R-CDs can not only effectively avoid self-fluorescence interference, but also have strong penetrability to tissues [23,24], which makes it particularly important and urgent to prepare an R-CDs-based fluorescence probe.

In this paper, R-CDs with dual-emission properties were prepared by the thermal solvent method. The surface morphology and photoluminescence characteristics of R-

CDs were studied. The fluorescence probe was constructed by using the R-CDs with dual emission to detect Mn^{2+} and Zn^{2+} . Its detection performance was analyzed. Finally, the constructed fluorescent probe was used to detect macroalgae produced in Fujian province, China. The accuracy of the method was verified by flame atomic absorption spectrometry (FAAS). The content of Mn and Zn elements in kelp (*Laminaria Japonica*) and laver (*Porphyra haitanensis*) samples was analyzed, and the proposed fluorescent probe could have potential application in dietary guidance and safety assessment.

2. Materials and Methods

2.1. Preparation of R-CDs

The R-CDs were prepared by the thermal solvent method, which can be described as follows: 0.6804 g reduced glutathione (Macklin, Shanghai, China) and 0.6106 g o-phenylenediamine (Merck, Darmstadt, Germany) were dissolved in 20 mL of formamide (Macklin, Shanghai, China) at room temperature. The obtained mixture was transferred into a Teflon-lined stainless steel autoclave, which was then kept in an air-circulating oven at 160 °C for 2 h. After the reaction, the autoclave was naturally cooled down to room temperature. The obtained solution was centrifuged at the speed of 1000 rpm for 20 min to remove large particles. The upper solution was diluted and dialyzed (molecular weight cut-off = 1000 Da) against ultrapure water for a week. The purified R-CDs solution was freeze-dried to obtain dark green powder for characterization. Ultrapure water (DI, >18.25 M Ω) was prepared by the Millipore Milli-Q Water Purification System (Merck, Billerica, MA, USA) for the preparation of all solutions in this work.

2.2. Structural Characterization of R-CDs

Fourier transform infrared spectroscopy (FT-IR) was obtained using a VERTEX 80V FT-IR spectrometer (Bruker, Billerica, MA, USA). FT-IR samples were prepared by mixing the powders of KBr and R-CDs in a ratio of 1:150. The obtained mixture was made into tablets. TEM (Shimadzu, Tokyo, Japan) samples were prepared by dropping the aqueous solution containing R-CDs onto carbon-coated grids and allowing the excess solvent to evaporate. The structure of the as-prepared R-CDs was characterized by XRD-6000 (Shimadzu, Tokyo, Japan). The fluorescence measurements were performed with a fluorescence spectrophotometer RF-5301PC (Shimadzu, Tokyo, Japan). The samples were excited from 360 to 420 nm, and the emission spectrum in the range of 220 to 900 nm was measured. The slit width was fixed at 10 nm for emission. The ultraviolet–visible (UV–VIS) spectra were recorded on a UV-2600 ultraviolet–visible spectrophotometer (Shimadzu, Tokyo, Japan), with scanning wavelength ranging from 200 nm to 800 nm using a xenon lamp and a tungsten lamp.

2.3. Signal-Off Detection of Mn^{2+}

For the detection of Mn^{2+} , 1 mL of purified R-CDs solution and varying concentrations of Mn^{2+} ion standard solution (Macklin, Shanghai, China) were separately added into the mixture of 980 μ L of 0.1 M HEPES buffer solution (Solarbio, Beijing, China). Then, the mixture was thoroughly shaken and equilibrated at room temperature. The fluorescence spectra with 420 nm excitation wavelength and 680 nm emission wavelength were recorded and used for quantitative analysis.

2.4. Ratiometric Detection of Zn^{2+}

For the detection of Zn^{2+} , 1 mL of purified R-CDs solution and varying concentrations of Zn^{2+} ion standard solution (Macklin, Shanghai, China) were separately added into the mixture of 980 μ L of 0.1 M HEPES buffer solution (Solarbio, Beijing, China). Then, the mixture was thoroughly shaken and equilibrated at room temperature. The fluorescence spectra with excitation at 420 nm and emission at 650 nm and 680 nm were recorded and used for quantitative analysis.

2.5. Sample Pretreatment

In this work, 20 different brands of macroalgae samples were purchased from supermarkets and retailers in Fujian province. Four hundred milligrams of the cleaned and dried samples was ground into powder, added with 5 mL HNO_3 into the microwave digestion tank, and digested with an 800 W microwave digestion instrument. The digested sample was heated up to 140–160 °C to remove excess acid. After cooling to room temperature, approximately 1 mL of sample solution remained and was transferred to a volumetric flask with ultrapure water to 25 mL. The sample solution could be diluted with need. Blank samples were prepared according to the same method without adding macroalgae.

2.6. FAAS Determination

A series of standard concentrations of Mn solution and Zn solution were prepared. The absorbance is plotted as the function of metal element concentration to obtain a calibration curve for quantitative analysis. The pretreated sample was placed in FAAS (AA-6300C, Shimadzu, Tokyo, Japan), and the contents of Mn and Zn elements were detected according to the test parameters of different elements. Among them, the test parameters for Mn detection were lamp current 2.0 mA, wavelength 279.5 nm, slit 0.1 nm, negative high pressure -344 V, air flow $6.0 \text{ L}\cdot\text{min}^{-1}$, acetylene flow $1.0 \text{ L}\cdot\text{min}^{-1}$. The test parameters for Zn detection were lamp current 2.0 mA, wavelength 213.9 nm, slit 0.2 nm, negative high pressure -309 V, air flow $6.0 \text{ L}\cdot\text{min}^{-1}$, and acetylene flow $1.0 \text{ L}\cdot\text{min}^{-1}$.

3. Results and Discussion

3.1. Photoluminescence Performance of R-CDs

As shown in Figure 1A, the UV–VIS absorption peak of the synthesized CDs absorption spectrum at 270 nm could be attributed to the $\pi-\pi^*$ transition of the conjugated aromatic sp^2 bonds [25,26]. The absorption spectrum of CDs also displayed several characteristic absorbing peaks at 395 nm, 420 nm, 640 nm, and 680 nm, which could be attributed to the $n-\pi^*$ and $\pi-\pi^*$ transitions of the aromatic π system containing the C=O, C=N, and C=S bonds, respectively [27]. These heteratomic groups could form polycyclic aromatic hydrocarbon or oxygen-containing structures on the surface of CDs. Additionally, the CDs had an excitation peak at 420 nm and an emission peak at 680 nm. The fluorescence excitation band of CDs overlapped with its main UV–VIS absorption band, indicating that the emission was closely related to these absorption bands caused by related structures [28]. The maximum absorption wavelength of CDs was used as the fluorescence excitation wavelength to obtain the fluorescence emission spectrum of CDs. Figure 1B shows the emission spectrum of the dual-emission fluorescence CDs. The quantum yield of R-CDs was calculated to be 13.64%. Under single-wavelength excitation, there were two maximum emission peaks in the blue ($\lambda_{\text{Em}} = 442$ nm) and red ($\lambda_{\text{Em}} = 680$ nm) regions. When the excitation wavelength increases from 360 nm to 430 nm, the two fluorescence emission peaks do not shift. It was indicated that the synthesized CDs showed excitation wavelength-independent fluorescent emission. This characteristic may be related to the surface state or the uniform particle size of CDs, which can avoid the interference of autoluminescence in application. As λ_{Ex} increases from 360 nm to 430 nm, the fluorescence intensity at $\lambda_{\text{Em}} = 442$ nm and 680 nm increases and then decreases. When $\lambda_{\text{Ex}} = 380$ nm, the fluorescence intensity at $\lambda_{\text{Em}} = 442$ nm is the strongest. When $\lambda_{\text{Ex}} = 420$ nm, the fluorescence intensity at $\lambda_{\text{Em}} = 680$ nm is the strongest. Under short-wavelength light excitation, CDs have two characteristic fluorescence emission peaks in the blue and red regions of the spectrum. These dual-fluorescence bands observed may be attributed to core- and surface-state emission [29]. Being capable of excitation at different wavelengths makes the CDs attractive for a variety of applications. In this case, red fluorescence ($\lambda_{\text{Em}} = 680$ nm) was selected in biological studies to reduce the interference caused by biomolecules' self-fluorescence, resulting in minimal light damage and deeper tissue penetration [30]. Therefore, the red carbon dots (R-CDs) prepared in this work were used as fluorescent probes for metal element detection.

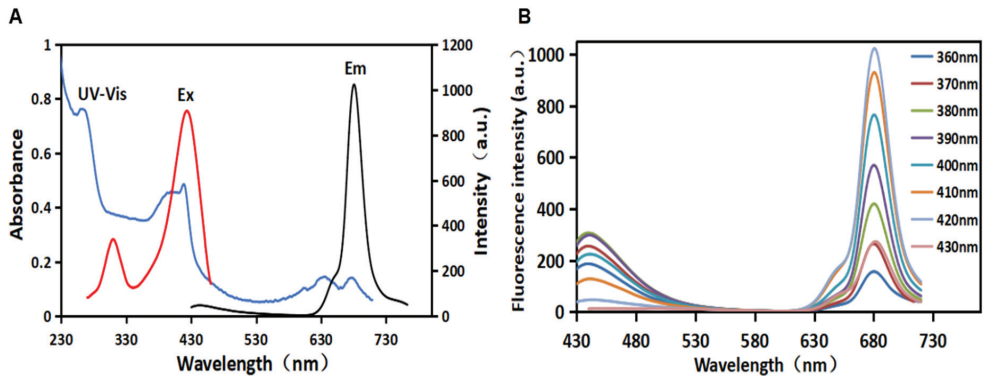


Figure 1. UV-visible absorption spectrum (blue), excitation spectrum (red), and emission spectrum (black) of R-CDs (A); fluorescence emission spectra of R-CDs (B).

3.2. Structural Characterization of R-CDs

The morphology and size of R-CDs were observed by TEM. As can be seen from Figure 2A, R-CDs showed good dispersion, no agglomeration, and the morphology was quasi-spherical. The average particle size of R-CDs was estimated as 5.46 ± 1.03 nm by counting the size of more than 100 particles, without any large particles or aggregation. It was indicated that the reaction process was stable, and no adverse reactions occurred. Figure 2B shows clear lattice fringes with a spacing of 0.32 nm, corresponding to the 002 crystal plane of graphite carbon, indicating that the material contained a graphite-like structure [31].

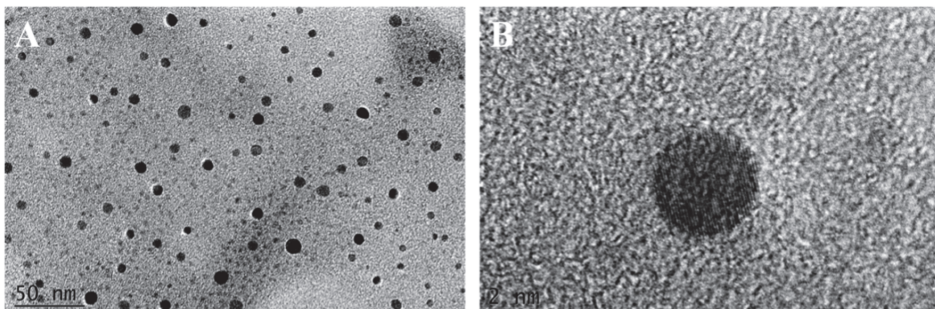


Figure 2. TEM (A) and HRTEM images (B) of R-CDs.

R-CDs were characterized by XRD. As shown in Figure 3A, R-CDs had a wide diffraction peak at $2\theta = 26^\circ$ corresponding to plane 002 of the sp^2 hybrid ink carbon, which was consistent with the TEM results [31]. The FT-IR spectrum of R-CDs is shown in Figure 3B. A wide FT-IR absorption band appeared at $3000\text{--}3500\text{ cm}^{-1}$, which was caused by the stretching vibration of the O-H bond and the N-H bond [24]. Two characteristic absorption peaks appeared at 1079 cm^{-1} and 1391 cm^{-1} , which were caused by the stretching vibration of the C-O bond and the C-N bond. The peak at 1612 cm^{-1} was caused by the C=O stretching vibration [32]. The results show that there were abundant functional groups on the surface of R-CDs, such as amino, hydroxyl, and carboxyl groups, demonstrating the good hydrophilicity of R-CDs.

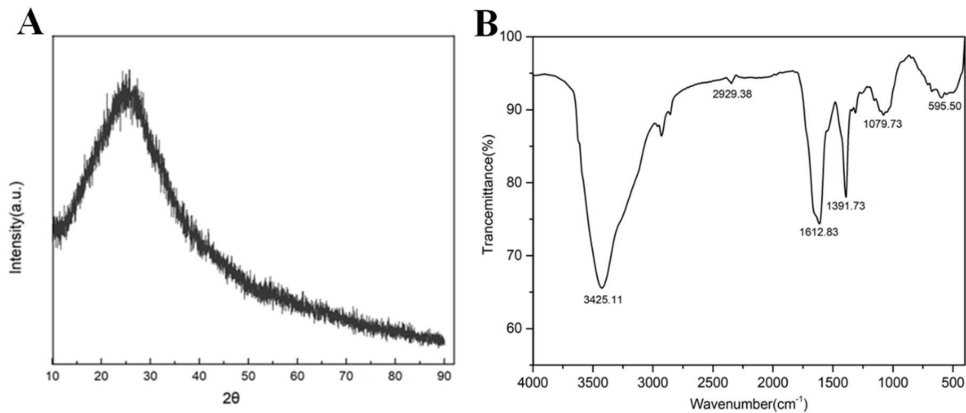


Figure 3. XRD (A) and FT-IR spectra of R-CDs (B).

The XPS spectra were obtained using a GENESIS 60S XPS (EDAX, Warrendale, PA, USA). Figure S1 shows the full spectrum of XPS. There were four characteristic peaks of R-CDs, corresponding to the C1s peak at 284.6 eV, the O1s peak at 530.25 eV, the N1s peak at 398.97 eV, and the S2p peak at 162.1 eV, and the contents of corresponding elements were 56.56%, 24.67%, 16.12%, and 2.65%, respectively. The results show that N and S can be doped into R-CDs by changing the composition and proportion of synthetic materials. Photoelectron spectrum C1s (Figure S2A) shows that C1s was fitted by three peaks located at 284.82 eV, 288.27 eV, and 286.12 eV, corresponding to C-C/C=C, -COOH, and C-O/C-N respectively. Photoelectron spectrum O1s (Figure S2B) showed that O1s was fitted by two peaks, corresponding to 531.37 eV C=O and 532.87 eV C-OH, respectively. N1s (Figure S3C) was fitted to obtain four main peaks of 398.52 eV, 399.57 eV, 400.12 eV, and 401.07 eV, corresponding to C=N, pyridine N, pyrrole N, and graphite N, respectively. The peaks of S2p (Figure S3D) at 161.12 eV and 163.22 eV were attributed to S2p1/2, S2p1/2, and S2p3/2. Peaks at 163.67 eV and 164.82 eV were classified as -C-SO and -C-SO₂. R-CDs had a conjugated Sp² domain rich in oxygen/nitrogen surface groups. Nitrogen could use the unpaired electrons to improve the emission characteristics of R-CDs. The energy gap regulation in R-CDs also depended on the N and O content. The oxygen-containing functional groups, particle size, and graphite nitrogen determined the fluorescence characteristics of R-CDs. Zeta potential showed that the surface potential of R-CDs was −20 eV, demonstrating a strong negative charge and containing a large number of oxygen carboxyl groups on the surface. The more carboxyl groups on the surface of R-CDs or the higher oxidation degree, the R-CDs more easily emitted in the red spectral region.

3.3. Stability of R-CDs

The pH, ionic strength, and UV lamp irradiation were investigated for the study of R-CDs stability. The pH value affected the emission of R-CDs. As shown in Figure S3, the fluorescence intensity of R-CDs in acidic solution increased upon enhancing the pH value. Under the alkaline condition, the red emission spectra can be deconvoluted into two peaks at 650 nm and 680 nm. As the pH value increased, peak intensity dominated at 650 nm, and the opposite effect was observed at lower pH. This phenomenon was estimated to be caused by the chemical properties of surface functional groups of R-CDs that affected their electronic properties. The pH-dependent fluorescence was associated with protonation of amino groups, deprotonation of carboxyl groups, or tautomerism of amides. As shown in Figure S4A, when the concentration of NaCl reached 1 mol/L, the fluorescence intensity was not significantly affected, indicating that R-CDs had good stability in the high-ionic-intensity environment. The fluorescence intensity of R-CDs was measured by a fluorescence spectrophotometer after being irradiated under an excitation UV lamp at 365 nm for 90 min

(Figure S4B), and it was found that the fluorescence intensity decreased by only about 15%. This indicated that R-CDs have good photobleaching resistance.

3.4. Photoluminescence Mechanism of R-CDs

As shown in Figure 4A, R-CDs, as fluorescent probes, were synthesized using glutathione and o-phenylenediamine as raw materials and formamide as solvent to detect metal elements. The incorporation of metal elements into carbon-based nanomaterials could enhance the conductivity and electrical capacitance. The metal-decorated nanomaterials exhibited a saturated absorption process of optical nonlinearity by near-resonant energy transfer [33]. Therefore, the proposed carbon-based fluorescent probe was applied to investigate the interaction between carbon dots and Mn^{2+}/Zn^{2+} , and the possible photoluminescence mechanism was discussed. The fluorescence spectra of R-CDs and R-CDs mixed with Mn^{2+} are shown in Figure 4B. It was found that the presence of Mn^{2+} could effectively quench the fluorescence of R-CDs at 680 nm. The average fluorescence lifetimes (τ) were calculated to be 4.38 ns for R-CDs and 4.37 ns for R-CDs + Mn^{2+} . This indicated that the fluorescence quenching was caused by the static quenching. This phenomenon may be related to the coordination of $-NH_2$ on the surface of R-CDs and Mn^{2+} . Electrons transferred from the excited state of R-CDs to the unfilled orbital of Mn^{2+} , forming a new electron–hole recombination, which was consistent with a previous report [34]. It can promote the nonradiative recombination process of excitons through an effective electron transfer process, and finally quench the fluorescence of R-CDs at 680 nm. The spectra result of Zn^{2+} mixed with R-CDs showed that the presence of Zn^{2+} led to a newly generated fluorescence peak at 650 nm and quenching of the fluorescence peak at 680 nm (Figure 4C). The average fluorescence lifetimes (τ) were calculated to be 3.20 ns for R-CDs and 3.25 ns for R-CDs + Zn^{2+} . The slightly changed lifetime indicated that the fluorescence quenching was caused by the static quenching. The quenching was attributed to the chelation between Zn^{2+} with nitrogen and oxygen atoms and nonradiative recombination through the charge transfer [35]. The 30 nm blue shift of R-CDs after adding Zn^{2+} might be due to the coordination-induced surface passivation [36,37].

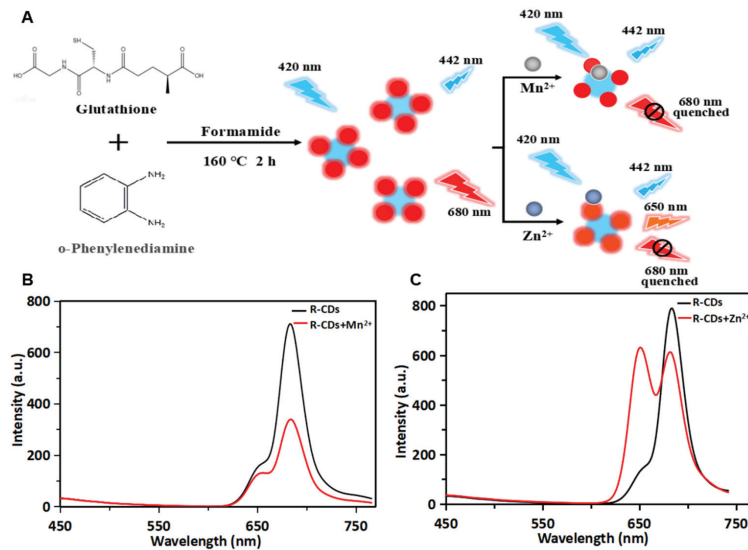


Figure 4. Schematic illustration of the preparation of R-CDs and the application in the detection of Mn^{2+} and Zn^{2+} (A). Fluorescence spectra of R-CDs (black curve) and R-CDs + Mn^{2+} (red curve) (B). Fluorescence spectra of R-CDs (black curve) and R-CDs + Zn^{2+} (red curve) (C).

3.5. Signal-Off Analysis of Mn^{2+}

Based on the quenching of R-CDs fluorescence by Mn^{2+} , a method for the rapid detection of Mn^{2+} in the “signal-off” mode was established. Under the optimal detection conditions (see Supplementary Materials and Figure S5 for details), the fluorescence quenching ability of R-CDs with different concentrations of Mn^{2+} was investigated. Figure 5A records the fluorescence spectra of R-CDs when Mn^{2+} with different concentrations (2–50 ng/mL) was added. It can be seen that the fluorescence intensity at 680 nm was the maximum when no target element existed. The emission of R-CDs gradually decreased with the increase in Mn^{2+} concentration, showing a good quenching effect. As shown in Figure 5B, the fluorescence intensity could be completely quenched when the concentration of Mn^{2+} exceeded 90 ng/mL. It can be clearly seen that the fluorescence intensity was inversely proportional to the Mn^{2+} concentration in the range of 1–50 ng/mL, and the linear equation was $y = -12.296x + 725.44$ with $R^2 = 0.999$. The detection limit of the method was estimated to be 0.0127 ng/mL (equivalent to 0.23 nmol/L). In this work, R-CDs were synthesized by the thermal solvent method at one time. The operation was simple, and the R-CDs surface was rich in functional groups containing nitrogen and oxygen, so Mn^{2+} can be specifically detected without additional chemical modification. Compared with other published methods for Mn^{2+} detection (Table 1), R-CDs-based signal-off analysis of Mn^{2+} showed a lower detection limit and higher sensitivity.

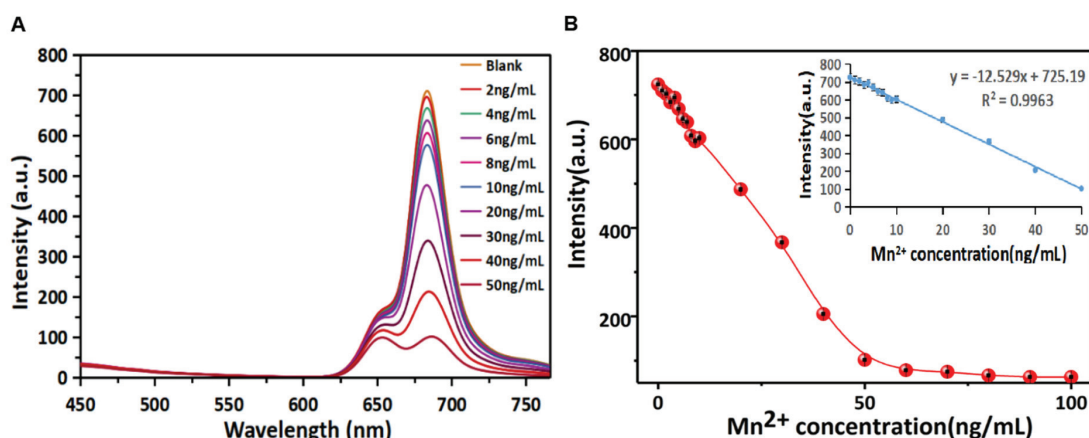


Figure 5. Fluorescence responses of the R-CDs upon the addition of different concentrations of Mn^{2+} (A) and the linear correlation of fluorescence intensity versus the concentrations of Mn^{2+} in the range from 0 ng/mL to 100 ng/mL (B).

Table 1. Comparison between this method and other methods for the detection of Mn^{2+} .

Detection Method	Material	LOD	Linear Range	Ref.
Electrochemical	Mn(II)-IIP/MWCNT-Chit-IL/GC	0.15 $\mu\text{mol/L}$	2–9 $\mu\text{mol/L}$	[38]
Colorimetric	Silver nanoparticles	20 nmol/L	0–700 nmol/L	[39]
Fluorescence	Polymer dot	0.4 $\mu\text{mol/L}$	1.5–100 $\mu\text{mol/L}$	[40]
Fluorescence	Silicon nanoparticles	0.2 $\mu\text{mol/L}$	2.5–250 $\mu\text{mol/L}$	[41]
Fluorescence	R-CDs	0.23 nmol/L	18.2–910 nmol/L	This method

Specificity is also an important factor in the evaluation of the analytical performance of fluorescent probes. Sixteen interference ions were selected for specificity experiments. A certain amount of R-CDs solution was mixed with 20 μL of interfering ions (20 ng/mL), and the changes in fluorescence intensities were recorded under the same conditions. As

shown in Figure 6, when R-CDs were mixed with other interfering ions, the fluorescence intensity of the (R-CDs + M^{n+}) did not change significantly compared with the fluorescence intensity of R-CDs. However, when Mn^{2+} was added to the (R-CDs + M^{n+}) mixture, the fluorescence intensity decreased significantly, which was consistent with the change in fluorescence intensity of (R-CDs + Mn^{2+}). The results show that the fluorescent probe had good selectivity for Mn^{2+} . Among all kinds of interference ions, Cd^{2+} and Zn^{2+} showed different degrees of interference. In the real macroalgae sample, the content of Mn^{2+} and Zn^{2+} is much higher than that of Cd^{2+} [42,43], and the interference caused by Cd^{2+} can be ignored.

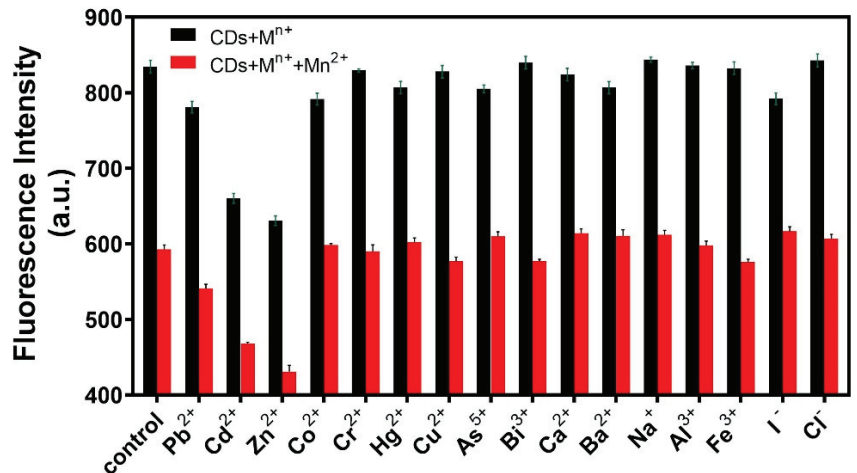


Figure 6. Specificity of the fluorescence probe for Mn^{2+} analysis.

3.6. Ratiometric Analysis of Zn^{2+}

Under the optimal detection conditions (see Supplementary Materials and Figure S6 for details), the fluorescence performance of R-CDs with different concentrations of Zn^{2+} was investigated. In Figure 7A, the fluorescence spectra of R-CDs with different concentrations (1–50 ng/mL) of Zn^{2+} are recorded. The intensity at a wavelength of 680 nm displayed negligible change at the low concentration range. When the concentration increased higher than 20 ng/mL, the emission intensity decreased. Meanwhile, it was observed that the fluorescence intensity at 650 nm increased gradually when the concentration of Zn^{2+} increased from 1 ng/mL to 50 ng/mL. As shown in Figure 7B, the fluorescence intensity change at $\lambda_{Em} = 650$ nm was proportional to the Zn^{2+} concentration in the range of 1–50 ng/mL, and the linear equation was $y = 15.852x + 144.7$ with $R^2 = 0.9984$. The detection limit of the method was estimated to be 1.25 ng/mL (equivalent to 19.1 nmol/L). Compared with other published methods for Zn^{2+} detection (Table 2), R-CDs analysis of Zn^{2+} shows a lower detection limit and higher sensitivity.

To evaluate the specificity of the fluorescent probe, sixteen interference ions were selected. A certain amount of R-CDs solution was mixed with 20 μ L of interfering ions (20 ng/mL), and the changes in fluorescence intensities were recorded under the same conditions. As shown in Figure 8, when R-CDs were mixed with other interfering ions, the fluorescence intensity of the (R-CDs + M^{n+}) did not change significantly compared with the fluorescence intensity of R-CDs. However, when Zn^{2+} was added to the (R-CDs + M^{n+}) mixture, the fluorescence intensity increased significantly, which was consistent with the change of fluorescence intensity of (R-CDs + Zn^{2+}). The results show that the fluorescent probe had good selectivity for Zn^{2+} .

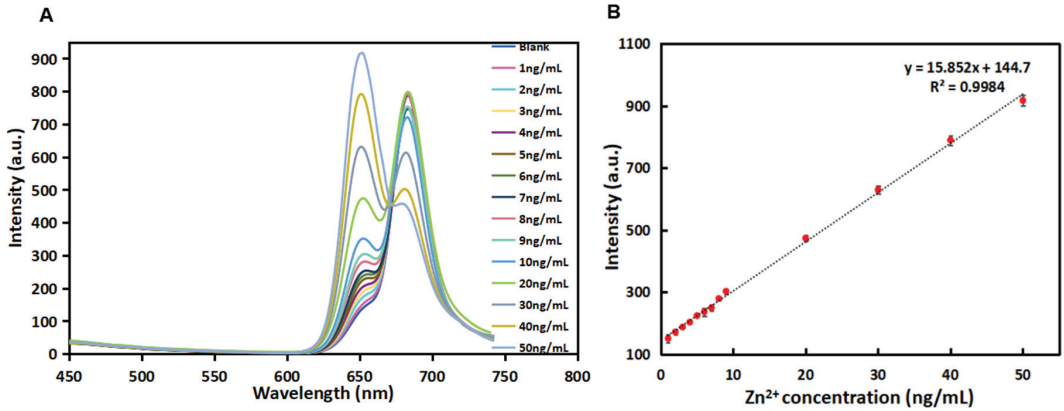


Figure 7. Fluorescence responses in the $\lambda_{Em} = 650$ nm of the R-CDs upon the addition of different concentrations of Zn^{2+} (A) and linear correlation of fluorescence intensity versus the concentrations of Zn^{2+} in the range from 1 ng/mL to 50 ng/mL (B).

Table 2. Comparison between this method and other methods for the detection of Zn^{2+} .

Detection Method	Material	LOD	Linear Range	Ref.
Electrochemical	Bismuth—nitride nanocomposites	0.5 $\mu\text{g/L}$	1~20 $\mu\text{g/L}$	[44]
Fluorescence	Lanthanide complexes	1.2 $\mu\text{mol/L}$	-	[45]
Fluorescence	Thiourea based chemical sensor	0.67 $\mu\text{mol/L}$	-	[46]
Fluorescence	Novel fluorescent peptide-based probe	26.77 nmol/L	-	[47]
Fluorescence	CDs	19.1 nmol/L	1~50 ng/mL	This method

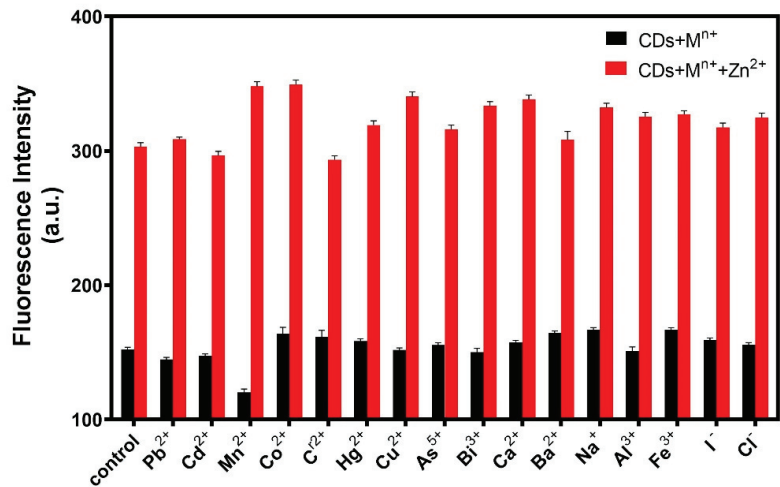


Figure 8. Specificity of the fluorescence probe for sensing Zn^{2+} .

3.7. Detection of Metal Elements in Macroalgae by R-CDs

The content of Mn^{2+} and Zn^{2+} in twenty algal samples was investigated. Sample Nos. 1–8 were laver, Nos. 9–15 were kelp, and Nos. 16–20 were laver products. The

R-CDs were used as a fluorescent probe to detect the content of Mn and Zn elements in the samples. FAAS was applied for verification of the proposed method. The results are shown in Tables 3 and 4. It was found that the detection results of the R-CDs method were consistent with that of the national standard method, demonstrating the good accuracy of the proposed method. The R-CDs could be used as a new detection fluorescence probe to detect Mn and Zn elements.

Table 3. Comparison of Mn²⁺ content in samples detected by two methods.

No.	R-CDs	RSD	FAAS	RSD
1	34.95	5.13%	34.17	1.19%
2	33.59	6.81%	37.32	0.8%
3	30.11	4.30%	29.30	2.36%
4	35.45	2.69%	26.24	1.62%
5	105.96	4.28%	116.46	2.20%
6	30.96	2.98%	33.00	1.12%
7	32.53	3.54%	49.18	3.99%
8	28.90	6.98%	31.00	0.75%
9	41.55	6.90%	45.60	1.13%
10	32.83	7.24%	28.14	3.18%
11	40.84	5.85%	31.05	1.13%
12	19.88	1.88%	23.44	1.40%
13	27.08	3.27%	31.76	2.58%
14	27.64	5.32%	43.35	2.85%
15	48.26	1.06%	46.90	3.57%
16	26.23	6.55%	24.35	3.47%
17	12.11	4.51%	17.68	0.93%
18	10.52	1.14%	10.44	1.95%
19	20.63	7.79%	25.70	4.07%
20	24.36	4.01%	26.29	1.32%

Concentration unit is mg/kg.

Table 4. Comparison of Zn²⁺ content in samples detected by two methods.

No.	R-CDs	RSD	FAAS	RSD
1	85.14	3.02%	105.16	6.03%
2	93.76	5.57%	103.95	1.19%
3	69.89	2.64%	65.46	5.55%
4	79.17	10.06%	88.40	1.23%
5	51.71	3.23%	61.10	1.83%
6	47.18	4.39%	70.07	7.16%
7	52.58	4.75%	61.95	3.98%
8	32.72	2.14%	29.74	0.97%
9	49.00	1.51%	48.07	1.20%
10	18.30	0.91%	15.82	4.15%
11	25.83	1.13%	28.92	1.69%
12	33.81	5.79%	31.98	3.68%
13	34.21	1.16%	47.01	1.01%
14	33.79	2.62%	44.01	1.30%
15	30.92	4.01%	28.30	2.76%
16	18.75	3.97%	28.04	6.19%
17	26.22	0.79%	32.27	2.40%
18	27.69	0.23%	19.57	3.25%
19	36.11	4.21%	36.45	2.65%
20	44.14	1.36%	49.03	5.34%

Concentration unit is mg/kg.

Based on the results in Tables 3 and 4, it could be concluded that the average content of Mn²⁺ in laver produced in Fujian was 41.56 mg/kg, and the No. 5 sample produced in Quanzhou showed the highest content of Mn element of 105.96 mg/kg. The average content

of Mn^{2+} in kelp was 34.01 mg/kg, and the concentration ranged from 27 to 49 mg/kg. The average Mn^{2+} content of laver products from Fujian was 37.71 mg/kg. After the deep processing, the formation process of the product had no great influence on the content of Mn^{2+} .

The average Zn^{2+} content of laver from Fujian was 57.45 mg/kg, and the concentration ranged from 30 to 94 mg/kg. The average content of Zn^{2+} in kelp was 32.27 mg/kg, and the concentration ranged from 18 to 50 mg/kg. The average Zn^{2+} content in laver products was 30.58 mg/kg. The Zn^{2+} content of Nos. 1–4 laver raw materials purchased by supermarkets was higher than that of Nos. 5–8 samples purchased by retailers. The Zn^{2+} content in laver was decreased after processing. The content of Mn^{2+} and Zn^{2+} in laver was higher than that of kelp. The daily Mn^{2+} supply for adults is 2.5 to 5 mg, and the daily Zn^{2+} supply for adults is 15 to 20 mg. Therefore, laver and kelp can be selected as the daily food supplementing of Mn and Zn.

3.8. Recovery

The No. 18 sample was selected for standard recovery of Mn^{2+} detection. A certain amount of Mn^{2+} standard solution was added, and the concentrations of samples were adjusted to 0.4 mg/mL, 2 mg/mL, and 4 mg/mL Mn^{2+} , respectively. The responses were analyzed by the R-CDs fluorescence probe. The No. 10 sample was selected for standard recovery of Zn^{2+} detection. The results are shown in Tables 5 and 6. The spiked recoveries of Mn^{2+} were all in the range of 82–120%, with relative standard deviations less than 10%. The recoveries of Zn^{2+} ranged from 97% to 120% with standard deviations less than 10%. The experimental results showed that the R-CDs fluorescence probe had good stability and accuracy for the detection of Mn^{2+} and Zn^{2+} .

Table 5. Recovery of fluorescent probe detecting Mn^{2+} .

Sample	Original Content	Add Scalar	Final Content	Recovery	Recovery Rate	RSD
blank	0.002	0.4	0.4002	0.409~0.432	102.2~107.9%	7.6%
blank	0.002	2	2.002	2.136~2.36	106.7~117.7%	3.5%
blank	0.002	4	4.002	3.30~3.483	82.4~95.7%	9.47%
18	0.168	0.4	0.568	0.558~0.594	98.3~104.6%	2.19%
18	0.168	2	2.168	1.807~2.193	83.3~101.2%	7.0%
18	0.168	4	4.168	4.205~4.393	100.9~105.4%	1.73%

Concentration unit is mg/mL.

Table 6. Recovery of fluorescent probe detecting Zn^{2+} .

Sample	Original Content	Add Scalar	Final Content	Recovery	Recovery Rate	RSD
blank	0.0577	0.4	0.4577	0.461~0.475	100.7~103.7%	1.16%
blank	0.0577	2	2.0577	2.115~2.141	102.9~104.0%	2.01%
blank	0.0577	4	4.0577	3.943~4.120	97.2~101.53%	8.81%
10	0.293	0.4	0.693	0.734~0.751	106.1~108.4%	2.59%
10	0.293	2	2.293	2.719~2.722	118.5~118.7%	5.28%
10	0.293	4	4.293	4.158~4.201	98.09~99.1%	3.87%

Concentration unit is mg/mL.

4. Conclusions

In this study, R-CDs were prepared by the thermal solvent method. The structure and properties of the R-CDs were characterized and analyzed. The results showed that the synthesized R-CDs had excitation wavelength-independent fluorescence emission. Mn^{2+} and Zn^{2+} were detected by the R-CDs-based fluorescence probes. It was found that there was a good linear relationship between fluorescence intensity and Mn^{2+} concentration, with a linear range of 1–50 ng/mL and a measuring limit of 0.23 nmol/L. Meanwhile, the

fluorescence intensity showed a good linear relationship with the concentration of Zn^{2+} . The linear range was 1–50 ng/mL, and the detection limit was 19.1 nmol/L. This method was simple to operate and quick to respond without chemical modification of the probe. The quantitative determination of Mn^{2+} and Zn^{2+} in macroalgae from Fujian province was carried out based on the established fluorescence probe method. The experimental results showed that macroalgae were rich in Mn and Zn elements. It was found that Mn and Zn contents in laver were higher than that in kelp. Through this work, the distribution characteristics of the main metal elements in kelp and laver products in the future were preliminarily understood. It provided basic data for dietary guidance and health evaluation of kelp and laver to support the value of the macroalgae industry.

Supplementary Materials: The following supporting information can be downloaded at: <https://www.mdpi.com/article/10.3390/bios12050359/s1>, Figure S1: Full XPS spectra of R-CDs. Figure S2: XPS C1s (A), O1s (B), N1s (C), and S2p (D) spectra of R-CDs. Figure S3: Effect of pH on the fluorescence emission of R-CDs. Figure S4: Fluorescence intensity changes of R-CDs in different concentration solutions of NaCl (A) and under continuous UV illumination (B). Figure S5: Optimization of pH value (A), buffer solution type (B), and reaction time (C). Figure S6: Optimization of buffer solution type (A) and reaction time (B).

Author Contributions: Conceptualization, project administration, H.X.; funding acquisition, H.X., H.Z. and Z.L.; methodology and data curation, Y.L.; validation and formal analysis, X.Y.; investigation, Z.L.; writing—original draft preparation, H.X. and X.Y.; writing—review and editing, H.X. and P.L.; supervision, Y.W., P.L. and S.Z. All authors have read and agreed to the published version of the manuscript.

Funding: We greatly appreciate the financial support from the Natural Science Foundation of Fujian Province (2019J05046), the Regional Development Project of Fujian Provincial Science and Technology Plan Project (2020N3003), the Program for Leading Talent in Fujian Provincial University (660160190), the Special Fund for Scientific and Technological Innovation at Fujian Agriculture and Forestry University of China (CXZX2020114A), the Nature Science Foundation of China (22064018), and the Nature Science Foundation of Guangxi Province of China (2019JJA120031).

Institutional Review Board Statement: Not applicable.

Informed Consent Statement: Not applicable.

Data Availability Statement: Not applicable.

Conflicts of Interest: The authors declare no conflict of interest.

References

1. Sánchez-Quiles, D.; Marbà, N.; Tovar-Sánchez, A. Trace metal accumulation in marine macrophytes: Hotspots of coastal contamination worldwide. *Sci. Total Environ.* **2017**, *576*, 520–527. [\[CrossRef\]](#)
2. Liu, Y.; Wu, S.; Hua, C.; Han, X. Effect of synergistic sorption of Cr(VI) and Mn(II) in aqueous solution using magnetic nanoparticles. *Desalin. Water Treat.* **2014**, *52*, 22–24. [\[CrossRef\]](#)
3. Dai, Z.; Canary, J.W. Tailoring tripodal ligands for zinc sensing. *New J. Chem.* **2007**, *31*, 1708–1718. [\[CrossRef\]](#)
4. Nolan, E.M.; Lippard, S.J. Tools and Tactics for the Optical Detection of Mercuric Ion. *ChemInform* **2008**, *39*, 3443–3480. [\[CrossRef\]](#)
5. Muhammad, S.; Muhammad, R.; Muhammad, H. Organic Material Based Fluorescent Sensor for Hg^{2+} : A Brief Review on Recent Development. *J. Fluoresc.* **2017**, *27*, 257–317.
6. Yu, Y.; Liu, C.; Tian, B.; Cai, X.; Zhu, H.; Jia, P.; Li, Z.; Zhang, X.; Sheng, W.; Zhu, B. A novel highly selective ratiometric fluorescent probe with large emission shift for detecting mercury ions in living cells and zebrafish. *Dye. Pigment.* **2020**, *177*, 108290. [\[CrossRef\]](#)
7. Zhou, B.; Qin, S.; Chen, B.; Han, Y. A new BODIPY-based fluorescent “turn-on” probe for highly selective and rapid detection of mercury ions. *Tetrahedron Lett.* **2018**, *59*, 4359–4363. [\[CrossRef\]](#)
8. Wu, Y.P.; Tian, J.W.; Liu, S.; Li, B.; Zhao, J.; Ma, L.F.; Li, D.-S.; Lan, Y.-Q.; Bu, X. Bi-Microporous Metal-Organic Frameworks with Cubane $[M_4(OH)_4]$ (M = Ni, Co) Clusters and Pore-Space Partition for Electrocatalytic Methanol Oxidation Reaction. *Angew. Chem.* **2019**, *58*, 12313–12317. [\[CrossRef\]](#)
9. Rong, Z.; Shulan, J.; Naixin, W.; Lin, W.; Guojun, Z.; Jian-Rong, L. Coordination-driven in situ self-assembly strategy for the preparation of metal-organic framework hybrid membranes. *Angew. Chem.* **2014**, *53*, 9775–9779.
10. Lv, X.L.; Yuan, S.; Xie, L.H.; Darke, H.F.; Chen, Y.; He, T.; Dong, C.; Wang, B.; Zhang, Y.-Z.; Li, J.-R.; et al. Ligand Rigidification for Enhancing the Stability of Metal-Organic Frameworks. *J. Am. Chem. Soc.* **2019**, *141*, 10283–10293. [\[CrossRef\]](#)

11. Chen, Y.; Li, S.; Pei, X.; Zhou, J.; Feng, X.; Zhang, S.; Cheng, Y.; Li, H.; Han, R.; Wang, B. A Solvent-Free Hot-Pressing Method for Preparing Metal-Organic-Framework Coatings. *Angew. Chem.* **2016**, *55*, 3419–3423. [[CrossRef](#)]
12. Shamsipur, M.; Barati, A.; Karami, S. Long-wavelength, multicolor, and white-light emitting carbon-based dots: Achievements made, challenges remaining, and applications. *Carbon* **2017**, *124*, 429–472. [[CrossRef](#)]
13. Wang, R.; Lu, K.Q.; Tang, Z.R.; Xu, Y.J. Recent progress in carbon quantum dots: Synthesis, properties and applications in photocatalysis. *J. Mater. Chem. A* **2017**, *5*, 3717–3734. [[CrossRef](#)]
14. Li, K.; Liu, W.; Ni, Y.; Li, D.; Lin, D.; Su, Z.; Wei, G. Technical synthesis and biomedical applications of graphene quantum dots. *J. Mater. Chem. B* **2017**, *5*, 4811–4826. [[CrossRef](#)]
15. Dong, J.; Wang, K.; Sun, L.; Sun, B.; Yang, M.; Chen, H.; Wang, Y.; Sun, J.; Dong, L. Application of graphene quantum dots for simultaneous fluorescence imaging and tumor-targeted drug delivery. *Sens. Actuators B Chem.* **2018**, *256*, 616–623. [[CrossRef](#)]
16. Farshbaf, M.; Davaran, S.; Rahimi, F.; Annabi, N.; Salehi, R.; Akbarzadeh, A. Carbon quantum dots: Recent progresses on synthesis, surface modification and applications. *Artif. Cells Nanomed. Biotechnol.* **2017**, *46*, 1331–1348. [[CrossRef](#)]
17. Shen, J.; Zhu, Y.; Yang, X.; Li, C. Graphene Quantum Dots: Emergent Nanolights for Bioimaging, Sensors, Catalysis and Photovoltaic Devices. *ChemInform* **2012**, *43*, 3686–3699.
18. Hola, K.; Bourlinos, A.B.; Kozak, O.; Berka, K.; Siskova, K.; Havrdova, M.; Tucek, J.; Safarova, K.; Otyepka, M.; Giannelis, E.P.; et al. Photoluminescence effects of graphitic core size and surface functional groups in carbon dots: COO-Induced red-shift emission. *Carbon* **2014**, *70*, 279–286. [[CrossRef](#)]
19. Ahmadian-Fard-Fini, S.; Salavati-Niasari, M.; Ghanbari, D. Hydrothermal green synthesis of magnetic Fe₃O₄-carbon dots by lemon and grape fruit extracts and as a photoluminescence sensor for detecting of E. coli bacteria. *Spectrochim. Acta Part A Mol. Biomol. Spectrosc.* **2018**, *203*, 481–493. [[CrossRef](#)]
20. Xu, Q.; Wei, J.; Wang, J.; Liu, Y.; Li, N.; Chen, Y.; Gao, C.; Znahg, W.; Sreeprasad, T.S. Facile synthesis of copper doped carbon dots and their application as a turn-off fluorescent probe in the detection of Fe³⁺ ions. *RSC Adv.* **2016**, *6*, 28745–28750. [[CrossRef](#)]
21. Liu, H.; Zhang, Y.; Liu, J.H.; Hou, P.; Zhou, J.; Huang, C.Z. Preparation of nitrogen-doped carbon dots with high quantum yield from Bombyx mori silk for Fe(III) ions detection. *RSC Adv.* **2017**, *7*, 50584–50590. [[CrossRef](#)]
22. He, H.; Yang, Y.; Li, J.; Lai, X.; Chen, X.; Wang, L.; Zhang, W.; Huang, Y.; Zhang, P. Enhanced fluorescence of Zn-doped carbon quantum dots using zinc citrate chelate as precursor for fluorescent sensor applications. *Mater. Sci. Eng. B* **2021**, *264*, 114955. [[CrossRef](#)]
23. Huang, L.; Zhao, Y.; Zhang, H.; Huang, K.; Yang, J.; Han, G. Expanding Anti-Stokes Shifting in Triplet-Triplet Annihilation Upconversion for In Vivo Anticancer Prodrug Activation. *Angew. Chem.* **2017**, *56*, 14592–14596. [[CrossRef](#)]
24. Li, Z.; Zhang, Y.; Wu, X.; Wu, X.; Maudgal, R.; Zhang, H.; Han, G. In Vivo Repeatedly Charging Near-Infrared-Emitting Mesoporous SiO₂/ZnGa₂O₄:Cr³⁺ Persistent Luminescence Nanocomposites. *Adv. Sci.* **2015**, *2*, 1500001. [[CrossRef](#)]
25. Surana, K.; Mehra, R.M.; Soni, S.S.; Bhattacharya, B. Real-time photovoltaic parameters assessment of carbon quantum dots showing strong blue emission. *RSC Adv.* **2022**, *12*, 1352–1360. [[CrossRef](#)]
26. Krishnaiah, P.; Atchudan, R.; Perumal, S.; Salama, E.; Lee, Y.R.; Jeon, B. Utilization of waste biomass of *Poa pratensis* for green synthesis of n-doped carbon dots and its application in detection of Mn²⁺ and Fe³⁺. *Chemosphere* **2022**, *286*, 131764. [[CrossRef](#)]
27. Lu, S.; Sui, L.; Liu, J.; Zhu, S.; Chen, A.; Jin, M.; Yang, B. Near-Infrared Photoluminescent Polymer-Carbon Nanodots with Two-Photon Fluorescence. *Adv. Mater.* **2017**, *29*, 1603443. [[CrossRef](#)]
28. Pan, L.; Sun, S.; Zhang, L.; Jiang, K.; Lin, H. Near-infrared emissive carbon dots for two-photon fluorescence bioimaging. *Nanoscale* **2016**, *8*, 17350–17356. [[CrossRef](#)]
29. Zhu, S.; Song, Y.; Zhao, X.; Shao, J.; Zhang, J.; Yang, B. The photoluminescence mechanism in carbon dots (graphene quantum dots, carbon nanodots, and polymer dots): Current state and future perspective. *Nano Res.* **2015**, *8*, 355–381. [[CrossRef](#)]
30. Li, L.; Li, K.; Liu, Y.; Xu, H.; Yu, X. Red emission fluorescent probes for visualization of monoamine oxidase in living cells. *Sci Rep.* **2016**, *6*, 1–8. [[CrossRef](#)]
31. Miao, X.; Qu, D.; Yang, D.; Nie, B.; Zhao, Y.; Fan, H.; Sun, Z. Synthesis of Carbon Dots with Multiple Color Emission by Controlled Graphitization and Surface Functionalization. *Adv. Mater.* **2018**, *30*, 1704740. [[CrossRef](#)]
32. Pan, L.; Sun, S.; Zhang, A.; Jiang, K.; Zhang, L.; Dong, C.; Huang, Q.; Wu, A.; Lin, H. Truly Fluorescent Excitation-Dependent Carbon Dots and Their Applications in Multicolor Cellular Imaging and Multidimensional Sensing. *Adv. Mater.* **2015**, *27*, 7782–7787. [[CrossRef](#)]
33. Mercado-Zúñiga, C.; Torres-Torres, C.; Trejo-Valdez, M.; Torres-Martínez, R.; Cervantes-Sodi, F.; Vargas-García, J.R. Influence of silver decoration on the nonlinear optical absorption exhibited by multiwall carbon nanotubes. *J. Nanopart. Res.* **2014**, *16*, 1–9. [[CrossRef](#)]
34. Jain, R.; Thakur, A.; Kaur, P.; Kim, K.; Devi, P. Advances in imaging-assisted sensing techniques for heavy metals in water: Trends, challenges, and opportunities. *Trends Anal. Chem.* **2020**, *123*, 115758. [[CrossRef](#)]
35. Wang, Y.; Lao, S.; Ding, W.; Zhang, Z.; Liu, S. A novel ratiometric fluorescent probe for detection of iron ions and zinc ions based on dual-emission carbon dots. *Sens. Actuators B* **2018**, *284*, 186–192. [[CrossRef](#)]
36. Kumar, V.V.; Thiagarajan, R.; Anthony, S.P. Fluorescent carbon quantum dots chemosensor for selective turn-on sensing of Zn²⁺ and turn-off sensing of Pb²⁺ in aqueous medium and Zebra fish egg. *New J. Chem.* **2017**, *41*, 15157–15164. [[CrossRef](#)]
37. Yang, M.; Tang, Q.; Meng, Y.; Liu, J.; Feng, T.; Zhao, X.; Zhu, S.; Yu, W.; Yang, B. Reversible “Off-On” Fluorescence of-Passivated Carbon Dots: Mechanism and Potential for the Detection of EDTA and Zn²⁺. *Langmuir* **2018**, *34*, 7767–7775. [[CrossRef](#)]

38. Roushani, M.; Saedi, Z.; Hamdi, F.; Dizajdizi, B.Z. Preparation an electrochemical sensor for detection of manganese (II) ions using glassy carbon electrode modified with multi walled carbon nanotube-chitosan-ionic liquid nanocomposite decorated with ion imprinted polymer. *J. Electroanal. Chem.* **2017**, *804*, 1–6. [[CrossRef](#)]
39. He, Y.; Zhang, X. Ultrasensitive colorimetric detection of manganese(II) ions based on anti-aggregation of unmodified silver nanoparticles. *Sens. Actuators B Chem.* **2016**, *222*, 320–324. [[CrossRef](#)]
40. Zhao, L.; Li, H.; Liu, H.; Liu, M.; Huang, N.; He, Z.; Li, Y.; Chen, Y.; Ding, L. Microwave-assisted facile synthesis of polymer dots as a fluorescent probe for detection of cobalt(II) and manganese(II). *Anal. Bioanal. Chem.* **2019**, *411*, 2373–2381. [[CrossRef](#)]
41. Meng, L.; Yuan, Y.; Pu, G.; Xu, N. An “on–off–on” fluorescence assay based on silicon nanoparticles for selective detection of manganese(II). *Anal. Methods* **2017**, *9*, 2553–2560. [[CrossRef](#)]
42. Giusti, L. Heavy metal contamination of brown seaweed and sediments from the UK coastline between the Wear river and the Tees river. *Environ. Int.* **2001**, *26*, 275–286. [[CrossRef](#)]
43. Brito, G.B.; de Souza, T.L.; Bressy, F.C.; Moura, C.W.N.; Korn, M.G.A. Levels and spatial distribution of trace elements in macroalgae species from the Todos os Santos Bay, Bahia, Brazil. *Mar. Pollut. Bull.* **2012**, *64*, 2238–2244. [[CrossRef](#)]
44. Winnett, M.R.; Mini, P.; Grace, M.R.; Tuck, K.L. Time-Resolved Terbium-Based Probe for the Detection of Zinc(II) Ions: Investigation of the Formation of a Luminescent Ternary Complex. *Inorg. Chem.* **2020**, *59*, 118–127. [[CrossRef](#)]
45. So, H.; Cho, H.; Lee, H.; Tran, M.C.; Kim, K.; Kim, C. Detection of zinc (II) and hypochlorite by a thiourea-based chemosensor via two emission channels and its application in vivo. *Microchem. J.* **2020**, *155*, 104788. [[CrossRef](#)]
46. Wang, P.; Wang, S.; Chen, L.; Wang, W.; Wang, B.; Liao, Y. A novel peptide-based fluorescent probe for sensitive detection of zinc (II) and its applicability in live cell imaging. *Spectrochim. Acta Part A Mol. Biomol. Spectrosc.* **2020**, *240*, 118549. [[CrossRef](#)]
47. Zhu, X.; Liu, B.; Li, L.; Wu, L.; Chen, S.; Huang, L.; Yang, J.; Liang, S.; Xiao, K.; Hu, J.; et al. A micromilled microgrid sensor with delaminated MXene-bismuth nanocomposite assembly for simultaneous electrochemical detection of lead(II), cadmium(II) and zinc(II). *Mikrochim. Acta* **2019**, *186*, 1–7. [[CrossRef](#)]



A Smartphone Integrated Platform for Ratiometric Fluorescent Sensitive and Selective Determination of Dipicolinic Acid

Xiang Li ^{1,*}, Junsong Wu ², Huaguang Hu ¹, Fangfang Liu ¹ and Jialian Wang ^{1,*}¹ School of Marine and Biological Engineering, Yancheng Teachers University (YCTU), Yancheng 224002, China² Department of Basic Medical Science, Jiangsu Vocational College of Medicine, Yancheng 224005, China

* Correspondence: lix01@yctu.edu.cn (X.L.); wangjl@yctu.edu.cn (J.W.)

Abstract: A desirable lanthanide-based ratiometric fluorescence probe was designed as a multifunctional nanoplatform for the determination of dipicolinic acid (DPA), a unique bacterial endospore biomarker, with high selectivity and sensitivity. The carbon dots (CDs) with blue emission wavelengths at 470 nm are developed with europium ion (Eu³⁺) to form Eu³⁺/CDs fluorescent probes. DPA can specifically combine with Eu³⁺ and then transfer energy from DPA to Eu³⁺ sequentially through the antenna effect, resulting in a distinct increase in the red fluorescence emission peak at 615 nm. The fluorescence intensity ratio of Eu³⁺/CDs (fluorescence intensity at 615 nm/fluorescence intensity at 470 nm) showed good linearity and low detection limit. The developed ratiometric nanoplatform possesses great potential for application in complex matrices owing to its specificity for DPA. In addition, the integration of a smartphone with the Color Picker APP installed enabled point-of-care testing (POCT) with quantitative measurement capabilities, confirming the great potential of the as-prepared measurement platform for on-site testing.

Keywords: ratiometric; fluorescence; determination of dipicolinic acid; smartphone-based detection

1. Introduction

Inhalation of 10⁴ or more concentration of *Bacillus anthracis* (*B. anthracis*) spores can lead to a mortality of as high as 75%, even within 24 to 48 h of drug treatment [1,2], indicating that *B. anthracis* spores poses a serious threat to human health and public safety [3,4]. Therefore, sensitive and selective determination of *B. anthracis* spores had a critical role to play in early clinical diagnosis and preventing disease outbreaks [5,6]. Dipicolinic acid (DPA), making up approximately 5–15% of the dry weight of anthrax spores, was an extremely important component and major biomarker of anthrax spores [7–10]. Consequently, the level of anthrax spores could be detected and evaluated through the concentration of DPA. Recently, although considerable strategies for the determination of DPA had been constructed, including electrochemical assays, Surface-enhanced Raman spectroscopy (SERS), mass spectrometry (MS), colorimetric methods, etc. [11,12]. These strategies are usually cumbersome, time-consuming and require large instruments, which may not be suitable for on-site rapid detection of DPA. In general, fluorescence-based sensing was a promising optical candidate for addressing the above-mentioned problems in DPA determination [13–15]. However, the further application of fluorescent probes was greatly restricted by the shortcomings of their used currently, such as complicated synthesis processes, poor fluorescence stability and low sensitivity [16].

Lanthanide-based fluorescence nanoprobles had been constructed and employed to the determination of targeting on account of that special optical properties such as large Stokes shifts, long fluorescent lifetimes and high fluorescence stability [17–20]. In fluorescence measurements, DPA acted as a single ligand coordinated with Eu³⁺ or terbium ions (Tb³⁺) and then sensitized lanthanide ions emission by transferring excitation energy to the lanthanide ions by an “antenna effect”, a strategy that can be employed to sensing of

Citation: Li, X.; Wu, J.; Hu, H.; Liu, F.; Wang, J. A Smartphone Integrated Platform for Ratiometric Fluorescent Sensitive and Selective Determination of Dipicolinic Acid. *Biosensors* **2022**, *12*, 668. <https://doi.org/10.3390/bios12080668>

Received: 5 July 2022

Accepted: 17 August 2022

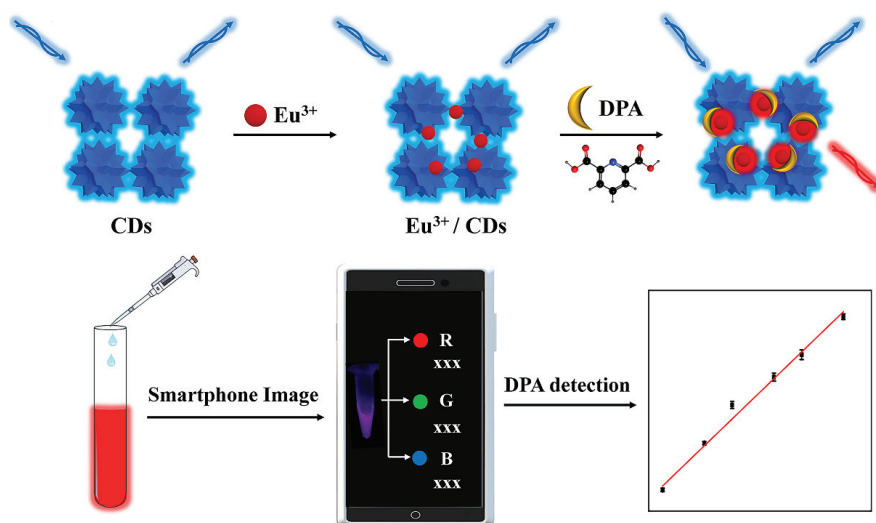
Published: 22 August 2022



Copyright: © 2022 by the authors. Licensee MDPI, Basel, Switzerland. This article is an open access article distributed under the terms and conditions of the Creative Commons Attribution (CC BY) license (<https://creativecommons.org/licenses/by/4.0/>).

DPA levels [21,22]. Ratiometric fluorescence detection strategies, recording fluorescence emission at two different wavelengths, had attracted increasing attention and interest from researchers because of the increased accuracy and reproducibility of target assays as well as the reduction of false positive or false negative signal results compared to strategies with a single emission signal [23–27].

Herein, a desirable ratiometric fluorescence platform was fabricated for the highly sensitive and selective detection of the *B. anthracis* biomarker DPA by integrating Eu^{3+} and CDs ($\text{Eu}^{3+}/\text{CDs}$) in Scheme 1. Taking into consideration fully the coordination binding of DPA to Eu^{3+} in the complex of $\text{Eu}^{3+}/\text{CDs}$, the formed complex of $\text{Eu}^{3+}/\text{DPA}$ then emitted a red fluorescence while the blue fluorescence of CDs was not changed. Therefore, the fluorescence ratio (F_{615}/F_{470}) of red fluorescence to blue fluorescence as a signal can be augmented with increasing concentrations of DPA. Furthermore, the developed strategy was further utilized for the sensitivity detection of DPA in real samples by integrating a smartphone with Color Picker APP. The ratiometric fluorescence sensing platform based on $\text{Eu}^{3+}/\text{CDs}$ fluorescent probes has the ability to rapidly detect DPA in the field and thus assess the infection level of anthrax spores, which has great potential in food safety and healthcare.



Scheme 1. Illustration of the ratiometric fluorescence sensing for DPA detection.

2. Materials and Methods

2.1. Materials and Reagents

Chemicals including $\text{Eu}(\text{NO}_3)_3 \cdot 6\text{H}_2\text{O}$, dipicolinic acid (DPA) were purchased from Aladdin Reagent Co., Ltd. (Shanghai, China). Polyethylenimine was purchased from Sigma-Aldrich. Citric acid, glutamic acid (Glu), cysteine (Cys), glutathione (GSH), adenosine triphosphate (ATP), sodium chloride (KCl), ferric chloride hexahydrate ($\text{FeCl}_3 \cdot 6\text{H}_2\text{O}$), zinc nitrate (ZnNO_3) and nickel chloride hexahydrate ($\text{NiCl}_2 \cdot 6\text{H}_2\text{O}$) were purchased from Sinopharm Group Chemical Reagent Co., Ltd. Milk was purchased from the local supermarket.

2.2. Preparation of CDs

CDs were synthesized according to reported work [28]. First, the citric acid and polyethylenimine was dissolved in 10 mL DI water under stirring. Then, the mixture solution was poured into a poly(p-phenol)-lined stainless-steel autoclave and heated at $200\text{ }^\circ\text{C}$ for 5 h. After that, the obtained solution was dialyzed to remove unreacted impurities.

2.3. Determination of DPA with Eu^{3+} /CDs Sensing System

To determine the optimal incubation time, the DPA (100 μM) was incubated and stirred with Eu^{3+} /CDs in Phosphate Buffer (PB) (10 mM, pH = 7.5) for different minutes (1–20 min) at 25 °C. Then, the fluorescence intensity of the sensing system was recorded by fluorescence spectrometry at 285 nm excitation. Similarly, only the incubation temperature (25–55 °C) was changed in above sensing system to determine the optimal incubation temperature. After adding Eu^{3+} /CDs into PB, the DPA with different concentrations (0–200 μM) was added above the solution and stirred for 10 min at 25 °C. Then, the fluorescence intensity of the sensing system was recorded by fluorescence spectrometry at 285 nm excitation. For interference experiments, the DPA, GSH, Cys, Glu, ATP, Cl^- , Zn^{2+} , Ni^{2+} and Fe^{3+} were added to Eu^{3+} /CDs solution, respectively. The final concentration of DPA and other interfering substances was 50 μM . Finally, the emission spectra at 285 nm excitation of these reaction solutions were recorded.

2.4. DPA Sensing in Real Samples

As for DPA detection in real samples, milk was selected as samples. The purchased milk was treated in the same way as previously reported [29]. In order to remove proteins, the purchased milk was sonicated for 30 min with trichloroacetic acid and then the mixture was centrifuged for 5 min. The filter paper was used to filter the supernatant to remove the lipids. DPA with various concentrations (0, 10, 20 and 50 μM) was spiked into the treated milk for further analysis, which then were added into the Eu^{3+} /CDs sensing system. The fluorescence responses were measured under the excitation at 285 nm after incubating for 10 min.

2.5. The Smartphone-Integrated Assay for DPA Detection

For the smartphone-based assay for DPA detection, the samples were incubated with Eu^{3+} /CDs and stirred for 10 min. Then, the fluorescent image was recorded and analyzed using the Color Picker APP on the smartphone to access its RGB intensity for analysis. It is worth noting that the samples were placed in a dark lamphouse to avoid environmental interference.

3. Results

3.1. The Principle of Ratiometric Fluorescence Strategy for DPA Determination

The ligand-containing DPA coordinated with Eu^{3+} and the triplet excited state of the ligand transferred energy to the emitting state of Eu^{3+} to enhance the fluorescence intensity (Figure S1 in Supplementary), which then directly detect DPA [30,31]. Considering that a single variation in signal was susceptible to environmental interference, a ratiometric fluorescent sensor was constructed to overcome these problems and improve the sensitivity and selectivity. As shown in Figure 1, the CDs emitted bright blue fluorescence at 470 nm (curve a), and its fluorescence intensity was not compromised when adding Eu^{3+} (curve b). The blue fluorescence can be obviously observed under the UV irradiation, seen in the insert photos. In the presence of DPA, the combined with the complex of Eu^{3+} /CDs can obviously enhance the fluorescence at 615 nm due to the occurrence of antenna effect, while the blue fluorescence kept stability (curve c). The red fluorescence was easily found, seen in the insert photo. Therefore, the ratiometric strategy was established to sense the target based on the ratio of F_{615}/F_{470} against increasing concentrations of DPA, which also provided the basis for intelligent detection using the smartphone with Color Picker APP. Here, the F_{615} and F_{470} were the fluorescence emission intensity of Eu^{3+} /DPA at 615 nm and the CDs fluorescence emission intensity at 470 nm, respectively.

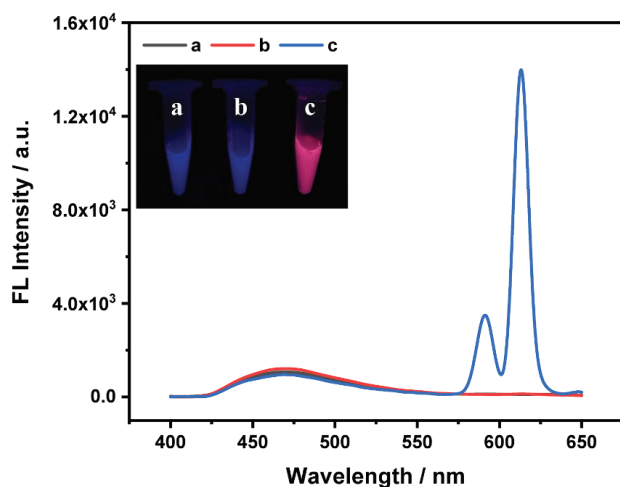


Figure 1. The fluorescence spectra and the corresponding photographs of CDs (a), CDs with Eu^{3+} (b), and Eu^{3+} /CDs with DPA (c).

3.2. Optimization of Detection Experimental Conditions

To guarantee the high sensitivity and stability of the Eu^{3+} /CDs nanoplatform for target monitoring, several important factors were investigated and optimized, including the concentration of Eu^{3+} , reaction temperature and incubation time. The concentration of Eu^{3+} was a key factor in the sensitivity of the assays. It can be seen that the blue fluorescent CDs maintains a stable fluorescence intensity with increasing the concentration of Eu^{3+} from 0 to 500 μM , which indicates that CDs can be used as an internal parameter (Figure 2A). Due to the energy transfer from DPA to Eu^{3+} , the red fluorescence intensity increased significantly after adding different concentrations of Eu^{3+} (Figure 2B). The fluorescence ratio of F_{615}/F_{470} was augmented with concentration of Eu^{3+} and reached a plateau at 50 μM . Here, the F_{615} and F_{470} were the emitted fluorescence intensity of Eu^{3+} /DPA at 615 nm and the CDs at 470 nm, respectively. Thus, Eu^{3+} at 50 μM was selected for the detection of DPA in the following experiments. In order to investigate whether the experiment can be performed in the field for rapid detection, the temperature and reaction time of testing were crucial. Learn from Figure 2C,D, the reaction of Eu^{3+} and DPA can be carried out rapidly at room temperature and takes only 10 min, indicating that the system had the capability of detecting DPA in a short time and with high stability, providing an important guarantee for subsequent field testing.

3.3. The DPA Detection with Eu^{3+} /CDs Probe

Under the optimal reaction conditions, the detection sensitivity of the as-prepared Eu^{3+} /CDs probe was examined by monitoring the ratio fluorescence response of the detection system as a function of different concentrations of DPA in Figure 3A. As the concentration of DPA increased from 0 to 200 μM , the coordination complex Eu^{3+} /DPA was formed, resulting in augmented red fluorescence, while the blue emission fluorescence remained relatively constant. To evaluate the sensitivity of the ratiometric fluorescence platform, the ratio of F_{615}/F_{470} was plotted against different concentrations of DPA, and the variation of ratio in Figure 3B,C was linear over the concentration range of 0–20 μM with a correlation coefficient R^2 of 0.9961 and 20–150 μM with a correlation coefficient R^2 of 0.9971. The limit of detection (LOD) was calculated to be as low as 1.18 μM according to the three times of signal-to-noise ratio, which confirmed the feasibility of the developed platform. The selectivity was further examined by measuring the fluorescence ratio of the system against other potential interfering analytes. As illustrated in Figure 3D, the fluorescence ratio of the target analyte DPA (50 μM) can be obviously monitored, which

was significantly higher than that of other analytes, which proves that only DPA target can cause the change of sensor signal. Therefore, the developed strategy was specific and selective for the detection of DPA and can greatly reduce the influence of other interferents.

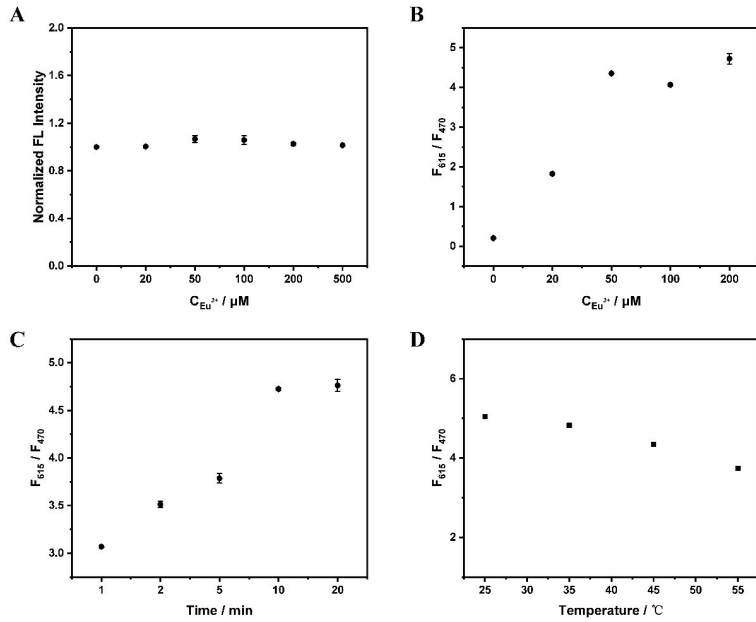


Figure 2. (A) The normalized fluorescence intensity of CDs against different concentrations of Eu^{3+} . (B) The ratio of F_{615}/F_{470} against different concentrations of Eu^{3+} in CDs with DPA. The reaction times (C) and different temperature (D) of the Eu^{3+}/CDs system in the presence of DPA.

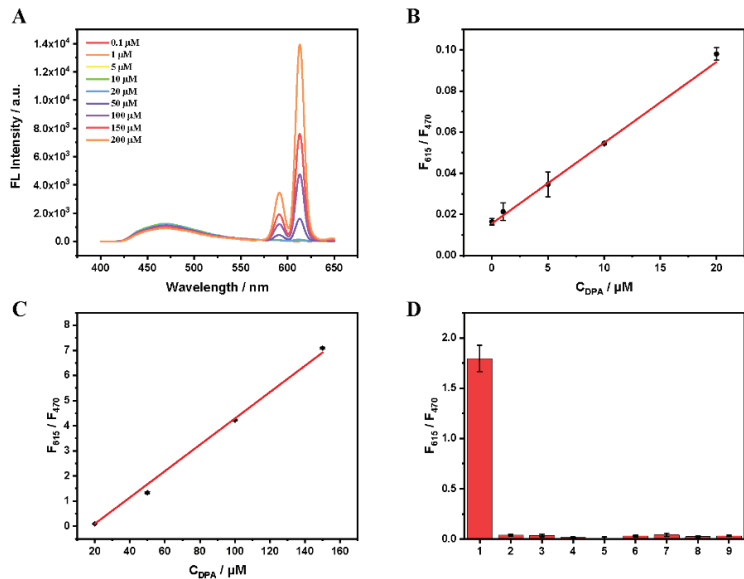


Figure 3. (A) The fluorescence spectra of Eu^{3+}/CDs in the presence of different concentrations of DPA. The standard curves of DPA detection in the range from 0–20 μM (B) and 20–150 μM (C). (D) Selectivity sensing of the ratiometric fluorescence platform in the presence of each interferences substance and DPA target (1: DPA, 2: Cys, 3: GSH, 4: ATP, 5: Glu, 6: Cl^{-} , 7: Fe^{3+} , 8: Zn^{2+} , 9: Ni^{2+}).

3.4. Sensitive Detection of DPA in Real Samples

To further explore the practicality of the proposed strategy, the milk samples with spiking a certain concentration of DPA were selected for the experiment. As displayed in Table 1, no DPA was detected in real samples. Then, the DPA with different concentrations (0, 10, 20, 50 μM) was spiked into the samples and then the same procedure was followed for quantification by the developed platform. The results showed satisfactory recoveries (97–99%) and accuracy (RSD < 4.05%) for detection of DPA, suggesting that the proposed platform can be used to determination the DPA in real food samples.

Table 1. Determination of spiked samples of DPA in real samples by the developed strategy.

Sample	Spiked (μM)	Found	Recovery (%)	RSD (%)
Milk	0	-	-	-
	10	9.9	99	1.65
	20	19.8	99	4.05
	50	48.5	97	2.9

3.5. Smartphone-Integrated DPA Detection in Real Samples

The current fluorescence assays usually require fluorescence spectrometer and specialized researchers, which is not suitable in on-site analysis [32–37]. In this research, a smartphone installed a Color Picker APP is used as a signal reader to detect the DPA by integrating with the as-prepared ratiometric fluorescent sensing, Figure 4A. The color of sample-triggered fluorescence photograph can be converted to digital values representing the blue (B), green (G) and red (R) color channels. The blue fluorescence (Blue channel) can gradually convert red fluorescence (Red channel) with increasing concentration of DPA range from 5 to 150 μM under UV light irradiation. Meanwhile, CIE coordinates can also prove the color changes from blue to red in Figure 4B. As shown in Figure 4A, the ratio of red (G) to blue (B) channel (R/B) was linearly related in the range of 5 to 150 μM .

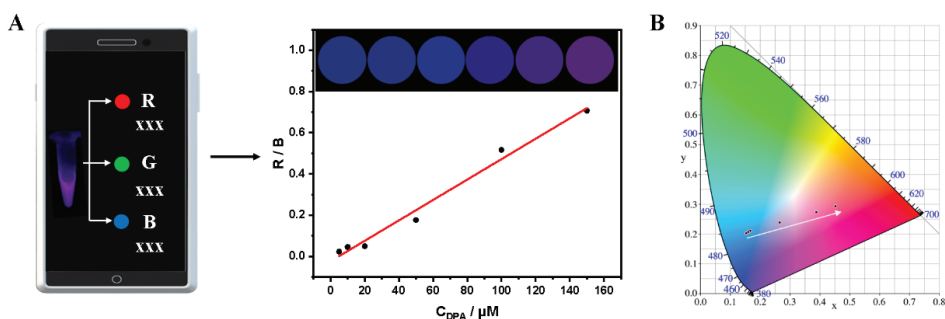


Figure 4. The smartphone-based sensor calibration plot based on ratio of R/B (A) and the CIE chromaticity coordinates of $\text{Eu}^{3+}/\text{CDs}$ (B) against concentrations of DPA range from 5 to 150 μM (Illustration: converted photos of $\text{Eu}^{3+}/\text{CDs}$ with different concentrations of DPA).

4. Conclusions

In summary, a ratiometric fluorescence strategy has been developed for sensitive and selective determination of DPA based on lanthanides-based $\text{Eu}^{3+}/\text{CDs}$ fluorescent sensor. In addition, the developed strategy can significantly reduce the interface from the complex matrixes and environments and that also improve the practicality and reliability. The determination of DPA is then qualified in real samples, showing the satisfactory recoveries from 97 to 99%. The obtained results of solution fluorescence within increasing concentration of DPA can be quantitatively analyzed by a smartphone loaded Color Picker APP, which can be applied to the POCT with accuracy and stability, exhibiting potential promising application in situ for DPA monitoring.

Supplementary Materials: The following supporting information can be downloaded at: <https://www.mdpi.com/article/10.3390/bios12080668/s1>, Figure S1: The fluorescence spectra of (a) Eu^{3+} , (b) DPA, and (c) Eu^{3+} /DPA.

Author Contributions: X.L. Conceptualization, Methodology, Supervision, Funding acquisition, Writing—Review & Editing. J.W. (Junsong Wu) Methodology, Validation. H.H. Methodology, Investigation. F.L. Validation, Investigation, Writing—Original Draft. J.W. (Jialian Wang) Methodology, Supervision, Writing—Review & Editing. All authors have read and agreed to the published version of the manuscript.

Funding: This work was supported by the Research on the Open Project program of the Beijing Laboratory of Food Quality and Safety, Beijing Technology and Business University (FQS-202007).

Institutional Review Board Statement: Not applicable.

Data Availability Statement: Not applicable.

Conflicts of Interest: The authors declare no conflict of interest.

References

- King, D.; Luna, V.; Cannons, A.; Cattani, J.; Amuso, P. Performance Assessment of Three Commercial Assays for Direct Detection of *Bacillus anthracis* Spores. *J. Clin. Microbiol.* **2003**, *41*, 3454–3455. [[CrossRef](#)] [[PubMed](#)]
- Hurtle, W.; Bode, E.; Kulesh, D.A.; Kaplan, R.S.; Garrison, J.; Bridge, D.; House, M.; Frye, M.S.; Loveless, B.; Norwood, D. Detection of the *Bacillus anthracis* gyrA Gene by Using a Minor Groove Binder Probe. *J. Clin. Microbiol.* **2004**, *42*, 179–185. [[CrossRef](#)] [[PubMed](#)]
- Enserink, M. This Time it was Real: Knowledge of Anthrax Put to the Test. *Science* **2001**, *294*, 490–491. [[CrossRef](#)] [[PubMed](#)]
- Zhang, X.Y.; Zhao, J.; Whitney, A.V.; Elam, J.W.; Duyne, R.P.V. Ultrastable Substrates for Surface-Enhanced Raman Spectroscopy: Al_2O_3 Overlayers Fabricated by Atomic Layer Deposition Yield Improved Anthrax Biomarker Detection. *J. Am. Chem. Soc.* **2006**, *128*, 10304–10309. [[CrossRef](#)]
- Liu, M.L.; Chen, B.B.; He, J.H.; Li, C.M.; Li, Y.F.; Huang, C.Z. Anthrax biomarker: An ultrasensitive fluorescent ratiometry of dipicolinic acid by using terbium (III)-modified carbon dots. *Talanta* **2019**, *191*, 443–448. [[CrossRef](#)]
- Cheng, H.W.; Huan, S.Y.; Yu, R.Q. Nanoparticle-based substrates for surface-enhanced Raman scattering detection of bacterial spores. *Analyst* **2012**, *137*, 3601–3608. [[CrossRef](#)]
- Bailey, G.F.; Karp, S.; Sacks, L.E. Ultraviolet-Absorption Spectra of Dry Bacterial Spores. *J. Bacteriol.* **1965**, *89*, 984–987. [[CrossRef](#)]
- Cable, M.L.; Kirby, J.P.; Sorasaene, K.; Gray, H.B.; Ponce, A. Bacterial Spore Detection by $[\text{Tb}^{3+}(\text{macrocycle})(\text{dipicolinate})]$ Luminescence. *J. Am. Chem. Soc.* **2007**, *129*, 1474–1475. [[CrossRef](#)]
- Rode, L.J.; Foster, J.W. Germination of Bacterial Spores by Long-Chain Alkyl Amines. *Nature* **1960**, *188*, 1132–1134. [[CrossRef](#)]
- Ratiu, I.A.; Bocos-Bintintan, V.; Patrut, A.; Moll, V.H.; Turner, M.; Thomasd, C.L.P. Discrimination of bacteria by rapid sensing their metabolic volatiles using an aspiration-type ion mobility spectrometer (a-IMS) and gas chromatography-mass spectrometry GC-MS. *Anal. Chim. Acta* **2017**, *982*, 209–217. [[CrossRef](#)]
- Li, D.; Truong, T.V.; Bills, T.M.; Holt, B.C.; VanDerwerken, D.N.; Williams, J.R.; Acharya, A.; Robison, R.A.; Tolley, H.D.; Milton, L.; et al. GC/MS Method for Positive Detection of *Bacillus anthracis* Endospores. *Anal. Chem.* **2012**, *84*, 1637–1644. [[CrossRef](#)]
- Shen, M.L.; Liu, B.; Xu, L.; Jiao, H. Ratiometric fluorescence detection of anthrax biomarker 2,6-dipicolinic acid using hetero MOF sensors through ligand regulation. *J. Mater. Chem. C* **2020**, *8*, 4392–4400. [[CrossRef](#)]
- Yin, S.N.; Tong, C.L. Europium (III)-Modified Silver Nanoparticles as Ratiometric Colorimetric and Fluorescent Dual-Mode Probes for Selective Detection of Dipicolinic Acid in Bacterial Spores and Lake Waters. *ACS Appl. Nano Mater.* **2021**, *4*, 5469–5477. [[CrossRef](#)]
- Donmez, M.; Yilmaz, M.D.; Kilbas, B. Fluorescent detection of dipicolinic acid as a biomarker of bacterial spores using lanthanide-chelated gold nanoparticles. *J. Hazard. Mater.* **2017**, *324*, 593–598. [[CrossRef](#)]
- Xu, J.; Shen, X.K.; Jia, L.; Zhang, M.M.; Zhou, T.; Wei, Y.K. Facile ratiometric fluorapatite nanoprobe for rapid and sensitive bacterial spore biomarker detection. *Biosens. Bioelectron.* **2017**, *87*, 991–997. [[CrossRef](#)]
- Xiu, L.F.; Huang, K.Y.; Zhu, C.T.; Zhang, Q.; Peng, H.P.; Xia, X.H.; Chen, W.; Deng, H.H. Rare-Earth Eu^{3+} /Gold Nanocluster Ensemble-Based Fluorescent Photoinduced Electron Transfer Sensor for Biomarker Dipicolinic Acid Detection. *Langmuir* **2021**, *37*, 949–956. [[CrossRef](#)]
- Donmez, M.; Oktem, H.A.; Yilmaz, M.D. Ratiometric fluorescence detection of an anthrax biomarker with Eu^{3+} -chelated chitosan biopolymers. *Carbohydr. Polym.* **2018**, *180*, 226–230. [[CrossRef](#)]
- Yang, Z.R.; Wang, M.M.; Wang, X.S.; Yin, X.B. Boric-Acid-Functional Lanthanide Metal-Organic Frameworks for Selective Ratiometric Fluorescence Detection of Fluoride Ions. *Anal. Chem.* **2017**, *89*, 1930–1936. [[CrossRef](#)]
- Rong, M.C.; Deng, X.Z.; Chi, S.T.; Huang, L.Z.; Zhou, Y.B.; Shen, Y.N.; Chen, X. Ratiometric fluorometric determination of the anthrax biomarker 2, 6-dipicolinic acid by using europium (III)-doped carbon dots in a test stripe. *Microchim. Acta* **2018**, *185*, 201. [[CrossRef](#)]

20. Yilmaz, M.D.; Oktem, H.A. Eriochrome Black T-Eu³⁺ Complex as a Ratiometric Colorimetric and Fluorescent Probe for the Detection of Dipicolinic Acid, a Biomarker of Bacterial Spores. *Anal. Chem.* **2018**, *90*, 4221–4225. [[CrossRef](#)]
21. Zhang, X.Y.; Young, M.A.; Lyandres, O.; Duyne, R.P.V. Rapid Detection of an Anthrax Biomarker by Surface-Enhanced Raman Spectroscopy. *J. Am. Chem. Soc.* **2005**, *127*, 4484–4489. [[CrossRef](#)]
22. Ai, K.; Zhang, B.H.; Lu, L.H. Europium-based fluorescence nanoparticle sensor for rapid and ultrasensitive detection of an anthrax biomarker. *Angew. Chem. Int. Ed.* **2009**, *48*, 304–308. [[CrossRef](#)]
23. Lee, M.H.; Kim, J.S.; Sessler, J.L. Small molecule-based ratiometric fluorescence probes for cations, anions, and biomolecules. *Chem. Soc. Rev.* **2015**, *44*, 4185–4191. [[CrossRef](#)]
24. Li, Y.Y.; Du, Q.Q.; Zhang, X.D.; Huang, Y.M. Ratiometric detection of tetracycline based on gold nanocluster enhanced Eu³⁺ fluorescence. *Talanta* **2020**, *206*, 120202. [[CrossRef](#)]
25. Yan, X.; Li, H.X.; Zheng, W.S.; Su, X.G. Visual and Fluorescent Detection of Tyrosinase Activity by Using a Dual-Emission Ratiometric Fluorescence Probe. *Anal. Chem.* **2015**, *87*, 904–8909. [[CrossRef](#)]
26. Wen, J.L.; Li, N.; Li, D.; Zhang, M.M.; Lin, Y.W.; Liu, Z.; Lin, X.; Shui, L. Cesium-Doped Graphene Quantum Dots as Ratiometric Fluorescence Sensors for Blood Glucose Detection. *ACS Appl. Nano Mater.* **2021**, *4*, 8437–8446. [[CrossRef](#)]
27. Zhan, Y.J.; Yang, S.T.; Chen, L.F.; Zeng, Y.B.; Li, L.; Lin, Z.Y.; Guo, L.H.; Xu, W. Ultrahigh Efficient FRET Ratiometric Fluorescence Biosensor for Visual Detection of Alkaline Phosphatase Activity and Its Inhibitor. *ACS Sustain. Chem. Eng.* **2021**, *9*, 12922–12929. [[CrossRef](#)]
28. Hao, T.; Wei, X.; Nie, Y.; Xu, Y.; Yan, Y.; Zhou, J. An eco-friendly molecularly imprinted fluorescence composite material based on carbon dots for fluorescent detection of 4-nitrophenol. *Microchim. Acta* **2016**, *183*, 2197–2203. [[CrossRef](#)]
29. Wang, T.L.; Mei, Q.S.; Tao, Z.H.; Wu, H.T.; Zhao, M.Y.; Wang, S.; Liu, Y.Q. A smartphone-integrated ratiometric fluorescence sensing platform for visual and quantitative point-of-care testing of tetracycline. *Biosens. Bioelectron.* **2020**, *148*, 111791. [[CrossRef](#)]
30. Li, X.Q.; Luo, J.J.; Deng, L.; Ma, F.H.; Yang, M.H. In situ incorporation of fluorophores in zeolitic imidazolate framework-8 (ZIF-8) for ratio-dependent detecting a biomarker of anthrax spores. *Anal. Chem.* **2020**, *92*, 7114–7122. [[CrossRef](#)]
31. Zhao, J.H.; Wang, S.; Lu, S.S.; Sun, J.; Yang, X.R. A luminescent europium-dipicolinic acid nanohybrid for the rapid and selective sensing of pyrophosphate and alkaline phosphatase activity. *Nanoscale* **2018**, *10*, 7163–7170. [[CrossRef](#)]
32. Wang, T.L.; Ji, X.Y.; Tao, Z.H.; Zhou, X.; Hao, Z.; Wang, X.K.; Gao, X.; Wang, S.; Liu, Y.Q. Dual stimuli-responsive lanthanide-based phosphors for an advanced full-color anti-counterfeiting system. *RSC Adv.* **2020**, *10*, 15573–15578. [[CrossRef](#)]
33. Liu, X.W.; Li, X.; Xu, S.L.; Guo, S.J.; Xue, Q.W.; Wang, H.S. Efficient ratiometric fluorescence probe based on dual-emission luminescent lanthanide coordination polymer for amyloid β -peptide detection. *Sens. Actuators B Chem.* **2021**, *352*, 131052. [[CrossRef](#)]
34. Hussain, S.; Chen, X.; Wang, C.F.; Hao, Y.; Tian, X.M.; He, Y.L.; Li, J.; Shahid, M.; Iyer, P.K.; Gao, R.X. Aggregation and Binding-Directed FRET Modulation of Conjugated Polymer Materials for Selective and Point-of-Care Monitoring of Serum Albumins. *Anal. Chem.* **2022**, *94*, 10685–10694. [[CrossRef](#)]
35. Hussain, S.; Malika, A.H.; Iyer, P.K. FRET-assisted selective detection of flavins via cationic conjugated polyelectrolyte under physiological conditions. *J. Mater. Chem. B* **2016**, *4*, 4439–4446. [[CrossRef](#)]
36. Malik, A.K.; Hussain, S.; Iyer, P.K. Aggregation-Induced FRET via Polymer-Surfactant Complexation: A New Strategy for the Detection of Spermine. *Anal. Chem.* **2016**, *88*, 7358–7364. [[CrossRef](#)]
37. Mondal, S.; Zehra, N.; Choudhury, A.; Iyer, P.K. Wearable Sensing Devices for Point of Care Diagnostics. *ACS Appl. Bio Mater.* **2021**, *4*, 47–70. [[CrossRef](#)]



Non-Destructive Screening of Sodium Metabisulfite Residue on Shrimp by SERS with Copy Paper Loaded with AgNP

Chao Yuan ^{1,†}, Yanan Zhao ^{2,†}, Xingjun Xi ^{3,*} and Yisheng Chen ^{2,*}

¹ State Key Laboratory of Biobased Material and Green Papermaking, Qilu University of Technology, Shandong Academy of Sciences, Jinan 250353, China

² College of Food Science and Engineering, Shanxi Agricultural University, Jinzhong 030801, China

³ Sub-Institute of Agricultural Food Standardization, China National Institute of Standardization, Beijing 100191, China

* Correspondence: xixj@cnis.ac.cn (X.X.); cheniyisheng@sxa.edu.cn (Y.C.)

† These authors contributed equally to this work.

Abstract: In order to prompt the appearance of the shrimp color, sodium metabisulfite is frequently added in shrimp processing, which is, however, prohibited in China and many other countries. This study aimed to establish a surface-enhanced Raman spectroscopy (SERS) method for screening sodium metabisulfite residues on shrimp surfaces, in a non-destructive manner. The analysis was carried out using a portable Raman spectrometer jointly with copy paper loaded with silver nanoparticles as the substrate material. The SERS response of sodium metabisulfite gives two fingerprint peaks at 620 (strong) and 927 (medium) cm^{-1} , respectively. This enabled unambiguous confirmation of the targeted chemical. The sensitivity of the SERS detection method was determined to be 0.1 mg/mL, which was equal to residual sodium metabisulfite on the shrimp surface at 0.31 mg/kg. The quantitative relationship between the 620 cm^{-1} peak intensities and the concentrations of sodium metabisulfite was established. The linear fitting equation was $y = 2375x + 8714$ with $R^2 = 0.985$. Reaching an ideal balance in simplicity, sensitivity, and selectivity, this study demonstrates that the proposed method is ideally suitable for in-site and non-destructive screening of sodium metabisulfite residues in seafood.

Keywords: sodium metabisulfite; surface-enhanced Raman spectroscopy; copy paper; AgNPs; shrimp

Citation: Yuan, C.; Zhao, Y.; Xi, X.; Chen, Y. Non-Destructive Screening of Sodium Metabisulfite Residue on Shrimp by SERS with Copy Paper Loaded with AgNP. *Biosensors* **2023**, *13*, 575. <https://doi.org/10.3390/bios13060575>

Received: 4 May 2023

Revised: 21 May 2023

Accepted: 23 May 2023

Published: 25 May 2023



Copyright: © 2023 by the authors. Licensee MDPI, Basel, Switzerland. This article is an open access article distributed under the terms and conditions of the Creative Commons Attribution (CC BY) license (<https://creativecommons.org/licenses/by/4.0/>).

1. Introduction

Sodium metabisulfite (sodium bisulfite), commonly known as “shrimp powder”, is often used as the blanching and preservative agent for shrimp processing. At the surface of shrimp, sodium metabisulfite generates reductive sulfite, resulting in significant color protection effects. More specifically, sulfite can effectively control the browning of shrimp color by inhibiting oxidase activity. Moreover, it can suppress the growth of microorganisms as well [1]. For these reasons, sodium metabisulfite is frequently added to shrimp in order to prompt the product’s appearance. However, this inevitably causes the problem of excessive residue. Remarkably, the toxicity of sodium metabisulfite to human beings had been experimentally evidenced, leading to strict restriction of it in seafood. From the existing report, it has been well known that high dosage exposure to metabisulfite can cause serious damage to a large array of organs, including the lung [2,3], cardiovascular, and nervous systems [4,5]. Therefore, sodium metabisulfite residue in shrimp poses a serious threat to human health. With this regard, the usage of sodium metabisulfite in shrimp is still prohibited in China and many other countries in the world.

As for residual analysis in food, HPLC had been the “gold method” in most controlling laboratories [6–8]. Nevertheless, all these methods based on column chromatography were not able to provide a timely and non-destructive solution for the screening of sodium metabisulfite residue on shrimp. On the contrary, surface-enhanced Raman spectroscopy

(SERS) is a simple and fast spectral analysis technology. Compared to other spectroscopic detection, SERS shows outstanding advantages in the following two aspects: (1) High sensitivity. The SERS effect enhances Raman scattering by molecules adsorbed on rough metal surfaces or by nanostructures such as noble metal (Ag or Au) nanoparticles, which is understood to be conditioned by the localization of detected molecules into abnormally strong nano-scale localized optical fields. Particularly, the enhancement factor can be as much as 10^{10} to 10^{15} if special geometric structures, the so-called “hot-spot” of nanoparticles, are formed. As reported by Nie, the optical responses of a single molecule and nanoparticles were recorded by SERS, showing intrinsic Raman enhancement factors on the order of 10^{14} to 10^{15} [9]. (2) Rich structural information. The featuring advantage of SERS is the sharp, fingerprint-like spectra pattern specific for the respective analyte. SERS spectra can give vibrational spectroscopic fingerprints from chemical and biological materials and therefore provide a comprehensive characterization tool to gain an understanding of the molecular structure [10,11]. Therefore, SERS offers high sensitivity and specificity in molecular identification and is a promising tool for the detection of adverse residues in food [12–19].

Though the unusual phenomenon of SERS was observed in 1977, there is still lots of controversy about its mechanism. Generally, two major theoretical explanations for the SERS mechanism have been proposed. The first is a chemical enhancement, which primarily involves the charge transfer mechanism. The other one is an electromagnetic enhancement that results from the amplification of the light intensity by the excitation of localized surface plasmon resonances. In both theories, the strength of SERS is critically dependent on the quality of the substrate material. A large array of SERS substrate materials had been proposed to increase the detectability of SERS as much as possible. Recently, emerging flexible SERS substrates as an alternative to colloidal and rigid SERS substrates have attracted remarkable attention [20–22]. More specifically, flexible SERS substrates highlight the advantage of easy sampling by wrapping or swabbing on irregular surfaces, which ideally facilitates the detection of chemical residues on food surfaces. In this way, analysis steps can be performed in a highly efficient way, and the interferences caused by co-extracted sample matrices can be perfectly circumvented. This opens a new horizon on the non-destructive and sensitive analysis of adverse residues on the surface of the food.

Compared to other flexible materials such as textiles, copy paper is the most commonly available flexible material ideally able to host nanoparticles of silver and gold, which is especially suitable for in-situ screening. Additionally, the copy paper itself does not generate any strong SERS signal, implying that background interference from the substrate material can be excluded. There have been many reports that evidenced that paper was able to facilitate on-site SERS detection of substance molecules in the field [23,24]. Loaded with Ag nanoparticle (AgNP), copy paper can be cut into any size and shape, bent, and folded [25]. Copy paper can also be covered on an irregular sample surface without destroying raw materials, which may reduce the number of “hot spots” during in situ detection [26]. Therefore, compared with other rigid substrate materials, copy paper-based flexible substrates displayed stronger detection ability and wider application on complex and irregular surfaces, allowing effective detection at low concentrations [27]. In this study, copy paper loaded with AgNP (AgNP–CP-) was fabricated in order to realize fast and simple screening of sodium metabisulfite on the surface of shrimp, which was illustrated in Figure 1.

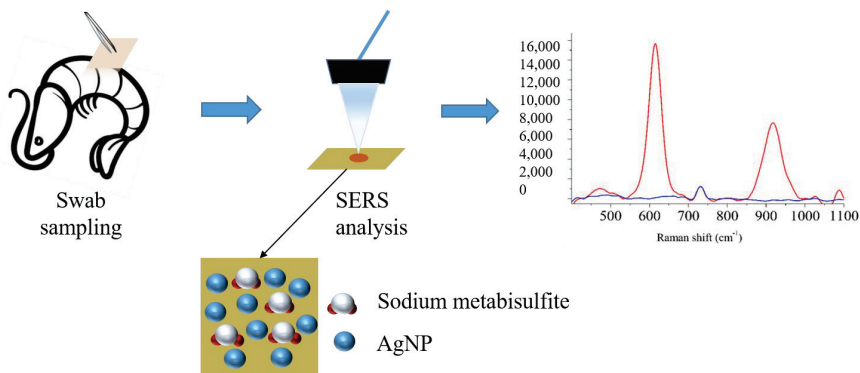


Figure 1. Schematic illustration of SERS detection of sodium metabisulfite residue on shrimp surface.

2. Materials and Methods

2.1. Chemicals and Equipment

Silver nitrate (AgNO_3 , purity $\geq 99.8\%$), sodium citrate ($\text{C}_6\text{H}_5\text{Na}_3\text{O}_7 \cdot 2\text{H}_2\text{O}$, purity $\geq 99\%$), and sodium metabisulfite were purchased from Sinopharm Chemical Reagent Co., LTD (Beijing, China). A4 copy paper was purchased from Deli Ltd. (Shanghai, China). The magnetic heating stirrer-MS-H-ProA was from Dragon Laboratory Instruments Ltd. (Shanghai, China). The portable Raman spectra analyzer-ATR3110 workstation was from Optosky Photonics Ltd. (Xiamen, China). Ultra-pure water (conductivity: $1.08 \mu\text{S}/\text{cm}$) was prepared by a Millipore Synergy system (Schwalbach, Germany). UV-vis spectrophotometer was from Jinghua Ltd. (Shanghai, China). Shrimp samples were purchased from a local supermarket.

2.2. Synthesis of AgNPs

The synthesis of AgNPs was principally based on the method proposed by Lee and Meisel [28] and characterized by UV-vis spectrophotometer and Scanning Electronic Microscopy. Briefly, 45.0 mg of AgNO_3 was dissolved in 250 mL of ultra-pure water. The mixture was evenly stirred and then boiled. Afterward, 5 mL of 1% trisodium citrate solution was added drop by drop to the boiling mixture; meanwhile, the mixture was magnetically stirred during the whole process to ensure uniform heating. After boiling for 1 h, heating was stopped, and the solution was cooled down to room temperature with continuous stirring. A grey-green colloidal solution of AgNPs was obtained, which was refrigerated at 4°C , sealed, and stored in the dark.

2.3. Fabrication of AgNP-CP

The blank copy paper was cut into $1 \text{ cm} \times 1 \text{ cm}$ pieces, which were soaked in the as-prepared AgNPs colloid. After the AgNPs were evenly adsorbed on the paper substrates, they were taken out and put into a closed space to dry naturally and set aside for later use.

2.4. Preparation of Standard Solutions

Preparation of sodium metabisulfite standard solution: 0.05 g of sodium metabisulfite solid powder was dissolved in 5 mL of ultra-pure water to prepare a 10 mg/mL sodium metabisulfite standard solution. The standard solution was serially diluted to prepare 5, 3, 1, 0.2, and 0.1 mg/mL solutions, which were sufficiently shaken before use.

2.5. Preparation of Shrimp Samples

The SERS detection process of sodium metabisulfite in shrimp is shown in Figure 1. The different diluted solutions of sodium metabisulfite (prepared 5, 3, 1, 0.2, and 0.1 mg/mL) were sprayed on the shrimp surface and allowed to dry.

2.6. SERS Sampling and Measurement

As for SERS analysis of the standard solution of sodium metabisulfite, 10 μL of the solution was applied within an area of 1 cm^2 square on clean glass. The liquid was allowed to dry at room temperature. Then, the AgNP-CP was wiped on the square area in order to sample the analyte onto the SERS substrate material. As for the analysis of the real shrimp sample, the AgNP-CP was wiped on the shrimp's surface. After that, the quantitative measurement was performed with a portable Raman spectrometer, with an excitation wavelength of 785 nm and laser power at 80 mW. The acquisition time was 500 ms with one accumulation. The integration time is 8000 ms, the signal-to-noise ratio threshold is 3, and the intensity threshold is 1000. Spectral data recorded by the Raman spectrometer were processed using Origin 8.5 software. Each sample was measured three times to obtain the average value.

3. Results and Discussion

3.1. Fabrication and Characterization of AgNP-CP

In this study, the colloid of AgNPs was first prepared. The significant surface plasma effect of AgNPs can be characterized by their light absorption spectrum. As shown in Figure 2a, the light absorption spectrum of the raw AgNPs colloid after 20-fold diluting was continuous and displayed the maximum absorption peak at 440 nm, indicating that the AgNPs prepared in this work had the effectiveness and could be applied to the study of nanomaterials.

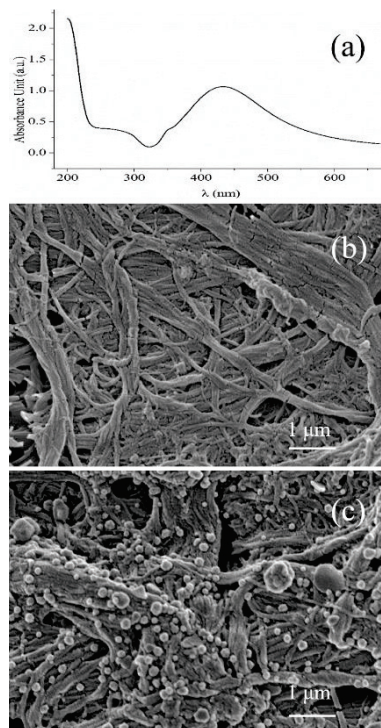


Figure 2. Ultraviolet absorption spectra of the AgNPs colloid (a); Microscopic structure of the blank copy paper (b) and copy paper loaded with AgNP by dipping (c).

Then the flexible SERS substrate was obtained by simply dipping the copy paper into the colloid of AgNPs. After that, the color of the copy paper became gray, evidencing that the dispersed AgNPs were absorbed in the fiber structure of cellulose. The color change was

resistant to rinsing, suggesting that absorption was strong enough. The electron microscope photographs enabled further insight into the morphology of the substrate. As shown in Figure 2b,c, lots of AgNPs uniformly anchored on the cellulose fiber structure can be observed after dipping, compared to that of the blank copy paper. This further evidenced the success of SERS substrate fabrication.

3.2. Usability Evaluation of the SERS Substrate

In order to access the usability of the as-prepared substrate, SERS measurement to the standard solution of sodium metabisulfite was carried out. As shown in Figure 3, the blue line represents the blank substrate response, and the red line represents the SERS signal of the sodium metabisulfite standard solution (10 mg/mL). It was apparent that the blank copy paper was inactive to SERS since the spectrum is a flat line. On the other hand, the copy paper became highly SERS active after being loaded with AgNPs. The SERS signal of the sodium metabisulfite aqueous solution displayed two characteristic peaks at 927 and 620 cm^{-1} , agreeing well with its Raman scatter pattern, comparatively shown in Figure 3a,b. The assignment of these characteristic peaks is listed in Table 1. Due to the electromagnetic coupling between S and Ag, S-O stretching vibration (symmetry + symmetry), and O-S-O symmetry, SO_2 binding to the surface of AgNPs generated two strong and comparable characteristic peaks at 927 and 620 cm^{-1} . Since the strength of the S-O tensile band can be variable, the characteristic peaks will deviate accordingly [29,30]. These results evidenced that SERS detection can provide an ambiguous tool for the identification and confirmation of metabisulfite ions on shrimp, even in the absence of the reference standard.

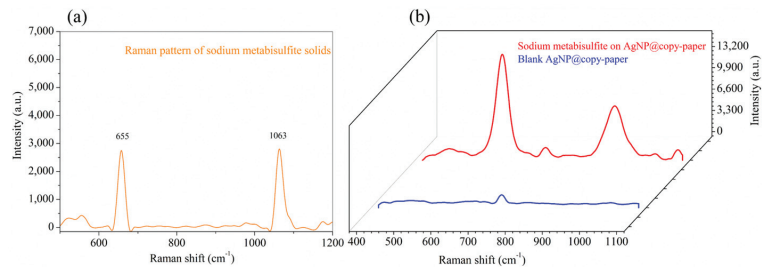


Figure 3. The Raman scattering spectrum of sodium metabisulfite (a); SERS spectra of the AgNP-CP with or without sodium metabisulfite standard solution (b).

Table 1. Distribution of the two characteristic peaks of sodium metabisulfite.

Fingerprint Peak (cm^{-1})	Intensity	Signal Assignment
620	Strong	Symmetrical bending vibrations of O-S-O
927	Medium	Symmetrical and asymmetric S-O stretching vibrations

3.3. Analysis Sensitivity

In routine screening tasks, the primary concern is whether the shrimp were treated with sodium metabisulfite or not. Therefore, the sensitivity of detection is of crucial importance. In order to evaluate the detectability of the developed method, a glass plate was used as the blank control first. More specifically, sodium metabisulfite solutions of different concentrations were added dropwise to the glass plate and air-dried. Then, the spot on the glass plates was wiped with AgNP-CP for SERS measurement. As shown in Figure 4a, the characteristic SERS peaks at 620 and 927 cm^{-1} were clearly distinguished even at a low concentration of 0.1 mg/mL sodium metabisulfite. In addition, parallel analyses of different concentrations of sodium metabisulfite were performed to verify the reliability of the AgNP-CP detection system over a range of 0.1–10 mg/mL (Figure 4b).

The results showed minor deviations in sensitivity with no obvious influence of the test solution concentration, evidencing good sensitivity and reliability of the analysis method. Moreover, the analysis sensitivity could be further enhanced by using other plasmonic Ag material with higher SERS activity [31–33].

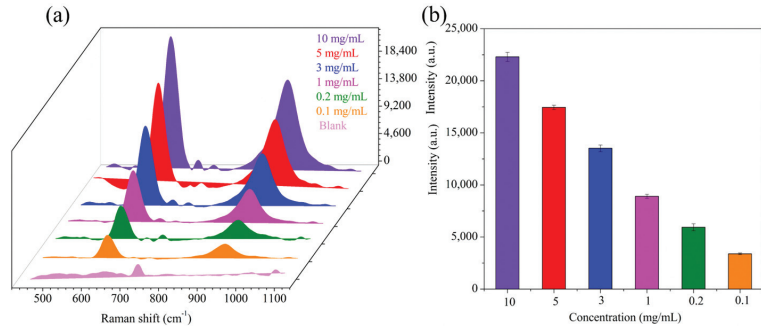


Figure 4. SERS spectra of AgNP-CP wipes of air-dried sodium metabisulfite solutions on glass plates (a); Error analysis of parallel detection for different concentrations of sodium metabisulfite standard solutions (0.1–10 mg/mL) (fingerprint peaks at 620 cm^{-1}) (b).

3.4. Precision Evaluation of the Analysis

The uniformity analysis of the detection was investigated using 1 mg/mL sodium metabisulfite solution as a probe and using the wiping method. A volume of $10\text{ }\mu\text{L}$ of the 1 mg/mL sodium metabisulfite solution was dropped on the glass plate and wiped after drying. Then, 20 points were randomly selected on a single AgNP-CPAgNP-CP piece to collect the SERS spectra. As shown in Figure 5a, the intensity of fingerprint peaks at 620 and 927 cm^{-1} did not fluctuate significantly, and the SERS signal display rate reached 100% in 20 measurements, indicating the uniform distribution of the test substance on the AgNP-CP detection system. Figure 5b shows that there was almost no significant change in the intensity of the 620 cm^{-1} peak, and the relative standard deviation (RSD) was only 1.2%, indicating the good performance of the SERS detection system. Moreover, the data in Figure 5c shows that the intensity of the SERS response peak 620 cm^{-1} from 20 randomly selected points did not change significantly. These results showed that the AgNP-CP detection system is simple, reliable, and has good uniformity.

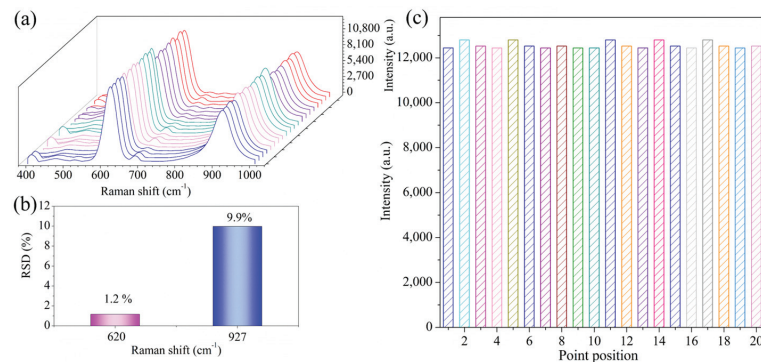


Figure 5. SERS spectrogram from 20 randomly selected points on a single piece of AgNP-CP (a), RSDs peak intensity at 20 random points, and (c) bar chart showing peak intensity data from the 20 random points (b).

3.5. Stability Evaluation of the Analysis

The stability test of the AgNP-CP was performed using the glass slide wiping test. AgNP-CP substrates of the same preparation batch were used for analysis. The soaked paper substrates were dried, placed in closed glassware, and then stored at 18 °C and 30% humidity in the dark. The interval of measurement was 24 h, and the test stability was checked for 5 days. For the wiping analysis method, we used 10 μL of 1 mg/mL sodium metabisulfite standard solution. The analysis of stability over five days is shown in Figure 6. The stability gradually decreased over time. On the fifth day, though the peak intensity (620 cm^{-1}) reduced to about half of that on the first day, the characteristic peaks at 620 and 927 cm^{-1} were still clear and easy to distinguish. Such a descending trend might be attributed to the oxidation of silver over storage, suggesting that the SERS substrate was better to be used shortly after fabrication.

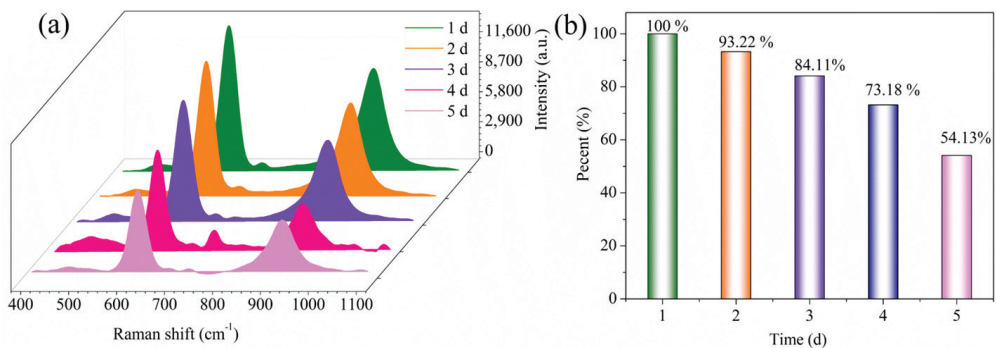


Figure 6. SERS spectrogram of 5-day stability test of AgNP-CP for sodium metabisulfite (a) and comparison of peak intensity at 620 cm^{-1} (b).

3.6. Analysis of Real Samples

Figure 7a shows the SERS spectra of shrimp surfaces sprayed with sodium metabisulfite standard solutions of different concentrations. After allowing the sodium metabisulfite solution to dry naturally, the shrimp surface was sprayed with prepared ethanol aqueous solution, and the surface wiping test was performed with AgNP-CP, and SERS signals were recorded (Figure 7b). The intensity of the two characteristic peaks at 620 and 927 cm^{-1} became gradually weaker as the sodium metabisulfite concentration decreased. Due to the specific influence of the shrimp on the substrate, the detection of sodium metabisulfite solution only reached 0.2 mg/mL. Then, we used the SERS peaks for quantitative analysis and established a standard curve between the concentrations of the test samples and the intensity of the peak at 620 cm^{-1} . The results are shown in Figure 7c. The standard curve was fitted to the $375x + 8714$ ($R^2 = 0.985$) equation. The LOD of the detection of sodium metabisulfite on the shrimp surface was 0.31 mg/kg. Compared with other SERS detection of sodium metabisulfite in recent years, our detection method is remarkably convenient, especially suitable for screening tasks (Table 2). A comparison of the data showed that the AgNP-CP has good sensitivity, and the test had a linear correlation of the standard curve for accurate and quantitative analysis. This suggested that the AgNP-CP assay can be used for the quantification of the residue of sodium metabisulfite on shrimp.

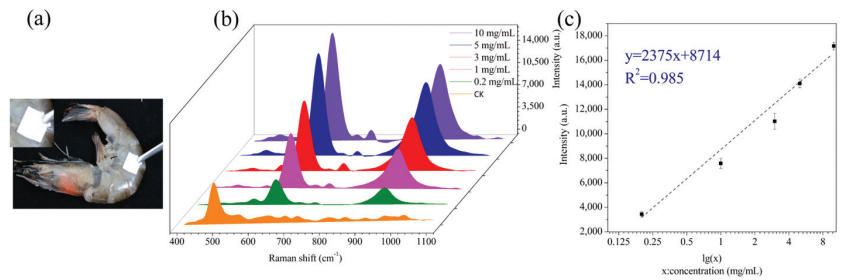


Figure 7. AgNP-CP wiping test on the shrimp surface (a), SERS sensitivity of the AgNP-CP wiping test, and (c) linear relationship between the intensity of 620 cm^{-1} peak and sodium metabisulfite concentration (b).

Table 2. Comparison of detection methods for sodium metabisulfite.

Method	Analyte	Sample Matrix	LOD	Reference
Near-infrared	Sodium metabisulfite	Fresh-cut potatoes	500 g/kg	[34]
Colorimetry	Sulfite	Foods	27.6 nM	[35]
RP-HPLC	Sodium metabisulfite	Drugs	95 mg/L	[36]
SERS	Sodium metabisulfite	Shrimp	0.31 mg/kg	This study

4. Conclusions

In this study, we developed a SERS method using a flexible AgNP-CP substrate material for the rapid determination of sodium metabisulfite on shrimp surface that can be conducted with a portable Raman spectrometer. AgNP-CP exhibited good adsorption uniformity, maintaining the reproducibility of the SERS results. The SERS detection sensitivity of AgNP-CP for sodium metabisulfite solution on the shrimp surface was 0.2 mg/mL , and the LOD value was 0.31 mg/kg . We also established a quantitative relationship between the intensity of the characteristic peak at 620 cm^{-1} and the sodium metabisulfite concentration. The linear fitting equation was $2375x + 8714$ ($R^2 = 0.985$), evidencing that this method could be used for quantitative screening. Generally, the proposed method demanded simple sample pre-treatment, short analysis time, and portable equipment, showing high simplicity and cost-effectiveness. Therefore, it might be suitable for on-site and non-destructive screening of the sodium metabisulfite residue on shrimp. However, the stability of the SERS activity of the substrate material over storage still needed to be further optimized.

Author Contributions: Conceptualization, Y.C.; methodology, C.Y. and Y.C.; resources, Y.Z.; data curation, Y.Z.; writing—original draft preparation, Y.Z.; writing—review and editing, C.Y.; supervision, C.Y. and X.X.; project administration, C.Y. and X.X.; funding acquisition, C.Y., Y.C. and X.X. All authors have read and agreed to the published version of the manuscript.

Funding: This work was financially supported by the Foundation (GZKF202125) of State Key Laboratory of Biobased Material and Green Papermaking, Qilu University of Technology, Shandong Academy of Sciences.

Institutional Review Board Statement: Not applicable.

Informed Consent Statement: Not applicable.

Data Availability Statement: The data will be available on request.

Conflicts of Interest: The author has no conflict of interest.

References

- Robbins, K.S.; Shah, R.; MacMahon, S.; de Jager, L.S. Development of a Liquid Chromatography–Tandem Mass Spectrometry Method for the Determination of Sulfite in Food. *J. Agric. Food Chem.* **2015**, *63*, 5126–5132. [[CrossRef](#)] [[PubMed](#)]
- Wang, X.; Cao, H.; Guan, X.L.; Long, L.H.; Hu, Z.L.; Ni, L.; Wang, F.; Chen, J.G.; Wu, P.F. Sulfite triggers sustained calcium overload in cultured cortical neurons via a redox-dependent mechanism. *Toxicol. Lett.* **2016**, *258*, 237–248. [[CrossRef](#)] [[PubMed](#)]
- Han, X.; Zhu, F.; Chen, L.; Wu, H.; Wang, T.; Chen, K. Mechanism analysis of toxicity of sodium sulfite to human hepatocytes L02. *Mol. Cell. Biochem.* **2020**, *473*, 25–37. [[CrossRef](#)] [[PubMed](#)]
- Yao, G.Y.; Yun, Y.; Sang, N. Differential Effects Between One Week and Four Weeks Exposure to Same Mass of SO₂ on Synaptic Plasticity in Rat Hippocampus. *Environ. Toxicol.* **2016**, *31*, 820–829. [[CrossRef](#)] [[PubMed](#)]
- Yao, G.; Yue, H.; Yun, Y.; Sang, N. Chronic SO₂ inhalation above environmental standard impairs neuronal behavior and represses glutamate receptor gene expression and memory-related kinase activation via neuroinflammation in rats. *Environ. Res.* **2015**, *137*, 85–93. [[CrossRef](#)] [[PubMed](#)]
- Pizzoferrato, L.; Quattrucci, E.; Di Lullo, G. Evaluation of an HPLC method for the determination of sulphiting agents in foods. *Food Addit. Contam.* **1990**, *7*, 189–195. [[CrossRef](#)] [[PubMed](#)]
- Theisen, S.; Hansch, R.; Kothe, L.; Leist, U.; Galensa, R. A fast and sensitive HPLC method for sulfite analysis in food based on a plant sulfite oxidase biosensor. *Biosens. Bioelectron.* **2010**, *26*, 175–181. [[CrossRef](#)] [[PubMed](#)]
- Chung, S.W.C.; Chan, B.T.-P.; Chan, A. Determination of free and reversibly-bound sulfite in selected foods by high-performance liquid chromatography with fluorometric detection. *J. AOAC Int.* **2008**, *91*, 98–102.
- Nie, S.; Emory, S.R. Probing Single Molecules and Single Nanoparticles by Surface-Enhanced Raman Scattering. *Science* **1997**, *275*, 1102–1106. [[CrossRef](#)]
- Chen, Y.; Huang, C.; Jin, Z.; Xu, X.; Cai, Y.; Bai, Y. HPTLC-bioautography/SERS screening nifedipine adulteration in food supplement based on Ginkgo biloba. *Microchem. J.* **2020**, *154*, 104647. [[CrossRef](#)]
- Chen, Y.; Huang, C.; Hellmann, B.; Xu, X. HPTLC-Densitometry Determination of Riboflavin Fortified in Rice Noodle: Confirmed by SERS-Fingerprint. *Food Anal. Methods* **2020**, *13*, 718–725. [[CrossRef](#)]
- Pan, C.; Chen, H.J.; Lin, Q.; Luo, S.H.; Gu, J.L.; Ye, S.Q.; Zeng, Y.M.; Ren, B.; Tian, Z.Q.; Xue, W.D.; et al. Evaluation of the SERS-based strategy in fast and on-site food safety inspection: Qualitative and quantitative analysis of trace unexpected herbicide in complicated herbicide matrix. *J. Raman Spectrosc.* **2020**, *51*, 2562–2567. [[CrossRef](#)]
- Xu, M.L.; Gao, Y.; Han, X.X.; Zhao, B. Detection of Pesticide Residues in Food Using Surface-Enhanced Raman Spectroscopy: A Review. *J. Agric. Food Chem.* **2017**, *65*, 6719–6726. [[CrossRef](#)]
- Xin, H.; Namgung, B.; Lee, L.P. Nanoplasmonic optical antennas for life sciences and medicine. *Nat. Rev. Mater.* **2018**, *3*, 228–243. [[CrossRef](#)]
- Ma, H.; Liu, S.; Liu, Y.; Zhu, J.; Han, X.X.; Ozaki, Y.; Zhao, B. In-situ fingerprinting phosphorylated proteins via surface-enhanced Raman spectroscopy: Single-site discrimination of Tau biomarkers in Alzheimer’s disease. *Biosens. Bioelectron.* **2021**, *171*, 112748. [[CrossRef](#)] [[PubMed](#)]
- Zhang, Y.; Yang, Z.; Zou, Y.; Farooq, S.; Li, Y.; Zhang, H. Novel Ag-coated nanofibers prepared by electrospinning as a SERS platform for ultrasensitive and selective detection of nitrite in food. *Food Chem.* **2023**, *412*, 135563. [[CrossRef](#)]
- Bhaskar, S.; Srinivasan, V.; Ramamurthy, S.S. Nd₂O₃-Ag Nanostructures for Plasmonic Biosensing, Antimicrobial, and Anticancer Applications. *ACS Appl. Nano Mater.* **2023**, *6*, 1129–1145. [[CrossRef](#)]
- Xiong, Y.; Shepherd, S.; Tibbs, J.; Bacon, A.; Liu, W.; Akin, L.D.; Ayupova, T.; Bhaskar, S.; Cunningham, B.T. Photonic Crystal Enhanced Fluorescence: A Review on Design Strategies and Applications. *Micromachines* **2023**, *14*, 668. [[CrossRef](#)]
- Beeram, R.; Vepa, K.R.; Soma, V.R. Recent Trends in SERS-Based Plasmonic Sensors for Disease Diagnostics, Biomolecules Detection, and Machine Learning Techniques. *Biosensors* **2023**, *13*, 328. [[CrossRef](#)]
- Zhang, D.; Pu, H.; Huang, L.; Sun, D.-W. Advances in flexible surface-enhanced Raman scattering (SERS) substrates for nondestructive food detection: Fundamentals and recent applications. *Trends Food Sci. Technol.* **2021**, *109*, 690–701. [[CrossRef](#)]
- Wang, Z.; Zhang, L.; Chen, Y. HPTLC+SRES screening of pesticide for point-of-care application as shown with thiram in juice. *Food Chem. X* **2023**, *18*, 100670. [[CrossRef](#)] [[PubMed](#)]
- Wang, S.; Hao, Q.; Zhao, Y.; Chen, Y. Two-Dimensional Printed AgNPs@Paper Swab for SERS Screening of Pesticide Residues on Apples and Pears. *J. Agric. Food Chem.* **2023**, *71*, 4982–4989. [[CrossRef](#)] [[PubMed](#)]
- Pilot, R. SERS detection of food contaminants by means of portable Raman instruments. *J. Raman Spectrosc.* **2018**, *49*, 954–981. [[CrossRef](#)]
- Restaino, S.M.; White, I.M. A critical review of flexible and porous SERS sensors for analytical chemistry at the point-of-sample. *Anal. Chim. Acta* **2019**, *1060*, 17–29. [[CrossRef](#)]
- Xie, J.; Li, L.; Khan, I.M.; Wang, Z.; Ma, X. Flexible paper-based SERS substrate strategy for rapid detection of methyl parathion on the surface of fruit. *Spectrochim. Acta Part A Mol. Biomol. Spectrosc.* **2020**, *231*, 118104. [[CrossRef](#)]
- Villa, J.E.L.; Quiñones, N.R.; Fantinatti-Garborggini, F.; Poppi, R.J. Fast discrimination of bacteria using a filter paper-based SERS platform and PLS-DA with uncertainty estimation. *Anal. Bioanal. Chem.* **2019**, *411*, 705–713. [[CrossRef](#)]
- Maddipatla, D.; Narakathu, B.B.; Atashbar, M. Recent Progress in Manufacturing Techniques of Printed and Flexible Sensors: A Review. *Biosensors* **2020**, *10*, 199. [[CrossRef](#)]

28. Lee, P.C.; Meisel, D. Adsorption and surface-enhanced Raman of dyes on silver and gold sols. *J. Phys. Chem.* **1982**, *86*, 3391–3395. [[CrossRef](#)]
29. Chen, M.; Yang, H.; Rong, L.; Chen, X. A gas-diffusion microfluidic paper-based analytical device (μ PAD) coupled with portable surface-enhanced Raman scattering (SERS): Facile determination of sulphite in wines. *Analyst* **2016**, *141*, 5511–5519. [[CrossRef](#)]
30. Deng, Z.; Chen, X.X.; Wang, Y.R.; Fang, E.H.; Zhang, Z.G.; Chen, X. Headspace Thin-Film Microextraction Coupled with Surface-Enhanced Raman Scattering as a Facile Method for Reproducible and Specific Detection of Sulfur Dioxide in Wine. *Anal. Chem.* **2015**, *87*, 633–640. [[CrossRef](#)]
31. Wang, Z.J.; Li, Q.; Tan, L.L.; Liu, C.G.; Shang, L. Metal-Organic Frameworks-Mediated Assembly of Gold Nanoclusters for Sensing Applications. *J. Anal. Test.* **2022**, *6*, 163–177. [[CrossRef](#)] [[PubMed](#)]
32. Verma, A.K.; Soni, R.K. Silver nanodendrites for ultralow detection of thiram based on surface-enhanced Raman spectroscopy. *Nanotechnology* **2019**, *30*, 385502. [[CrossRef](#)] [[PubMed](#)]
33. Cheng, D.; He, M.; Ran, J.; Cai, G.; Wu, J.; Wang, X. Depositing a flexible substrate of triangular silver nanoplates onto cotton fabrics for sensitive SERS detection. *Sens. Actuators B Chem.* **2018**, *270*, 508–517. [[CrossRef](#)]
34. Bai, X.; Xiao, Q.; Zhou, L.; Tang, Y.; He, Y. Detection of Sulfite Dioxide Residue on the Surface of Fresh-Cut Potato Slices Using Near-Infrared Hyperspectral Imaging System and Portable Near-Infrared Spectrometer. *Molecules* **2020**, *25*, 1651. [[CrossRef](#)] [[PubMed](#)]
35. Xiang, K.; Chang, S.; Feng, J.; Li, C.; Ming, W.; Liu, Z.; Liu, Y.; Tian, B.; Zhang, J. A colorimetric and ratiometric fluorescence probe for rapid detection of SO₂ derivatives bisulfite and sulfite. *Dye. Pigment.* **2016**, *134*, 190–197. [[CrossRef](#)]
36. Ivković, B.; Brborić, J.; Dobričić, V.; Čudina, O. Development and validation of a new isocratic RP-HPLC method for simultaneous determination of sodium metabisulfite and sodium benzoate in pharmaceutical formulation. *Acta Chromatogr.* **2019**, *31*, 133–137. [[CrossRef](#)]

Disclaimer/Publisher’s Note: The statements, opinions and data contained in all publications are solely those of the individual author(s) and contributor(s) and not of MDPI and/or the editor(s). MDPI and/or the editor(s) disclaim responsibility for any injury to people or property resulting from any ideas, methods, instructions or products referred to in the content.



Review

Determination Methods of the Risk Factors in Food Based on Nanozymes: A Review

Yihan Lang, Biao Zhang, Danfeng Cai, Wanjun Tu, Jingyi Zhang, Xuping Shentu *, Zihong Ye and Xiaoping Yu

Zhejiang Provincial Key Laboratory of Biometrology and Inspection & Quarantine, College of Life Sciences, China Jiliang University, Xueyuan Street, Xiasha Higher Education District, Hangzhou 310018, China

* Correspondence: stxp@cjlu.edu.cn; Tel.: +86-0571-8687-6237

Abstract: Food safety issues caused by foodborne pathogens, chemical pollutants, and heavy metals have aroused widespread concern because they are closely related to human health. Nanozyme-based biosensors have excellent characteristics such as high sensitivity, selectivity, and cost-effectiveness and have been used to detect the risk factors in foods. In this work, the common detection methods for pathogenic microorganisms, toxins, heavy metals, pesticide residues, veterinary drugs, and illegal additives are firstly reviewed. Then, the principles and applications of immunosensors based on various nanozymes are reviewed and explained. Applying nanozymes to the detection of pathogenic bacteria holds great potential for real-time evaluation and detection protocols for food risk factors.

Keywords: nanozyme; food hazards; biosensor; food safety; determination

1. Introduction

Agriculture and food production are directly related to the survival and development of mankind. Food safety remains one of the most crucial issues globally because food could be contaminated at all stages of production, packaging, storage, transportation, and value-added processing, giving rise to outbreaks of foodborne diseases [1]. The World Health Organization (WHO) pointed out that an estimated 600 million—almost 1 in 10 people in the world—fall ill after eating contaminated food and 420,000 die every year, resulting in the loss of 33 million healthy life years (DALYs). Food hazards have a variety of factors, such as plant, animal, and microbial metabolites, soil and water pollution hazards from the environment, and purposefully added illegal additives, generated during food packing and processing [2,3]. The review was organized by the category of food risk factors, including pathogenic microorganisms, toxins, heavy metals, pesticide residues, veterinary drugs, and others [4].

At present, the frequently used detection immunoassays, such as high-performance liquid chromatography (HPLC), gas chromatography (GC), mass spectrometry (MS), gas chromatography/mass spectrometry (GC-MS), liquid chromatography/mass spectrometry (LC-MS), and enzyme-linked immunosorbent assay (ELISA), have the advantages of outstanding specificity and accuracy [5]. However, they require tedious pretreatment steps, expensive instruments, specialized technical personnel, and a long testing cycle, which are inappropriate for point-of-care testing (POCT) [6]. In such contexts, with the rapid development and deepening understanding of nanotechnology, nanomaterial-based biosensors to detect food contamination and food adulteration have revolutionized the global food industry [7–9].

Nanozymes are artificial nanomaterials with intrinsic enzyme-like properties, which are distinct from “nano-enzymes” with natural enzymes or catalytic ligands immobilized on nanomaterials. On the whole, natural enzymes are readily digested by proteases and lose their enzymatic activity after exposure to extreme pH and high temperatures, which considerably impedes their practical application [10]. Nanozymes are structurally stable and capable of catalyzing reactions not only under mild physiological conditions but

Citation: Lang, Y.; Zhang, B.; Cai, D.; Tu, W.; Zhang, J.; Shentu, X.; Ye, Z.; Yu, X. Determination Methods of the Risk Factors in Food Based on Nanozymes: A Review. *Biosensors* **2023**, *13*, 69. <https://doi.org/10.3390/bios13010069>

Received: 15 November 2022

Revised: 14 December 2022

Accepted: 23 December 2022

Published: 31 December 2022



Copyright: © 2022 by the authors. Licensee MDPI, Basel, Switzerland. This article is an open access article distributed under the terms and conditions of the Creative Commons Attribution (CC BY) license (<https://creativecommons.org/licenses/by/4.0/>).

also retaining enzymatic activity in extreme environments. For instance, peroxidase substrates could be catalyzed by iron-based nanozymes at extreme pH (1–12) and temperature (−20–80 °C). The term “nano-zyme” was coined by Pasquato et al. in 2004 to employ triazacyclonane-functionalized gold nanoparticles as catalysts for transphosphorylation reactions [11]. In 2007, Yan et al. reported that Fe₃O₄ nanoparticles possessed the inherent catalytic activity of horseradish peroxidase (HRP), which could catalyze the conversion of substrates as natural peroxidase under mild physiological conditions [12].

To date, the catalytic performance of nanozymes have been extended from the initial single oxidoreductase (peroxidase) to the current four categories, including oxidoreductase, hydrolase, lyase and isomerase [13,14]. Dozens of inorganic nanomaterials have been found to hold different catalytic activities, for instance, cerium dioxide nanoparticles and ferromagnetic nanoparticles with peroxidase activity, gold nanoparticles with oxidase activity and cadmium sulfide and cadmium selenide nanoparticles with nitrate reductase activity [15,16]. The most outstanding feature of nanoparticles is their superior catalytic activity, low cost, high stability, and controllable and adjustable enzyme activity, which is unmatched by other simulated enzymes [17]. In addition, nanozymes can be size-controlled and surface-modified utilizing sophisticated nanotechnology to modulate their enzymatic activities, which is thought to be an inorganic material with unique physicochemical properties [18]. The discovery of nanozymes breaks the previous notion that inorganic nanomaterials are inert and reveals that they also hold catalytic activities similar to enzymes. Extensive experiments have confirmed that nanozymes are intended to be applied as an alternative to enzymes in the life sciences and the food industry (Table 1) [19,20]. However, the scant biometric events, inadequate water solubility, rational batch design, and catalytic mechanisms of synthetic enzymes based on nanomaterials and the lower catalytic efficiency of some nanozymes compared to natural enzymes are still the prime hindrances confining their applications [21].

At present, sustainably and environmentally conscious lifestyles are gradually being emphasized; therefore, it is particularly crucial to establish a testing system to ensure food safety. Based on the international publications, the main purpose of this paper is to highlight new research data on food hazard detection by nanozymes, summarize the general conclusions, and put forward our views on future development.

2. Pathogenic Microorganism

While physical and chemical contaminations also lead to foodborne diseases, biological contaminants, particularly microorganisms, are considered the greatest danger to food safety [22]. The majority of current conventional procedures for identifying and locating these pathogenic microorganisms are based on colony counting and cell cultures, which requires at least 3–4 days to obtain a presumptive result and about 7 days to produce a definitive identification summary [23]. *Escherichia coli*, *Salmonella enterica*, *Campylobacter jejuni*, *Staphylococcus aureus*, *Listeria monocytogenes* and *Bacillus cereus* are the main bacterium responsible for foodborne illnesses [24]. The search for disposable devices capable of in situ, rapid, and multiplex quantitative detection of pathogenic microorganisms has become a recent research trend, and several rapid determination methods are being more frequently applied, including polymerase chain reaction (PCR) [25]. Due to their speed and reliability, nanomaterials are being extensively utilized as transducing components for biosensors, potentially turning out in situ detection devices for biosecurity as well as clinical and food diagnostics (Figure 1) [26].

A brief description of the single detection mode or single-target nanozyme biosensors is given below. Hu et al. utilized the immune Ps-Pt (IPs-Pt) by growing platinum nanoparticles (Pt) on the surface of carboxyl-functionalized polymer nanospheres (Ps), establishing a quick and accurate colorimetric method for the detection of *Salmonella typhimurium*. The Pt gave the Ps-Pt an ultrahigh peroxidase-mimetic catalytic activity, and the carboxyl group allowed Ps-Pt to bind to streptavidin through covalent binding, with excellent activity and stability [27]. Taking advantage of BSA as a template, Liu et al. published a study of a

Co_3O_4 magnetic nanozyme (Co_3O_4 MNE) with peroxidase-mimetic activity which binds with a unique fusion phage protein. The Co_3O_4 MNE@fusion-pVIII particles were able to capture *Staphylococcus aureus* (*S. aureus*) and magnetically separate it from the milk [28]. For the semi-automatic detection of *Salmonella typhimurium*, an enzyme-free optical biosensor based on porous gold@Platinum nanocatalyst (Au@PtNCs) and a passive 3D micro-hybrid was created. It was able to magnetically separate 99% of the target bacteria from the sample in about 10 min. This study used immunomagnetic nanoparticles to separate target *Salmonella* cells, then immune Au@PtNCs were labeled onto the target cells and catalyzed with H_2O_2 -3,3',5,5'-tetramethylbenzidine (TMB) to signal output, and absorbance was measured at 652 nm to calculate the number of bacteria [29].

Multitarget and multimode detection is also one of the popular research directions. For the sake of developing an antibody-free LFIA with three signal readout modes for detecting *E. coli* O157:H7, Wang et al. proposed functional nanozyme/mannose-modified Prussian blue (man-PB) as a novel recognition reagent. The antigenic determinants on the surface of bacteria were more fully exposed as a result of the targeted binding of man-PB to the FimH protein in *E. coli* O157:H7 flagella, which improved the effectiveness of antibodies in recognizing the target bacteria [30]. Utilizing platinum/palladium nanoparticles as signal reporter molecules and a smartphone as a result recorder, Cheng et al. announced a quantitative dual fluorescence immunoassay for the simultaneous detection of two pathogens in milk. The peroxidase-like catalytic activity of Pd @ Pt nanoparticles was utilized for signal enhancement and dual detection in parallel design to eliminate cross-interference, resulting in a significant increase in sensitivity [31]. The signal output of various modes also holds a lot of promise concurrently. Based on Fe-doped polydopamine (Fe@PDA) with significant peroxidase-mimetic enzymatic activity and the capacity to emit green fluorescence, a fluorescent/colorimetric dual-mode determination method was developed. The platform contained *Listeria monocytogenes* (*L. monocytogenes*)-recognizing aptamer-modified Fe@PDA (apt/Fe@PDA) and vancomycin-functionalized Fe_3O_4 (van/ Fe_3O_4). Residual *L. monocytogenes* in environmental water were successfully detected with an LOD of 1.0 CFU/mL for fluorescence and 2.3 CFU/mL for colorimetric detection [32].

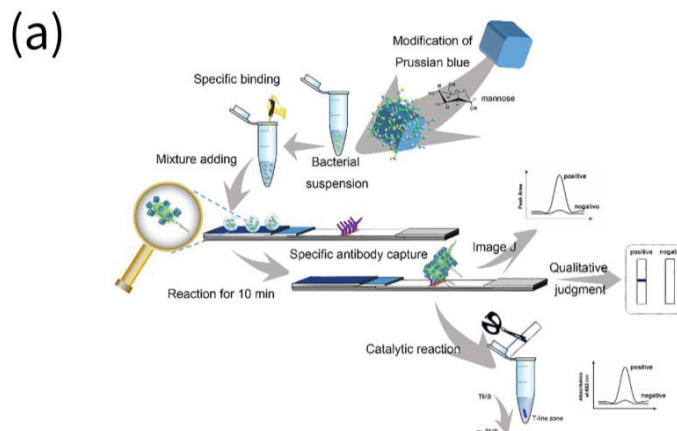


Figure 1. Cont.

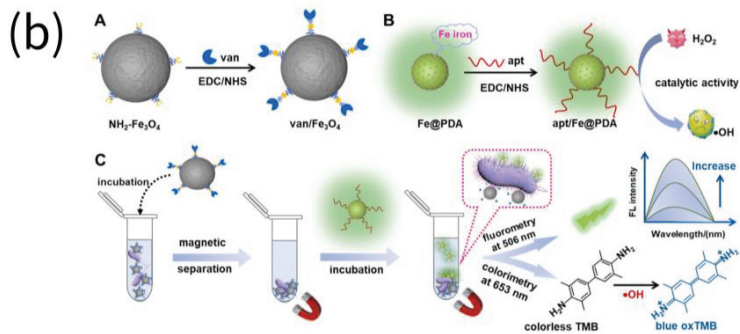


Figure 1. Assays for the detection of pathogenic micro-organisms in food by nanozymes. (a) *E. coli* O157:H7 were detected using mannose modified Prussian blue (man-PB) (reprinted with permission from [30], Copyright 2020, Elsevier). (b) *Listeria monocytogenes* were detected using Fe@PDA-based nanozyme (reprinted with permission from [32], Copyright 2022, Elsevier).

3. Toxins

Toxins generated by pathogens released into food are thought to be the main cause of foodborne disease outbreaks. These toxins induce cytotoxicity by changing the physiological activity and integrity of the plasma membrane [33]. Toxins have a variety of forms depending on where they originate, including bacterial toxins, mycotoxins, phycotoxins, and algal toxins, among which aflatoxin B1 (AFB1) and ochratoxin A (OTA) are the most toxic toxins. The former is one of the culprits of liver cancer and categorized as a Group I carcinogen by the International Agency for Research on Cancer (IARC), while the latter is categorized as a Group 2B carcinogen due to its nephrotoxicity and carcinogenicity [34,35]. Moreover, toxins persist in food even after the relevant pathogens have died, and prompt detection of low amounts of toxins is crucial for reducing poisoning and maintaining public health [36]. Existing toxin detection techniques are sensitive and specific, similar to pathogen detection techniques; however, they require additional instrumentation and operators. Advanced techniques applying nanomaterials as portable biosensors are essential for rapid field detection of specific pollutants (Figure 2).

Making use of MIL-88, with considerable Fe-MOFs-mimetic catalytic activity, and replacing natural enzymes such as HRP to catalyze TMB, an indirect competitive MOF-linked immunosorbent assay (MOFLISA) was developed for the high-throughput and high-sensitivity detection of AFB1. The approach is 20 times more effective than the standard ELISA and could effectively avoid the occurrence of false positives and false negatives during the detection of AFB1 [37]. Liu et al. constructed a microcystin-LR (MC-LR) immunosensor utilizing a double-integrated mimic nanozyme by coupling copper hydroxide nanozyme with G-quadruplex/hemin DNAzyme. Outstanding peroxidase activity was demonstrated by the double-integrated enzyme for the chromogenic reaction of 2,2'-azinobis-(3-ethylbenzothiazoline-6-sulfonic acid) (ABTS) [38].

The multimodal analysis method is more accurate and reliable due to the independence and complementarity of signals. PBNPs produced in situ on the surface of magnetic nanoparticles (MNPs) were taken by Lu et al. to build up a multimodal nanozyme-linked immunosorbent assay (NLISA) that included photothermal, colorimetric, and fluorescence analyses for testing AFB1. The introduced MNPs served as both loading carriers and precursors, quenched the fluorescence of Cy5, and then the generated PBNPs restored the fluorescence of Cy5. The photothermal and colorimetric signals could be applied for POCT and the fluorescence signal for ultrasensitive detection with an LOD of 0.54 fg/mL [39]. Chen et al. prepared Co nanoparticles/N-doped carbon nanotubes (Co/NCNT) with a hollow core/shell structure. While the hollow structure promoted the binding of the active center to the substrate and sped up the reaction, the synergistic effect of Co NPs and

NCNT boosted the simulated oxidase activity. Additionally, Co/NCNT produced blue TMB^+ , which quenched the fluorescence of AuAg nanoclusters (NCs) through the internal filtration effect (IFE). A colorimetric-fluorescent dual-mode immunosensor with an LOD of 0.21 ng/L (colorimetric) and 0.17 ng/L (fluorescent) for the sensitive detection of OTA was established [40]. Based on $\text{Cu}_2\text{O}@Fe(\text{OH})_3$ yolk-shell nanocages with catalytic activity similar to peroxidase, Zhu et al. developed a bimodal multicolorimetric and proportional fluorescence immunosensor capable of sensitively detecting OTA. $\text{Cu}_2\text{O}@Fe(\text{OH})_3$ efficiently etched Au nanorods (Au NRs), yielding observable color changes and LSPR shifts. It also quenched the emission peak of carbon dots (CDs) at 424 nm and produced a new emission peak at 563 nm to form a ratiometric fluorescence signal [41].

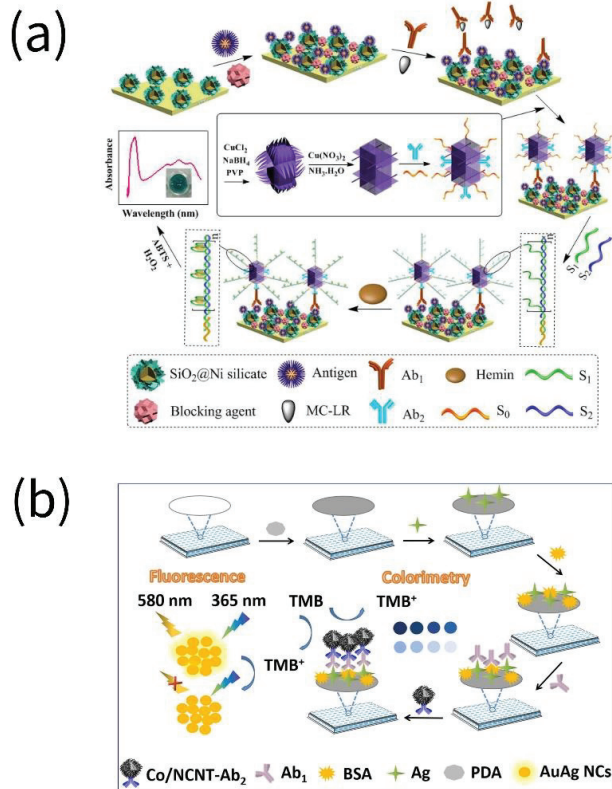


Figure 2. Assays for the detection of toxins in food by nanozymes. (a) Microcystin-LR (MC-LR) was detected using coupling copper hydroxide nanozyme and G-quadruplex/hemin DNAzyme (reprinted with permission from [38], Copyright 2019, American Chemical Society). (b) OTA was detected using ZIF-derived hollow Co/N-doped carbon nanotubes (CNTs) (reprinted with permission from [40], Copyright 2022, Elsevier).

4. Pesticide Residues

One of the major factors impacting food quality is contamination from pesticide residues [42]. The majority of pesticides are neurotoxic and carcinogenic to individuals, and their residues migrate through the food chain and environment and even persist in nature for more than 15 years [43]. To analyze pesticide residues in agricultural products and the environment at trace or even ultra-trace levels, the sensitive detection of pesticide residues primarily makes use of high-performance liquid chromatography (HPLC), gas chromatography (GC), gas chromatography/mass spectrometry (GC-MS) and HPLC-

MS/MS [44]. However, these methods are not appropriate for POCT, while the specific nanozyme structure holds a synergistic effect to raise the sensitivity of detected targets [45] (Figure 3). Pesticides can be broadly divided into four categories based on the chemical property of their active ingredients: organochlorines, organophosphates, carbamates and pyrethroids [46].

Applying a synthetic Fe-N/C SAzyme that directly oxidized TMB to produce blue oxidized product 3,3',5,5'-tetramethylbenzidine diamine (oxTMB), Ge et al. established a novel, extremely sensitive malathion colorimetric platform. L-ascorbic acid-2-phosphate (AA2P), a substrate of acid phosphatase (ACP), could be hydrolyzed to AA, inhibiting the oxidation reaction of TM and resulting in noticeable blue color fading. With the addition of malathion, AA synthesis was reduced and ACP activity was hampered, restoring the catalytic activity of the single-atom nanozyme [47]. Iron-based metal-organic gel (MOGs) nanosheet hybrids with AuNPs immobilization (AuNPs/MOGs (Fe)) were fabricated to detect organophosphorus (OPs), which displayed excellent chemiluminescence (CL) properties. The considerable enhancement of CL was blamed for the modification of AuNPs on the MOGs (Fe) nanosheet, which synergistically increased the CL reaction by speeding the formation of OH^\bullet , $\text{O}_2^{\bullet-}$ and $^1\text{O}_2$ [48].

The removal of peroxidase-like activity and color interference is crucial for colorimetric analysis of the nanozyme. The GeO_2 nanozyme was found that it only possessed peroxidase-like activity but no oxidase-like capability, which rendered the related detection system free from O_2 disturbance. In addition, the white GeO_2 nanozyme removed its color interference. Accordingly, a colorimetric sensing platform for ultra-trace detection of OPs pesticides with paraoxon as a representative model was proposed. In the absence of paraoxon, the active acetylcholinesterase (AChE) degraded the GeO_2 nanozyme and lost its peroxidase function by hydrolyzing acetylthiocholine (ATCh) to thiocholine (TCh). In the presence of paraoxon, AChE was irreversibly inactivated and TCh production was inhibited [49].

While most investigations have been devoted to further optimizing fluorescent probes or assays to enhance the sensitivity for OPs, Liang et al. conducted groundbreaking work on creating yeast-surface-displayed acetylcholinesterase (AChE) mutants (E69Y and E69Y/F330L) from the perspective of modifying the sensitivity of AChE for OPs. Using electronegative fluorescent gold nanoclusters (AuNCs) combined with AChE mutants, an ultra-trace fluorescence assay for OPs with the LOD of 3.3×10^{-14} M was established, indicating that the E69Y and F330L mutations had the potential to significantly improve the sensitivity of the nanozyme to OPs [50].

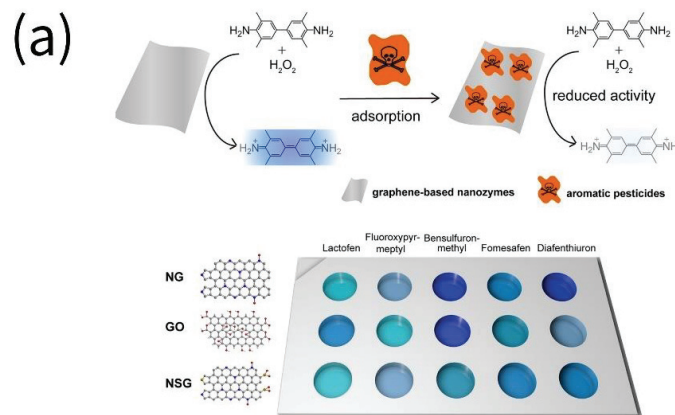


Figure 3. Cont.

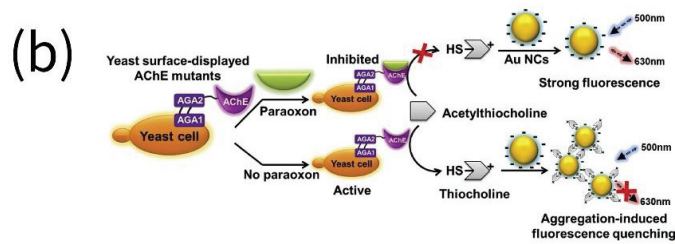


Figure 3. Assays for the detection of pesticide residues in food by nanozymes. (a) Five pesticides (i.e., lactofen, fluroxypyr-meptyl, bensulfuron-methyl, fomesafen and diafenthiuron) were detected using heteroatom-doped graphene sensor arrays (reprinted with permission from [51], Copyright 2020, American Chemical Society). (b) Paraoxon was detected using fluorescent AuNCs (reprinted with permission from [50], Copyright 2020, Elsevier).

5. Veterinary Drugs

Veterinary drugs are the substances applied to prevent, treat and diagnose animal diseases or purposefully regulate animal physiological functions and effectively help farmers solve the problems of livestock threatened by epidemics in breeding production, including antibiotics, antiparasitic and antifungal drugs, hormones, growth promoters, etc. [52]. In the ongoing expansion of the livestock industry today, the employment of veterinary drugs has been crucial in the production of animal-derived food [53]. Veterinary drug residues are the substances of prototype drugs and their metabolites as well as related impurities that accumulate or remain in the organisms or products of livestock and poultry (such as eggs, milk, meat, etc.) following drug application (Figure 4) [54].

Li et al. established the Fe-gallic acid (GA) nanozymes (FGN), an artificial multi-iron peroxidase with monoclonal antibody recognition activity and high catalytic performance inspired by polyphenol–protein interactions. Afterward, clenbuterol (CLL) in pork and poultry was determined applying the nanozyme-mediated dual colorimetric immunochromatographic in conjunction with smartphones, with a detection limit of 0.172 ng mL^{-1} [55]. Applying aggregation-induced (AI)-electrochemiluminescence (ECL)-containing covalent organic framework materials (COF-AI-ECL) as the signal element and Co_3O_4 nanozyme as the signal amplification component, a CAP molecularly imprinted sensor was established. Co_3O_4 catalytically amplified the ECL signal of COF-AI-ECL, which was effectively quenched by CAP; thus, the ECL signal was controlled by the elution and adsorption of CAP by molecularly imprinted polymer (MIP) [56]. Kanamycin (Kana) was detected on polyaniline-nanowire-functionalized reduced-graphene-oxide (PANI/rGO) framework by catalyzing H_2O_2 to generate oxygen using platinum nanozymes on hairpin DNA probes. The principle of signal amplification was to produce a sizable amount of Pt nanoparticles through the coupling of catalytic hairpin assembly (CHA) reaction and strand-displacement amplification (SDA) reaction [57].

Multisignal, enhanced ultrasensitive detection of veterinary drugs is considered an advanced academic research achievement. Utilizing planar VS_2/AuNPs nanocomposites as the electrode sensing platform, streptavidin-functionalized CoFe_2O_4 nanozyme, and methylene-blue-labeled hairpin DNA (MB-hDNA) as signal-amplifying components, an electrochemical aptamer sensor for kanamycin (Kana) proportional detection was developed. The VS_2/AuNPs nanocomposites were combined with hDNA complementarily hybridized with biotinylated Kana-aptamers, and the CoFe_2O_4 nanozyme immobilized on the aptamer sensor possessed excellent peroxidase-like catalytic activity. In the presence of Kana, aptamer biorecognition resulted in a decrease in nanozyme accumulation and an increase in the response of MB [58].

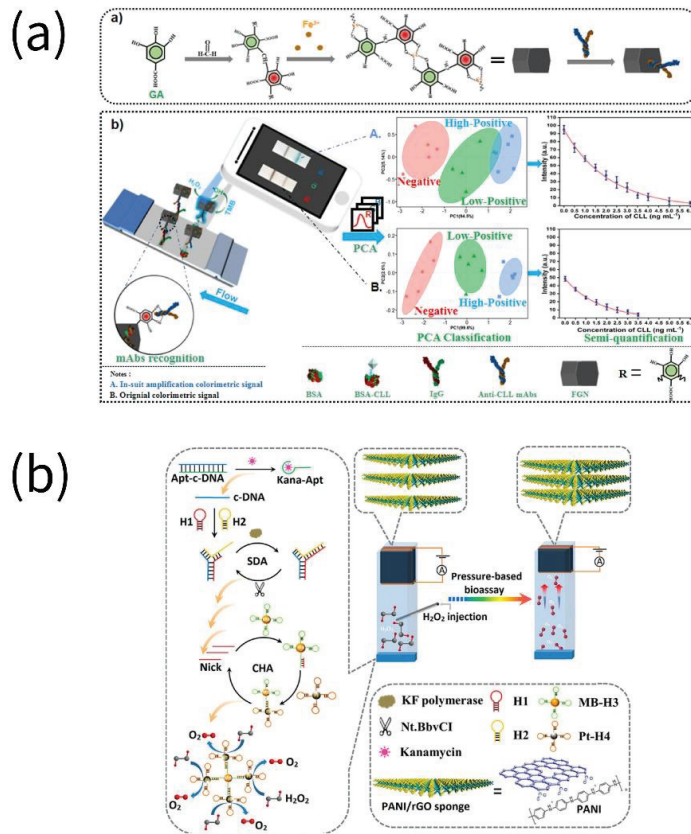


Figure 4. Assays for the detection of veterinary drugs in food by nanozymes. (a) Clenbuterol was detected using Fe-GA nanozymes (reprinted with permission from [55], Copyright 2022, Elsevier). (b) Kanamycin was detected using polyaniline-nanowire-functionalized reduced-graphene-oxide (PANI/rGO) framework (reprinted with permission from [57], Copyright 2018, American Chemical Society).

6. Heavy Metals

Excessive levels of heavy metal content in food are caused by heavy metal enrichment in the food chain due to sewage irrigation, automobile exhaust emissions, and the massive application of fertilizers and pesticides [59]. The main hazardous heavy metal ions (HMIs) include Ni²⁺, Cr⁶⁺, Pb²⁺, Hg²⁺, Cd²⁺ and Cu²⁺, and long-term exposure to these HMIs up to a certain threshold is associated with several health risks, such as Alzheimer’s disease and metabolic disorders [60]. They also impact the cardiovascular, neurological, and renal systems and cause organic injury to human organs. The traditional methods for detecting heavy metals in food mainly involve atomic absorption spectrometry (AAS), atomic fluorescence spectrometry (AFS), inductively coupled plasma/mass spectrometry (ICP-MS), inductively coupled plasma/atomic emission spectrometry (ICP-AES), and ultraviolet-visible spectrometry (UV-vis Spectrometry) [61,62]. Here are several instances of HMIs detection utilizing nanozyme sensors (Figure 5).

After realizing the remarkable selectivity and high-speed absorption of Hg by CuS nanostructures, Fang et al. first put forward an affordable Hg²⁺ nanosensor. CuS hollow nanospheres (HNSs) were the central component and performed three functions: they acted as a concentration carrier for Hg²⁺ pre-enrichment, a recognition unit for Hg²⁺ sensing, and

an amplifier and readout for peroxidase-mimetic signals [63]. Anchoring single-atom Fe on a monolayer of two-dimensional nitrogen-doped graphene, the synthesized SA-Fe/NG held excellent peroxidase-like activity, 100% Fe atom utilization and Fe-N-C structure. Based on the preferential specific interaction of TMB oxidation inhibitor 8-hydroxyquinoline (8-HQ) with Cr(VI), which restored oxTMB to blue color TMB, Mao et al. established a single-atom nanozyme colorimetric sensing method for Cr(VI) [64]. Bipyridine-containing COF nanosheets (Tp-Bpy NSs) with regular pore structure, abundant nitrogen-containing functional groups, and flexible topological connectivity were synthesized. AuNPs were generated in situ to form AuNPs@TP-Bpy. The majority of the anchored AuNPs were exposed to the two-dimensional pore structure of Tp-Bpy NSs, increasing the contact area. It was revealed that the ultra-sensitive detection performance of AuNPs@Tp-Bpy nanocomposites for Hg^{2+} was attributed to the synergistic effect of the enhanced catalytic activity of gold amalgam and the considerable access probability of TP-Bpy nanosheets for Hg^{2+} [65].

Regarding sensitive and rapid POCT for a wide range of HDMIs in food and environment, there are still a lot of technical barriers that need to be solved. Applying porous Co_3O_4 nanodisks with fairly strong peroxidase-like activity to detect multiple heavy metals, a colorimetric sensor was formed. The electron transferred between the porous Co_3O_4 nanodisks and TMB was blocked and the catalytic activity was significantly inhibited by HDMIs (Cd(II), Hg(II), Pb(II) and As), indicating that heavy metals had anti-competitive inhibition of peroxidase activity. The LOD values of this assay were $0.085 \mu\text{g L}^{-1}$ for Cd(II), $0.19 \mu\text{g L}^{-1}$ for Hg(II), $0.22 \mu\text{g L}^{-1}$ for Pb(II) and $0.156 \mu\text{g L}^{-1}$ for As. It is worth noting that when the concentration of heavy metals exceeded $5 \mu\text{g L}^{-1}$ or the change of absorbance was greater than 0.5, it could be distinguished by the naked eye [66].

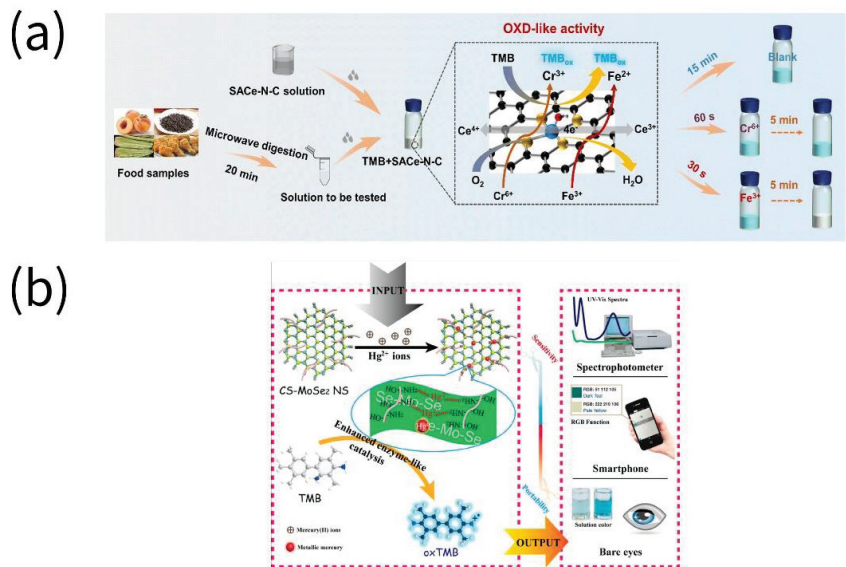


Figure 5. Assays for the detection of heavy metals in food by nanozymes. (a) Fe^{3+} and Cr^{6+} were detected using single-atom Ce-N-C (SACe-N-C) (reprinted with permission from [67], Copyright 2022, Elsevier). (b) Hg^{2+} was detected using chitosan-functionalized molybdenum (IV) selenide nanosheets (CS-MoSe₂ NS) (reprinted with permission from [68], Copyright 2019, American Chemical Society).

7. Others

Along with the aforementioned common food hazards, there are allergens, food additives, and illegal food additives that should not be ingested in excess and are damaging to the human organism [69]. Novel nanozyme biosensors for sensitive detection of histamine (HA), nitrite and Sudan are given below (Figure 6).

HA is a substance produced by the decarboxylation of histidine, a biogenic amine generated by the spoilage of high-protein foods, and plays an important role in inflammation and allergic reactions in humans [70]. Fish products are an integral component of the human diet, but fish is highly perishable, and histidine can be readily converted to HA through decarboxylation if transported or stored under improper conditions [71]. HA is highly toxic and causes headaches, nausea, and other adverse reactions when ingested in excess, even threatening life in severe cases [72]. Binding PBNPs to goat anti-mouse antibodies for the purpose of forming nanozyme–antibody conjugates, Liao et al. established a nanozyme-mediated ratiometric fluorescence immunoassay for testing HA. The oxidation of *o*-phenylenediamine (OPD) produced fluorescent 2,3-diaminophenothiazine (oxOPD) under the catalysis of PBNPs, which formed a new emission peak at 570 nm and quenched the fluorescence of CDs at 450 nm [73]. Covalently coupling DNA aptamers with excellent selectivity for HA to a gold nanoflower-modified ITO electrode (apt/AuNFs/ITO) and employing DNA/Au@FeCo NCs with peroxidase-like activity as electrochemical probes, an electrochemical sensor for the determination of HA was developed [74]. Wang et al. published a biomimetic enzyme-linked immunoassay (BELISA) based on the labeled Au@Pt@Au complex nanozyme with peroxidase-mimetic activity for detecting HA [75].

Nitrite exists in a variety of foods, and there are two main sources. First, when vegetables are pickled or cooked, the nitrate in them is reduced to nitrite under the action of reducing bacteria. Second, nitrite has antibacterial and antioxidant properties and thus is widely employed as a food additive in meat and dairy products [76]. However, excessive intake of nitrite has indirect carcinogenic, teratogenic, mutagenic, and other risks to humans, and a single intake of 0.3 g or more causes poisoning or even death [77]. Synthesizing bifunctional Mn-doped N-rich CDs (Mn-CDs) with controlled photoluminescence, high oxidase-like activity, abundant functional groups and favorable hydrophilicity which effectively catalyzed the oxidation of colorless TMB to blue TMB⁺, a bimodal colorimetric/fluorescence technique for the reliable and efficient determination of nitrite in complex matrices was established [78]. Another paper by the same authors investigated the carbon-supported Mn₃O₄ particles, utilizing the coupling of a specific diazotization reaction with oxidase-mimetic catalysis, a novel dual-mode and dual-scale electrochemical nitrite sensing method was built up [79]. Adegoke et al. synthesized a chemically modified AuNP-CeO₂ NP-anchored GO hybrid nanozyme (AuNP-CeO₂ NP@GO) applied to the catalytic colorimetric detection of nitrite, where AuNP-CeO₂ NP@GO yielded high peroxidase catalysis [80].

Sudan is frequently employed as a synthetic pigment in food additives, and the IARC has classified Sudan I, II, III and IV as animal carcinogens [81]. Sudan's consumption for improving the appearance and color of food products has been outlawed in China by the Food and Drug Administration [82]. A screen-printed electrochemical sensor based on La³⁺-doped Co₃O₄ nanocubes was established for the detection of Sudan I, utilizing the excellent catalytic properties, favorable adaptability in catalytic reactions, and interaction with oxygen groups in Co₃O₄ of nanozyme [83]. Ye et al. applied CuO nanoparticle-decorated 3D N-doped porous carbon (CuO/3D NPC)-modified electrodes with an excellent electrocatalytic activity of CuO, which exhibited high sensitivity and broad linear range for the detection of Sudan I [84]. A polystyrene-coated, magnetic Fe₃O₄ nanoparticle (PSt@Fe₃O₄) was employed as a solid-phase adsorbent for liquid–solid extraction prior to magnetic solid phase extraction (MSPE), making it applicable to solid food matrices. The non-polar Sudan dyes were adsorbed onto similarly structured non-polar polystyrene wrapped around nanoparticles and then released Sudan dyes using a desorbent for detection and quantification [85].

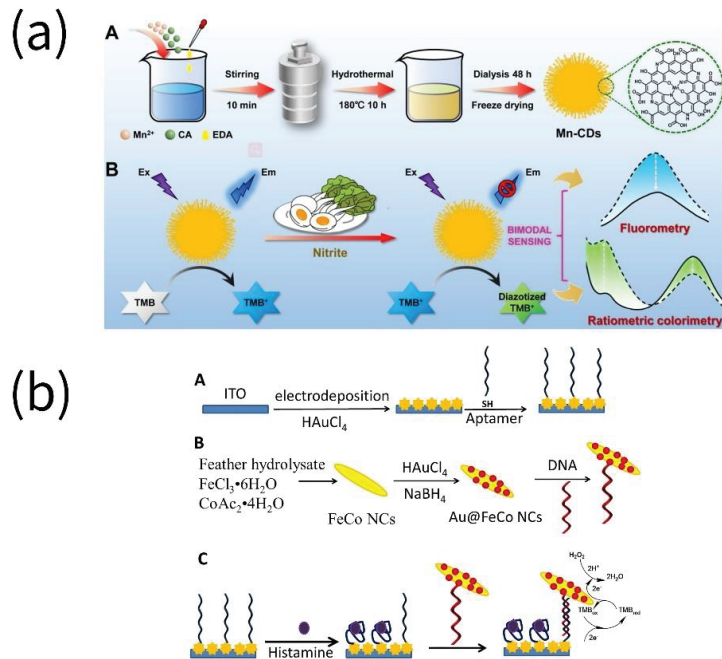


Figure 6. Assays for the detection of other food hazard substances in food by nanozymes. (a) Nitrite was detected using Mn-doped N-rich carbon dots (Mn-CDs) (reprinted with permission from [78], Copyright 2022, American Chemical Society). (b) Histamine was detected using DNA/Au@FeCo nanoflowers (NCs) (reprinted with permission from [74], Copyright 2022, Elsevier).

8. Conclusions and Perspectives

Public health risks related to food safety remain a top priority, and specific instances of nanozyme biosensors for detecting primary food pollutants were discussed. Although some of the drawbacks of conventional detection techniques have been overcome through the development of various nanomaterials, most nanozyme-based sensors require additional manipulation steps that add operational complexity compared to traditional methods, and considerable work remains to be completed before they could become viable alternatives to conventional assays, for instance, innovating the structure of immunosensors, exploring new nanozyme-based sensors, and optimizing existing nanozyme by combining experimental techniques and theoretical strategies. Future nanozyme developments will put more emphasis on being more portable, wide-ranging, and industrialized, such as by combining artificial intelligence (AI) and machine learning with food quality maintenance to facilitate rapid identification of food risk factors and through the proliferation of nanosensors associated with portable mobile devices to enable precise monitoring at home. We hope that this paper could provide new inspiration for the future outlook of nanozyme-based sensors for food safety analysis.

Table 1. Nanozyme-based biosensors for the detection of food contaminants.

Analytes	Biosensors	Nanozymes	LODs	Food Matrix	Ref.
Pathogenic microorganism					
<i>Escherichia coli</i> O157:H7 (<i>E. coli</i> O157:H7)	Colorimetric	Platinum-coated magnetic nanoparticle clusters (Pt/MNCs)	10 CFU/mL	milk	[86]
<i>E. coli</i> O157:H7	Colorimetric	Hemin-concanavalin A hybrid nanoflowers (HCH nanoflowers)	4.1 CFU/mL	milk	[87]
<i>Salmonella</i> Enteritidis	Colorimetric	Fe-MOF nanoparticles	34 CFU/mL	milk	[88]
<i>Salmonella typhimurium</i>	Colorimetric	Prussian blue nanoparticles (PBNPs)	6×10^3 CFU/mL	powdered milk	[89]
<i>Salmonella enterica</i> serovar typhimurium	Colorimetric	ZnFe ₂ O ₄ -reduced graphene oxide nanostructures	11 CFU/mL	milk	[90]
<i>Listeria monocytogenes</i> (<i>L. monocytogenes</i>)	Colorimetric	AgNCs	10 CFU/mL	pork	[91]
Toxins					
Aflatoxin B1 (AFB1)	Colorimetric	Mesoporous SiO ₂ /Au-Pt (m-SAP)	0.005 ng/mL	peanut	[92]
AFB1	Colorimetric	Porphyrin NanoMOFs (NanoPCN-223(Fe))	0.003 ng/mL	milk	[93]
AFB1 and <i>Salmonella</i> Enteritidis	Colorimetric/ Fluorescent	Pt@PCN-224-HRP-initiator DNA (PP-HRP-iDNA)	6.5×10^{-4} ng/mL and 4 CFU/mL for AFB1 and <i>Salmonella</i> Enteritidis respectively	rice and milk	[94]
Ochratoxin A (OTA)	Colorimetric	Co(OH) ₂ nanocages	2.6×10^{-4} ng/mL	corn	[95]
Saxitoxin (STX)	Colorimetric	AuNPs	4.246×10^{-4} nM	shellfish	[96]
Pesticide residues					
Diazinon	Fluorescent	Fe ₃ O ₄ nanoparticles@ZIF-8 (Fe ₃ O ₄ NPs@ZIF-8)	0.2 nM	water and fruit juices	[97]
Acetamiprid	Colorimetric	Gold nanoparticles (GNPs)	0.1 ng/mL	-	[98]
Methyl-paraoxon	Colorimetric/ Fluorescent	nanoceria	420 nM	Semen nelumbinis, Semen Armeniacaee Amarum, Rhizoma Dioscoreae	[99]
Paraoxon	Fluorescent	Carbon quantum dots (CQDs)	0.05 ng/mL	tap and river water	[100]
Paraoxon	Fluorescent	MnO ₂ Nanosheet-Carbon Dots	0.015 ng/mL	tap water, river water, rice, and cabbage	[101]

Table 1. Cont.

Analytes	Biosensors	Nanozymes	LODs	Food Matrix	Ref.
Paraoxon, Parathion, Fenitrothion and Diazinon	Colorimetric	AuNPs	0.13 ng/mL, 0.37 ng/mL, 0.42 ng/mL and 0.20 ng/mL for paraoxon, parathion, fenitrothion and diazinon, respectively	water	[102]
Glyphosate	Colorimetric/ Fluorescence/ Photothermal	N-CDs/FMOF-Zr	13.1 ng/mL, 1.5 ng/mL and 11.5 ng/mL for colorimetric, fluorescence and photothermal respectively	rice, millet, and soybeans	[103]
Veterinary drugs					
Tetracycline (TC)	Colorimetric	AuNCs	46 nM	drugs and milk	[104]
Kanamycin	Colorimetric	Gold nanoparticles (GNPs)	1.49 nM	-	[105]
Enrofloxacin	Chemiluminescence	Co(OH) ₂ nanosheets	4.1×10^{-5} ng/mL	shrimp, chicken, and duck meat	[106]
Norfloxacin (NOR)	Colorimetric	1-methyl-D-tryptophan-capped gold nanoclusters (1-Me-D-Trp@AuNCs)	200 nM	drugs	[107]
Sulfaquinoxaline (SQX)	Chemiluminescence	Cu(II)-anchored unzipped covalent triazine framework (UnZ-CCTF)	7.6×10^{-4} nM	milk	[108]
Chloramphenicol (CAP)	Electrochemiluminescence	Ulthathin PtNi	2.6×10^{-7} nM	pig urine, river water, and milk	[109]
Heavy metals					
Hg ²⁺	Colorimetric	Pt NP	16.9 nM, 26 nM and 47.3 nM for MilliQ water, tap water and ground waters, respectively	MilliQ water, tap water, and ground waters	[110]
Hg ²⁺ and MeHg	Fluorescent	Copper oxide-based nanocomposites	3.0 nM and 3.3 nM for Hg ²⁺ and MeHg, respectively	tap water, river water, seawater, and dogfish muscle	[111]
Ag ²⁺	Colorimetric	Chitosan-PtNPs (Ch-PtNPs)	4 nM	tap and lake water	[112]
Ag ²⁺	Colorimetric	Pt nanoparticles	7.8×10^{-3} nM	river water	[113]
Pb ²⁺	Colorimetric	Tungsten disulfide (WS ₂) nanosheets	4 ng/mL	tap water, soil, wheat, and fish serum	[114]
Pb ²⁺	Colorimetric	Au@Pt nanoparticles	3.0 nM	lake water	[115]
Pb ²⁺ and Hg ²⁺	Fluorescent	Metal-deposited bismuth oxyiodide (BiOI) nanonetworks	nanomolar quantities	tap water, river water, lake water, and sea water	[116]

Table 1. Cont.

Analytes	Biosensors	Nanozymes	LODs	Food Matrix	Ref.
Others					
Sulfide	Colorimetric	GMP-Cu nanozyme with laccase activity	670 nM	baking soda, rock sugar, konjac flour, and xylitol	[117]
Nitrite	Colorimetric/ Electrochemical	Histidine(His)@AuNCs/ rGO	2 nM and 700 nM for Colorimetric and Electrochemical respectively	sausage	[118]
Nitrite	Colorimetric	Hollow MnFeO particles	200 nM	sausage, pickles, and salted eggs	[119]
Salbutamol	Colorimetric	AgNPs	2.614×10^{-4} ng/mL	tap water and artificial urine	[120]

Author Contributions: Conceptualization, methodology, writing—original draft preparation, data curation, Y.L.; conceptualization, supervision, validation, B.Z.; validation, D.C., W.T. and J.Z.; project administration, writing—review and editing, funding acquisition, X.S., X.Y. and Z.Y. All authors have read and agreed to the published version of the manuscript.

Funding: This work was supported by the Key R&D Program of Zhejiang Province (2021C02061, 2022C02049).

Institutional Review Board Statement: Not applicable.

Informed Consent Statement: Not applicable.

Data Availability Statement: The datasets generated for this study are available on request to the corresponding author.

Conflicts of Interest: The authors declare that they have no known competing financial interests or personal relationships that could have appeared to influence the work reported in this paper.

References

- Shenashen, M.A.; Emran, M.Y.; El Sabagh, A.; Selim, M.M.; Elmarakbi, A.; El-Safty, S.A. Progress in Sensory Devices of Pesticides, Pathogens, Coronavirus, and Chemical Additives and Hazards in Food Assessment: Food Safety Concerns. *Prog. Mater. Sci.* **2022**, *124*, 100866. [CrossRef]
- van Asselt, E.D.; van der Fels-Klerx, H.J.; Marvin, H.J.P.; van Bokhorst-van de Veen, H.; Groot, M.N. Overview of Food Safety Hazards in the European Dairy Supply Chain: Food Safety Hazards in the Dairy Chain. *Compr. Rev. Food Sci. Food Saf.* **2017**, *16*, 59–75. [CrossRef] [PubMed]
- Proietti, I.; Frazzoli, C.; Mantovani, A. Identification and Management of Toxicological Hazards of Street Foods in Developing Countries. *Food Chem. Toxicol.* **2014**, *63*, 143–152. [CrossRef] [PubMed]
- Li, X.; Tan, C.-P.; Liu, Y.-F.; Xu, Y.-J. Interactions between Food Hazards and Intestinal Barrier: Impact on Foodborne Diseases. *J. Agric. Food Chem.* **2020**, *68*, 14728–14738. [CrossRef]
- Piatkowska, M.; Jedziniak, P.; Zmudzki, J. Multiresidue Method for the Simultaneous Determination of Veterinary Medicinal Products, Feed Additives and Illegal Dyes in Eggs Using Liquid Chromatography-Tandem Mass Spectrometry. *Food Chem.* **2016**, *197*, 571–580. [CrossRef]
- Fu, Y.; Zhao, C.; Lu, X.; Xu, G. Nontargeted Screening of Chemical Contaminants and Illegal Additives in Food Based on Liquid Chromatography-High Resolution Mass Spectrometry. *TrAC-Trend Anal. Chem.* **2017**, *96*, 89–98. [CrossRef]
- Li, G.; Xu, L.; Wu, W.; Wang, D.; Jiang, J.; Chen, X.; Zhang, W.; Poapolathep, S.; Poapolathep, A.; Zhang, Z.; et al. On-Site Ultrasensitive Detection Paper for Multiclass Chemical Contaminants via Universal Bridge-Antibody Labeling: Mycotoxin and Illegal Additives in Milk as an Example. *Anal. Chem.* **2019**, *91*, 1968–1973. [CrossRef]
- Huang, Y.; Ren, J.; Qu, X. Nanozymes: Classification, Catalytic Mechanisms, Activity Regulation, and Applications. *Chem. Rev.* **2019**, *119*, 4357–4412. [CrossRef]
- Zhang, X.; Wu, D.; Zhou, X.; Yu, Y.; Liu, J.; Hu, N.; Wang, H.; Li, G.; Wu, Y. Recent Progress in the Construction of Nanozyme-Based Biosensors and Their Applications to Food Safety Assay. *TrAC-Trend Anal. Chem.* **2019**, *121*, 115668. [CrossRef]
- Gao, L.; Yan, X. Nanozymes: An Emerging Field Bridging Nanotechnology and Biology. *Sci. China Life Sci.* **2016**, *59*, 400–402. [CrossRef]

11. Manea, F.; Houillon, F.B.; Pasquato, L.; Scrimin, P. Nanozymes: Gold-Nanoparticle-Based Transphosphorylation Catalysts. *Angew. Chem. Int. Edit.* **2004**, *116*, 6291–6295. [[CrossRef](#)]
12. Gao, L.; Zhuang, J.; Nie, L.; Zhang, J.; Zhang, Y.; Gu, N.; Wang, T.; Feng, J.; Yang, D.; Perrett, S.; et al. Intrinsic Peroxidase-like Activity of Ferromagnetic Nanoparticles. *Nat. Nanotechnol.* **2007**, *2*, 577–583. [[CrossRef](#)] [[PubMed](#)]
13. Xu, D.; Wu, L.; Yao, H.; Zhao, L. Catalase-Like Nanozymes: Classification, Catalytic Mechanisms, and Their Applications. *Small* **2022**, *18*, 2203400. [[CrossRef](#)] [[PubMed](#)]
14. Liang, M.; Yan, X. Nanozymes: From New Concepts, Mechanisms, and Standards to Applications. *Acc. Chem. Res.* **2019**, *52*, 2190–2200. [[CrossRef](#)] [[PubMed](#)]
15. Nath, I.; Chakraborty, J.; Verpoort, F. Metal Organic Frameworks Mimicking Natural Enzymes: A Structural and Functional Analogy. *Chem. Soc. Rev.* **2016**, *45*, 4127–4170. [[CrossRef](#)] [[PubMed](#)]
16. Sun, H.; Zhou, Y.; Ren, J.; Qu, X. Carbon Nanozymes: Enzymatic Properties, Catalytic Mechanism, and Applications. *Angew. Chem. Int. Edit.* **2018**, *57*, 9224–9237. [[CrossRef](#)]
17. Huang, L.; Sun, D.; Pu, H.; Wei, Q. Development of Nanozymes for Food Quality and Safety Detection: Principles and Recent Applications. *Compr. Rev. Food Sci. F* **2019**, *18*, 1496–1513. [[CrossRef](#)]
18. Rohani Bastami, T.; Bayat, M.; Paolesse, R. Naked-Eye Detection of Morphine by Au@Ag Nanoparticles-Based Colorimetric Chemosensors. *Sensors* **2022**, *22*, 2072. [[CrossRef](#)]
19. Jiang, D.; Ni, D.; Rosenkrans, Z.T.; Huang, P.; Yan, X.; Cai, W. Nanozyme: New Horizons for Responsive Biomedical Applications. *Chem. Soc. Rev.* **2019**, *48*, 3683–3704. [[CrossRef](#)]
20. Bastami, T.R.; Dabirifar, Z. AuNPs@PMo12 Nanozyme: Highly Oxidase Mimetic Activity for Sensitive and Specific Colorimetric Detection of Acetaminophen. *RSC. Adv.* **2020**, *10*, 35949–35956. [[CrossRef](#)]
21. Ruan, X.; Liu, D.; Niu, X.; Wang, Y.; Simpson, C.D.; Cheng, N.; Du, D.; Lin, Y. 2D Graphene Oxide/Fe-MOF Nanozyme Nest with Superior Peroxidase-Like Activity and Its Application for Detection of Woodsmoke Exposure Biomarker. *Anal. Chem.* **2019**, *91*, 13847–13854. [[CrossRef](#)] [[PubMed](#)]
22. Sayad, A.A.; Ibrahim, F.; Uddin, S.M.; Pei, K.X.; Mohkhtar, M.S.; Madou, M.; Thong, K.L. A Microfluidic Lab-on-a-Disc Integrated Loop Mediated Isothermal Amplification for Foodborne Pathogen Detection. *Sens. Actuat. B-Chem.* **2016**, *227*, 600–609. [[CrossRef](#)]
23. Shen, Y.; Xu, L.; Li, Y. Biosensors for Rapid Detection of Salmonella in Food: A Review. *Compr. Rev. Food Sci.* **2021**, *20*, 149–197. [[CrossRef](#)] [[PubMed](#)]
24. Alahi, M.E.E.; Mukhopadhyay, S.C. Detection Methodologies for Pathogen and Toxins: A Review. *Sensors* **2017**, *17*, 1885. [[CrossRef](#)]
25. Abdalhai, M.H.; Fernandes, A.M.; Xia, X.; Musa, A.; Ji, J.; Sun, X. Electrochemical Genosensor to Detect Pathogenic Bacteria (*Escherichia coli* O157:H7) As Applied in Real Food Samples (Fresh Beef) To Improve Food Safety and Quality Control. *J. Agric. Food Chem.* **2015**, *63*, 5017–5025. [[CrossRef](#)] [[PubMed](#)]
26. Primiceri, E.; Chiriaco, M.S.; de Feo, F.; Santovito, E.; Fusco, V.; Maruccio, G. A Multipurpose Biochip for Food Pathogen Detection. *Anal. Methods* **2016**, *8*, 3055–3060. [[CrossRef](#)]
27. Hu, J.; Tang, F.; Wang, L.; Tang, M.; Jiang, Y.-Z.; Liu, C. Nanozyme Sensor Based-on Platinum-Decorated Polymer Nanosphere for Rapid and Sensitive Detection of *Salmonella typhimurium* with the Naked Eye. *Sens. Actuat. B-Chem.* **2021**, *346*, 130560. [[CrossRef](#)]
28. Liu, P.; Wang, Y.; Han, L.; Cai, Y.; Ren, H.; Ma, T.; Li, X.; Petrenko, V.A.; Liu, A. Colorimetric Assay of Bacterial Pathogens Based on Co₃O₄ Magnetic Nanozymes Conjugated with Specific Fusion Phage Proteins and Magnetophoretic Chromatography. *ACS Appl. Mater. Interfaces* **2020**, *12*, 9090–9097. [[CrossRef](#)]
29. Zheng, L.; Cai, G.; Qi, W.; Wang, S.; Wang, M.; Lin, J. Optical Biosensor for Rapid Detection of *Salmonella typhimurium* Based on Porous Gold@Platinum Nanocatalysts and a 3D Fluidic Chip. *ACS Sens.* **2020**, *5*, 65–72. [[CrossRef](#)]
30. Wang, Z.; Yao, X.; Zhang, Y.; Wang, R.; Ji, Y.; Sun, J.; Zhang, D.; Wang, J. Functional Nanozyme Mediated Multi-Readout and Label-Free Lateral Flow Immunoassay for Rapid Detection of *Escherichia coli* O157:H7. *Food Chem.* **2020**, *329*, 127224. [[CrossRef](#)]
31. Cheng, N.; Song, Y.; Zeinhom, M.M.A.; Chang, Y.-C.; Sheng, L.; Li, H.; Du, D.; Li, L.; Zhu, M.-J.; Luo, Y.; et al. Nanozyme-Mediated Dual Immunoassay Integrated with Smartphone for Use in Simultaneous Detection of Pathogens. *ACS Appl. Mater. Interfaces* **2017**, *9*, 40671–40680. [[CrossRef](#)] [[PubMed](#)]
32. Shen, Y.; Gao, X.; Zhang, Y.; Chen, H.; Ye, Y.; Wu, Y. Polydopamine-Based Nanozyme with Dual-Recognition Strategy-Driven Fluorescence-Colorimetric Dual-Mode Platform for *Listeria monocytogenes* Detection. *J. Hazard. Mater.* **2022**, *439*, 129582. [[CrossRef](#)] [[PubMed](#)]
33. Stephen Inbaraj, B.; Chen, B.H. Nanomaterial-Based Sensors for Detection of Foodborne Bacterial Pathogens and Toxins as Well as Pork Adulteration in Meat Products. *J. Food Drug Anal.* **2016**, *24*, 15–28. [[CrossRef](#)] [[PubMed](#)]
34. Karczmarczyk, A.; Reiner-Rozman, C.; Hageneder, S.; Dubiak-Szepietowska, M.; Dostálek, J.; Feller, K.-H. Fast and Sensitive Detection of Ochratoxin A in Red Wine by Nanoparticle-Enhanced SPR. *Anal. Chim. Acta* **2016**, *937*, 143–150. [[CrossRef](#)] [[PubMed](#)]
35. Nishimwe, K.; Wanjuki, I.; Karangwa, C.; Darnell, R.; Harvey, J. An Initial Characterization of Aflatoxin B1 Contamination of Maize Sold in the Principal Retail Markets of Kigali, Rwanda. *Food Control* **2017**, *73*, 574–580. [[CrossRef](#)]
36. Martinović, T.; Andjelković, U.; Gajdošik, M.Š.; Rešetar, D.; Josić, D. Foodborne Pathogens and Their Toxins. *J. Proteomics* **2016**, *147*, 226–235. [[CrossRef](#)]
37. Xu, Z.; Long, L.; Chen, Y.; Chen, M.-L.; Cheng, Y.-H. A Nanozyme-Linked Immunosorbent Assay Based on Metal-Organic Frameworks (MOFs) for Sensitive Detection of Aflatoxin B1. *Food Chem.* **2021**, *338*, 128039. [[CrossRef](#)]

38. Liu, W.; Gan, C.; Chang, W.; Qileng, A.; Lei, H.; Liu, Y. Double-Integrated Mimic Enzymes for the Visual Screening of Microcystin-LR: Copper Hydroxide Nanozyme and G-Quadruplex/Hemin DNAzyme. *Anal. Chim. Acta* **2019**, *1054*, 128–136. [[CrossRef](#)]
39. Lu, D.; Jiang, H.; Zhang, G.; Luo, Q.; Zhao, Q.; Shi, X. An In Situ Generated Prussian Blue Nanoparticle-Mediated Multimode Nanozyme-Linked Immunosorbent Assay for the Detection of Aflatoxin B1. *ACS Appl. Mater. Interfaces* **2021**, *13*, 25738–25747. [[CrossRef](#)]
40. Chen, M.; Liu, Z.; Guan, Y.; Chen, Y.; Liu, W.; Liu, Y. Zeolitic Imidazolate Frameworks-Derived Hollow Co/N-Doped CNTs as Oxidase-Mimic for Colorimetric-Fluorescence Immunoassay of Ochratoxin A. *Sens. Actuat. B-Chem.* **2022**, *359*, 131609. [[CrossRef](#)]
41. Zhu, H.; Cai, Y.; Qileng, A.; Quan, Z.; Zeng, W.; He, K.; Liu, Y. Template-Assisted Cu₂O@Fe(OH)₃ Yolk-Shell Nanocages as Biomimetic Peroxidase: A Multi-Colorimetry and Ratiometric Fluorescence Separated-Type Immunosensor for the Detection of Ochratoxin A. *J. Hazard. Mater.* **2021**, *411*, 125090. [[CrossRef](#)] [[PubMed](#)]
42. Tomer, V.; Sangha, J.K.; Ramya, H.G. Pesticide: An Appraisal on Human Health Implications. *Proc. Natl. Acad. Sci. India Sect. B Biol. Sci.* **2015**, *85*, 451–463. [[CrossRef](#)]
43. Singh, B.K. Organophosphorus-Degrading Bacteria: Ecology and Industrial Applications. *Nat. Rev. Microbiol.* **2009**, *7*, 156–164. [[CrossRef](#)] [[PubMed](#)]
44. Huang, Y.; Shi, T.; Luo, X.; Xiong, H.; Min, F.; Chen, Y.; Nie, S.; Xie, M. Determination of Multi-Pesticide Residues in Green Tea with a Modified QuEChERS Protocol Coupled to HPLC-MS/MS. *Food Chem.* **2019**, *275*, 255–264. [[CrossRef](#)] [[PubMed](#)]
45. Zhang, B.; Zhou, R.; Zhang, H.; Cai, D.; Lin, X.; Lang, Y.; Qiu, Y.; Shentu, X.; Ye, Z.; Yu, X. A Smartphone Colorimetric Sensor Based on Pt@Au Nanozyme for Visual and Quantitative Detection of Omethoate. *Foods* **2022**, *11*, 2900. [[CrossRef](#)]
46. Naveen Prasad, S.; Bansal, V.; Ramanathan, R. Detection of Pesticides Using Nanozymes: Trends, Challenges and Outlook. *TrAC-Trend Anal. Chem.* **2021**, *144*, 116429. [[CrossRef](#)]
47. Ge, J.; Yang, L.; Li, Z.; Wan, Y.; Mao, D.; Deng, R.; Zhou, Q.; Yang, Y.; Tan, W. A Colorimetric Smartphone-Based Platform for Pesticides Detection Using Fe-N/C Single-Atom Nanozyme as Oxidase Mimetics. *J. Hazard. Mater.* **2022**, *436*, 129199. [[CrossRef](#)]
48. He, L.; Jiang, Z.W.; Li, W.; Li, C.M.; Huang, C.Z.; Li, Y.F. In Situ Synthesis of Gold Nanoparticles/Metal-Organic Gels Hybrids with Excellent Peroxidase-Like Activity for Sensitive Chemiluminescence Detection of Organophosphorus Pesticides. *ACS Appl. Mater. Interfaces* **2018**, *10*, 28868–28876. [[CrossRef](#)]
49. Liang, X.; Han, L. White Peroxidase Mimicking Nanozymes: Colorimetric Pesticide Assay without Interferences of O₂ and Color. *Adv. Funct. Mater.* **2020**, *30*, 2001933. [[CrossRef](#)]
50. Liang, B.; Han, L. Displaying of Acetylcholinesterase Mutants on Surface of Yeast for Ultra-Trace Fluorescence Detection of Organophosphate Pesticides with Gold Nanoclusters. *Biosens. Bioelectron.* **2020**, *148*, 111825. [[CrossRef](#)]
51. Zhu, Y.; Wu, J.; Han, L.; Wang, X.; Li, W.; Guo, H.; Wei, H. Nanozyme Sensor Arrays Based on Heteroatom-Doped Graphene for Detecting Pesticides. *Anal. Chem.* **2020**, *92*, 7444–7452. [[CrossRef](#)] [[PubMed](#)]
52. Wu, D.; Du, D.; Lin, Y. Recent Progress on Nanomaterial-Based Biosensors for Veterinary Drug Residues in Animal-Derived Food. *TrAC-Trend Anal. Chem.* **2016**, *83*, 95–101. [[CrossRef](#)]
53. Wu, L.; Zhou, S.; Wang, G.; Yun, Y.; Liu, G.; Zhang, W. Nanozyme Applications: A Glimpse of Insight in Food Safety. *Front. Bioeng. Biotechnol.* **2021**. [[CrossRef](#)] [[PubMed](#)]
54. Wang, B.; Xie, K.; Lee, K. Veterinary Drug Residues in Animal-Derived Foods: Sample Preparation and Analytical Methods. *Foods* **2021**, *10*, 555. [[CrossRef](#)] [[PubMed](#)]
55. Li, Y.; Liu, S.; Yin, X.; Wang, S.; Tian, Y.; Shu, R.; Jia, C.; Chen, Y.; Sun, J.; Zhang, D.; et al. Nature-Inspired Nanozymes as Signal Markers for in-Situ Signal Amplification Strategy: A Portable Dual-Colorimetric Immunochromatographic Analysis Based on Smartphone. *Biosens. Bioelectron.* **2022**, *210*, 114289. [[CrossRef](#)]
56. Li, S.; Ma, X.; Pang, C.; Wang, M.; Yin, G.; Xu, Z.; Li, J.; Luo, J. Novel Chloramphenicol Sensor Based on Aggregation-Induced Electrochemiluminescence and Nanozyme Amplification. *Biosens. Bioelectron.* **2021**, *176*, 112944. [[CrossRef](#)]
57. Zeng, R.; Luo, Z.; Zhang, L.; Tang, D. Platinum Nanozyme-Catalyzed Gas Generation for Pressure-Based Bioassay Using Polyaniline Nanowires-Functionalized Graphene Oxide Framework. *Anal. Chem.* **2018**, *90*, 12299–12306. [[CrossRef](#)] [[PubMed](#)]
58. Tian, L.; Zhang, Y.; Wang, L.; Geng, Q.; Liu, D.; Duan, L.; Wang, Y.; Cui, J. Ratiometric Dual Signal-Enhancing-Based Electrochemical Biosensor for Ultrasensitive Kanamycin Detection. *ACS Appl. Mater. Interfaces* **2020**, *12*, 52713–52720. [[CrossRef](#)]
59. Briffa, J.; Sinagra, E.; Blundell, R. Heavy Metal Pollution in the Environment and Their Toxicological Effects on Humans. *Heliyon* **2020**, *6*, e04691. [[CrossRef](#)]
60. Liu, L.; Lin, H. Paper-Based Colorimetric Array Test Strip for Selective and Semiquantitative Multi-Ion Analysis: Simultaneous Detection of Hg²⁺, Ag⁺, and Cu²⁺. *Anal. Chem.* **2014**, *86*, 8829–8834. [[CrossRef](#)]
61. Fang, Y.; Pan, Y.; Li, P.; Xue, M.; Pei, F.; Yang, W.; Ma, N.; Hu, Q. Simultaneous Determination of Arsenic and Mercury Species in Rice by Ion-Pairing Reversed Phase Chromatography with Inductively Coupled Plasma Mass Spectrometry. *Food Chem.* **2016**, *213*, 609–615. [[CrossRef](#)] [[PubMed](#)]
62. Ebrahimi-Najafabadi, H.; Pasdaran, A.; Rezaei Bezenjani, R.; Bozorgzadeh, E. Determination of Toxic Heavy Metals in Rice Samples Using Ultrasound Assisted Emulsification Microextraction Combined with Inductively Coupled Plasma Optical Emission Spectroscopy. *Food Chem.* **2019**, *289*, 26–32. [[CrossRef](#)] [[PubMed](#)]
63. Fang, Y.; Zhang, Y.; Cao, L.; Yang, J.; Hu, M.; Pang, Z.; He, J. Portable Hg²⁺ Nanosensor with Ppt Level Sensitivity Using Nanozyme as the Recognition Unit, Enrichment Carrier, and Signal Amplifier. *ACS Appl. Mater. Interfaces* **2020**, *12*, 11761–11768. [[CrossRef](#)] [[PubMed](#)]

64. Mao, Y.; Gao, S.; Yao, L.; Wang, L.; Qu, H.; Wu, Y.; Chen, Y.; Zheng, L. Single-Atom Nanozyme Enabled Fast and Highly Sensitive Colorimetric Detection of Cr(VI). *J. Hazard. Mater.* **2021**, *408*, 124898. [[CrossRef](#)] [[PubMed](#)]
65. Cui, W.; Zhang, C.; Jiang, W.; Liang, R.; Wen, S.; Peng, D.; Qiu, J. Covalent Organic Framework Nanosheet-Based Ultrasensitive and Selective Colorimetric Sensor for Trace Hg²⁺ Detection. *ACS Sustain. Chem. Eng.* **2019**, *7*, 9408–9415. [[CrossRef](#)]
66. Zou, W.; Tang, Y.; Zeng, H.; Wang, C.; Wu, Y. Porous Co₃O₄ Nanodisks as Robust Peroxidase Mimetics in an Ultrasensitive Colorimetric Sensor for the Rapid Detection of Multiple Heavy Metal Residues in Environmental Water Samples. *J. Hazard. Mater.* **2021**, *417*, 125994. [[CrossRef](#)]
67. Song, G.; Zhang, Q.; Liang, S.; Yao, Y.; Feng, M.; Majid, Z.; He, X.; Huang, K.; Li, J.-C.; Cheng, N. Oxidation Activity Modulation of a Single Atom Ce-N-C Nanozyme Enabling a Time-Resolved Sensor to Detect Fe³⁺ and Cr⁶⁺. *J. Mater. Chem. C* **2022**. [[CrossRef](#)]
68. Huang, L.; Zhu, Q.; Zhu, J.; Luo, L.; Pu, S.; Zhang, W.; Zhu, W.; Sun, J.; Wang, J. Portable Colorimetric Detection of Mercury(II) Based on a Non-Noble Metal Nanozyme with Tunable Activity. *Inorg. Chem.* **2019**, *58*, 1638–1646. [[CrossRef](#)]
69. Carrocho, M.; Barreiro, M.F.; Morales, P.; Ferreira, I.C.F.R. Adding Molecules to Food, Pros and Cons: A Review on Synthetic and Natural Food Additives. *Compr. Rev. Food Sci. Food Saf.* **2014**, *13*, 377–399. [[CrossRef](#)]
70. Gagic, M.; Jamroz, E.; Krizkova, S.; Milosavljevic, V.; Kopel, P.; Adam, V. Current Trends in Detection of Histamine in Food and Beverages. *J. Agric. Food Chem.* **2019**, *67*, 773–783. [[CrossRef](#)]
71. Li, Q.; Ren, S.; Peng, Y.; Lv, Y.; Wang, W.; Wang, Z.; Gao, Z. A Colorimetric Strip for Rapid Detection and Real-Time Monitoring of Histamine in Fish Based on Self-Assembled Polydiacetylene Vesicles. *Anal. Chem.* **2020**, *92*, 1611–1617. [[CrossRef](#)] [[PubMed](#)]
72. Lehane, L.; Olley, J. Histamine Fish Poisoning Revisited. *Int. J. Food Microbiol.* **2000**, *58*, 1–37. [[CrossRef](#)] [[PubMed](#)]
73. Liao, C.; Jia, B.; Wang, H.; Sun, Y.; Xu, X.; Wei, X.; Shen, Y.; Lei, H.; Xu, Z.; Luo, L. Prussian Blue Nanoparticles-Enabled Sensitive and Accurate Ratiometric Fluorescence Immunoassay for Histamine. *Food Chem.* **2022**, *376*, 131907. [[CrossRef](#)] [[PubMed](#)]
74. Xu, S.; Wu, F.; Mu, F.; Dai, B. The Preparation of Fe-Based Peroxidase Mimetic Nanozymes and for the Electrochemical Detection of Histamine. *Electroanal. Chem.* **2022**, *908*, 116088. [[CrossRef](#)]
75. Wang, X.; Chen, Y.; Yu, R.; Wang, R.; Xu, Z. A Sensitive Biomimetic Enzyme-Linked Immunoassay Method Based on Au@Pt@Au Composite Nanozyme Label and Molecularly Imprinted Biomimetic Antibody for Histamine Detection. *Food Agr. Immunol.* **2021**, *32*, 592–605. [[CrossRef](#)]
76. Yue, R.; Lu, Q.; Zhou, Y. A Novel Nitrite Biosensor Based on Single-Layer Graphene Nanoplatelet-Protein Composite Film. *Biosens. Bioelectron.* **2011**, *26*, 4436–4441. [[CrossRef](#)]
77. Camargo, J.A.; Alonso, A.; Salamanca, A. Nitrate Toxicity to Aquatic Animals: A Review with New Data for Freshwater Invertebrates. *Chemosphere* **2005**, *58*, 1255–1267. [[CrossRef](#)]
78. Wang, M.; Zhu, H.; Liu, B.; Hu, P.; Pan, J.; Niu, X. Bifunctional Mn-Doped N-Rich Carbon Dots with Tunable Photoluminescence and Oxidase-Mimetic Activity Enabling Bimodal Ratiometric Colorimetric/Fluorometric Detection of Nitrite. *ACS Appl. Mater. Interfaces* **2022**, *14*, 44762–44771. [[CrossRef](#)]
79. Wang, M.; Zhao, M.; Liu, P.; Zhu, H.; Liu, B.; Hu, P.; Niu, X. Coupling Diazotization with Oxidase-Mimetic Catalysis to Realize Dual-Mode Double-Ratiometric Colorimetric and Electrochemical Sensing of Nitrite. *Sens. Actuat. B-Chem.* **2022**, *355*, 131308. [[CrossRef](#)]
80. Adegoke, O.; Zolotovskaya, S.; Abdolvand, A.; Daeid, N.N. Rapid and Highly Selective Colorimetric Detection of Nitrite Based on the Catalytic-Enhanced Reaction of Mimetic Au Nanoparticle-CeO₂ Nanoparticle-Graphene Oxide Hybrid Nanozyme. *Talanta* **2021**, *224*, 121875. [[CrossRef](#)]
81. Payal, A.; Krishnamoorthy, S.; Elumalai, A.; Moses, J.A.; Anandharamakrishnan, C. A Review on Recent Developments and Applications of Nanozymes in Food Safety and Quality Analysis. *Food Anal. Methods* **2021**, *14*, 1537–1558. [[CrossRef](#)]
82. Prabakaran, E.; Pandian, K. Amperometric Detection of Sudan I in Red Chili Powder Samples Using Ag Nanoparticles Decorated Graphene Oxide Modified Glassy Carbon Electrode. *Food Chem.* **2015**, *166*, 198–205. [[CrossRef](#)] [[PubMed](#)]
83. Mahmoudi-Moghaddam, H.; Tajik, S.; Beitollahi, H. Highly Sensitive Electrochemical Sensor Based on La³⁺-Doped Co₃O₄ Nanocubes for Determination of Sudan I Content in Food Samples. *Food Chem.* **2019**, *286*, 191–196. [[CrossRef](#)] [[PubMed](#)]
84. Ye, Q.; Chen, X.; Yang, J.; Wu, D.; Ma, J.; Kong, Y. Fabrication of CuO Nanoparticles-Decorated 3D N-Doped Porous Carbon as Electrochemical Sensing Platform for the Detection of Sudan I. *Food Chem.* **2019**, *287*, 375–381. [[CrossRef](#)]
85. Yu, X.; Lee, J.K.; Liu, H.; Yang, H. Synthesis of Magnetic Nanoparticles to Detect Sudan Dye Adulteration in Chilli Powders. *Food Chem.* **2019**, *299*, 125144. [[CrossRef](#)]
86. Kwon, D.; Lee, S.; Ahn, M.M.; Kang, I.S.; Park, K.-H.; Jeon, S. Colorimetric Detection of Pathogenic Bacteria Using Platinum-Coated Magnetic Nanoparticle Clusters and Magnetophoretic Chromatography. *Anal. Chim. Acta* **2015**, *883*, 61–66. [[CrossRef](#)]
87. Wang, K.-Y.; Bu, S.-J.; Ju, C.-J.; Li, C.-T.; Li, Z.-Y.; Han, Y.; Ma, C.-Y.; Wang, C.-Y.; Hao, Z.; Liu, W.-S.; et al. Hemin-Incorporated Nanoflowers as Enzyme Mimics for Colorimetric Detection of Foodborne Pathogenic Bacteria. *Bioorg. Med. Chem. Lett.* **2018**, *28*, 3802–3807. [[CrossRef](#)]
88. Cheng, N.; Zhu, C.; Wang, Y.; Du, D.; Zhu, M.-J.; Luo, Y.; Xu, W.; Lin, Y. Nanozyme Enhanced Colorimetric Immunoassay for Naked-Eye Detection of *Salmonella enteritidis*. *J. Anal. Test.* **2019**, *3*, 99–106. [[CrossRef](#)]
89. Farka, Z.; Čunderlová, V.; Horáčková, V.; Pastucha, M.; Mikušová, Z.; Hlaváček, A.; Skládal, P. Prussian Blue Nanoparticles as a Catalytic Label in a Sandwich Nanozyme-Linked Immunosorbent Assay. *Anal. Chem.* **2018**, *90*, 2348–2354. [[CrossRef](#)]

90. Wu, S.; Duan, N.; Qiu, Y.; Li, J.; Wang, Z. Colorimetric Aptasensor for the Detection of *Salmonella Enterica Serovar Typhimurium* Using ZnFe₂O₄-Reduced Graphene Oxide Nanostructures as an Effective Peroxidase Mimetics. *Int. J. Food Microbiol.* **2017**, *261*, 42–48. [[CrossRef](#)]
91. Liu, Y.; Wang, J.; Song, X.; Xu, K.; Chen, H.; Zhao, C.; Li, J. Colorimetric Immunoassay for *Listeria Monocytogenes* by Using Core Gold Nanoparticles, Silver Nanoclusters as Oxidase Mimetics, and Aptamer-Conjugated Magnetic Nanoparticles. *Microchim. Acta* **2018**, *185*, 1–7. [[CrossRef](#)] [[PubMed](#)]
92. Wu, L.; Zhou, M.; Wang, Y.; Liu, J. Nanozyme and Aptamer- Based Immunosorbent Assay for Aflatoxin B1. *J. Hazard. Mater.* **2020**, *399*, 123154. [[CrossRef](#)] [[PubMed](#)]
93. Peng, S.; Li, K.; Wang, Y.; Li, L.; Cheng, Y.-H.; Xu, Z. Porphyrin NanoMOFs as a Catalytic Label in Nanozyme-Linked Immunosorbent Assay for Aflatoxin B1 Detection. *Analytical Biochem.* **2022**, *655*, 114829. [[CrossRef](#)] [[PubMed](#)]
94. Ren, L.; Hong, F.; Zeng, L.; Chen, Y. “Three-in-One” Zr-MOF Multifunctional Carrier-Mediated Fluorescent and Colorimetric Dual-Signal Readout Biosensing Platform to Enhance Analytical Performance. *ACS Appl. Mater. Interfaces* **2022**, *14*, 51234–51243. [[CrossRef](#)] [[PubMed](#)]
95. Zhu, H.; Quan, Z.; Hou, H.; Cai, Y.; Liu, W.; Liu, Y. A Colorimetric Immunoassay Based on Cobalt Hydroxide Nanocages as Oxidase Mimics for Detection of Ochratoxin A. *Anal. Chim. Acta* **2020**, *1132*, 101–109. [[CrossRef](#)] [[PubMed](#)]
96. Zhao, Y.; Li, L.; Ma, R.; Wang, L.; Yan, X.; Qi, X.; Wang, S.; Mao, X. A Competitive Colorimetric Aptasensor Transduced by Hybridization Chain Reaction-Facilitated Catalysis of AuNPs Nanozyme for Highly Sensitive Detection of Saxitoxin. *Anal. Chim. Acta* **2021**, *1173*, 338710. [[CrossRef](#)]
97. Bagheri, N.; Khataee, A.; Hassanzadeh, J.; Habibi, B. Sensitive Biosensing of Organophosphate Pesticides Using Enzyme Mimics of Magnetic ZIF-8. *Spectrochim. Acta A* **2019**, *209*, 118–125. [[CrossRef](#)]
98. Weerathunge, P.; Ramanathan, R.; Shukla, R.; Sharma, T.K.; Bansal, V. Aptamer-Controlled Reversible Inhibition of Gold Nanozyme Activity for Pesticide Sensing. *Anal. Chem.* **2014**, *86*, 11937–11941. [[CrossRef](#)]
99. Wei, J.; Yang, L.; Luo, M.; Wang, Y.; Li, P. Nanozyme-Assisted Technique for Dual Mode Detection of Organophosphorus Pesticide. *Ecotox. Environ. Safte.* **2019**, *179*, 17–23. [[CrossRef](#)]
100. Wu, X.; Song, Y.; Yan, X.; Zhu, C.; Ma, Y.; Du, D.; Lin, Y. Carbon Quantum Dots as Fluorescence Resonance Energy Transfer Sensors for Organophosphate Pesticides Determination. *Biosens. Bioelectron.* **2017**, *94*, 292–297. [[CrossRef](#)]
101. Yan, X.; Song, Y.; Zhu, C.; Li, H.; Du, D.; Su, X.; Lin, Y. MnO₂ Nanosheet-Carbon Dots Sensing Platform for Sensitive Detection of Organophosphorus Pesticides. *Anal. Chem.* **2018**, *90*, 2618–2624. [[CrossRef](#)] [[PubMed](#)]
102. Satnami, M.L.; Korram, J.; Nagwanshi, R.; Vaishnav, S.K.; Karbhal, I.; Dewangan, H.K.; Ghosh, K.K. Gold Nanoprobe for Inhibition and Reactivation of Acetylcholinesterase: An Application to Detection of Organophosphorus Pesticides. *Sens. Actuat. B-Chem.* **2018**, *267*, 155–164. [[CrossRef](#)]
103. Luo, X.; Huang, G.; Bai, C.; Wang, C.; Yu, Y.; Tan, Y.; Tang, C.; Kong, J.; Huang, J.; Li, Z. A Versatile Platform for Colorimetric, Fluorescence and Photothermal Multi-Mode Glyphosate Sensing by Carbon Dots Anchoring Ferrocene Metal-Organic Framework Nanosheet. *J. Hazard. Mater.* **2023**, *443*, 130277. [[CrossRef](#)] [[PubMed](#)]
104. Zhang, Z.; Tian, Y.; Huang, P.; Wu, F.-Y. Using Target-Specific Aptamers to Enhance the Peroxidase-like Activity of Gold Nanoclusters for Colorimetric Detection of Tetracycline Antibiotics. *Talanta* **2020**, *208*, 120342. [[CrossRef](#)] [[PubMed](#)]
105. Sharma, T.K.; Ramanathan, R.; Weerathunge, P.; Mohammadtaheri, M.; Daima, H.K.; Shukla, R.; Bansal, V. Aptamer-Mediated ‘Turn-off/Turn-on’ Nanozyme Activity of Gold Nanoparticles for Kanamycin Detection. *Chem. Commun.* **2014**, *50*, 15856–15859. [[CrossRef](#)] [[PubMed](#)]
106. Pei, Y.; Zeng, L.; Wen, C.; Wu, K.; Deng, A.; Li, J. Detection of Enrofloxacin by Flow Injection Chemiluminescence Immunoassay Based on Cobalt Hydroxide Nanozyme. *Microchim. Acta* **2021**, *188*, 1–10. [[CrossRef](#)]
107. Song, Y.; Qiao, J.; Liu, W.; Qi, L. Norfloxacin Detection Based on the Peroxidase-like Activity Enhancement of Gold Nanoclusters. *Anal. Bioanal. Chem.* **2021**, *413*, 979–985. [[CrossRef](#)]
108. Ma, X.; Li, S.; Pang, C.; Xiong, Y.; Li, J. A Cu(II)-Anchored Unzipped Covalent Triazine Framework with Peroxidase-Mimicking Properties for Molecular Imprinting-Based Electrochemiluminescent Detection of Sulfaquinoxaline. *Microchim. Acta* **2018**, *185*, 546. [[CrossRef](#)]
109. Zhu, X.; Gao, L.; Tang, L.; Peng, B.; Huang, H.; Wang, J.; Yu, J.; Ouyang, X.; Tan, J. Ultrathin PtNi Nanozyme Based Self-Powered Photoelectrochemical Aptasensor for Ultrasensitive Chloramphenicol Detection. *Biosens. Bioelectron.* **2019**, *146*, 111756. [[CrossRef](#)]
110. Kora, A.J.; Rastogi, L. Peroxidase Activity of Biogenic Platinum Nanoparticles: A Colorimetric Probe towards Selective Detection of Mercuric Ions in Water Samples. *Sens. Actuat. B-Chem.* **2018**, *254*, 690–700. [[CrossRef](#)]
111. Lien, C.; Yu, P.; Chang, H.; Hsu, P.; Wu, T.; Lin, Y.; Huang, C.; Lai, J. DNA Engineered Copper Oxide-Based Nanocomposites with Multiple Enzyme-like Activities for Specific Detection of Mercury Species in Environmental and Biological Samples. *Anal. Chim. Acta* **2019**, *1084*, 106–115. [[CrossRef](#)] [[PubMed](#)]
112. Deng, H.; He, S.; Lin, X.; Yang, L.; Lin, Z.; Chen, R.; Peng, H.; Chen, W. Target-Triggered Inhibiting Oxidase-Mimicking Activity of Platinum Nanoparticles for Ultrasensitive Colorimetric Detection of Silver Ion. *Chinese Chem. Lett.* **2019**, *30*, 1659–1662. [[CrossRef](#)]
113. Wang, Y.; Wang, M.; Wang, L.; Xu, H.; Tang, S.; Yang, H.; Zhang, L.; Song, H. A Simple Assay for Ultrasensitive Colorimetric Detection of Ag⁺ at Picomolar Levels Using Platinum Nanoparticles. *Sensors* **2017**, *17*, 2521. [[CrossRef](#)] [[PubMed](#)]

114. Tang, Y.; Hu, Y.; Yang, Y.; Liu, B.; Wu, Y. A Facile Colorimetric Sensor for Ultrasensitive and Selective Detection of Lead(II) in Environmental and Biological Samples Based on Intrinsic Peroxidase-Mimic Activity of WS₂ Nanosheets. *Anal. Chim. Acta* **2020**, *1106*, 115–125. [[CrossRef](#)]
115. Xie, Z.; Shi, M.; Wang, L.; Peng, C.; Wei, X. Colorimetric Determination of Pb²⁺ Ions Based on Surface Leaching of Au@Pt Nanoparticles as Peroxidase Mimic. *Microchim. Acta* **2020**, *187*, 255. [[CrossRef](#)]
116. Hsu, C.; Lien, C.; Harroun, S.; Ravindranath, R.; Chang, H.; Mao, J.; Huang, C. Metal-Deposited Bismuth Oxide Nanonetworks with Tunable Enzyme-like Activity: Sensing of Mercury and Lead Ions. *Mater. Chem. Front.* **2017**, *1*, 893–899. [[CrossRef](#)]
117. Huang, H.; Li, M.; Hao, M.; Yu, L. (Lucy); Li, Y. A Novel Selective Detection Method for Sulfide in Food Systems Based on the GMP-Cu Nanozyme with Laccase Activity. *Talanta* **2021**, *235*, 122775. [[CrossRef](#)]
118. Liu, L.; Du, J.; Liu, W.; Guo, Y.; Wu, G.; Qi, W.; Lu, X. Enhanced His@AuNCs Oxidase-like Activity by Reduced Graphene Oxide and Its Application for Colorimetric and Electrochemical Detection of Nitrite. *Anal. Bioanal. Chem.* **2019**, *411*, 2189–2200. [[CrossRef](#)]
119. Wang, M.; Liu, P.; Zhu, H.; Liu, B.; Niu, X. Ratiometric Colorimetric Detection of Nitrite Realized by Stringing Nanozyme Catalysis and Diazotization Together. *Biosensors* **2021**, *11*, 280. [[CrossRef](#)]
120. He, H.; Sun, T.; Liu, W.; Xu, Z.; Han, Z.; Zhao, L.; Wu, X.; Ning, B.; Bai, J. Highly Sensitive Detection of Salbutamol by ALP-Mediated Plasmonic ELISA Based on Controlled Growth of AgNPs. *Microchem. J.* **2020**, *156*, 104804. [[CrossRef](#)]

Disclaimer/Publisher’s Note: The statements, opinions and data contained in all publications are solely those of the individual author(s) and contributor(s) and not of MDPI and/or the editor(s). MDPI and/or the editor(s) disclaim responsibility for any injury to people or property resulting from any ideas, methods, instructions or products referred to in the content.



Review

Towards Development of Molecularly Imprinted Electrochemical Sensors for Food and Drug Safety: Progress and Trends

Shuhong Zhou ^{1,†}, Chen Liu ^{2,†}, Jianguo Lin ¹, Zhi Zhu ³, Bing Hu ⁴ and Long Wu ^{1,3,*}

¹ Key Laboratory of Fermentation Engineering (Ministry of Education), College of Bioengineering and Food, Hubei University of Technology, Wuhan 430068, China; zhouwx777@163.com (S.Z.); jianguolin@hbut.edu.cn (J.L.)

² Leibniz-Institute of Photonic Technology, Leibniz Research Alliance-Leibniz Health Technologies, Albert-Einstein-Str. 9, 07745 Jena, Germany; chen.liu@leibniz-ipht.de

³ Key Laboratory of Tropical and Vegetables Quality and Safety for State Market Regulation, School of Food Science and Engineering, Hainan University, Haikou 570228, China; z0108150427@163.com

⁴ Key Laboratory of Biotechnology and Bioresources Utilization of Ministry of Education, School of Life Sciences, Dalian Minzu University, Dalian 116600, China; hubing19871121@163.com

* Correspondence: longquan.good@163.com

† These authors contribute equally to the work.

Abstract: Due to their advantages of good flexibility, low cost, simple operations, and small equipment size, electrochemical sensors have been commonly employed in food safety. However, when they are applied to detect various food or drug samples, their stability and specificity can be greatly influenced by the complex matrix. By combining electrochemical sensors with molecular imprinting techniques (MIT), they will be endowed with new functions of specific recognition and separation, which make them powerful tools in analytical fields. MIT-based electrochemical sensors (MIECs) require preparing or modifying molecularly imprinted polymers (MIPs) on the electrode surface. In this review, we explored different MIECs regarding the design, working principle and functions. Additionally, the applications of MIECs in food and drug safety were discussed, as well as the challenges and prospects for developing new electrochemical methods. The strengths and weaknesses of MIECs including low stability and electrode fouling are discussed to indicate the research direction for future electrochemical sensors.

Citation: Zhou, S.; Liu, C.; Lin, J.; Zhu, Z.; Hu, B.; Wu, L. Towards Development of Molecularly Imprinted Electrochemical Sensors for Food and Drug Safety: Progress and Trends. *Biosensors* **2022**, *12*, 369. <https://doi.org/10.3390/bios12060369>

Received: 28 April 2022

Accepted: 25 May 2022

Published: 27 May 2022



Copyright: © 2022 by the authors. Licensee MDPI, Basel, Switzerland. This article is an open access article distributed under the terms and conditions of the Creative Commons Attribution (CC BY) license (<https://creativecommons.org/licenses/by/4.0/>).

Keywords: electrochemical sensors; molecularly imprinted polymers; separation and detection; food safety; antibiotics detection

1. Introduction

Since food and drug safety are closely related to human health, it is essential to develop rapid and effective analytical methods to monitor food and drugs and control their safety. Electrochemical sensors are a class of chemical sensors in which an electrode is used as a transducer to give an electrochemical signal for analytes [1,2]. Most electrochemical sensors are small-sized devices with simple operations and rapid detection, which make them suitable for on-site applications and popular in the analysis of food and drugs [3,4]. However, electrochemical sensors suffer from some limitations when they are applied in food and drug detection: (1) it is difficult to achieve high sensitivity and accuracy due to the lack of effective standards for constructing the sensors; (2) the complex sample matrix has great effects on the stability and reproducibility of the electrochemical signal output. Therefore, there is a great need to improve electrochemical sensors to meet the requirements in food and drug safety detection.

To achieve higher performance of electrochemical sensors, numerous studies have been carried out, mainly including the development of new electrodes, modification of

electrodes, construction of detection modes, and design of signal labels [5–8]. To overcome the limitations associated with high costs and complex processing procedures of traditional electrodes (glassy carbon electrodes, silver, and gold electrodes, etc.), simple screen-printed electrodes [9], indium tin oxide (ITO) electrodes [10], paper-based electrodes [11] and micro-electrodes [12], have been developed in different applications. Usually, they cannot achieve desirable sensitivity due to their limited specific surface area. So, nanomaterials with various functions are widely used to modify the electrodes and improve detection sensitivity [13]. However, most of the modifications are performed by simply adsorbing the nanomaterials on the electrode surface to obtain a large specific surface area and efficient electron transfer rate [14,15], and the physical adsorption is not reliable enough to give stable signals, thus it will result in a low reproducibility in measurements. For the detection mode, different electrochemical sensors can be constructed according to the distinct receptors of enzymes, antibodies, and aptamers, including enzyme sensors, immunoassays, and DNA sensors, to meet the requirements of analytes in complex samples [16–19]. Commonly, the sensing structures are built by physical adsorption depending on the interaction of Van der Waals force between receptors and electrode surface, which readily gives rise to non-specific adsorption with weak adsorption, and thus could lead to a decrease in the overall stability of electrochemical sensors [20,21]. The last, but not least, electrochemical signal label is closely related to detection sensitivity and accuracy, and the design of the signal includes an electroactive substance and signal amplification strategy. To indicate analytes, various electroactive substances are used as electrochemical signals with signal amplification to improve detection sensitivity [22,23]. However, the single-signal output is prone to be influenced by external environmental interferences, so it is necessary to design the signals to eliminate the interferences and enhance the sensitivity.

The above-mentioned four aspects describe the electrochemical sensors from the development of the electrode to the design of the signal. Unfortunately, current work mainly focuses on improving one part of them but ignores the importance of studying the four aspects as a whole [24–26]. Since the electrode interface, recognition element and signal outputs are the unified whole of electrochemical sensors, it is difficult to achieve desired detection performance by only enhancing one part, either developing new electrodes or constructing a detection mode [27–29]. That is, only by considering mutual influences from different aspects, can it be possible to construct stable and reliable electrochemical sensing methods. The molecular imprinting technique (MIT) coupled with electrochemical sensors provides an opportunity to address the above concerns. As it is known that MIPs are characterized by predetermined structure-activity, specific recognition, and wide practicability [30,31]. As MIPs have specific recognition for target molecules, they can act as receptors to construct MIT-based electrochemical sensors (MIECs) with high specificity [32]. However, the relatively low adsorption capacity and mechanic properties of MIPs have become another challenge. It was reported that nanomaterials can effectively increase the specific surface area of MIPs and improve their conductivity, which makes MIECs more sensitive and stable [33,34]. Besides that, by adding nanomaterials such as gold nanoparticles (AuNP) into MIPs, they can provide an internal reference signal, and thus reduce the background interference [35]. In this regard, nanomaterials play a vital role in constructing MIECs with stable and accurate electrochemical signals.

Based on the above discussions, though MIECs suffer from the limitations such as low conductivity and stability, they are still one of the few sensors that can hopefully improve the detection performance in whole aspects. With careful design and modifications, the setbacks of MIECs can be overcome to a large extent. In general, MIECs can be regarded as new kinds of analytical methods that readily realize sensitive, specific, accurate and rapid detection, with the integrated improvement from electrodes to signals. This review summarizes all kinds of MIECs as well as the preparation of MIPs, design of electrochemical signals, functions of MIECs and applications in food and drug safety, aiming to present a general comment on the development of MIECs and make a bridge between MIPs and

electrochemical sensors (Figure 1). Furthermore, critical perspectives and discussions are given on the current progress and trends of MIECs and their application prospects.

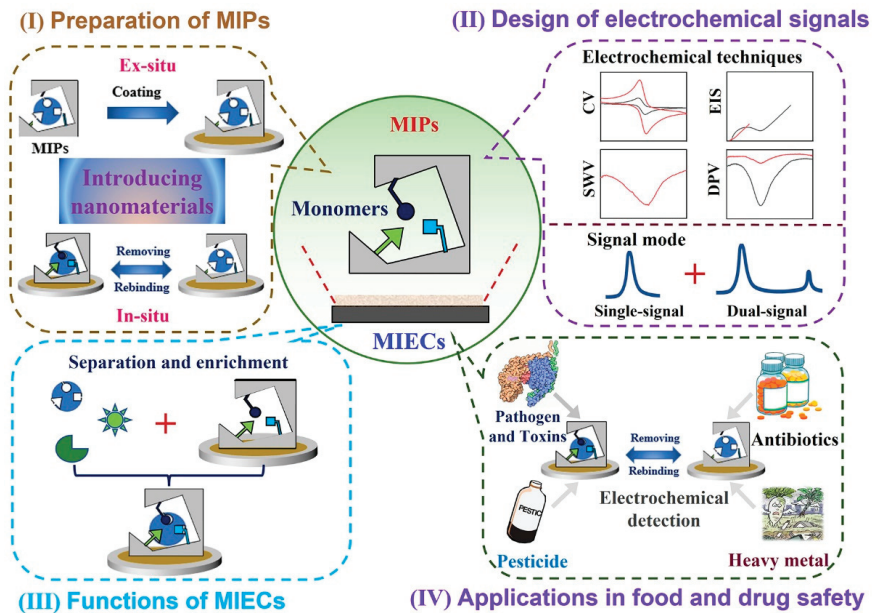


Figure 1. Schematic presentation of MIECs: (I) preparation of MIPs, (II) design of electrochemical signal, (III) functions of MIECs and (IV) applications in food and drug safety detection.

2. Brief Introduction of MIECs

2.1. Principle of MIECs

MIECs are integrated sensing techniques that use MIPs as recognition elements and electrochemical platforms as signal transducers (Figure 2). When the MIPs are well-prepared on the surface of the electrode, they can specifically recognize the analyte and indicate the molecular information (structure, concentration, conductivity, etc.) based on different electrochemical signals (CV for cyclic voltammetry, EIS for electrochemical impedance spectroscopy, SWV for Square-wave voltammetry, DPV for differential pulse voltammetry). As the analytes bind with MIPs, the direct detection can be achieved by the change in the state of MIPs or surface potential, which is due to a change in properties of the system without any electrodic reaction of analytes. As the specificity of MIPs towards analytes, the changes are only dependent on the amounts of analytes, and thus can be measured by the CV or EIS with variations of current or resistance. For example, Hedborg et al. reported the first MIPs-based capacitance sensor with capacitive or impedance detection, which is based on the principle of plate-capacitor with double layer phenomenon [36]. When analytes rebind with MIPs, the capacitance will vary with the concentration of analytes. This impedometric binding detection can be achieved by MIECs without the electrodic reaction of analytes.

Furthermore, if the analytes are electroactive substances, they will undergo an electrodic reaction when applied with an electrochemical technique such as SWV or DPV. By this means, the analytes will show a redox peak with a specific location. Moreover, the redox peak current will vary with the concentrations of analytes. In the label-free measurements, MIPs only act as receptors for the specific recognition with analytes. In a word, the MIECs combine the working principle of MIPs and that of electrochemical sensors to achieve detection specificity and sensitivity.

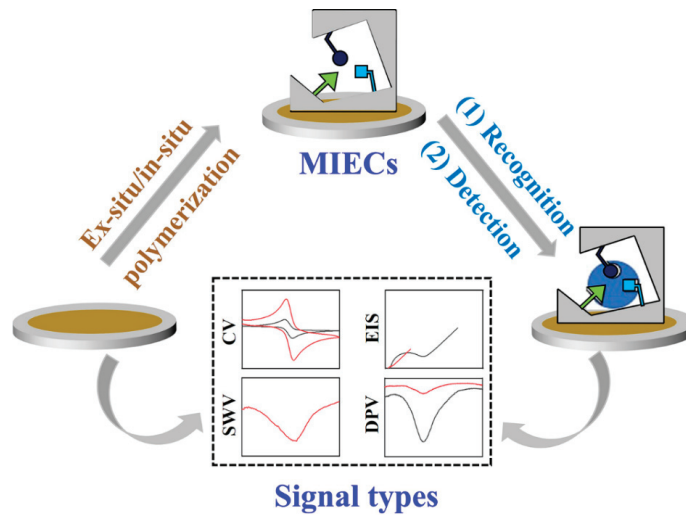


Figure 2. Illustration of working principle of MIECs from the preparation of MIPs to electrochemical signal output.

2.2. The Classification of MIECs

Since the electrochemical signals are output through the electrodes connected system, the electrodes used in MIECs can be varied with different applications. With the modification of MIPs on the electrode, either via an ex-situ or in-situ method, different kinds of electrodes vary in their functions. Besides the commonly used glass carbon electrode (GCE) and gold electrode, many other electrodes such as the ITO electrode, screen-printed electrode (SPE), and paper-based electrode are developed owing to the low cost and easy preparation. Thus, MIPs can be modified on different electrodes to achieve different operations. For example, on an ITO electrode, a researcher can conduct the surface pretreatment to make it more hydrophilicity prior to the MIPs modification [37]. However, for GCE or gold electrodes, it will be impossible because such operations can cause great damage to the electrodes. As most of the fundamental studies are completed via the GCE or gold electrode, we only introduce the MIECs based on the GCE or gold electrode operation system, so that the results can be compared under the same standard.

Regardless of the difference in electrodes, the MIECs can be divided into two groups according to different preparation methods of MIPs, which are (i) MIPs generated by an in-situ method such as electropolymerization of the monomer and (ii) the preformed MIPs will be coated on the electrode, also named as an ex-situ method [38,39]. For the in-situ method, MIPs can be directly obtained by electropolymerization without any processing requirement. The thickness of MIPs can be easily controlled by the applied current density and voltage. On the other hand, the ex-situ method for MIPs usually involves either spin-coating or spray-coating on the surface of the electrode as a thin film [40]. In the ex-situ approaches, preformed polymers on the surface of nanoparticles, especially the metallic nanoparticles are the widely used form, with the advantages of enhancing conductivity and mechanical stability.

2.3. The Construction of MIECs

MIECs are constructed by merging MIPs and electrochemical sensing platforms, and MIPs contribute to the function of specific recognition. Based on the electrode, MIPs are firstly synthesized through an ex-situ or in-situ polymerization method (Figure 3). Initiated by an inducer (catalyst, light, electricity, etc.), functional monomer produces polymers with molecule templates via covalent or non-covalent forces, and after polymerization of the crosslinker, the polymers are branded with the size and shape of template molecules [41,42].

After removing the template, the polymers remain at binding sites that are complementary to a template. By this means, a molecular memory is recorded by the polymer, in which the target molecule can rebind on the imprinted material with high specificity. Because of this, the MIPs can also be used in the sample pretreatment to separate and enrich the analytes.

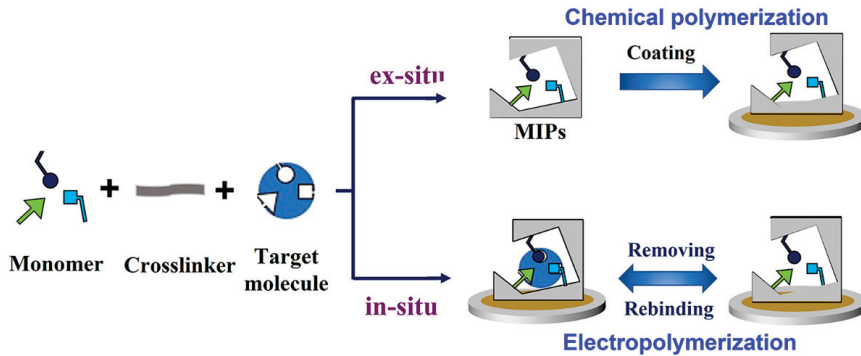


Figure 3. Schematic view of the construction of MECs through an ex-situ/in-situ method.

Usually, MIPs behave with relatively low conductivity and mechanical stability due to the poor electron transport rate (ETR) and soft structure of polymers [43]. To enhance the specific surface area of the electrode and accelerate the ETR, some metallic nanomaterials such as gold nanoparticles (AuNP) are widely adopted in MECs [44]. Prior to the polymerization, solid metallic nanoparticles are firstly modified on the electrode to provide a new substrate for polymers, so that ex-situ or in-situ prepared MIPs could have a rigid skeleton and a flexible surface, which are favorable for both their mechanical stability and recognition flexibility. Meanwhile, for the design of signal output, additional signal molecules can be introduced in the MIPs as an internal reference signal.

3. Applications of MIECs in Food Safety and Drug Detection

As a new kind of polymer material, MIPs have long been used in the field of analytical science. Compared with natural antibodies, MIPs can be easily modified and controllable in the affinity of receptor sites, which makes it more accessible to recognize different kinds of molecules, no matter small ones or big macromolecules [45,46]. In addition, MIPs show high stability, strong resistance to the environment and biocompatibility, which mean that they are of low cytotoxicity, and can be stored and used in harsh conditions, such as in low or high temperatures, extreme pH solutions, and strong ion strengths [47,48]. Because of their advantages, such as being lightweight, low-cost and easy to use, electrochemical sensors with a high diversity of electroanalytical techniques are expected to be the future generation of analytical systems. Taking the merits of MIPs and electrochemical sensors, MIECs behave promisingly in applications in food and drug safety detection (Figure 4).

3.1. Pathogen and Toxins

The ingestion of pathogen and toxin-contaminated food can cause severe illnesses, which pose a huge threat to human health [45,46]. A trace level of pathogen or toxin in the human body could inflict biological damage or even death [47]. Foodborne pathogens such as *Salmonella enterica*, *Listeria monocytogenes*, *Escherichia coli*, and *Staphylococcus aureus*, are responsible for poisoning food and water. Some mycotoxins produced by fungi, such as aflatoxins, fumonisins, ochratoxin A, and patulin can also induce physiological abnormalities in humans and animals, and most of them are tumorigenic [48,49]. Various analytical methods have been developed for the detection of pathogens and toxins in food samples, and MIECs have attracted much attention due to their high selectivity and sensitivity, as well as low cost and easy operation.

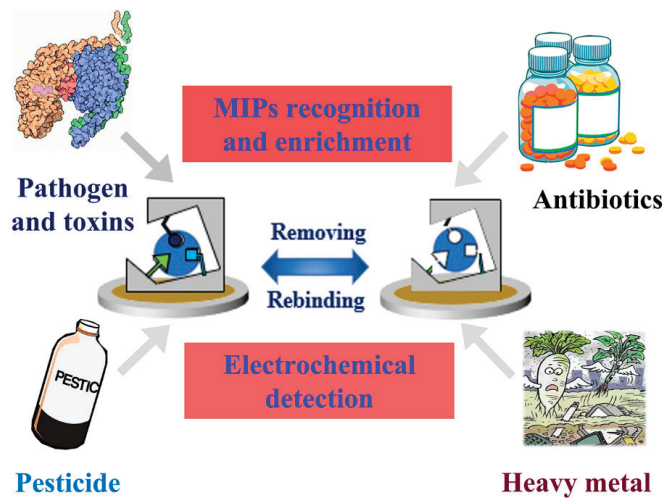


Figure 4. Schematic presentation of MIECs in the applications of food and drug safety detection.

For instance, Golabi et al. reported an electrochemical biosensor based on a whole-cell imprinting approach, which can deliver the rapid detection of *S. epidermidis* [50]. The cell-imprinted polymer with a boronic acid group endows a high affinity for bacteria, which was further used for the label-free detection of *S. epidermidis* via EIS with a linear response in the range of 10^3 – 10^7 CFU/mL. However, the presence of boronic acid groups will lead to non-specific absorption, making it less sensitive to the target. Thus, further studies can be carried out to eliminate the undesirable effects. Furthermore, Li et al. developed MIECs for *Listeria monocytogenes* (LM) based on 3-thiopheneacetic acid (TPA) as the functional monomer [51]. MIPs were prepared via the in-situ electropolymerization of TPA on the GCE surface in the presence of LM, which was denoted as LIP/GCE. In this case, $[\text{Fe}(\text{CN})_6]^{4-/3-}$ is used as a probe to indicate the amount of LM. When LM cells are captured by LIP/GCE, the imprinted cavity will be filled up with LM and the access of $[\text{Fe}(\text{CN})_6]^{4-/3-}$ to the electrode surface is blocked. As a result, the peak current of $[\text{Fe}(\text{CN})_6]^{4-/3-}$ decreases with the increasing LM concentration. Finally, the MIECs behaved at a low limit of detection (6 CFU/mL) and a wide linear range (10 to 10^6 CFU/mL).

In addition, Guo et al. constructed MIECs for the determination of patulin based on electropolymerization technology with modifications of carbon dots, chitosan, and Au NP [52]. Wherein, 2-oxindole was adopted as a template to replace patulin and form the molecularly imprinted cavity at a lower cost, and the modifiers were used to increase electroactive areas and acquire distinct signals. The MIECs showed a linear range from 1 pM to 1 nM with the limit of detection (LOD) of 0.757 pM. Munawar et al. fabricated an ex-situ MIPs for the electrochemical detection of fumonisin B₁ (FB₁) [53]. The MIPs were firstly prepared and then covalently attached to the working electrode. With the probing redox couple of $[\text{Fe}(\text{CN})_6]^{4-/3-}$, this sensor was allowed to detect FB₁ via the impedimetric or voltammetric technique. The EIS and DPV techniques behaved in a linear detection range from 1 fM to 10 pM with LODs of 0.03 and 0.7 fM, respectively.

With the aid of MIPs, MIECs can easily achieve specific and sensitive detection of pathogens and toxins in food samples. However, the cell imprinting strategy still suffers from partial non-specific recognition, which requires further improvement in the blotting templates and preparation methods. On the other hand, though the electropolymerization strategy is convenient to prepare MIPs, functionalized nanomaterials are still needed to enhance the conductive properties of the electrodes.

3.2. Pesticide Residue

Pesticides are favored in agriculture for crops and seed protection, as they help raise the output of agricultural products. Though the use of pesticides can produce significant market prospects and huge social benefits, the pesticide residues in food materials also have deleterious effects on human health [54,55]. Most of the used pesticides and their residues have long-term stability and biological effects due to their high persistence in the environment [56]. For months or years, the toxicity and potential carcinogenicity of the pesticide residues still exist [57,58]. So, the pesticide residues are easy to accumulate in the human body through the food chain. To ensure food safety for consumers, it is vital to develop sensitive and effective methods for pesticide residue detection. MIECs could be a potential candidate for pesticide residue monitoring.

As an instance, Dai et al. developed novel MIECs for selective and sensitive detection of imidacloprid residues [59]. With the strategy of dual-template molecularly imprinted polymers (DMIPs), two different templates and thionine (TH) were electropolymerized, and TH with redox peak acts as an internal signal. For the two templates, one is a non-electroactive template for a single signal, and another is an electroactive template for dual signals. Thus, non-electroactive bensulfuron-methyl (BSM) and electroactive imidacloprid (IMI) can be detected with different modes: the occupation of the imprinted cavities with BSM indicates a single-signal output of TH, and that of IMI shows an on-off ratiometric signal. By this means, the sensor behaved in wide linear ranges of 10 nM–10 μ M and 0.1 Mm–0.1 mM, with LODs of 7.8×10^{-9} M and 6.5×10^{-8} M for BSM and IMI, respectively. This study demonstrated the feasibility of DMIPs coupled with electrochemical techniques in the analysis of pesticide residues, which provided a new idea to construct selective MIECs for electroactive and non-electroactive template detection.

Based on Co₃O₄ nanowire and core-shell Co₃O₄@MOF-74 nanocomposite, Karimi-Maleh et al. developed a MIECs method for fenamiphos (FEN) analysis [60]. After the modification of nanocomposites on pretreated carbon electrodes, the preparation of MIPs was carried out by the in-situ electropolymerization with pyrrole as monomer and FEN as a template. The MIECs behaved in a linear detection range from 0.01 nM to 1.0 nM with a limit of quantification (LOQ) and LOD of 1.0×10^{-11} M and 3.0×10^{-12} M, respectively. Co₃O₄@MOF-74 nanocomposites provided a high surface area and fast electron transfer rate in the detection. However, the synthesis of nanocomposites with a high temperature may increase the cost, so it would be better to develop greener and more energy-efficient nanomaterials.

As discussed above, MIECs can achieve specific and sensitive detection of pesticides. Still, there are some limitations with MIECs. For example, with the popularization of pesticides, different pesticides often exist in one food sample. It is difficult for MIECs to detect multiple pesticides at the same time. Therefore, it can be an alternative to exploring the MIPs with diverse functional monomers.

3.3. Heavy Metal Ions

Heavy metal ions are commonly found in wastewater and classified as water pollutants. However, even in the soil, heavy metal ions are dangerous because they can be adsorbed by crops, fruits, and vegetables [61]. For instance, heavy metals such as mercury, lead, cadmium, chromium and arsenic are non-degradable and ubiquitously distributed, and they are considered hazardous compounds even at a low concentration [62]. With the intake of those heavy metal ions, people could suffer from enzyme inhibition, oxidative stress and impaired antioxidant metabolism [63]. Hence, it is critical to develop suitable techniques for the fast and accurate detection of metal ions. Most heavy metal ions are electrically active and highly susceptible to exchange electrons and produce characteristic electrochemical signals. MIECs can be the appropriate tool for the detection and quantification of heavy metal ions.

To impart selectivity of electrochemical sensors, modifiers with a strong affinity are commonly used to recognize target ions. For example, Motlagh et al. prepared a novel

nanostructured cadmium(II) ion-imprinted polymers (IIPs) by a sol-gel process [64]. For the preparation of Cd-IIP materials, an ex-situ surface imprinting strategy combined with a sol-gel process was adopted to fabricate the carbon paste electrode. The electrochemical sensor was employed for voltammetry detection of Cd(II) with a linear range of 0.5–40 $\mu\text{g L}^{-1}$ and LOD of 0.15 $\mu\text{g L}^{-1}$. Similarly, Sebastian et al. adopted Pb(II) ions as a template to prepare IIPs by modifying multiwalled carbon nanotubes (MWCNT) on Pt electrodes [65]. The sites imprinted in MWCNT/IIPs are highly selective to Pb(II) ions and the Pt electrode showed a sensitive response with the modified nanostructure. CV and DPV tests were conducted to discuss the features of the IIP electrochemical sensor. The sensing system behaved with an LOD of $2 \times 10^{-2} \mu\text{M}$ for Pb(II) ions, revealing promising applications in the detection of environmental and food samples.

Similar to MIPs, the IIPs can impart electrochemical techniques with selectivity and simplicity in the detection of real samples. However, IIPs may suffer some limitations including low binding capacity, irregular shape, poor target site accessibility, and heterogeneous binding site distributions. To avoid the limitations indicated, new technologies should be developed to prepare IIPs with good accessibility, high affinity, and selectivity to the target ions. Due to their high porosity, adjustable structures, and good stability, metal-organic frameworks (MOFs) can be used as efficient substrates to prepare IIPs and construct electrochemical sensors [66].

3.4. Antibiotics Monitoring

Antibiotics are a class of antimicrobial compounds that are widely used in human or veterinary medicine to treat diseases, especially in the livestock industry and aquaculture [67]. However, the abuse of antibiotics could result in sustainable adverse effects on human health and the environment. The constant intake of antibiotics could cause immunopathological effects, hepatotoxicity, carcinogenicity, bone marrow toxicity, reproductive disorders, or even anaphylactic shock [68]. When antibiotics enter the water and land environment, the cycle of water will make it a significant local point of contamination. The overdosage of antibiotics in animals can lead to antibiotic residues in foodstuffs such as meat, chicken, egg, milk, and fish [69]. Through the enrichment of the food chain or the transfer of water, the antibiotics will finally accumulate in the human body and pose potential risks to human health. Therefore, it is imperative to develop effective methods of monitoring the antibiotic residues.

Paracetamol (PR), a kind of analgesic, antipyretic and anti-inflammatory drug, and is one of the most commonly consumed pharmaceuticals. In a normal dose, PR does not produce any harmful side effects, however, overdose intake of the drug could cause pancreas inflammation or even kidney damage and hepatotoxicity [70]. For instance, Dai et al. reported MIECs for the detection of PR based on Prussian blue (PB) embedded MIPs as a reference signal [71]. Herein, the inner layer of PB acts as an internal electrochemical signal and the target PR as another signal. When PR molecules were captured and incorporated with the cavity on the outer layer of MIPs, the redox current of PR increased while that of PB decreased due to the occupied sites' blocked electron transfer, which finally manifested as an "on and off" signal output mode. As a result, the sensor displayed a concentration range from 1.0 nM to 0.1 mM with a LOD of 0.53 nM, as well as recoveries in the range between 94.6 and 104.9%, revealing it is acceptable in the practical applications.

Detection resolution has been identified as an important factor in newly developed analytical techniques, which reflect their ability to distinguish the details of analytes with similar structures. For instance, propranolol (prop), an important and widely used β -adrenaline antagonist for the treatment of cardiovascular diseases, has a similar chemical structure to salbutamol [72]. Moreover, prop has two enantiomers of S-prop and r-prop, and only S-prop has pharmacological performance. Based on the reduced graphene oxide (rGO) and chitosan-based MIPs, Liu et al. developed a differential potential ratio sensing platform for binary molecular recognition of prop [73]. In the platform, MIPs specifically recognize and capture prop enantiomers, rGO acts as a conductive substrate to produce an amplified

signal, and the potential difference between the R-/S-prop offers the ratiometric signal. As a result, the method gained a distinct potential difference of 135 mV with a detection range from 50 μM to 1000 μM in the racemic mixture, which reveals great potential in the fields of pharmacological detection and clinical analysis.

Chlorpromazine (CPZ) is an antipsychotic drug used to treat psychiatric and personality disorders, and clinical monitoring of CPZ is necessary. Liu et al. presented Pt/Co₃O₄ nanoparticles and methylene blue (MB) monomer-based MIPs for selective detection of CPZ [74]. Wherein, MB molecule in MIPs provides a fixed internal signal, and the signal of CPZ changes with concentrations, which is a typical on/off ratiometric signal output mode. Under optimal conditions, the method showed a linear range of 0.005–9 μM with a LOD of 2.6 nM and recoveries of 95.3–108.0% in pharmaceutical samples. The dual-signal output mode provides built-in signal calibration to eliminate interference and adjusts the signal fluctuation, thus can effectively improve detection stability and accuracy.

Besides food safety and drug detection, MIECs combined with nanomaterials have also shown good performance for the screening of biomarkers. As biomarkers are closely related to some diseases, it is important to achieve stable and sensitive detection of biomarkers for the early diagnosis. To fulfill the rapid screening, comprehensive procedures must be taken to treat the complex media, which usually involves preconcentration and separation. MIECs can take the role to realize the separation and detection at the same time. For example, Anirudhan et al. reported MIECs for the detection of 2-aminoadipic acid (2-AAA), a diabetes biomarker, based on the surface modification of electrode with a drop-casting method [75]. The modified MIP electrode showed good DPV results for 2-AAA with an LOD of 0.40×10^{-11} M, demonstrating the high selectivity and sensitivity of the MIECs for real sample analysis.

4. Discussion

MIECs are a class of newly developed sensing methods that combine the sensitivity of electrochemical techniques and the selectivity of MIPs. The most important part of constructing MIECs is to prepare MIPs-based electrodes, which can be regarded as a form of electrode modification with MIPs, which include the in-situ electropolymerization and ex-situ polymerization and modification. For the electropolymerization method, it can directly synthesize MIPs with electroactive monomers on the electrode by applying an appropriate potential or performing CV scans. On the other hand, the ex-situ modification of electrodes can be conducted by incubating preformed MIPs on the electrode surface, which can be more flexible to meet the requirements for different applications. However, the in-situ method can obtain an entire molecularly imprinted electrode without worrying about the shed of MIPs from the electrode, which means the in-situ MIPs could exhibit a more accurate and stable performance. In the detection process, redox products will be generated and get fouled on the electrode surface, which could block the reversibility of binding on the transducer surface. MIPs can decrease the foul of the electrode due to the analyte species being freely diffused in the pores or channels of MIPs.

According to the electrochemical properties of MIPs, different signals (CV, EIS, DPV, SWV, etc.) can be chosen to detect the analytes. To build different signal output modes, the detection strategies can be divided into a single signal and dual signals, and the dual-signal output mode includes on/off and on-off modes, which can provide a built-in correction factor to eliminate the interferences and improve stability. As the single signal readily changes with the external conditions, dual ratiometric signals are widely accepted as an effective strategy to improve the detection stability and accuracy. In fact, electrochemical detection is a process of surface reaction with the participation of electrons. In the presence of MIPs layers, analytes can be specifically recognized through the pores or channels and then detected with oxidized peaks. MIPs surface also acts as a film for recognition and reaction, which can be served as a platform for studying the mechanisms such as reaction kinetics.

This review mainly presented the MIECs from the preparation of MIPs to various applications. To better understand the performance of MIECs in different analytical fields, Table 1 summarized detection parameters such as relative standard derivation (RSD), linear detection range and LOD, revealing their good stability and sensitivity.

Table 1. Summary of MIECs methods in different applications (not given: N).

Type of Application	Test Target	R Value	RSD	Linear Range	LOD	References
Pathogen and toxins	<i>S. epidermidis</i>	0.9730	N	10^3 – 10^7 CFU/mL	7.5×10^{-8} M	[50]
	LM	N	N	10 – 10^6 CFU/mL	6 CFU/mL	[51]
	Patulin	0.9953	7.3%	1×10^{-12} – 1×10^{-9} M	7.57×10^{-13} M	[52]
	FB1	0.9899 0.9798	N N	1 fM–10 pM	0.03 fM 0.7 fM	[53]
Pesticide residue	IMI	0.9987	4.5%	1.0×10^{-7} – 1.0×10^{-4} M	6.5×10^{-8} M	[59]
	FEN	0.9995	N	1.0×10^{-11} – 1.0×10^{-9} M	3.0×10^{-12} M	[60]
Heavy metal ions	Cd(II)	0.9989	2.7%	0.5–40 $\mu\text{g L}^{-1}$	0.15 $\mu\text{g L}^{-1}$	[64]
	Pb(II)	0.9993	N	1–5 ppm	2×10^{-2} μM	[65]
Antibiotics monitoring	PR	N	1.2%	1.0 nM–0.1 mM	0.53 nM	[71]
	s/r-Prop	N	N	50 μM –1000 μM	N	[73]
	CPZ	0.9981	0.94%	0.005–9 μM	2.6 nM	[74]

5. Conclusions

This review specified recent advances and applications of several newly developed MIECs in food and drug safety. A growing number of research papers related to MIECs demonstrate that MIPs coupled with electrochemical sensors outcompete traditional electrochemical sensors in selectivity and stability. MIPs have been successfully prepared on electrodes to specifically capture analytes with electrochemical signals. Meanwhile, the MIP techniques can achieve one step of separation and detection with simple procedures and easy operations. In addition to MIPs preparation, the signal output can be designed to obtain enhanced detection robustness. For example, the dual-signal output mode is widely used as an effective strategy to avoid signal fluctuation, and thus can improve detection performance such as anti-jamming ability and reproducibility. In this regard, MIECs open a new avenue to enhance the detection performance of traditional electrochemical methods.

Despite significant breakthroughs in the design and construction of MIECs, it still remains a great challenge to make MIECs a powerful tool to meet the requirements in practical applications. For instance, the molecularly imprinted electrodes are still prone to fouling, and their surfaces are difficult to strip for further use. Furthermore, the detection mode is still dependent on the traditional electrode system, which makes it difficult to achieve effective and high-throughput detection. At present, there is no widely accepted standard in practice for constructing electrochemical sensors, so the detection reproducibility could not be guaranteed. To overcome these limitations, the preparation of MIPs must be improved to obtain a more homogeneously binding site population with a high affinity for the target analyte. It can be another way to break the limitations by merging MIECs with nanotechnology to construct new nanobiosensors [76]. It is urgent to improve the protocols of MIECs with specificity, selectivity, and sensitivity in commercial applications. As the electrochemically synthesized MIPs are complex and versatile, it is also important to study the mechanism and set common criteria for the preparations. Considerable effort has been devoted to dealing with the above problems. We believe that in the near future, the limitations of MIECs will be successfully addressed and the MIECs will occupy an important position in the sensor market.

Author Contributions: Conceptualization, L.W. and J.L.; methodology, S.Z.; software, C.L.; validation, Z.Z., L.W. and S.Z.; formal analysis, L.W.; investigation, C.L.; resources, L.W.; data curation, B.H.; writing—original draft preparation, S.Z.; writing—review and editing, L.W.; visualization, B.H.; supervision, L.W.; project administration, J.L.; funding acquisition, L.W. All authors have read and agreed to the published version of the manuscript.

Funding: This work was supported by the Hainan Provincial Natural Science Foundation of China (321QN183), the National Natural Science Foundation of China (31801638), the Fund of Key Laboratory of Fermentation Engineering (Ministry of Education) (202105FE09), Hainan University Start-up Scientific Research Projects of China (KYQD(ZR)-21044), and Key Laboratory of Tropical Fruits and Vegetables Quality and Safety for State Market Regulation (ZX-2022001), the specific research fund of The Innovation Platform for Academicians of Hainan Province (YSPTZX202152), Liaoning province livelihood science and technology project (2021JH2/10200019), and Dalian key science and technology project (2021JB12SN038).

Institutional Review Board Statement: Not applicable.

Informed Consent Statement: Not applicable.

Conflicts of Interest: The authors declare no conflict of interest.

References

- Mahato, K.; Wang, J. Electrochemical sensors: From the bench to the skin. *Sens. Actuators B Chem.* **2021**, *344*, 130178. [\[CrossRef\]](#)
- Wu, L.; Zhang, C.; Long, Y.; Chen, Q.; Zhang, W.; Liu, G. Food additives: From functions to analytical methods. *Crit. Rev. Food Sci. Nutr.* **2021**, *611*–621. [\[CrossRef\]](#) [\[PubMed\]](#)
- Cho, I.-H.; Kim, D.H.; Park, S. Electrochemical biosensors: Perspective on functional nanomaterials for on-site analysis. *Biomater. Res.* **2020**, *24*, 1–12. [\[CrossRef\]](#)
- Dong, X.; Xie, S.; Zhu, J.; Liu, H.; Zhao, Y.; Ni, T.; Wu, L.; Zhu, Y. Mesoporous CoOx/C Nanocomposites Functionalized Electrochemical Sensor for Rapid and Continuous Detection of Nitrite. *Coatings* **2021**, *11*, 596. [\[CrossRef\]](#)
- Ding, R.; Cheong, Y.H.; Ahamed, A.; Lisak, G. Heavy Metals Detection with Paper-Based Electrochemical Sensors. *Anal. Chem.* **2021**, *93*, 1880–1888. [\[CrossRef\]](#)
- Tajik, S.; Beitollahi, H.; Ahmadi, S.A.; Askari, M.B.; Di Bartolomeo, A. Screen-printed electrode surface modification with NiCo₂O₄/RGO nanocomposite for hydroxylamine detection. *Nanomaterials* **2021**, *11*, 3208. [\[CrossRef\]](#)
- Wu, L.; Wang, Y.; Zhou, S.; Zhu, Y.; Chen, X. Enzyme-induced Cu²⁺/Cu⁺ conversion as the electrochemical signal for sensitive detection of ethyl carbamate. *Anal. Chim. Acta* **2021**, *1151*, 338256. [\[CrossRef\]](#)
- Wu, L.; Ding, F.; Yin, W.; Ma, J.; Wang, B.; Nie, A.; Han, H. From Electrochemistry to Electroluminescence: Development and Application in a Ratiometric Aptasensor for Aflatoxin B1. *Anal. Chem.* **2017**, *89*, 7578–7585. [\[CrossRef\]](#)
- Costa-Rama, E.; Fernández-Abedul, M.T. Paper-Based screen-printed electrodes: A new generation of low-cost electroanalytical platforms. *Biosensors* **2021**, *11*, 51. [\[CrossRef\]](#)
- El-Said, W.A.; Al-Bogami, A.S.; Alshitari, W. Synthesis of gold nanoparticles@ reduced porous graphene-modified ITO electrode for spectroelectrochemical detection of SARS-CoV-2 spike protein. *Spectrochim. Acta Part A Mol. Biomol. Spectrosc.* **2022**, *264*, 120237. [\[CrossRef\]](#)
- Lu, Q.; Su, T.; Shang, Z.; Jin, D.; Shu, Y.; Xu, Q.; Hu, X. Flexible paper-based Ni-MOF composite/AuNPs/CNTs film electrode for HIV DNA detection. *Biosens. Bioelectron.* **2021**, *184*, 113229. [\[CrossRef\]](#)
- Daly, R.; Narayan, T.; Shao, H.; O’Riordan, A.; Lovera, P. Platinum-Based Interdigitated Micro-Electrode Arrays for Reagent-Free Detection of Copper. *Sensors* **2021**, *21*, 3544. [\[CrossRef\]](#) [\[PubMed\]](#)
- Tajik, S.; Orooji, Y.; Ghazanfari, Z.; Karimi, F.; Beitollahi, H.; Varma, R.S.; Jang, H.W.; Shokouhimehr, M. Nanomaterials modified electrodes for electrochemical detection of Sudan I in food. *J. Food Meas. Charact.* **2021**, *15*, 3837–3852. [\[CrossRef\]](#)
- Wu, L.; Luo, Y.; Liu, C.; Li, J.; Li, D. Highly Adjustable Three-Dimensional Hollow Pt(Au)Cu Nanonetwork Structures as Enhancing Electrocatalysts for Alcohol Oxidation Reaction. *J. Electrochem. Soc.* **2020**, *167*, 066518. [\[CrossRef\]](#)
- Chen, Y.; Liu, B.; Chen, Z.; Zuo, X. Innovative Electrochemical Sensor Using TiO₂ Nanomaterials to Detect Phospho-peptides. *Anal. Chem.* **2021**, *93*, 10635–10643. [\[CrossRef\]](#) [\[PubMed\]](#)
- Wu, L.; Yan, H.; Wang, J.; Liu, G.; Xie, W. Tyrosinase incorporated with Au-Pt@ SiO₂ nanospheres for electrochemical detection of bisphenol A. *J. Electrochem. Soc.* **2019**, *166*, B562. [\[CrossRef\]](#)
- Ranjan, P.; Singhal, A.; Yadav, S.; Kumar, N.; Murali, S.; Sanghi, S.K.; Khan, R. Rapid diagnosis of SARS-CoV-2 using potential point-of-care electrochemical immunosensor: Toward the future prospects. *Int. Rev. Immunol.* **2021**, *40*, 126–142. [\[CrossRef\]](#)
- Wu, L.; Yin, W.; Tang, K.; Li, D.; Shao, K.; Zuo, Y.; Han, H. Enzymatic biosensor of horseradish peroxidase immobilized on Au-Pt nanotube/Au-graphene for the simultaneous determination of antioxidants. *Anal. Chim. Acta* **2016**, *933*, 89–96. [\[CrossRef\]](#)
- Elugoke, S.E.; Adekunle, A.S.; Fayemi, O.E.; Akpan, E.D.; Mamba, B.B.; Sherif, E.M.; Ebenso, E.E. Molecularly imprinted polymers (MIPs) based electrochemical sensors for the determination of catecholamine neurotransmitters—Review. *Electrochem. Sci. Adv.* **2021**, *1*, e2000026. [\[CrossRef\]](#)

20. Wu, L.; Li, G.; Xu, X.; Zhu, L.; Huang, R.; Chen, X. Application of nano-ELISA in food analysis: Recent advances and challenges. *TrAC Trends Anal. Chem.* **2019**, *113*, 140–156. [[CrossRef](#)]
21. Qureshi, S.; Asif, M.; Sajid, H.; Gilani, M.A.; Ayub, K.; Mahmood, T. First-principles study for electrochemical sensing of neurotoxin hydrazine derivatives via hg-C3N4 quantum dot. *Surf. Interfaces* **2022**, 30101913.
22. Chen, Q.; Yao, C.; Yang, C.; Liu, Z.; Wan, S. Development of an in-situ signal amplified electrochemical assay for de-tECTION of *Listeria monocytogenes* with label-free strategy. *Food Chem.* **2021**, *358*, 129894. [[CrossRef](#)] [[PubMed](#)]
23. Xie, J.; Cheng, D.; Li, P.; Xu, Z.; Zhu, X.; Zhang, Y.; Yao, S. Au/Metal–Organic Framework Nanocapsules for Elec-trochemical Determination of Glutathione. *ACS Appl. Nano Mater.* **2021**, *4*, 4853–4862. [[CrossRef](#)]
24. Isailović, J.; Vidović, K.; Hočevar, S.B. Simple electrochemical sensors for highly sensitive detection of gaseous hydrogen peroxide using polyacrylic-acid-based sensing membrane. *Sens. Actuators B Chem.* **2022**, *352*, 131053. [[CrossRef](#)]
25. Oberhaus, F.V.; Frense, D. Catalysing electropolymerization: High-quality polythiophene films for electrochemical sensors by the utilization of fluorine based Lewis acid catalysts. *Electrochim. Acta* **2022**, *402*, 139536. [[CrossRef](#)]
26. Wu, L.; Zhou, S.; Wang, G.; Yun, Y.; Liu, G.; Zhang, W. Nanozyme Applications: A Glimpse of Insight in Food Safety. *Front. Bioeng. Biotechnol.* **2021**, *9*, 727886. [[CrossRef](#)]
27. Meng, T.; Zhao, D.; Ye, H.; Feng, Y.; Wang, H.; Zhang, Y. Construction of an ultrasensitive electrochemical sensing platform for microRNA-21 based on interface impedance spectroscopy. *J. Colloid Interface Sci.* **2020**, *578*, 164–170. [[CrossRef](#)]
28. Castle, L.M.; Schuh, D.A.; Reynolds, E.E.; Furst, A.L. Electrochemical Sensors to Detect Bacterial Foodborne Pathogens. *ACS Sens.* **2021**, *6*, 1717–1730. [[CrossRef](#)]
29. Huang, S.; Zhang, L.; Dai, L.; Wang, Y.; Tian, Y. Nonenzymatic Electrochemical Sensor with Ratiometric Signal Output for Selective Determination of Superoxide Anion in Rat Brain. *Anal. Chem.* **2021**, *93*, 5570–5576. [[CrossRef](#)]
30. Zhu, Y.; Wu, L.; Yan, H.; Lu, Z.; Yin, W.; Han, H. Enzyme induced molecularly imprinted polymer on SERS substrate for ultrasensitive detection of patulin. *Anal. Chim. Acta* **2020**, *1101*, 111–119. [[CrossRef](#)]
31. Wu, L.; Yan, H.; Li, G.; Xu, X.; Zhu, L.; Chen, X.; Wang, J. Surface-Imprinted Gold Nanoparticle-Based Surface-Enhanced Raman Scattering for Sensitive and Specific Detection of Patulin in Food Samples. *Food Anal. Methods* **2019**, *12*, 1648–1657. [[CrossRef](#)]
32. Lahcen, A.A.; Amine, A. Recent Advances in Electrochemical Sensors Based on Molecularly Imprinted Polymers and Nanomaterials. *Electroanalysis* **2019**, *31*, 188–201. [[CrossRef](#)]
33. Ann Maria, C.G.; Anitha, V.; Nidhin, M. Recent Advances in Nanomaterials Based Molecularly Imprinted Electrochemical Sensors. *Crit. Rev. Anal. Chem.* **2021**, *51*, 1–10.
34. Motia, S.; Bouchikhi, B.; Llobet, E.; El Bari, N. Synthesis and characterization of a highly sensitive and selective elec-trochemical sensor based on molecularly imprinted polymer with gold nanoparticles modified screen-printed electrode for glycerol determination in wastewater. *Talanta* **2020**, *216*, 120953. [[CrossRef](#)] [[PubMed](#)]
35. Sarpong, K.A.; Zhang, K.; Luan, Y.; Cao, Y.; Xu, W. Development and application of a novel electrochemical sensor based on AuNPS and difunctional monomer-MIPs for the selective determination of Tetrabromobisphenol-S in water samples. *Microchem. J.* **2020**, *154*, 104526. [[CrossRef](#)]
36. Hedborg, E.; Winquist, F.; Lundström, I.; Andersson, L.I.; Mosbach, K. Some studies of molecularly-imprinted polymer membranes in combination with field-effect devices. *Sens. Actuators A Phys.* **1993**, *37*, 796–799. [[CrossRef](#)]
37. Aydın, E.B.; Aydın, M.; Sezgintürk, M.K. Fabrication of electrochemical immunosensor based on acid-substituted poly(pyrrole) polymer modified disposable ITO electrode for sensitive detection of CCR4 cancer biomarker in human serum. *Talanta* **2021**, *222*, 121487. [[CrossRef](#)]
38. Kaya, H.K.; Cinar, S.; Altundal, G.; Bayramli, Y.; Unaleroglu, C.; Kuralay, F. A novel design thia-bilane structure-based molecular imprinted electrochemical sensor for sensitive and selective dopamine determination. *Sens. Actuators B Chem.* **2021**, *346*, 130425. [[CrossRef](#)]
39. Dechtrirat, D.; Sookcharoenpinyo, B.; Prajongtat, P.; Sriprachuabwong, C.; Sanguankiat, A.; Tuantranont, A.; Han-nongbua, S. An electrochemical MIP sensor for selective detection of salbutamol based on a graphene/PEDOT: PSS modi-fied screen printed carbon electrode. *RSC Adv.* **2018**, *8*, 206–212. [[CrossRef](#)]
40. Petrucci, E.; Orsini, M.; Porcelli, F.; De Santis, S.; Sotgiu, G. Effect of Spin Coating Parameters on the Electrochemical Properties of Ruthenium Oxide Thin Films. *Electrochem* **2021**, *2*, 83–94. [[CrossRef](#)]
41. He, S.; Zhang, L.; Bai, S.; Yang, H.; Cui, Z.; Zhang, X.; Li, Y. Advances of molecularly imprinted polymers (MIP) and the application in drug delivery. *Eur. Polym. J.* **2020**, *143*, 110179. [[CrossRef](#)]
42. Kadhem, A.J.; Gentile, G.J.; Fidalgo de Cortalezzi, M.M. Molecularly Imprinted Polymers (MIPs) in Sensors for Envi-ronmental and Biomedical Applications: A Review. *Molecules* **2021**, *26*, 6233. [[CrossRef](#)] [[PubMed](#)]
43. Zhang, Y.; Zhang, W.; Zhang, L.; Song, G.; Wang, N.; Xu, W.; Huang, W. A molecularly imprinted electrochemical BPA sensor based on multi-walled carbon nanotubes modified by CdTe quantum dots for the detection of bisphenol A. *Microchem. J.* **2021**, *170*, 106737. [[CrossRef](#)]
44. Rezaei, F.; Ashraf, N.; Zohuri, G.H.; Arbab-Zavar, M.H. Water-compatible synthesis of core-shell polysilicate molecularly imprinted polymer on polyvinylpyrrolidone capped gold nanoparticles for electrochemical sensing of uric acid. *Microchem. J.* **2022**, *177*, 107312. [[CrossRef](#)]
45. Alahi, M.E.E.; Mukhopadhyay, S.C. Detection methodologies for pathogen and toxins: A review. *Sensors* **2017**, *17*, 1885. [[CrossRef](#)]

46. Anal, A.K.; Koirala, S.; Shrestha, S. Gut Microbiome and Their Possible Roles in Combating Mycotoxins. In *Mycotoxins Food Beverages*; CRC Press: Boca Raton, FL, USA, 2021; pp. 213–235. [[CrossRef](#)]
47. Banerji, R.; Karkee, A.; Kanojija, P.; Saroj, S.D. Pore-forming toxins of foodborne pathogens. *Compr. Rev. Food Sci. Food Saf.* **2021**, *20*, 2265–2285. [[CrossRef](#)]
48. Hatta, M.; Hanif, E.M.; Chin, S.-F.; Neoh, H.-M. Pathogens and Carcinogenesis: A Review. *Biology* **2021**, *10*, 533. [[CrossRef](#)]
49. Wu, L.; Zhou, M.; Wang, Y.; Liu, J. Nanozyme and aptamer-based immunosorbent assay for aflatoxin B1. *Hazard. Mater.* **2020**, *399*, 123154. [[CrossRef](#)]
50. Golabi, M.; Kuralay, F.; Jager, E.W.; Beni, V.; Turner, A.P. Electrochemical bacterial detection using poly(3-aminophenylboronic acid)-based imprinted polymer. *Biosens. Bioelectron.* **2017**, *93*, 87–93. [[CrossRef](#)]
51. Li, Q.; Guo, Z.; Qiu, X.; Lu, W.; Yang, W.; Wang, Q.; Wu, Q. Simple electrochemical detection of *Listeria monocytogenes* based on a surface-imprinted polymer-modified electrode. *Anal. Methods* **2021**, *13*, 4864–4870. [[CrossRef](#)]
52. Guo, W.; Pi, F.; Zhang, H.; Sun, J.; Zhang, Y.; Sun, X. A novel molecularly imprinted electrochemical sensor modified with carbon dots, chitosan, gold nanoparticles for the determination of patulin. *Biosens. Bioelectron.* **2017**, *98*, 299–304. [[CrossRef](#)] [[PubMed](#)]
53. Munawar, H.; Garcia-Cruz, A.; Majewska, M.; Karim, K.; Kutner, W.; Piletsky, S.A. Electrochemical determination of fumonisin B1 using a chemosensor with a recognition unit comprising molecularly imprinted polymer nanoparticles. *Sens. Actuators B Chem.* **2020**, *321*, 128552. [[CrossRef](#)]
54. Ferdous, Z.; Zulfiqar, F.; Datta, A.; Hasan, A.K.; Sarker, A. Potential and challenges of organic agriculture in Bangla-desh: A review. *J. Crop Improv.* **2021**, *35*, 403–426. [[CrossRef](#)]
55. Cioffi, A.; Mancini, M.; Gioia, V.; Cinti, S. Office Paper-Based Electrochemical Strips for Organophosphorus Pesticide Monitoring in Agricultural Soil. *Environ. Sci. Technol.* **2021**, *55*, 8859–8865. [[CrossRef](#)] [[PubMed](#)]
56. Pérez-Fernández, B.; Mercader, J.V.; Checa-Orrego, B.I.; De La Escosura-Muñiz, A.; Costa-García, A. A monoclonal antibody-based immunosensor for the electrochemical detection of imidacloprid pesticide. *Analyst* **2019**, *144*, 2936–2941. [[CrossRef](#)] [[PubMed](#)]
57. Tu, X.; Gao, F.; Ma, X.; Zou, J.; Yu, Y.; Li, M.; Qu, F.; Huang, X.; Lu, L. Mxene/carbon nanohorn/ β -cyclodextrin-Metal-organic frame-works as high-performance electrochemical sensing platform for sensitive detection of carbendazim pesticide. *J. Hazard. Mater.* **2020**, *396*, 122776. [[CrossRef](#)]
58. Zhao, Y.; Zheng, X.; Wang, Q.; Zhe, T.; Bai, Y.; Bu, T.; Zhang, M.; Wang, L. Electrochemical behavior of reduced graphene oxide/cyclodextrins sensors for ultrasensitive detection of imidacloprid in brown rice. *Food Chem.* **2020**, *333*, 127495. [[CrossRef](#)]
59. Dai, Y.; Kan, X. From non-electroactive to electroactive species: Highly selective and sensitive detection based on a dual-template molecularly imprinted polymer electrochemical sensor. *Chem. Commun.* **2017**, *53*, 11755–11758. [[CrossRef](#)]
60. Karimi-Maleh, H.; Yola, M.L.; Atar, N.; Orooji, Y.; Karimi, F.; Kumar, P.S.; Rouhi, J.; Baghayeri, M. A novel detection method for organophosphorus insecticide fenamiphos: Molecularly imprinted electrochemical sensor based on core-shell Co₃O₄@MOF-74 nanocomposite. *J. Colloid Interface Sci.* **2021**, *592*, 174–185. [[CrossRef](#)]
61. Malik, L.A.; Bashir, A.; Qureashi, A.; Pandith, A.H. Detection and removal of heavy metal ions: A review. *Environ. Chem. Lett.* **2019**, *17*, 1495–1521. [[CrossRef](#)]
62. Vahidinia, A.; Samiee, F.; Faradmal, J.; Rahmani, A.; Javad, M.T.; Leili, M. Mercury, Lead, Cadmium, and Barium Levels in Human Breast Milk and Factors Affecting Their Concentrations in Hamadan, Iran. *Biol. Trace Element Res.* **2019**, *187*, 32–40. [[CrossRef](#)] [[PubMed](#)]
63. Gumpu, M.B.; Sethuraman, S.; Krishnan, U.M.; Rayappan, J.B.B. A review on detection of heavy metal ions in water—An electrochemical approach. *Sens. Actuators B Chem.* **2015**, *213*, 515–533. [[CrossRef](#)]
64. Ghanei-Motlagh, M.; Taher, M.A. Novel imprinted polymeric nanoparticles prepared by sol-gel technique for electrochemical detection of toxic cadmium (II) ions. *Chem. Eng. J.* **2017**, *327*, 135–141. [[CrossRef](#)]
65. Sebastian, M.; Mathew, B. Ion imprinting approach for the fabrication of an electrochemical sensor and sorbent for lead ions in real samples using modified multiwalled carbon nanotubes. *J. Mater. Sci.* **2018**, *53*, 3557–3572. [[CrossRef](#)]
66. Zhang, Z.; Lou, Y.; Guo, C.; Jia, Q.; Song, Y.; Tian, J.-Y.; Zhang, S.; Wang, M.; He, L.; Du, M. Metal-organic frameworks (MOFs) based chemosensors/biosensors for analysis of food contaminants. *Trends Food Sci. Technol.* **2021**, *118*, 569–588. [[CrossRef](#)]
67. Majdinasab, M.; Mishra, R.K.; Tang, X.; Marty, J.L. Detection of antibiotics in food: New achievements in the development of biosensors. *TrAC Trends Anal. Chem.* **2020**, *127*, 115883. [[CrossRef](#)]
68. Dutta, T.; Yadav, S.; Chatterjee, A. Antibiotics as feed additives for livestock: Human health concerns. *Indian J. Anim. Health* **2019**, *58*, 121–136. [[CrossRef](#)]
69. Treiber, F.; Beranek-Knauer, H. Antimicrobial Residues in Food from Animal Origin—A Review of the Literature Focusing on Products Collected in Stores and Markets Worldwide. *Antibiotics* **2021**, *10*, 534. [[CrossRef](#)]
70. Henrique, J.M.; Monteiro, M.K.; Cardozo, J.C.; Martinez-Huitle, C.A.; da Silva, D.R.; dos Santos, E.V. Integrated-electrochemical approaches powered by photovoltaic energy for detecting and treating paracetamol in water. *J. Electroanal. Chem.* **2020**, *876*, 114734. [[CrossRef](#)]
71. Dai, Y.; Li, X.; Lu, X.; Kan, X. Voltammetric determination of paracetamol using a glassy carbon electrode modified with Prussian Blue and a molecularly imprinted polymer, and ratiometric read-out of two signals. *Mikrochim. Acta* **2016**, *183*, 2771–2778. [[CrossRef](#)]

72. Dos Santos, A.M.; Wong, A.; Fatibello-Filho, O. Simultaneous determination of salbutamol and propranolol in biological fluid samples using an electrochemical sensor based on functionalized-graphene, ionic liquid and silver nanoparticles. *J. Electroanal. Chem.* **2018**, *824*, 1–8. [[CrossRef](#)]
73. Liu, B.; Lian, H.; Chen, L.; Wei, X.; Sun, X. Differential potential ratiometric sensing platform for enantio-recognition of chiral drugs. *Anal. Biochem.* **2019**, *574*, 39–45. [[CrossRef](#)] [[PubMed](#)]
74. Liu, C.; Wei, X.; Wang, X.; Shi, J.; Chen, Z.; Zhang, H.; Zhang, W.; Zou, X. Ratiometric electrochemical analysis on a flexi-bly-fabricated vibratory electrode module for reliable and selective determination of imidacloprid. *Sens. Actuators B Chem.* **2021**, *329*, 129228. [[CrossRef](#)]
75. Anirudhan, T.; Mani, A.; Athira, V. Molecularly imprinted electrochemical sensing platform for 2-Amino adipic acid, a diabetes biomarker. *React. Funct. Polym.* **2021**, *168*, 105056. [[CrossRef](#)]
76. Sargazi, S.; Mukhtar, M.; Rahdar, A.; Bilal, M.; Barani, M.; Díez-Pascual, A.M.; Behzadmehr, R.; Pandey, S. Opportunities and challenges of using high-sensitivity nanobiosensors to detect long noncoding RNAs: A preliminary review. *Int. J. Biol. Macromol.* **2022**, *205*, 304–315. [[CrossRef](#)]



Review

Chitosan-Based Hydrogels for Bioelectronic Sensing: Recent Advances and Applications in Biomedicine and Food Safety

Si Wu ^{1,2}, Shijing Wu ¹, Xinyue Zhang ¹, Tao Feng ^{1,2,*} and Long Wu ^{3,*}

¹ College of Resources and Environmental Engineering, Wuhan University of Science and Technology, Wuhan 430081, China

² Hubei Key Laboratory for Efficient Utilization and Agglomeration of Metallurgical Mineral Resources, Wuhan University of Science and Technology, Wuhan 430081, China

³ School of Food Science and Engineering, Key Laboratory of Tropical and Vegetables Quality and Safety for State Market Regulation, Hainan University, Haikou 570228, China

* Correspondence: fengtaowhu@163.com (T.F.); longquan.good@163.com (L.W.)

Abstract: Due to the lack of efficient bioelectronic interfaces, the communication between biology and electronics has become a great challenge, especially in constructing bioelectronic sensing. As natural polysaccharide biomaterials, chitosan-based hydrogels exhibit the advantages of flexibility, biocompatibility, mechanical tunability, and stimuli sensitivity, and could serve as an excellent interface for bioelectronic sensors. Based on the fabrication approaches, interaction mechanisms, and bioelectronic communication modalities, this review divided chitosan-based hydrogels into four types, including electrode-based hydrogels, conductive materials conjugated hydrogels, ionically conductive hydrogels, and redox-based hydrogels. To introduce the enhanced performance of bioelectronic sensors, as a complementary alternative, the incorporation of nanoparticles and redox species in chitosan-based hydrogels was discussed. In addition, the multifunctional properties of chitosan-based composite hydrogels enable their applications in biomedicine (e.g., smart skin patches, wound healing, disease diagnosis) and food safety (e.g., electrochemical sensing, smart sensing, artificial bioelectronic tongue, fluorescence sensors, surface-enhanced Raman scattering). We believe that this review will shed light on the future development of chitosan-based biosensing hydrogels for micro-implantable devices and human–machine interactions, as well as potential applications in medicine, food, agriculture, and other fields.

Citation: Wu, S.; Wu, S.; Zhang, X.; Feng, T.; Wu, L. Chitosan-Based Hydrogels for Bioelectronic Sensing: Recent Advances and Applications in Biomedicine and Food Safety. *Biosensors* **2023**, *13*, 93. <https://doi.org/10.3390/bios13010093>

Received: 30 November 2022
Revised: 13 December 2022
Accepted: 4 January 2023
Published: 6 January 2023

Keywords: chitosan; bioelectronic sensors; biomedicine; food safety

1. Introduction

Flexible bioelectronic sensors have emerged to mimic biological functions, including human motion tracking [1,2], health monitoring [3,4], disease diagnosis [5], artificial bioelectronic tongues [6], and so on. Intrinsically, biology and electronics are essentially different, both in their mechanical and sensory properties. Electronic devices are solid and robust, while biological tissue is soft and elastic. On the other hand, their methods of signal transmitting are distinct from each other. Electromagnetic radiation makes long-distance communication possible, but this method does not exist in biological systems. Another challenge of bioelectronic sensors is to select reliable communication modalities at the interfaces connecting the device and biological tissue. Thus, it is of critical significance to bridge the gap between electronics and biology, with the end goal of fabricating a flexible bioelectronic interface and enlisting proper signaling modalities for bioelectronics.

Hydrogels have become competitive candidates due to their analogous tissue structure, excellent biocompatibility, and tunable functions [7–10]. The properties of hydrogels can be easily changed by external stimulus. For instance, chitosan forms hydrogels at a pH over 6.5; agarose and gelatin are dissolved at high temperatures; and alginate and calcium ions



Copyright: © 2023 by the authors. Licensee MDPI, Basel, Switzerland. This article is an open access article distributed under the terms and conditions of the Creative Commons Attribution (CC BY) license (<https://creativecommons.org/licenses/by/4.0/>).

can form gels [11–14]. Therefore, hydrogels are able to act as an excellent interface for the perception and transition of biological signals.

Chitosan is a natural polymer derived from chitin, which exists widely in nature [15]. It is a prospective material for flexible bioelectronics, owing to its biosafety, chemical reactivity, similar water content, and Young's moduli to tissue and cells, as well as its dynamic reconfigurable functions [16]. Biosensors with adhesive properties that can attach to wet and dynamic surfaces have drawn much attention in tissue engineering, human–machine interfaces, and wound dressings. As such, a carrier is required to connect biology and electronics. Chitosan exhibits antimicrobial and biocompatible properties, and it also serves as a good bio-adhesive [17]. Thus, chitosan-based hydrogels show great potential to construct a simple, biocompatible, and multifunctional interface between biology and electronics.

Figure 1 demonstrates the mechanism of chitosan-based bioelectronic sensors from bio-recognition to data processing. Therein, chitosan-based hydrogel acts as a bridge to connect biology and electronics, and the analytes can be recognized by bio-elements such as antibodies and aptamers. Then, the interaction is transferred to optical/electronic signals, which are finally amplified into measurable outcomes. This review aims to summarize the fabrication approach and the interaction mechanism of chitosan-based composite hydrogels. We briefly classified the hydrogel bioelectronics into four types [18]: (i) electrode-based hydrogels, (ii) conductive materials conjugated hydrogels, (iii) ionically conductive hydrogels, (iv) redox-based hydrogels. Afterward, we discussed the recent progress of chitosan-based composite hydrogels in biomedicine and food applications. Finally, we concluded the challenges and perspectives of chitosan-based hydrogel bioelectronics in further applications.

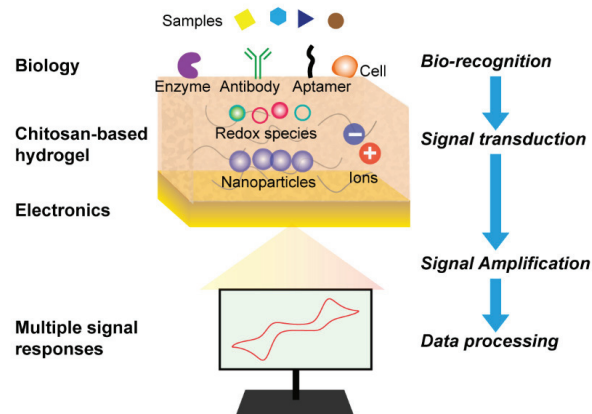


Figure 1. Schematic illustration of chitosan-based bioelectronic sensors.

2. Fabrication and Interaction Mechanism of Chitosan-Based Hydrogels

Chitosan is a kind of stimuli-sensitive polymer with reactive amine and hydroxyl groups, which endow chitosan-based hydrogels with functional properties (e.g., self-assemble, self-healing, shape memory, etc.) [19]. The interaction between hydrogels and biology strongly depends on the communication modality of bioelectronics. The conductivity of bioelectronic sensors is easily obtained by integration of metal nanomaterials [20–23], carbon-based nanomaterials [1,24–27], or other conductive polymers (e.g., polyaniline, polypyrrole) [28,29] into hydrogel networks. Furthermore, the redox-active polymers can also communicate with biological molecules through redox modality, which is widely used for signal processing in biology [30,31]. As illustrated in Figure 2, we summarized the hydrogel bioelectronics into four types: conductive electrode-based chitosan hydrogels, electron conductive polymers integrated chitosan hydrogels, ionic conductive polymers combined chitosan hydrogels, and redox-active species modified chitosan hydrogels.

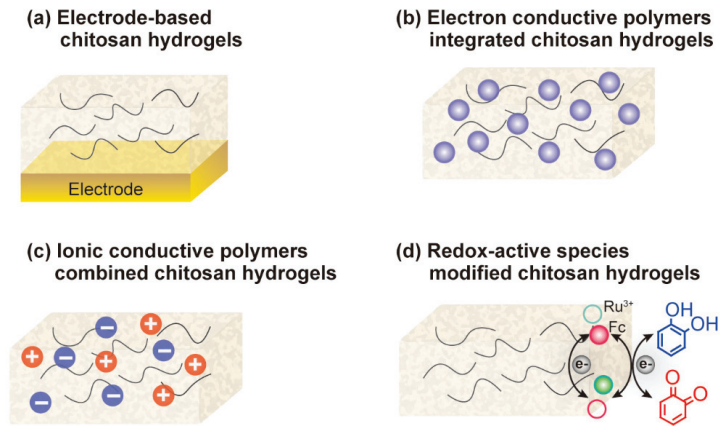


Figure 2. Chitosan-based hydrogels. (a) Electrode-based chitosan hydrogels. (b) Electron conductive polymers integrated chitosan hydrogels. (c) Ionic conductive polymers combined chitosan hydrogels. (d) Redox-active species modified chitosan hydrogels.

2.1. Electrode-Based Hydrogels

The pH cues generated by electrical signals can induce self-assembly of chitosan on the electrode surface to form hydrogels (Figure 3a). Thus, the hierarchical structure of chitosan-based hydrogels can be programmed and reconfigured by controlling electrodes and electrical inputs [32]. The electrochemical technique is simple, spatially controllable, and allows for bioelectronic applications. As shown in Figure 3b, patterned hydrogels are easily achieved by varying the electrode shapes and electrical signals, thus endowing the materials with unique functions and properties [33]. Electrodes can also be used to print patterns on hydrogels. As an example, Silva et al. introduced an electro-assisted printing approach to fabricate patterned chitosan and alginate conductive hydrogels on gold and ITO electrodes through covalent cross-linking and ionic polymerization mechanisms [34]. Figure 3c demonstrates that the UoS letters were printed using a high-molecular-weight chitosan at 1.8 V. The unique pH-responsiveness of chitosan allows it to form hydrogels easily on the electrode.

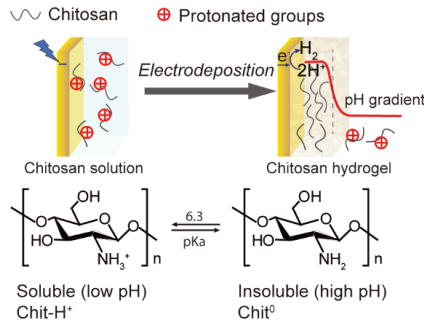
2.2. Conductive Materials Conjugated Hydrogels

The conductivity of hydrogels is easily achieved by integrating with conductive materials [35,36]. Metal nanoparticles and nanowires are intensively adopted to impart electrical conductivity to hydrogels. However, the heavy aggregation and poor stretchability limit their applications. Thus, the assembly of nanomaterials into the three-dimensional (3D) structure of hydrogels has attracted much attention. For instance, Yu et al. proposed a flexible and robust bioelectronic aerogel based on silver nanowires (AgNWs) assembled by a chitosan network and in situ synthesis of poly(acrylamide-sodium acrylate) hydrogel [37]. The composition of AgNWs enhanced the mechanical and antibacterial properties of the hydrogels, providing a new approach for the construction of 3D nanostructures into the hydrogels.

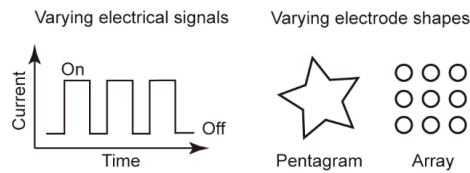
Another effective strategy for the fabrication of conductive bioelectronics is through in situ polymerization. For example, Duan et al. synthesized an ultra-stretchable, tough, and conductive chitosan-based hydrogel through in situ polymerization of acrylamide and aniline [29]. Lin et al. enlisted the graft copolymerization mechanism to fabricate highly conductive chitosan-polyacrylate/polyaniline hydrogels with good electrochemical performance [38]. The stretchability and conductivity properties of flexible hydrogels enable the bioelectronic applications. Some studies focused on the antibacterial properties of hydrogels. Based on the polymerization of pyrrole grafting, Zn²⁺ chelating, and borax cross-linking, Zhang et al. prepared conducting, self-healing, and antibacterial chitosan-

based hydrogels with the ability to promote wound healing [39]. Conductive nanomaterials and polymers which conjugate chitosan hydrogels are promising for flexible bioelectronic interfaces due to their adhesive, mechanical, and conductive properties.

(a) Chitosan-based hydrogels induced by electrical signal



(b) Patterned hydrogels



(c) Electro-assisted printing

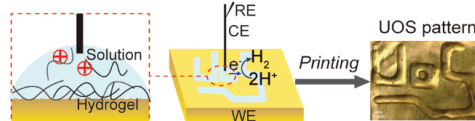


Figure 3. Electrofabrication of electrode-based chitosan hydrogels. (a) Chitosan-based hydrogels induced by electrical signals. (b) Patterned hydrogels formed by varying electrical signals or electrode shapes. (c) Electro-assisted printing of chitosan hydrogels. Adapted with permission from ref [33]. Copyright (2022) Springer Nature.

2.3. Ionically Conductive Hydrogels

Bioelectronic sensors based on electronic conductive hydrogels can communicate with biology using electrical signals. However, when the hydrogels are attached to skin or tissue, some metal nanomaterials may do harm to the cells. Moreover, conductive material-conjugated hydrogels are usually not transparent, and may limit their ability to visually detect the target products. Therefore, the strong demand for biocompatibility and the transparency of the hydrogels makes them essential in the bioelectronic applications on some special occasions (e.g., soft biosensors, optoelectronic sensors, etc.) [40]. The biology (e.g., the nervous and neuromuscular systems) can perceive signals through ionic electrical modality [31]. Thus, ionic conductive hydrogels can serve as an excellent transparent interface for the communication between biology and electronics.

Ionic hydrogels usually contain three important elements, which are water, polymer, and ionic conductors [41]. Ionic conductors are ionotropic, conductive, and water-dependent. Therefore, water is used as a medium to dissolve and transport ions, while polymers provide mechanical strength and 3D network structures of the hydrogels [42,43]. (Poly)electrolytes are usually introduced into hydrogels to acquire ion conductivity, including metal salt ions (lithium chloride, sodium chloride, potassium chloride, and aluminum chloride) [44–50] and Zwitterionic [51,52]. For instance, Khan et al. introduced a novel chitosan/poly(acrylamide-co-acrylic acid) hydrogel with self-healing and anti-freezing

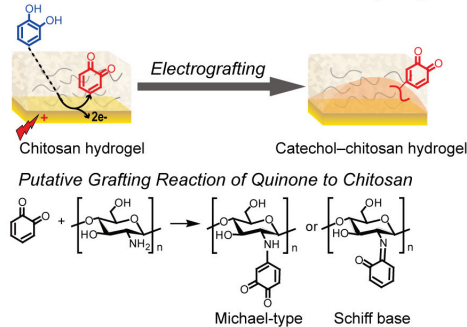
properties, while the ion conductivity was achieved through sodium chloride electrolytes. Thus, the employment of ionically conductive chitosan-based hydrogels has broadened the biomimetic applications, such as artificial bioelectronic tongues to detect food safety and quality, and smart actuators or robots to diagnose diseases in human body.

2.4. Redox-Based Hydrogels

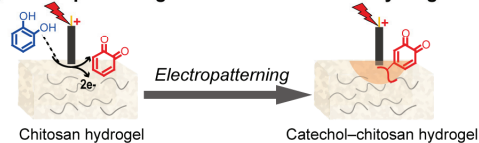
There are three main communication modalities that biology uses for signal processing, including the ionic electrical modality, the molecularly specific modality and the redox modality [30,31]. Recently, redox modality has been verified as an effective approach for biology communication. For instance, reactive oxygen species (ROS) may cause oxidative stress, may promote the connections between the gut microbiota and the brain [53,54], and are relevant to some neurodegenerative diseases (Alzheimer's and Parkinson's disease), aging [55], etc.

Phenolic compounds are abundant antioxidants in nature, and phenolic hydroxyl groups exhibit redox activity. As illustrated in Figure 4a, catechol–chitosan hydrogel can be fabricated on the electrodes by applying an oxidative potential. The phenolic hydroxyl group of catechol moieties can be easily oxidized under electrochemical conditions and grafted with the amino group of chitosan through a Michael type or Schiff base reaction [56]. Figure 4b demonstrates that catechol patterns can be printed on the surface of the chitosan-based hydrogel by moving the electrode and imposing positive voltage [57,58].

(a) Electrofabrication of Catechol–chitosan Hydrogel



(b) Electropatterning of Catechol–chitosan Hydrogel



(c) Redox-based Catechol–chitosan Hydrogel

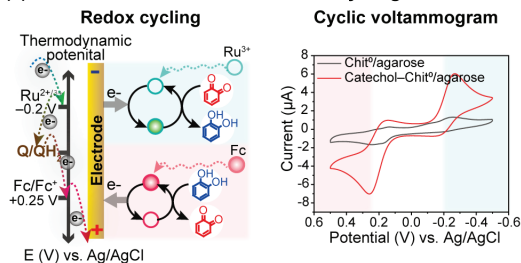


Figure 4. Redox-based hydrogels. (a) Electrofabrication of catechol–chitosan hydrogel. (b) Electropatterning of catechol–chitosan hydrogel. (c) The redox cycling and cyclic voltammogram of redox-based catechol–chitosan hydrogel. Adapted with permission from ref. [30]. Copyright (2019) ACS publications.

As shown in Figure 4c, catechol-modified chitosan hydrogel serves as a redox capacitor. The redox states of catechol are reversibly switchable in the presence of redox mediators. Thus, electrons can be transferred and stored between the electrode and the redox active catechol–chitosan hydrogel [59]. The catechol–chitosan hydrogel is able to interact with biological information, such as reactive oxygen species (NO, H₂O₂) [60,61], virulence factors of pathogenic bacteria (Pyocyanin) [62], bio-related reductants (NADPH [63], ascorbic acid [64], oxidants (O₂) [65]), etc. For instance, Wu et al. fabricated a catechol–chitosan-based microfluidic channel modularity, which enables the in situ monitoring of information in biology [66]. Furthermore, the incorporation of nanoparticles enhances the performance of hydrogels and synergistically amplifies the redox-based electrochemical signals. For instance, Yan et al. added magnetic nanoparticles into a catechol–chitosan redox capacitor and allowed the chemical signals to be converted and amplified enzymatically and magnetically [67].

3. Functional Properties and Applications of Chitosan-Based Hydrogels

Biomimetic flexible, wearable, and implantable devices have attracted much attention in biomedical and food applications. Figure 5 gives a list of characteristics of chitosan-based bioelectronics, including stimuli-sensitive properties, tunable mechanics, good biocompatibility, strong tissue adhesion, optical transparency, flexible and conductive substrate, and self-healing and antibacterial functions [68].

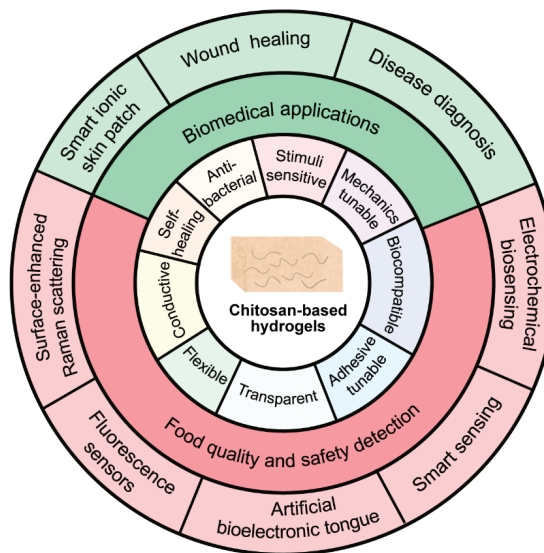


Figure 5. Properties and applications of chitosan-based hydrogels.

These properties of hydrogels provide the capability to communicate between biology and electronics, which sheds light on its applications in biomedicine (e.g., smart skin patches, wound healing, disease diagnosis) and food safety (e.g., electrochemical sensing, smart sensing, artificial bioelectronic tongues to detect food quality and safety, fluorescence sensors, and the surface-enhanced Raman scattering approach for signal amplification).

4. Biomedical Applications

Chitosan-based hydrogels have been researched extensively in the bioengineering field for their simple fabrication, non-toxicity, and good biocompatibility [69]. The bioelectronic communication abilities of smart skin patch hydrogels enable human health diagnoses and signal interaction. The adhesive and antibacterial abilities of hydrogels promote wound

healing and prevent secondary injuries. The biomedical applications of chitosan-based hydrogels as bioelectronic sensors are shown in Table 1.

Table 1. Chitosan-based bioelectronic sensing and its biomedical applications.

Materials	Hydrogel Types	Interaction Mechanisms	Properties	Applications	Ref.
Quaternized chitosan/polyacrylic acid hydrogel	Conductive polymers combined hydrogel	Polymerization, physical cross-linking	Mechanic tunable, adhesion reversible, pH sensitive, thermosensitive, biosafe, self-healing, conductive	Smart ionic skin patch	[70]
Chitosan/collagen-graphene oxide quantum dots hydrogel	Combined biopolymeric conductive hydrogel	Blending, condensation reaction	Biocompatible, injectable, thermally stable, promotes gene expression	Cardiac healing	[71]
Catechol–chitosan hydrogel	Redox-active hydrogel	Chemical cross-linking	Adhesive, self-sealing, hemostatic	Hemostatic needle coating	[72]
Chitosan-poly pyrrole/Zn-functionalized chitosan/poly(vinyl alcohol) hydrogel	Conductive polymers combined hydrogel	Polymerization, chemical and physical cross-linking	Stretchable, flexible, self-healing, biocompatible, antibacterial	Chronic Wound Treatment	[39]
Polydopamine-carboxymethyl chitosan hydrogel	Gold electrode-based hydrogel	Polymerization, chemical cross-linking	Biocompatible, non-immunogenic, flexible, conductive, antioxidant, adhesive	Real-time wound monitoring	[73]
Hyperbranched Polyglycidyl ether /chitosan/ human-like collagen/MXene sheets/graphene hydrogel	Conductive polymers combined hydrogel	Polymerization, chemical and physical cross-linking	Flexible, antibacterial, electroactive, bio-adhesive, self-healing, hemostatic	Wound treatment, health monitoring	[74]
Quaternized chitosan/oxidized dextran/tobramycin/polydopamine@poly pyrrole hydrogel	Conductive polymers combined hydrogel	Polymerization, chemical and physical cross-linking	Transparent, antioxidant, antibacterial, conductive, self-healing	Drug Release, wound healing	[75]
Chitosan quaternary ammonium salt/ sodium alginate hydrogel	Polyelectrolyte composite hydrogel	Physical cross-linking	Flexible, conductive, biocompatible, adhesive, hemostatic	Wound healing	[76]
Chitosan/carbon nanotubes hydrogel	Gold electrode-based hydrogel	Physical cross-linking	Conductive, redox active	Point-of-care testing for tumors	[77]
Catechol–chitosan-diatom hydrogel	Ionically conductive hydrogel	Chemical and physical cross-linking	Stretchable, skin-attachable, biocompatible, self-healing, self-powered	Real time health monitoring	[78]

4.1. Smart Ionic Skin Patch

Hydrogel exhibits similarities to human skin, and can be used as a smart ionic skin for health monitoring [79]. Moreover, the hydrogel bioelectronics offer the ability to sense external stimuli and transmit signals in biology. Much attention has been focused on hydrogel-integrated bioelectronics, including the performance of the hydrogels and the interaction between the hydrogel and the environment (e.g., external stimuli). However, it remains a challenge to prepare hydrogels that sense and respond to multiple signals simultaneously. Shi et al. developed a smart quaternized chitosan–polyacrylic acid hydrogel skin patch, which exhibited excellent conductivity, biosafety, and tunable adhesive ability [70]. The hydrogel skin patch offers bioelectronic temperature- and pressure-sensing functions that can even distinguish different physiological signals simultaneously.

4.2. Wound Healing

The adhesive ability of biology and electronics together is also of critical importance for flexible bioelectronics. Existing tissue adhesives are cytotoxic, incompatible, and easily fall off [80]. Therefore, the fixation, biosafety and tunable adhesion of hydrogel are required on tissue or skin to avoid secondary damage and to promote wound healing [81]. The secondary damage and even inflammation may be caused when the hydrogel patch is removed from the skin [3,82]. Thus, the ability of hydrogels to reversibly adhere to wet and dynamic surfaces is critical in tissue engineering and wound healing. Mussel inspired biomimetic hydrogels have been extensively studied because of their reversible adhesive properties [83,84]. Catechol–chitosan-coated needles can even prevent blood loss in clinical experiments [72]. However, the adhesion generated from catechol chemistry is insufficient.

Recently, bioinspired [44,51] and tough adhesives inspired by slugs' defensive mucus [85] have been proposed to have strong and dynamic adhesive abilities. Tough hydrogel adhesion has been proposed based on topology connection and dissipation mechanics [86]. Li et al. established tough adhesives for various wet and dynamic surfaces through the synergy of two layers: chitosan, as the interfacial bridging layer, shows an adhesion energy of over 1000 J m^{-2} ; while the alginate–polyacrylamide hydrogel matrix layer can dissipate energy during deformation [85].

Considering the antibacterial and bioelectronic communication requirements for wound dressings, metal nanomaterials are incorporated into hydrogels. To avoid wound infection and inflammation, Pan et al. assembled AgNWs into chitosan networks and demonstrated a novel adhesive hydrogel conductor through in situ poly(acrylamide-sodium acrylate) hydrogel polymerization in a chitosan-AgNW aerogel structure. The aero-hydrogel hybrid conductor, with adhesive, biocompatible, and anti-bacterial capabilities, can be used as an excellent flexible bioelectronic interface for soft implantable devices [37].

4.3. Disease Diagnosis

The development of a bioelectronic sensor that can recognize the molecules in biological fluids and enable point-of-care detection is of critical importance. Catecholamines (e.g., dopamine, noradrenaline) are relevant to memory, cognition, and some diseases [87]. Shukla et al. fabricated a chitosan-based composite hydrogel embedded with carbon nanotubes, and explored two models for electrochemical information processing. The electrochemical sensor platform was able to quickly and efficiently detect the dopamine in urine samples without pre-treatment, which offers potential capability for clinical diagnosis and therapeutic monitoring of pheochromocytoma as well as other diseases [74]. However, the oxidation of dopamine may cause the contamination of the electrode, making it unable to be reused. Kim et al. proposed a catechol–chitosan–diatom hydrogel, which is flexible, self-healing, and conductive. The self-powered bioelectronic sensor can be used to diagnose body vibrations of Parkinson's patients [75].

5. Food Quality and Safety Detection

In recent years, as the factories and industries have accelerated the economic boom, their wastes and byproducts have severe effects on the environment (e.g., atmosphere, water, oil), with various contaminants. The absorption of contaminants, especially heavy metals, by animals and plants is mainly driven by the level of contaminants in the environment and their accumulation and transformation in living organisms. Finally, some contaminants will be transferred to the human body through the food chain. On the other hand, with the common occurrence of food safety issues, food safety has become a highlighted public concern worldwide. Food contaminants such as pathogens, pesticides, and biotoxins induce food poisoning or diseases, which can cause serious threats to human health. Therefore, it is essential to develop rapid, sensitive, and accurate methods for the detection of such food contaminants.

The traditional methods to monitor food quality and identify adulterated food products include HPLC, GC-MS, and chromatography [88,89]. Although these methods are effective, they are usually time-consuming, cost-prohibitive, and complex to operate. New devices (e.g., electrochemical sensors, cellphones) and methods (e.g., artificial bioelectronic sensing) are being developed and applied in food quality and safety detection [90,91].

5.1. Electrochemical Biosensing

The electrochemical biosensor platform has developed rapidly due to its simple operation, low cost, quick response, and high sensitivity. Chitosan hydrogel is able to immobilize biomolecules, which offers biosensing ability for the detection of nutrients (e.g., glucose, antioxidants) and toxic species (e.g., pesticides, mycotoxins, heavy metal ions) in food products [92]. Artigues et al. fabricated a glucose oxidase-immobilized and a titanium dioxide nanotube-coated chitosan biosensor, which showed great stability (20 days) and

sensitivity ($8.53 \pm 2.39 \mu\text{A mM}^{-1}$) for glucose detection in various food samples [93]. Ochratoxin A (OTA) is a highly toxic mold metabolite that widely contaminates food products. Li et al. developed chitosan/dipeptide nanofibrous hydrogels modified with DNA and OTA aptamer. The concentration of OTA can be detected with a low detection limit of 0.03 ng mL^{-1} . Moreover, the biosensor can be applied in white wine samples according to the impedance changes [94].

5.2. Smart Sensing

Smart phones are commonly used in our daily life. The high resolution of the camera and various apps in cellphones provides the ability to quickly analyze information. Enzyme-based biosensors can recognize the target markers and transduce the signal into an amplified and measurable signal. Wu et al. fabricated a catechol-patterned chitosan hydrogel that can identify high-fructose corn syrup in real samples. The grafted catechol moieties are able to accept electrons from glucose through an enzymatic reaction, and the changes in optical signal can be easily analyzed by smart phone imaging [95].

5.3. Artificial Bioelectronic Tongue

The tongue is sensitive to five basic tastes, namely sweet, sour, bitter, salty, and umami. Various bioelectronic tongues are widely used to detect the quality and safety of foods [96,97]. Water-soluble flavors can be identified by changes in electrical signals generated by binding receptors or ion migration [98]. The concentration of different tastes is a key point in the food industry, as it affects the flavor of foods and beverages. Moreover, a bitter flavor is related to some poisons [99]. Therefore, the application of artificial bioelectronic tongues in food detection, the pharmaceutical industry, and environmental monitoring has attracted significant attention. As shown in Figure 6, Khan et al. fabricated a chitosan/poly(acrylamide-co-acrylic acid) hydrogel-based bioelectronic sensor to mimic the human tongue with a detection limit at the micromolar level. The bioelectronic tongue is flexible, self-healing, and anti-freezing, so it can also work in a -5°C environment [6]. Nanostructured hydrogel sensors enable improved capabilities of the bioelectronic tongue. Salvo-Comino et al. proposed a bi-sensor using layer-by-layer construction of anionic sulfonated copper phthalocyanine, chitosan, and ionic liquid. Galactose oxidase was immobilized on the top of the layer, and offers the ability of detecting lactose concentration and freshness of milk [100].

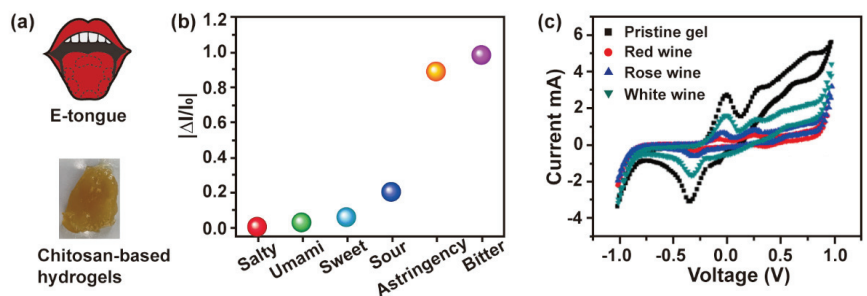


Figure 6. (a) Schematic and photograph of a chitosan-based bioelectronic sensor. (b) Selective sensing of five tastes and astringency by E-tongue. (c) Cyclic voltammetry measurement of real beverage samples. Adapted with permission from ref [6]. Copyright (2022) Elsevier.

5.4. Fluorescence Sensors

Due to their high sensitivity, strong selectivity, ease of use, good portability, and non-invasiveness, chitosan-based fluorescent probes have been widely used in the detection of food contaminants, especially of heavy metals. Different mechanisms have been reported on fluorescent probes interacting with food contaminants, including intramolecular charge

transfer enhancement and fluorescence quenching. The former mechanism leads to a fluorescent “turn on” response, and the latter one gives “turn off” signals.

Based on the Schiff base formation reaction, fluorescent chitosan hydrogels (FCHs) were obtained by introducing fluorophore BODIPY onto chitosan [101]. The combination of FCHs with $\text{Hg}^{2+}/\text{Hg}^+$ led to the quenching of the fluorescence, which showed strong selectivity for $\text{Hg}^{2+}/\text{Hg}^+$ with an adsorption capacity of $120.79 \text{ mg}\cdot\text{g}^{-1}$. With the functional modification of chitosan, they were multi-functionalized with strong selectivity, high adsorption capacity, hydrophily, etc.

5.5. Surface-Enhanced Raman Scattering

SERS, short for surface-enhanced Raman scattering or surface-enhanced Raman spectroscopy, is a surface sensitive technique coupled with a rough metal surface, known as a SERS substrate. The incident laser stimulates the electrons on the SERS substrate surface to produce surface plasmon resonance with surface-attached molecules, which can greatly enhance the Raman signal. As a rapid, non-destructive, and sensitive method, SERS has been widely applied in the detection of food contaminants.

A biosynthesis method was proposed for the preparation of Au-embedded chitosan (Au@CS) by adding AuCl_4 ions into chitosan [102]. Using this method, the flexible Au@CS acted as a reliable and sensitive SERS substrate, which enabled label-free detection of melamine in milk and thiamethoxam in fruit peels, with limits of quantification of 1.5 mg/kg and 0.001 mg/kg , respectively. Furthermore, a labeled SERS aptasensor was proposed for the detection of *E. coli* based on silver nanoparticles and *E. coli* aptamer (Apt)-modified chitosan (Apt-Ag@CS) [103]. When Apt-Ag@CS was further incubated with *E. coli*, 4-mercaptobenzoic acid (4-MBA), and apt-modified gold nanostars, it allowed for specific Raman signal amplification and detection of *E. coli*, with a detection limit of 3.46 CFU/mL . Chitosan-based SERS substrates provided a new direction for the detection of *E. coli* in practical food samples.

6. Conclusions and Future Prospects

Chitosan hydrogels serve as an excellent interfacial material to bridge biology and electronics, and have the capability for bioelectronic communication due to their biocompatibility, stimulus response, and tissue-like structure. Compared to other materials, chitosan-based hydrogels are simple to fabricate (physical and chemical methods), reconfigurable (reversible structure), and easy to modify (functional groups), so they have unique properties and behaviors (e.g., self-healing, adhesion, conductivity, etc.). This review illustrates the fabrication and mechanism of four types of chitosan-based hydrogel bioelectronics, including electrode-based hydrogels, conductive materials conjugated hydrogels, ionically conductive hydrogels, and redox-based hydrogels. The combination of different materials imparts functional properties to the hydrogels. For instance, the integration of nanoparticles enhances the mechanical properties and conductivity of the hydrogel, the modification of catechol provides redox activity and adhesion of hydrogel, etc. The functional properties of chitosan-based composite hydrogels give it its potential application in biomedicine and food safety. Chitosan-based hydrogels can be used as smart skin patches, wound dressings, or disease diagnosis biosensors. In food safety inspection and quality supervision, chitosan-based hydrogels can be used as a smart sensor to verify adulterated or fake foods, and as artificial bioelectronic tongues to detect food quality and concentration.

However, there are still some limitations for the broad application of chitosan-based hydrogels. The primary one is the impact of the addition of nanoparticles on biosafety. Therefore, the concentration and cytocompatibility of different nanoparticles should be investigated. The network structure of the hydrogel is also beneficial for the encapsulation and immobilization of nanoparticles. The second is that the reusability of biosensors needs to be improved. This requires elucidating the contamination mechanism of electrodes and constructing sensor interfaces with anti-fouling capability. Additionally, the ability of

chitosan-based bioelectronic sensors to access biological information and actuate signals requires further investigation. A mediated electrochemical probing system and information analysis offers an opportunity for biodevice communication [58].

In the future, chitosan-based hydrogels are promising as self-powered biosensors that can harvest energy from living organisms, and can also be used for health monitoring and real-time monitoring [104]. Its potential applications include microchip sensors for wireless communication and wireless electricity charging [5], as well as soft implantable biosensors that perform multiple tasks. Moreover, human-machine interaction is expected to be achieved through bioelectronic communication [105]. It is expected that multi-scale networked and automated monitoring will be achieved through machine learning by connecting materials, device design, and artificial intelligence. We believe that chitosan-based composite hydrogels will overcome these challenges and enable widespread applications in biomedical, food, agricultural and other fields in the future.

Author Contributions: Conceptualization, S.W. (Si Wu) and L.W.; methodology, S.W. (Si Wu); software, S.W. (Si Wu); validation, S.W. (Si Wu), T.F. and L.W.; formal analysis, X.Z.; investigation, X.Z.; resources, S.W. (Si Wu); data curation, S.W. (Shijing Wu); writing—original draft preparation, S.W. (Si Wu); writing—review and editing, L.W.; visualization, S.W. (Shijing Wu); supervision, S.W. (Si Wu), T.F. and L.W.; project administration, T.F.; funding acquisition, S.W. (Si Wu), T.F. and L.W. All authors have read and agreed to the published version of the manuscript.

Funding: This work was supported by the Technology Innovation Special Foundation of Hubei Province (2020ZYD019), National Natural Science Foundation of China (22204124), the Key Research and Development Program of Hubei Province (2021BCD002), the Natural Science Foundation of Hubei Province of China (2022CFB613), the Hainan Provincial Natural Science Foundation of China (321QN183, 322MS015), Fund of Key Laboratory of Fermentation Engineering (Ministry of Education) (202105FE09), Key Laboratory of Tropical Fruits and Vegetables Quality and Safety for State Market Regulation (ZX-2022001) and the specific research fund of The Innovation Platform for Academicians of Hainan Province (YSPTZX202152).

Institutional Review Board Statement: Not applicable.

Informed Consent Statement: Not applicable.

Data Availability Statement: No new data were created or analyzed in this study. Data sharing is not applicable to this article.

Conflicts of Interest: The authors declare no conflict of interest.

References

- Lee, S.W.; Park, J.J.; Park, B.H.; Mun, S.C.; Park, Y.T.; Liao, K.; Seo, T.S.; Hyun, W.J.; Park, O.O. Enhanced Sensitivity of Patterned Graphene Strain Sensors Used for Monitoring Subtle Human Body Motions. *ACS Appl. Mater. Interfaces* **2017**, *9*, 11176–11183. [[CrossRef](#)] [[PubMed](#)]
- Wang, Y.; Niu, W.; Lo, C.Y.; Zhao, Y.; He, X.; Zhang, G.; Wu, S.; Ju, B.; Zhang, S. Interactively Full-Color Changeable Electronic Fiber Sensor with High Stretchability and Rapid Response. *Adv. Funct. Mater.* **2020**, *30*, 2000356. [[CrossRef](#)]
- Webb, R.C.; Bonifas, A.P.; Behnaz, A.; Zhang, Y.; Yu, K.J.; Cheng, H.; Shi, M.; Bian, Z.; Liu, Z.; Kim, Y.S.; et al. Ultrathin Conformal Devices for Precise and Continuous Thermal Characterization of Human Skin. *Nat. Mater.* **2013**, *12*, 938–944. [[CrossRef](#)] [[PubMed](#)]
- Luo, N.; Dai, W.; Li, C.; Zhou, Z.; Lu, L.; Poon, C.C.Y.; Chen, S.C.; Zhang, Y.; Zhao, N. Flexible Piezoresistive Sensor Patch Enabling Ultralow Power Cuffless Blood Pressure Measurement. *Adv. Funct. Mater.* **2016**, *26*, 1178–1187. [[CrossRef](#)]
- You, I.; Kim, B.; Park, J.; Koh, K.; Shin, S.; Jung, S.; Jeong, U. Stretchable E-Skin Apexcardiogram Sensor. *Adv. Mater.* **2016**, *28*, 6359–6364. [[CrossRef](#)]
- Khan, A.; Ahmed, S.; Sun, B.Y.; Chen, Y.C.; Chuang, W.T.; Chan, Y.H.; Gupta, D.; Wu, P.W.; Lin, H.C. Self-Healable and Anti-Freezing Ion Conducting Hydrogel-Based Artificial Bioelectronic Tongue Sensing toward Astringent and Bitter Tastes. *Biosens. Bioelectron.* **2022**, *198*, 113811. [[CrossRef](#)]
- Liu, X.; Liu, J.; Lin, S.; Zhao, X. Hydrogel Machines. *Mater. Today* **2020**, *36*, 102–124. [[CrossRef](#)]
- Yin, X.Y.; Zhang, Y.; Xiao, J.; Moorlag, C.; Yang, J. Monolithic Dual-Material 3D Printing of Ionic Skins with Long-Term Performance Stability. *Adv. Funct. Mater.* **2019**, *29*, 1904716. [[CrossRef](#)]
- Zhu, Z.; Park, H.S.; McAlpine, M.C. 3D Printed Deformable Sensors. *Sci. Adv.* **2020**, *6*, eaba5575. [[CrossRef](#)]
- Zhang, Y.S.; Khademhosseini, A. Advances in Engineering Hydrogels. *Science* **2017**, *356*, eaaf3627. [[CrossRef](#)]

11. Thambi, T.; Phan, V.H.G.; Lee, D.S. Stimuli-Sensitive Injectable Hydrogels Based on Polysaccharides and Their Biomedical Applications. *Macromol. Rapid Commun.* **2016**, *37*, 1881–1896. [[CrossRef](#)] [[PubMed](#)]
12. Nordin, N.; Bordonali, L.; Badilita, V.; MacKinnon, N. Spatial and Temporal Control Over Multilayer Bio-Polymer Film Assembly and Composition. *Macromol. Biosci.* **2019**, *19*, 1800372. [[CrossRef](#)]
13. Vivcharenko, V.; Wojcik, M.; Przekora, A. Cellular Response to Vitamin C-Enriched Chitosan/Agarose Film with Potential Application as Artificial Skin Substitute for Chronic Wound Treatment. *Cells* **2020**, *9*, 1185. [[CrossRef](#)] [[PubMed](#)]
14. Blacklow, S.O.; Li, J.; Freedman, B.R.; Zeidi, M.; Chen, C.; Mooney, D.J. Bioinspired Mechanically Active Adhesive Dressings to Accelerate Wound Closure. *Sci. Adv.* **2019**, *5*, aaw3963. [[CrossRef](#)]
15. Shariatinia, Z.; Jalali, A.M. Chitosan-Based Hydrogels: Preparation, Properties and Applications. *Int. J. Biol. Macromol.* **2018**, *115*, 194–220. [[CrossRef](#)]
16. Lee, K.Y.; Mooney, D.J. Hydrogels for Tissue Engineering. *Chem. Rev.* **2001**, *101*, 1869–1879. [[CrossRef](#)]
17. Li, J.; Yu, X.; Martinez, E.E.; Zhu, J.; Wang, T.; Shi, S.; Shin, S.R.; Hassan, S.; Guo, C. Emerging Biopolymer-Based Bioadhesives. *Macromol. Biosci.* **2022**, *22*, 2100340. [[CrossRef](#)]
18. Yuk, H.; Lu, B.; Zhao, X. Hydrogel Bioelectronics. *Chem. Soc. Rev.* **2019**, *48*, 1642–1667. [[CrossRef](#)] [[PubMed](#)]
19. Yan, K.; Xiong, Y.; Wu, S.; Bentley, W.E.; Deng, H.; Du, Y.; Payne, G.F.; Shi, X.W. Electro-Molecular Assembly: Electrical Writing of Information into an Erasable Polysaccharide Medium. *ACS Appl. Mater. Interfaces* **2016**, *8*, 19780–19786. [[CrossRef](#)] [[PubMed](#)]
20. Song, P.; Qin, H.; Gao, H.L.; Cong, H.P.; Yu, S.H. Self-Healing and Superstretchable Conductors from Hierarchical Nanowire Assemblies. *Nat. Commun.* **2018**, *9*, 2786. [[CrossRef](#)]
21. Gao, H.L.; Xu, L.; Long, F.; Pan, Z.; Du, Y.X.; Lu, Y.; Ge, J.; Yu, S.H. Macroscopic Free-Standing Hierarchical 3D Architectures Assembled from Silver Nanowires by Ice Templating. *Angew. Chemie-Int. Ed.* **2014**, *53*, 4561–4566. [[CrossRef](#)] [[PubMed](#)]
22. Ahn, Y.; Lee, H.; Lee, D.; Lee, Y. Highly Conductive and Flexible Silver Nanowire-Based Microelectrodes on Biocompatible Hydrogel. *ACS Appl. Mater. Interfaces* **2014**, *6*, 18401–18407. [[CrossRef](#)]
23. Zhang, Y.; He, P.; Luo, M.; Xu, X.; Dai, G.; Yang, J. Highly Stretchable Polymer/Silver Nanowires Composite Sensor for Human Health Monitoring. *Nano Res.* **2020**, *13*, 919–926. [[CrossRef](#)]
24. Tang, P.; Yan, H.; Chen, L.; Wu, Q.; Zhao, T.; Li, S.; Gao, H.; Liu, M. Anisotropic Nanocomposite Hydrogels with Enhanced Actuating Performance through Aligned Polymer Networks. *Sci. China Mater.* **2020**, *63*, 832–841. [[CrossRef](#)]
25. Deng, J.; Yuk, H.; Wu, J.; Varela, C.E.; Chen, X.; Roche, E.T.; Guo, C.F.; Zhao, X. Electrical Bioadhesive Interface for Bioelectronics. *Nat. Mater.* **2021**, *20*, 229–236. [[CrossRef](#)] [[PubMed](#)]
26. Liao, H.; Guo, X.; Wan, P.; Yu, G. Conductive MXene Nanocomposite Organohydrogel for Flexible, Healable, Low-Temperature Tolerant Strain Sensors. *Adv. Funct. Mater.* **2019**, *29*, 1904507. [[CrossRef](#)]
27. Fu, S.; Zhu, Y.; Zhang, Y.; Zhang, M.; Wang, D. Recent Advances in Carbon Nanomaterials-Based Electrochemical Sensors for Phenolic Compounds Detection. *Microchem. J.* **2021**, *171*, 106776. [[CrossRef](#)]
28. Liang, S.; Zhang, Y.; Wang, H.; Xu, Z.; Chen, J.; Bao, R.; Tan, B.; Cui, Y.; Fan, G.; Wang, W.; et al. Paintable and Rapidly Bondable Conductive Hydrogels as Therapeutic Cardiac Patches. *Adv. Mater.* **2018**, *30*, 1704235. [[CrossRef](#)]
29. Duan, J.; Liang, X.; Guo, J.; Zhu, K.; Zhang, L. Ultra-Stretchable and Force-Sensitive Hydrogels Reinforced with Chitosan Microspheres Embedded in Polymer Networks. *Adv. Mater.* **2016**, *28*, 8037–8044. [[CrossRef](#)]
30. Go, Y.M.; Jones, D.P. The Redox Proteome. *J. Biol. Chem.* **2013**, *288*, 26512–26520. [[CrossRef](#)]
31. Wu, S.; Kim, E.; Li, J.; Bentley, W.E.; Shi, X.-W.; Payne, G.F. Catechol-Based Capacitor for Redox-Linked Bioelectronics. *ACS Appl. Electron. Mater.* **2019**, *1*, 1337–1347. [[CrossRef](#)] [[PubMed](#)]
32. Yan, K.; Liu, Y.; Zhang, J.; Correa, S.O.; Shang, W.; Tsai, C.C.; Bentley, W.E.; Shen, J.; Scarcelli, G.; Raub, C.B.; et al. Electrical Programming of Soft Matter: Using Temporally Varying Electrical Inputs to Spatially Control Self Assembly. *Biomacromolecules* **2018**, *19*, 364–373. [[CrossRef](#)] [[PubMed](#)]
33. Munoz-Robles, B.G.; Kopyeva, I.; DeForest, C.A. Surface Patterning of Hydrogel Biomaterials to Probe and Direct Cell–Matrix Interactions. *Adv. Mater. Interfaces* **2020**, *7*, 1–25. [[CrossRef](#)]
34. Da Silva, A.C.; Wang, J.; Minev, I.R. Electro-Assisted Printing of Soft Hydrogels via Controlled Electrochemical Reactions. *Nat. Commun.* **2022**, *13*, 1353. [[CrossRef](#)]
35. Liao, M.; Wan, P.; Wen, J.; Gong, M.; Wu, X.; Wang, Y.; Shi, R.; Zhang, L. Wearable, Healable, and Adhesive Epidermal Sensors Assembled from Mussel-Inspired Conductive Hybrid Hydrogel Framework. *Adv. Funct. Mater.* **2017**, *27*, 1703852. [[CrossRef](#)]
36. Liang, Y.; Zhao, X.; Hu, T.; Chen, B.; Yin, Z.; Ma, P.X.; Guo, B. Adhesive Hemostatic Conducting Injectable Composite Hydrogels with Sustained Drug Release and Photothermal Antibacterial Activity to Promote Full-Thickness Skin Regeneration During Wound Healing. *Small* **2019**, *15*, e1900046. [[CrossRef](#)]
37. Pan, Z.; Wang, Z.Y.; Wang, M.H.; Yang, L.; Yu, S.H. Adhesive Aero-Hydrogel Hybrid Conductor Assembled from Silver Nanowire Architectures. *Sci. China Mater.* **2021**, *64*, 2868–2876. [[CrossRef](#)]
38. Lin, L.; Wu, Q. Improved Conductivity of Polysaccharide-Co-Polyacrylate/Polyaniline Conducting Hydrogels. *Polym. Polym. Compos.* **2012**, *20*, 377–386. [[CrossRef](#)]
39. Zhang, J.; Wu, C.; Xu, Y.; Chen, J.; Ning, N.; Yang, Z.; Guo, Y.; Hu, X.; Wang, Y. Highly Stretchable and Conductive Self-Healing Hydrogels for Temperature and Strain Sensing and Chronic Wound Treatment. *ACS Appl. Mater. Interfaces* **2020**, *12*, 40990–40999. [[CrossRef](#)]

40. Kim, J.H.; Kim, S.R.; Kil, H.J.; Kim, Y.C.; Park, J.W. Highly Conformable, Transparent Electrodes for Epidermal Electronics. *Nano Lett.* **2018**, *18*, 4531–4540. [[CrossRef](#)]
41. Liu, Q.; Yang, S.; Ren, J.; Ling, S. Flame-Retardant and Sustainable Silk Ionotronic Skin for Fire Alarm Systems. *ACS Mater. Lett.* **2020**, *2*, 712–720. [[CrossRef](#)]
42. Yang, C.; Suo, Z. Hydrogel Ionotronics. *Nat. Rev. Mater.* **2018**, *3*, 125–142. [[CrossRef](#)]
43. Leger, J.; Berggren, M.; Carter, S. *Iontronics: Ionic Carriers in Organic Electronic Materials and Devices*; CRC Press: Boca Raton, FL, USA, 2011; p. 247.
44. Gao, Z.; Li, Y.; Shang, X.; Hu, W.; Gao, G.; Duan, L. Bio-Inspired Adhesive and Self-Healing Hydrogels as Flexible Strain Sensors for Monitoring Human Activities. *Mater. Sci. Eng. C* **2020**, *106*, 110168. [[CrossRef](#)] [[PubMed](#)]
45. Han, X.; Jiang, D.; Qu, X.; Bai, Y.; Cao, Y.; Luo, R.; Li, Z. A Stretchable, Self-Healable Triboelectric Nanogenerator as Electronic Skin for Energy Harvesting and Tactile Sensing. *Materials* **2021**, *14*, 1689. [[CrossRef](#)]
46. Sarwar, M.S.; Dobashi, Y.; Preston, C.; Wyss, J.K.M.; Mirabbasi, S.; David, J.; Madden, W. Bend, Stretch, and Touch: Locating a Finger on an Actively Deformed Transparent Sensor Array. *Sci. Adv.* **2017**, *3*, e1602200. [[CrossRef](#)] [[PubMed](#)]
47. Lei, Z.; Wang, Q.; Sun, S.; Zhu, W.; Wu, P. A Bioinspired Mineral Hydrogel as a Self-Healable, Mechanically Adaptable Ionic Skin for Highly Sensitive Pressure Sensing. *Adv. Mater.* **2017**, *29*, 1700321. [[CrossRef](#)] [[PubMed](#)]
48. Yang, N.; Qi, P.; Ren, J.; Yu, H.; Liu, S.; Li, J.; Chen, W.; Kaplan, D.L.; Ling, S. Polyvinyl Alcohol/Silk Fibroin/Borax Hydrogel Ionotronics: A Highly Stretchable, Self-Healable, and Biocompatible Sensing Platform. *ACS Appl. Mater. Interfaces* **2019**, *11*, 23632–23638. [[CrossRef](#)] [[PubMed](#)]
49. Lei, Z.; Wang, Q.; Wu, P. A Multifunctional Skin-like Sensor Based on a 3D Printed Thermo-Responsive Hydrogel. *Mater. Horizons* **2017**, *4*, 694–700. [[CrossRef](#)]
50. Zhang, C.; Sun, W.; Chen, H.; Liu, L.; Li, B.; Li, D. Electromechanical Deformation of Conical Dielectric Elastomer Actuator with Hydrogel Electrodes. *J. Appl. Phys.* **2016**, *119*, 1223. [[CrossRef](#)]
51. Pei, X.; Zhang, H.; Zhou, Y.; Zhou, L.; Fu, J. Stretchable, Self-Healing and Tissue-Adhesive Zwitterionic Hydrogels as Strain Sensors for Wireless Monitoring of Organ Motions. *Mater. Horizons* **2020**, *7*, 1872–1882. [[CrossRef](#)]
52. Zhang, J.; Zhang, Q.; Liu, X.; Xia, S.; Gao, Y.; Gao, G. Flexible and Wearable Strain Sensors Based on Conductive Hydrogels. *J. Polym. Sci.* **2022**, *60*, 2663–2678. [[CrossRef](#)]
53. Parvez, S.; Long, M.J.C.; Poganik, J.R.; Aye, Y. Correction to Redox Signaling by Reactive Electrophiles and Oxidants. *Chem. Rev.* **2019**, *119*, 4464–4469. [[CrossRef](#)] [[PubMed](#)]
54. Petra, A.I.; Panagiotidou, S.; Hatzigelaki, E.; Stewart, J.M.; Conti, P.; Theoharides, T.C. Gut-Microbiota-Brain Axis and Its Effect on Neuropsychiatric Disorders with Suspected Immune Dysregulation. *Clin. Ther.* **2015**, *37*, 984–995. [[CrossRef](#)] [[PubMed](#)]
55. Valko, M.; Leibfritz, D.; Moncol, J.; Cronin, M.T.D.; Mazur, M.; Telser, J. Free Radicals and Antioxidants in Normal Physiological Functions and Human Disease. *Int. J. Biochem. Cell Biol.* **2007**, *39*, 44–84. [[CrossRef](#)] [[PubMed](#)]
56. Wu, L.-Q.; McDermott, M.K.; Zhu, C.; Ghodssi, R.; Payne, G.F. Mimicking Biological Phenol Reaction Cascades to Confer Mechanical Function. *Adv. Funct. Mater.* **2006**, *16*, 1967–1974. [[CrossRef](#)]
57. Wu, S.; Yan, K.; Zhao, Y.; Tsai, C.C.; Shen, J.; Bentley, W.E.; Chen, Y.; Deng, H.; Du, Y.; Payne, G.F.; et al. Electrical Writing onto a Dynamically Responsive Polysaccharide Medium: Patterning Structure and Function into a Reconfigurable Medium. *Adv. Funct. Mater.* **2018**, *28*, 1803139. [[CrossRef](#)]
58. Wu, S.; Zhao, Z.; Rzas, J.R.; Kim, E.; Li, J.; VanArsdale, E.; Bentley, W.E.; Shi, X.; Payne, G.F. Hydrogel Patterning with Catechol Enables Networked Electron Flow. *Adv. Funct. Mater.* **2021**, *31*, 2007709. [[CrossRef](#)]
59. Wu, S.; Kim, E.; Chen, C.Y.; Li, J.; VanArsdale, E.; Grieco, C.; Kohler, B.; Bentley, W.E.; Shi, X.; Payne, G.F. Catechol-Based Molecular Memory Film for Redox Linked Bioelectronics. *Adv. Electron. Mater.* **2020**, *6*, 2000452. [[CrossRef](#)]
60. Kim, E.; Li, J.; Kang, M.; Kelly, D.L.; Chen, S.; Napolitano, A.; Panzella, L.; Shi, X.; Yan, K.; Wu, S.; et al. Redox Is a Global Biodevice Information Processing Modality. *Proc. IEEE* **2019**, *107*, 1402–1424. [[CrossRef](#)]
61. Kim, E.; Liu, Z.; Liu, Y.; Bentley, W.E.; Payne, G.F. Catechol-Based Hydrogel for Chemical Information Processing. *Biomimetics* **2017**, *2*, 11. [[CrossRef](#)]
62. Vanarsdale, E.; Hörnström, D.; Sjöberg, G.; Järbur, I.; Pitzer, J.; Payne, G.F.; Van Maris, A.J.A.; Bentley, W.E. A Coculture Based Tyrosine-Tyrosinase Electrochemical Gene Circuit for Connecting Cellular Communication with Electronic Networks. *ACS Synth. Biol.* **2020**, *9*, 1117–1128. [[CrossRef](#)] [[PubMed](#)]
63. Kim, E.; Liu, Y.; Bentley, W.E.; Payne, G.F. Redox Capacitor to Establish Bio-Device Redox-Connectivity. *Adv. Funct. Mater.* **2012**, *22*, 1409–1416. [[CrossRef](#)]
64. Liu, H.; Qu, X.; Kim, E.; Lei, M.; Dai, K.; Tan, X.; Xu, M.; Li, J.; Liu, Y.; Shi, X.; et al. Bio-Inspired Redox-Cycling Antimicrobial Film for Sustained Generation of Reactive Oxygen Species. *Biomaterials* **2018**, *162*, 109–122. [[CrossRef](#)]
65. Kim, E.; Liu, Y.; Baker, C.J.; Owens, R.; Xiao, S.; Bentley, W.E.; Payne, G.F. Redox-Cycling and H₂O₂ Generation by Fabricated Catecholic Films in the Absence of Enzymes. *Biomacromolecules* **2011**, *12*, 880–888. [[CrossRef](#)] [[PubMed](#)]
66. Shang, W.; Chen, C.Y.; Lo, K.; Payne, G.F.; Bentley, W.E. Chip Modularity Enables Molecular Information Access from Organ-on-chip Devices with Quality Control. *Sensors Actuators B Chem.* **2019**, *295*, 30–39. [[CrossRef](#)]
67. Yan, K.; Liu, Y.; Guan, Y.; Bhokisham, N.; Tsao, C.Y.; Kim, E.; Shi, X.W.; Wang, Q.; Bentley, W.E.; Payne, G.F. Catechol–chitosan Redox Capacitor for Added Amplification in Electrochemical Immunoanalysis. *Colloids Surf. B Biointerfaces* **2018**, *169*, 470–477. [[CrossRef](#)]

68. Annu; Raja, A.N. Recent Development in Chitosan-Based Electrochemical Sensors and Its Sensing Application. *Int. J. Biol. Macromol.* **2020**, *164*, 4231–4244. [[CrossRef](#)]
69. Ou, Y.; Tian, M. Advances in Multifunctional Chitosan-Based Self-Healing Hydrogels for Biomedical Applications. *J. Mater. Chem. B* **2021**, *9*, 7955–7971. [[CrossRef](#)]
70. Shi, X.; Wu, P. A Smart Patch with On-Demand Detachable Adhesion for Bioelectronics. *Small* **2021**, *17*, 2101220. [[CrossRef](#)]
71. Si, R.; Gao, C.; Guo, R.; Lin, C.; Li, J.; Guo, W. Human Mesenchymal Stem Cells Encapsulated-Coacervated Photoluminescent Nanodots Layered Bioactive Chitosan/Collagen Hydrogel Matrices to Indorse Cardiac Healing after Acute Myocardial Infarction. *J. Photochem. Photobiol. B Biol.* **2020**, *206*, 111789. [[CrossRef](#)]
72. Shin, M.; Park, S.G.; Oh, B.C.; Kim, K.; Jo, S.; Lee, M.S.; Oh, S.S.; Hong, S.H.; Shin, E.C.; Kim, K.S.; et al. Complete Prevention of Blood Loss with Self-Sealing Haemostatic Needles. *Nat. Mater.* **2017**, *16*, 147–152. [[CrossRef](#)] [[PubMed](#)]
73. Nguyen, N.; Lin, Z.H.; Barman, S.R.; Korupalli, C.; Cheng, J.Y.; Song, N.X.; Chang, Y.; Mi, F.L.; Song, H.L.; Sung, H.W.; et al. Engineering an Integrated Electroactive Dressing to Accelerate Wound Healing and Monitor Noninvasively Progress of Healing. *Nano Energy* **2022**, *99*, 107393. [[CrossRef](#)]
74. Luo, X.; Liu, Y.; Qin, R.; Ao, F.; Wang, X.; Zhang, H.; Yang, M.; Liu, X. Tissue-Nanoengineered Hyperbranched Polymer Based Multifunctional Hydrogels as Flexible “Wounded Treatment-Health Monitoring” Bioelectronic Implant. *Appl. Mater. Today* **2022**, *29*, 101576. [[CrossRef](#)]
75. Huang, Y.; Mu, L.; Zhao, X.; Han, Y.; Guo, B. Bacterial Growth-Induced Tobramycin Smart Release Self-Healing Hydrogel for Pseudomonas Aeruginosa-Infected Burn Wound Healing. *ACS Nano* **2022**, *16*, 13022–13036. [[CrossRef](#)]
76. Chen, F.; Wu, M.; Dong, Q.; Ke, M.; Liang, X.; Ai, J.; Cheng, Q.; Cai, L.; Tong, Z.; Chen, Y. Arbitrarily Shapeable and Conductive Hydrogel with “Magic Cube” like Structure for Real-Time Monitoring and Promoting Wound Healing. *Compos. Part B Eng.* **2022**, *238*, 109903. [[CrossRef](#)]
77. Shukla, R.P.; Aroosh, M.; Matzafi, A.; Ben-Yoav, H. Partially Functional Electrode Modifications for Rapid Detection of Dopamine in Urine. *Adv. Funct. Mater.* **2021**, *31*, 2004146. [[CrossRef](#)]
78. Kim, J.N.; Lee, J.; Lee, H.; Oh, I.K. Stretchable and Self-Healable Catechol–chitosan–Diatom Hydrogel for Triboelectric Generator and Self-Powered Tremor Sensor Targeting at Parkinson Disease. *Nano Energy* **2021**, *82*, 105705. [[CrossRef](#)]
79. Wen, J.; Tang, J.; Ning, H.; Hu, N.; Zhu, Y.; Gong, Y.; Xu, C.; Zhao, Q.; Jiang, X.; Hu, X.; et al. Multifunctional Ionic Skin with Sensing, UV-Filtering, Water-Retaining, and Anti-Freezing Capabilities. *Adv. Funct. Mater.* **2021**, *31*, 2011176. [[CrossRef](#)]
80. Vakalopoulos, K.A.; Wu, Z.; Kroese, L.; Kleinrensink, G.J.; Jeekel, J.; Vendamme, R.; Dodou, D.; Lange, J.F. Mechanical Strength and Rheological Properties of Tissue Adhesives with Regard to Colorectal Anastomosis an Ex Vivo Study. *Ann. Surg.* **2015**, *261*, 323–331. [[CrossRef](#)]
81. Liu, H.; Wang, C.; Li, C.; Qin, Y.; Wang, Z.; Yang, F.; Li, Z.; Wang, J. A Functional Chitosan-Based Hydrogel as a Wound Dressing and Drug Delivery System in the Treatment of Wound Healing. *RSC Adv.* **2018**, *8*, 7533–7549. [[CrossRef](#)]
82. Duarte, A.P.; Coelho, J.F.; Bordado, J.C.; Cidade, M.T.; Gil, M.H. Surgical Adhesives: Systematic Review of the Main Types and Development Forecast. *Prog. Polym. Sci.* **2012**, *37*, 1031–1050. [[CrossRef](#)]
83. Sedó, J.; Saiz-Poseu, J.; Busqué, F.; Ruiz-Molina, D. Catechol-Based Biomimetic Functional Materials. *Adv. Mater.* **2013**, *25*, 653–701. [[CrossRef](#)]
84. Faure, E.; Falentin-Daudré, C.; Jérôme, C.; Lyskawa, J.; Fournier, D.; Woisel, P.; Detrembleur, C. Catechols as Versatile Platforms in Polymer Chemistry. *Prog. Polym. Sci.* **2013**, *38*, 236–270. [[CrossRef](#)]
85. Li, J.; Celiz, A.D.; Yang, J.; Yang, Q.; Wamala, I.; Whyte, W.; Seo, B.R.; Vasilyev, N.V.; Vlassak, J.J.; Suo, Z.; et al. Tough Adhesives for Diverse Wet Surfaces. *Science* **2017**, *357*, 378–381. [[CrossRef](#)]
86. Yang, J.; Bai, R.; Chen, B.; Suo, Z. Hydrogel Adhesion: A Supramolecular Synergy of Chemistry, Topology, and Mechanics. *Adv. Funct. Mater.* **2020**, *30*, 1901693. [[CrossRef](#)]
87. Jenkins, P.O.; Mehta, M.A.; Sharp, D.J. Catecholamines and Cognition after Traumatic Brain Injury. *Brain* **2016**, *139*, 2345–2371. [[CrossRef](#)] [[PubMed](#)]
88. Puscas, A.; Hosu, A.; Cimpoiu, C. Application of a Newly Developed and Validated High-Performance Thin-Layer Chromatographic Method to Control Honey Adulteration. *J. Chromatogr. A* **2013**, *1272*, 132–135. [[CrossRef](#)] [[PubMed](#)]
89. Yeganeh-Zare, S.; Farhadi, K.; Amiri, S. Rapid Detection of Apple Juice Concentrate Adulteration with Date Concentrate, Fructose and Glucose Syrup Using HPLC-RID Incorporated with Chemometric Tools. *Food Chem.* **2022**, *370*, 131015. [[CrossRef](#)]
90. Li, Y.; Sun, J.; Mao, W.; Tang, S.; Liu, K.; Qi, T.; Deng, H.; Shen, W.; Chen, L.; Peng, L. Antimony-Doped Tin Oxide Nanoparticles as Peroxidase Mimics for Paper-Based Colorimetric Detection of Glucose Using Smartphone Read-Out. *Microchim. Acta* **2019**, *186*, 403. [[CrossRef](#)]
91. Yang, J.; Shen, M.; Luo, Y.; Wu, T.; Chen, X.; Wang, Y.; Xie, J. Advanced Applications of Chitosan-Based Hydrogels: From Biosensors to Intelligent Food Packaging System. *Trends Food Sci. Technol.* **2021**, *110*, 822–832. [[CrossRef](#)]
92. Ye, Y.; Guo, H.; Sun, X. Recent Progress on Cell-Based Biosensors for Analysis of Food Safety and Quality Control. *Biosens. Bioelectron.* **2019**, *126*, 389–404. [[CrossRef](#)]
93. Artigues, M.; Gilabert-Porres, J.; Teixidó, R.; Borrós, S.; Abellà, J.; Colominas, S. Analytical Parameters of a Novel Glucose Biosensor Based on Grafted Pfm as a Covalent Immobilization Technique. *Sensors* **2021**, *21*, 4185. [[CrossRef](#)]
94. Li, X.; Falcone, N.; Hossain, M.N.; Kraatz, H.B.; Chen, X.; Huang, H. Development of a Novel Label-Free Impedimetric Electrochemical Sensor Based on Hydrogel/Chitosan for the Detection of Ochratoxin A. *Talanta* **2021**, *226*, 122183. [[CrossRef](#)]

95. Wu, S.; Rzasa, J.R.; Kim, E.; Zhao, Z.; Li, J.; Bentley, W.E.; Payne, N.N.; Shi, X.; Payne, G.F. Catechol Patterned Film Enables the Enzymatic Detection of Glucose with Cell Phone Imaging. *ACS Sustain. Chem. Eng.* **2021**, *9*, 14836–14845. [[CrossRef](#)]
96. Fang Wong, S.; Mei Khor, S. Differential Colorimetric Nanobiosensor Array as Bioelectronic Tongue for Discrimination and Quantitation of Multiple Foodborne Carcinogens. *Food Chem.* **2021**, *357*, 129801. [[CrossRef](#)] [[PubMed](#)]
97. Liu, J.; Zhang, N.; Li, J.; Li, M.; Wang, G.; Wang, W.; Fan, Y.; Jiang, S.; Chen, G.; Zhang, Y.; et al. A Novel Umami Electrochemical Biosensor Based on AuNPs@ZIF-8/Ti₃C₂ MXene Immobilized T1R1-VFT. *Food Chem.* **2022**, *397*, 133838. [[CrossRef](#)] [[PubMed](#)]
98. Motsuo, R. Role of Saliva in the Maintenance of Taste Sensitivity. *Crit. Rev. Oral Biol. Med.* **2000**, *11*, 216–229. [[CrossRef](#)]
99. Liu, Q.; Zhang, D.; Zhang, F.; Zhao, Y.; Jimmy Hsia, K.; Wang, P. Biosensor Recording of Extracellular Potentials in the Taste Epithelium for Bitter Detection. *Sens. Actuators B Chem.* **2013**, *176*, 497–504. [[CrossRef](#)]
100. Salvo-Comino, C.; García-Hernández, C.; García-Cabezón, C.; Rodríguez-Méndez, M.L. Discrimination of Milks with a Multisensor System Based on Layer-by-Layer Films. *Sensors* **2018**, *18*, 2716. [[CrossRef](#)]
101. Li, C.; Duan, L.; Cheng, X. Facile Method to Synthesize Fluorescent Chitosan Hydrogels for Selective Detection and Adsorption of Hg²⁺/Hg⁺. *Carbohydr. Polym.* **2022**, *288*, 119417. [[CrossRef](#)]
102. Fu, F.; Yang, B.; Hu, X.; Tang, H.; Zhang, Y.; Xu, X.; Zhang, Y.; Touhid, S.S.B.; Liu, X.; Zhu, Y.; et al. Biomimetic Synthesis of 3D Au-Decorated Chitosan Nanocomposite for Sensitive and Reliable SERS Detection. *Chem. Eng. J.* **2020**, *392*, 123693. [[CrossRef](#)]
103. Ye, Y.; Qi, X.; Wang, H.; Zhao, B.; Xu, L.; Zhang, Y.; Wang, X.; Zhou, N. A Surface-Enhanced Raman Scattering Aptasensor for Escherichia Coli Detection Based on High-Performance 3D Substrate and Hot Spot Effect. *Anal. Chim. Acta* **2022**, *1221*, 340141. [[CrossRef](#)] [[PubMed](#)]
104. Chen, Y.; Zhang, Y.; Liang, Z.; Cao, Y.; Han, Z.; Feng, X. Flexible Inorganic Bioelectronics. *npj Flex. Electron.* **2020**, *4*, 2. [[CrossRef](#)]
105. Dixon, T.A.; Williams, T.C.; Pretorius, I.S. Sensing the Future of Bio-Informational Engineering. *Nat. Commun.* **2021**, *12*, 388. [[CrossRef](#)] [[PubMed](#)]

Disclaimer/Publisher’s Note: The statements, opinions and data contained in all publications are solely those of the individual author(s) and contributor(s) and not of MDPI and/or the editor(s). MDPI and/or the editor(s) disclaim responsibility for any injury to people or property resulting from any ideas, methods, instructions or products referred to in the content.

MDPI
St. Alban-Anlage 66
4052 Basel
Switzerland
www.mdpi.com

Biosensors Editorial Office
E-mail: biosensors@mdpi.com
www.mdpi.com/journal/biosensors



Disclaimer/Publisher's Note: The statements, opinions and data contained in all publications are solely those of the individual author(s) and contributor(s) and not of MDPI and/or the editor(s). MDPI and/or the editor(s) disclaim responsibility for any injury to people or property resulting from any ideas, methods, instructions or products referred to in the content.



Academic Open
Access Publishing

[mdpi.com](https://www.mdpi.com)

ISBN 978-3-0365-9483-5